Effets de gaz-réel sur la transition freestream et les pertes au sein des turbines ORC

Aurélien Bienner

HESAM UNIVERSITÉ

Arts et Métiers Sciences et Technologies

ÉCOLE DOCTORALE SCIENCES ET MÉTIERS DE L'INGÉNIEUR

Laboratoire de dynamique des fluides (DynFluid)
Campus de Paris

THÈSE

présentée par : **Aurélien BIENNER**

soutenue le : **8 avril 2024**

pour obtenir le grade de : **Docteur d'HESAM Université**

préparée à : **École Nationale Supérieure d'Arts et Métiers**

Spécialité : **Mécanique**

Real gas effects on freestream turbulence induced transition and losses in ORC turbines

THÈSE DIRIGÉE PAR :

M. Xavier GLOERFELT
Mme. Paola CINNELLA

Jury

M. Christophe BAILLY, Professeur, Ecole Centrale de Lyon	Président
M. Richard SANDBERG, Professor, University of Melbourne	Rapporteur
M. Rene PECNIK, Professor, Delft University of Technology	Rapporteur
M. Stefan AUS DER WIESCHE, Professor, Fachhochschule Münster	Examinateur
M. Xavier GLOERFELT, Professeur, Arts et Métiers Paris	Directeur
Mme. Paola CINNELLA, Professeur, Sorbonne Université	Directrice

T H È S E

Remerciements

La réalisation de cette thèse a été rendu possible grâce à l'aide et au soutien continu de nombreux individus, et je voudrais exprimer ma reconnaissance à chacun d'eux pour leur contribution précieuse. Je souhaiterais tout d'abord remercier mon directeur de thèse Xavier Gloerfelt pour son encadrement tout au long de ce travail. Merci pour tous ces échanges très intéressants pour lesquels j'ai pris beaucoup de plaisir et qui m'ont fait fortement progresser. Ta disponibilité et ton aide ont été essentiels pour mener à bien ce projet de recherche, et je t'en suis profondément reconnaissant. J'aimerais ensuite remercier ma directrice de thèse Paola Cinnella pour son suivi durant ces 3 années. Merci pour ton aide et ton soutien tout au long de cette période, et notamment lors des conférences auxquels nous avons participé.

Je voudrais ensuite remercier les membres de mon jury, qui ont accepté de relire ce travail et participer à ma soutenance de thèse. Merci tout d'abord à Christophe Bailly d'avoir accepté de faire partie de mon comité de suivi de thèse, puis d'avoir présidé ce jury. Je tiens ensuite à remercier Richard Sandberg et Rene Pecnik d'avoir accepté d'être rapporteur de ce manuscrit, ainsi que pour leur précieux retours. Merci également à Stefan aus der Wiesche d'avoir participé en tant qu'examinateur à ma soutenance et pour ses remarques pertinentes.

Ce travail s'inscrivant dans le cadre d'une collaboration international avec l'université technologique de Münster, j'aimerais donc naturellement adressé mes remerciements à l'ensemble des personnes impliquées dans le projet. Merci en particulier à Stefan aus der Wiesche et Leander Hake pour tous ces échanges intéressants et cette collaboration fructueuse.

Je voudrais maintenant prendre le temps de remercier l'ensemble des personnes que je côtoie quotidiennement au laboratoire DynFluid depuis maintenant plus de 3 ans. Un grand merci à tous pour tous ces échanges riches et intéressants que nous avons pu avoir, et que j'ai vraiment apprécié. Merci notamment à Nicolas, Luca, Ismaïl, Jean-Christophe R., Jean-Christophe L. et Junior pour ces toutes ces discussions que nous avons eu ensemble. Merci Simon d'avoir accepté de partager ton bureau avec moi. Merci également Noureddine

et Patricia pour votre arrivée, qui a su dynamiser encore davantage le laboratoire. Je remercie également les anciens doctorants & post-doctorants -Maximilien, Camille, Antoine, Enza, J-C, Cosimo, Soufiane, Gabriele, Özgür, Ricardo- d'avoir partagé chacun à sa façon une partie de cette thèse avec moi. Merci également à ceux qui m'ont précédé à DynFluid -Alessandro, Mateus, Donato, Simon, Erwan, Léo, Paul, Nicola- mais également côté Sorbonne -Camille, Louenas, Paul-, et je leur souhaite une bonne continuation pour la suite de leurs travaux. J'ai trouvé l'environnement du laboratoire exceptionnellement agréable et stimulant, et il me manquera assurément à l'avenir.

Enfin, un grand merci à ma famille et à mes proches pour leur soutien tout au long de cette thèse, ainsi que pour leur présence lors de la soutenance. Merci à mes amis de collège, de prépa et d'École pour leur encouragements durant la thèse et d'avoir accepté de bonne grâce de m'appeler Docteur à l'issue de la soutenance. Merci à ma famille, qui m'a toujours encouragé dans mes projets, et également pour m'avoir donné l'occasion de perfectionner mes compétences pédagogiques lorsque je tentais de leur expliquer mon sujet de recherche. Merci Guillaume d'avoir partagé mon quotidien pendant ces deux premières années de thèse, malgré le fait que mon investissement limité dans Rocket League est pu malheureusement être source de frustration pour toi. Enfin, merci Jeanne d'avoir terminé cette aventure en beauté à mes côtés, cela n'étant que le prélude d'une autre aventure encore plus longue et prometteuse avec toi.

Abstract

Organic Rankine Cycle (ORC) systems appear as one of the solutions to answer the current energy and environmental challenges, owing to their significant potential for generating power. A key component for ORC is the expander, most often a turbine. For small systems, the latter works in the transonic to supersonic regimes and can be affected by the properties of the organic vapor used and exhibit strong non-ideal effects. In the present study, we investigate boundary layer (BL) transitions and loss mechanisms in turbines under conditions representative of ORC for the organic vapor Novec649.

We begin by reporting the first direct numerical simulation (DNS) and large-eddy simulations (LES) of transitional and turbulent BL of Novec at high-subsonic conditions. In the turbulent state, the profiles of dynamic flow properties are found to be little affected by the gas properties and remain very close to incompressible DNS databases, despite the high-subsonic flow speed and even if genuine but very small compressibility effects are present. Our LES strategy, which is based on the implicit subgrid-scale modeling, a target resolution at the wall but also an implicit time integration approach, is then validated against the reference DNS. LES are then performed to investigate the influence of forcing frequency and amplitude of the oblique modes on the established turbulent state.

As it is the most-likely transition mechanism in turbines, we investigate after that for the first time the freestream turbulence (FST)-induced transition of dense-gas BL on zero-pressure-gradient flat plates. Due to the high Reynolds number conditions, the thin BL experience large-scale incoming turbulent structures which can, for relatively high intensities, promote non-linear growth mechanism, characterized by low-speed Λ-shaped structures, instead of the classical laminar streak growth mechanism. Simulations in air are also performed at Mach 0.1 and 0.9, as a comparison of an incompressible-like and compressible perfect gas flows, respectively. Compared to Novec, air BL are found to be slightly more unstable but retains overall similar characteristics, in particular concerning the transition mechanisms observed.

ABSTRACT

In order to tackle a more realistic configuration and to see the influence of the high-Reynolds number conditions on receptivity effects, we then investigate, by means of LES, the FST induced transition past the thick leading edge of an idealized blade. In such conditions, the FST is characterized by relatively large scales compared to the BL size, but at the same time small compared to the blade thickness. This scale separation strongly influence the downstream evolution of the transitional boundary layer, leading ultimately to the formation of clusters of laminar streaks, modulated by the intense large-scale structures that develops at the leading-edge. Despite their low population, the low-speed streaks are found to be the turbulent spots precursors whereas the low-speed Λ structures, observed prior to the apparition of laminar streaks, do not take part in the transition because of the strong favorable pressure gradient present in the region where they appear.

Finally, the flow around the full idealized blade vane configuration is investigated. To cope with the stringent numerical requirements due to the high Reynolds number conditions, a RANS-LES approach is selected and the boundary-layers are modeled in RANS without transition model, justified by the transition occurring rapidly on the blade. In particular, the Delayed Detached-Eddy Simulations (DDES) approach is selected to accelerate the transition to resolved turbulence in separated shear layers, allowing fine-detail analysis of unsteady flow phenomena in the wake. As the non-ideality of the flow increases, a lower pressure ratio is achieved and the losses increases. With regards to air, Novec's high heat capacity reduces temperature fluctuations, suppressing the so-called energy separation phenomena, while accentuating pressure fluctuations in the wake. A large part of the losses are found to occurs in the wake region and, compared to DDES, RANS simulations leads to an underestimation of the losses by about 20% as it does not correctly model this part of the flow.

Keywords: High-fidelity simulations, LES, Implicit residual smoothing, Boundary layers transition, Freestream turbulence induced transition, ORC, Turbines, Losses, Unsteady wake

Résumé étendu

Introduction

Les systèmes basés sur les cycles de Rankine organique (ORC) apparaissent de plus en plus comme l'une des solutions pour répondre aux défis énergétiques et environnementaux actuels en raison de leur important potentiel en termes de récupération d'énergie [1]. Les ORC sont basés sur le cycle thermodynamique classique de Rankine, un cycle fonctionnant en boucle fermée et réalisé au moyen d'un compresseur, d'un détendeur et d'échangeurs de chaleur (voir Fig. 1 à gauche), qui est utilisé depuis longtemps pour récupérer l'énergie à partir de sources de chaleur. A la place de l'eau, les fluides de travail des ORC sont des composés organiques complexes caractérisés par une complexité moléculaire faible à élevée, des poids moléculaires modérés à élevés et des températures d'ébullition relativement basses [2]. L'utilisation de ces fluides organiques donne un degré de liberté supplémentaire au cycle thermodynamique, permettant l'exploitation de sources de chaleur à des températures plus basses que celles atteignables avec de l'eau [1]. Les ORC sont par exemple utilisés pour récupérer l'énergie à partir de sources d'énergie renouvelable telles que les réservoirs géothermiques, le rayonnement solaire et le gradient thermique océanique, mais aussi la chaleur fatale des installations industrielles ou des gaz d'échappement des moteurs.

Dans les conditions thermodynamiques typiques des applications ORC, les fluides de travail organiques peuvent fonctionner dans ce qu'on appelle le régime des gaz denses. Les gaz denses sont généralement définis comme des fluides monophasiques, caractérisés par des molécules suffisamment complexes, travaillant dans des conditions de pression et de température du même ordre de grandeur que leur point critique thermodynamique (voir, par exemple, Guardone *et al.* [4] et les références citées). Dans de telles conditions, les effets des gaz réels jouent un rôle crucial dans le comportement dynamique du fluide [5], d'une manière qui dépend fortement de sa complexité moléculaire et de son poids, ce qui détermine à son tour le nombre de degrés de liberté vibrationnels actifs selon la température de travail du fluide. Pour décrire le comportement dynamique des gaz des fluides,

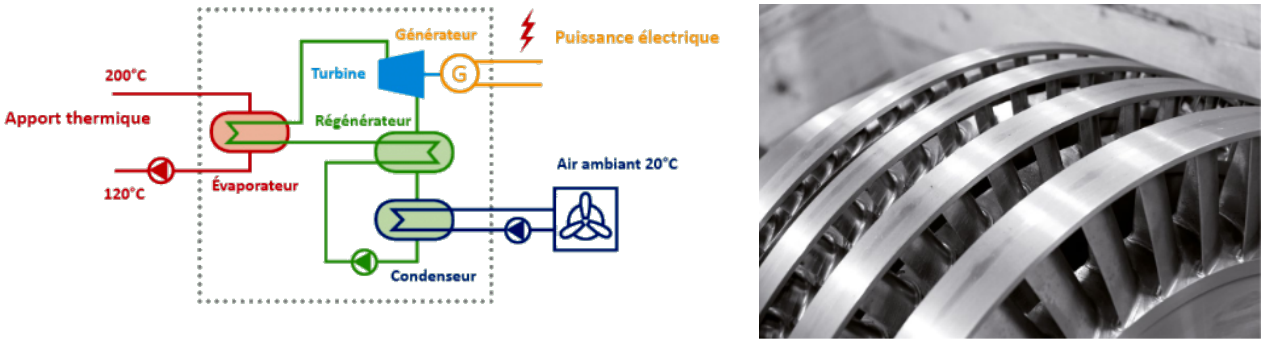

Figure 1: Gauche: Cycle de Rankine organique (site web d'Enertime [3]). Droite: Exemple d'une turbine axiale à plusieurs étages (site web d'Enertime [3]).

Thompson [6] a introduit la dérivée fondamentale de la dynamique des gaz :

$$\Gamma := \frac{v^3}{2c^2}\left.\frac{\partial^2 p}{\partial v^2}\right|_s = 1 + \frac{\rho}{c}\left.\frac{\partial c}{\partial \rho}\right|_s, \tag{1}$$

où ρ est la densité, $v = 1/\rho$ le volume spécifique, p la pression, s l'entropie, et $c = \sqrt{\partial p/\partial \rho|_s}$ la vitesse du son. La première égalité dans l'équation (1) montre que Γ est lié à la courbure des lignes isentropiques dans le plan p-v ; selon la deuxième définition, Γ est une mesure du taux de variation de la vitesse du son dans les transformations isentropiques. Un régime de gaz dense, défini par $\Gamma < 1$, implique $\partial c/\partial \rho|_s < 0$, ce qui signifie que la vitesse du son augmente dans les expansions isentropiques et diminue dans les compressions isentropiques, contrairement au cas des gaz parfaits, où :

$$\Gamma = \frac{\gamma + 1}{2}, \tag{2}$$

$\gamma = c_p/c_v$ étant le rapport de la chaleur spécifique isobare c_p à la chaleur spécifique isochore c_v. Pour la stabilité thermodynamique, γ est toujours supérieur à l'unité, donc $\Gamma > 1$ pour les gaz parfaits. Au contraire, les gaz lourds caractérisés par des rapports élevés c_v/R (R étant la constante des gaz) présentent des plages étendues de densité et de pressions où Γ est inférieur à l'unité. Les molécules les plus complexes, appelées fluides Bethe–Zel'dovich–Thompson (BZT) [7, 8, 6], sont même caractérisées par des conditions de plage thermodynamique où Γ devient négatif (la "zone d'inversion"), ce qui peut entraîner des effets de compressibilité non classiques dans les régimes d'écoulement transsonique et supersonique. Dans la limite de basse densité, où le comportement du gaz parfait est retrouvé, la complexité moléculaire du gaz joue toujours un rôle, conduisant à un rapport de chaleur spécifique γ très proche de 1 : pour $\gamma \to 1$ les transformations isentropiques des gaz idéaux, pour lesquelles la loi isentropique bien connue de Laplace ($pv^\gamma = \text{const}$) est valide, deviennent également isothermes ($pv = \text{const}$).

Dans la plupart des ORC, même si différentes alternatives de détendeurs existent [9], le fluide de travail est généralement détendu dans une turbine (voir Fig. 1.1 à droite). Ce dernier composant peut être critique pour l'efficacité du cycle et, dans le but d'atteindre des performances toujours plus élevées, il est de la plus haute importance d'estimer les divers mécanismes de perte. Les origines des pertes au sein des turbines sont détaillées dans la revue de Denton [10]. En l'absence de transfert de chaleur et d'effets de non-équilibre, la création d'entropie provient du frottement visqueux dans les couches de cisaillement. En particulier, compte tenu de la grande proportion de parois, une source majeure de pertes dans les turbines est souvent les couches limites. Ces pertes sont influencées par l'état de la couche limite, c'est-à-dire laminaire ou turbulent, et son développement. Être capable de prédire la transition laminaire-turbulente des couches limites est donc très important, pour savoir où l'écoulement est susceptible d'être turbulent ou de se séparer car cela affectera directement les pertes estimées. Une autre source importante de pertes est liée au développement du sillage, provenant des couches de cisaillement libres se formant au bord de fuite et étant directement affectées par l'état des couches limites se détachant. Comme cela peut représenter une proportion importante des pertes de profil [11], la prédiction correcte de la formation du sillage au niveau du bord de fuite est également d'une importance primordiale.

Dans le cadre de ce travail, les mécanismes de transition et de perte dans les turbines ORC sont étudiés à l'aide de simulations hautes fidélités. En particulier, le fluide de travail considéré est le Novec649, un fluide à faible impact sur l'environnement déjà utilisé au sein des ORC. Plus précisément, les objectifs de la thèse sont les suivants :

1. Tout d'abord, les effets des gaz réels sur le développement d'une couche limite de gaz dense sont quantifiés dans des conditions thermodynamiques représentatives des applications ORC. Ainsi, une référence numérique d'une couche limite turbulente de Novec649 est obtenu et est ensuite utilisée pour évaluer notre stratégie numérique basée sur des simulations des grandes échelles de la turbulence (LES) et une intégration temporelle implicite.

2. Ensuite, la transition de couche limites de gaz dense induite par la turbulence extérieure est étudiée dans une configuration canonique, à savoir une configuration de plaque plane à gradient de pression nul. Différentes conditions de turbulence extérieure sont testées. En particulier, l'influence de grandes structures turbulentes sur la transition est examinée.

3. Ensuite, nous étudions la transition induite par la turbulence extérieure dans une configuration plus

complexe, à savoir un bord d'attaque de turbine, afin de comprendre l'influence de la réceptivité du bord d'attaque et du gradient de pression favorable sur la transition.

4. Enfin, nous nous intéressons à l'écoulement à travers une configuration d'aube de turbine idéalisée pour obtenir plus d'informations sur les pertes dans les turbines ORC pour les gaz non idéaux.

La thèse est organisée comme suit. Dans le Chapitre 2, les équations de référence et les méthodes numériques sont décrites, et en particulier la mise en œuvre et l'amélioration de la stratégie temporelle implicite (voir la section 2.4). Dans le Chapitre 3, les résultats d'une DNS de référence pour l'état de transition et turbulent d'une couche limite de Novec649 sont présentés et comparés aux simulations LES. Le Chapitre 4 présente diverses simulations LES de transitions induites par la turbulence extérieure sur une couche limite de Novec649 sous différentes conditions de turbulence extérieure. Pour caractériser l'influence de gaz réel sur la transition, les simulations sont comparées à des couches limites d'air dans des conditions quasi-incompressible à Mach M=0.1 et compressibles à M=0.9. Dans le Chapitre 5, les résultats des simulations LES de transition autour d'un bord d'attaque épais de turbine sont discutés. Enfin, dans le Chapitre 6, l'écoulement de Novec649 dans un régime de gaz dense autour d'une configuration d'aube de turbine idéalisée est étudié au moyen de simulations RANS-LES.

Chapitre 2 : Équations résolues et méthodes numériques

Les simulations sont réalisées au sein du code de calcul MUSICAA (MUltiblock solver IN COmputational AEroacoustics and AEroacoustics), un solveur différence finies d'ordre élevées bien validé et très performant écrit en Fortran et parallélisé avec la bibliothèque MPI. Le code résout les équations compressibles de Navier-Stokes et s'appuie sur une stratégie parallèle multi-blocs, ainsi que sur une transformation de coordonnées pour les grilles structurées curvilignes. Afin de pouvoir étudier les écoulements de gaz parfaits et réels, le solveur est équipé de plusieurs équations d'état. Dans ce qui suit, l'air est modélisé comme un gaz parfait et les propriétés de transports pour l'air sont obtenues à l'aide de la loi de Sutherland. Concernant le Novec, comme des conditions relativement diluées pour la phase vapeur sont considérées, une équation d'état cubique est choisie pour réduire le surcoût lors des intégrations par simulation directe, à savoir l'équation d'état de Peng-Robinson [12] modifiée par Stryjek & Vera [13]. De plus, le modèle de viscosité pour les gaz denses de Chung, Lee & Starling est sélectionné. Ce choix de modélisation du fluide Novec est validé par rapport au modèle de référence REFPROP à l'aide d'une couche limite laminaire. Il conduit, dans les conditions thermodynamiques considérées, à des

résultats satisfaisants.

Dans la suite, les équations de Navier-Stokes compressibles sont discrétisées par des différences finies centrées, d'ordre 10 et d'ordre 4 respectivement pour les flux eulériens et les flux visqueux. Les oscillations maille à maille sont dissipées à l'aide d'un filtrage sélectif centré d'ordre 10. Pour les configurations transsoniques ou supersoniques (chapitre 6), pour capturer les chocs, le filtrage sélectif d'ordre élevé est combiné à un terme d'ordre faible activé à proximité des discontinuités de l'écoulement repéré grâce à un détecteur de choc. Dans les simulations des grandes échelles réalisées dans cette thèse, le filtrage sélectif est directement utilisé comme terme de régularisation à la place d'un modèle de sous-maille explicite, cette approche implicite ayant été démontré comme étant la plus intéressante en termes de précision et de coût de calcul par Aubard *et al.* [14] et Gloerfelt & Cinnella [15]. Concernant l'intégration en temps, le Runge–Kutta (RK4) explicite à quatre étapes et à faible stockage de Jameson *et al.* [16] est sélectionné. Son ordre de précision est égal à 4 pour les équations linéaires et se réduit à 2 pour les problèmes non linéaires.

Dans les simulations directes et des grandes échelles, de très petits pas d'espace sont utilisés à proximité des parois solides afin de résoudre les structures de la couche limite. En raison des critères de stabilité CFL restrictifs des schémas temporelles explicites, le pas de temps numérique maximal autorisé est également très petit, notamment comparé au pas de temps maximal autorisé par la physique, ce qui entraîne des coûts de calcul élevés. Pour relâcher cette contrainte et pouvoir augmenter le CFL, le RK4 est combiné avec un opérateur de lissage des résidus d'ordre 4 (IRS4) initialement introduit par Cinnella & Content [17]. Dans le cadre de cette thèse, plusieurs améliorations ont été introduites par rapport à la version originale afin d'accroître la robustesse à des niveaux élevés de CFL et de permettre l'utilisation de grilles curvilignes. Tout d'abord, nous avons montré que l'utilisation d'une stratégie de filtrage sélectif au lieu de la viscosité artificielle améliore l'amortissement des modes sous-résolus, ce qui renforce la robustesse. En effet, les termes de dissipation numérique dans le schéma spatial ont tendance à être contractés à zéro par l'opérateur IRS4, ce qui peut compromettre l'élimination efficace des oscillations parasites près de la coupure de maillage. Au contraire, le filtrage est indépendant de la méthode d'avancement dans le temps et peut être appliqué à la fin de chaque itération temporelle pour amortir les oscillations entre les grilles. Ensuite, nous avons introduit des opérateurs IRS à nombre de points réduit pour remplir la matrice IRS près des limites du domaine. Les coefficients sur la première ligne de la matrice pentadiagonale correspondent à un opérateur IRS1 décentré, et les coefficients IRS2 sont utilisés pour la deuxième ligne. Cette approche présente de meilleures propriétés de stabilité que la simple troncature de la matrice de l'opérateur. De plus, nous avons discuté de la mise en oeuvre parallèle et multi-blocs de la

méthode. Cette dernière repose sur un chevauchement entre domaines adjacents, où les points fantômes sont communiqués. La largeur optimale du chevauchement est de l'ordre de 2CFL+1, ce qui limite la propagation des erreurs numériques dues aux approximations matricielles à l'intérieur des régions chevauchées. Enfin, L'IRS4 a été reformulé dans un contexte de différences finies sur grilles curvilignes. Le couplage des directions du maillage par la transformation des coordonnées est pris en compte en utilisant le rayon spectral de la jacobienne du flux eulérien, moyenné sur toutes les directions, comme échelle de vitesse caractéristique dans l'opérateur de l'IRS4. Au final, avec un surcoût entre 15 et 30% par implicite direction, l'utilisation de l'IRS4 conduit à des gains de temps de calcul importants d'un facteur 3 à 5, tout en préservant la précision globale des simulations.

Chapitre 3 : Écoulements de couche limite haut-subsonique de vapeur organique

Dans ce chapitre, nous présentons des études DNS et LES des écoulements de la couche limite (BL) de Novec649 dans des conditions représentatives des applications ORC. Une motivation importante est de réaliser une DNS de référence pour le développement spatial d'une couche limite et de quantifier les effets de gaz réel dans des conditions réalistes. En particulier, nous réalisons une transition modale à partir d'une paire de modes obliques, déterminée grâce à une étude préliminaire de stabilité linéaire réalisée dans [18]. Malgré un écoulement haut-subsonique à Mach 0.9, le comportement dynamique de la couche limite turbulente de Novec est très proche des bases de données incompressibles en air, même si de véritables effets de compressibilité (mais très faible) sont néanmoins observés sur les grandeurs thermophysiques. De plus, à cause de la capacité calorifique élevé du Novec, on observe que le mode thermique est fortement amorti et le mode acoustique est renforcé.

Ensuite, différentes LES sont réalisées sur la même configuration pour évaluer notre stratégie numérique, notamment l'intégration temporelle implicite. Les résultats des LES résolues en paroi sont très proches de la DNS, ce qui valide la résolution de grille choisie ainsi que la modélisation implicite des échelles de sous-maille. En raison d'un filtrage moins fréquent, la stratégie LES implicite en temps basée sur l'IRS4 est plus performante que l'approche explicite, avec un gain en coût de calcul autour de 3.5. De plus, l'application du filtre en dehors de l'opérateur IRS4 n'a pas d'impact sur le résultat tout en renforçant la stabilité de l'approche pour des CFL élevés. Enfin, dans la configuration étudiée, l'intégration des termes visqueux à chaque ou à la dernière sous-étape RK n'a pas d'impact sur les résultats.

Dans des LES supplémentaires, nous faisons également varier l'amplitude et la fréquence des modes

obliques induisant la transition afin de déterminer l'influence des paramètres de forçage et évaluer quand un état turbulent d'équilibre est atteint. Comme $Re_{\theta,in}$ est relativement élevé, les effets de mémoire persistent dans la couche limite turbulente. Les légères différences observées dans la couche limite turbulente en faisant varier les paramètres de forçage sont dues à l'historique de la transition, comme le révèle la décomposition du coefficient de frottement C_f.

Chapitre 4 : Influence de grandes structures turbulentes à l'extérieure de la couche limite sur la transition bypass dans les écoulements d'air et de vapeur organique

Dans ce chapitre, la transition induite par la turbulence extérieure dans des couches limites à gradient de pression nul sur plaques planes est étudiée à l'aide de simulations LES. Les conditions d'écoulement pour la couche limite de Novec649 sont choisies comme représentatives des turbomachines ORC, avec M=0.9, une température de 100 °C et une pression de 4 bars. En particulier, nous nous intéressons à l'influence des échelles intégrale longitudinales (L_f) élevées sur la transition bypass pour différentes intensités de turbulence extérieure (T_u). L'échelle intégrale longitudinale L_f est augmentée d'un facteur sept entre les cas de faible et de fort L_f. Des intensités de turbulence extérieure plus importantes favorisent toujours la transition, tandis que augmenter L_f conduit à un double effet selon l'intensité T_u sélectionné. Pour T_u=2.5%, un L_f plus grand accélère la transition et l'inverse est observé à 4%. De plus, T_u & L_f influencent également la longueur de la région de transition et la taille des stries laminaires. Enfin, L_f influence la distribution de l'amplitude des stries laminaires, comme démontré par un algorithme de détection de stries.

Une comparaison avec des écoulements en air dans des conditions bas-subsonique (M=0.1) et haut-subsonique (M=0.9) est effectuée pour observer indépendamment les effets du gaz dense et de la compressibilité sur la transition bypass. Tout d'abord, entre les cas air M=0.1 et 0.9, nous observons que la compressibilité retarde légèrement la transition à cause de la génération de stries thermiques. Dans les couches limites Novec, bien que les stries thermiques soient très faible à cause de la capacité calorifique élevé du Novec, la transition est encore davantage retardé. La croissance des stries est peu affectée par les effets de compressibilité ou de gaz dense et globalement, par rapport à l'influence des paramètres de la turbulence extérieure, les effets de gaz réel et de la compressibilité sont mineurs.

Une analyse détaillée des mécanismes de formation des spots turbulents est ensuite réalisée. Dans les cas où L_f est élevé, on observe la présence de structures basse vitesse en forme de Λ dans la couche limite apparaissant

avant les stries laminaires, que ce soit dans les écoulements en air ou en Novec. L'augmentation de L_f et de T_u favorise l'apparition de ces structures. Les ruptures turbulentes précoces de ces Λ entrent en compétition avec le mécanisme d'instabilité de stries. La position d'apparition des spots turbulents est obtenue à l'aide d'une discrimination laminaire-turbulente. Dans les cas où T_u=4%, le L_f le plus grand conduit à une distribution de l'apparition des spots turbulents à deux maximums. Cependant, même dans ce cas, la majorité des ruptures turbulentes se produit toujours par le biais d'instabilités de stries.

Enfin, l'influence de la turbulence extérieure sur la couche limite turbulente est également analysée. Comme les intensités de turbulence sont modérées (T_u<3.5% au dessus des couches limites turbulentes), les effets observés sont faibles. Dans le cas où L_f et T_u sont les plus élevés, la turbulence extérieure augmente légèrement le frottement à la paroi C_f et les fluctuations de vitesses en proche paroi. Le sillage de la couche limite est également légèrement affecté. La décomposition C_f de Renard-Deck montre que l'augmentation de C_f est principalement due à la contribution de la couche visqueuse interne.

Chapitre 5 : Effets du bord d'attaque sur la transition induite par la turbulence extérieure pour un écoulement de vapeur organique

Dans ce chapitre, une étude numérique est menée pour étudier la transition induite par la turbulence extérieure sur une aube idéalisée représentative des turbines ORC afin de faire la lumière sur les effets de réceptivité du bord d'attaque. La transition de la vapeur organique Novec dans la région du bord d'attaque (LE) est étudiée à l'aide d'une simulation LES résolue à la paroi. L'écoulement accélère de M=0.5 à 1 entre l'entrée et la sortie du domaine.

Par rapport aux études précédentes, le nombre de Reynolds basé sur la demi-épaisseur de la pale est supérieur d'un ordre de grandeur en raison de la densité élevée du Novec649. En raison des conditions en nombre de Reynolds élevé, les structures turbulente sont à la fois petites par rapport à la taille caractéristique du bord d'attaque, mais grandes par rapport à l'épaisseur de la couche limite. La turbulence d'entrée s'enroule autour du bord d'attaque en s'étirant et en s'inclinant, ce qui amplifie les fluctuations agissant sur la couche limite en train de se développer. Ces structures enveloppées apparaissent comme des clusters de petits tourbillons orientés dans le sens du courant, qui conduisent en aval à la formation de stries laminaires. Cette disposition à grande échelle dans le sens de l'envergure, sous forme d'amas, module le développement des stries laminaires et l'étalement des spots turbulents dans le sens de l'envergure. L'effet combiné du gradient favorable et de la modulation par les grandes échelles retarde et allonge la transition par rapport aux résultats obtenus sur plaques

planes (voir chapitre 4).

Globalement, la transition se produit quand même relativement tôt à $x/ch \sim 5\%$. L'origine des spots turbulents est analysée en détail à l'aide d'une discrimination laminaire-turbulente. Les précurseurs des spots sont systématiquement les stries laminaires basse vitesse au travers de deux mécanismes, les instabilités de stries et les interactions entre stries. Concernant le premier, aucune instabilité canonique évidente (sinueuse ou variqueuse) n'est observée. Concernant le deuxième, une grande partie des spots turbulents sont issues des interactions entre les stries laminaires voisines, qui rentrent en collision en raison de l'environnement très perturbé de l'écoulement. Des structures basses vitesses en Λ sont effectivement observées dans la couche limite mais le fort gradient favorable associé à la région où elles apparaissent les empêchent de participer à la transition.

Enfin, l'influence des propriétés du Novec sur les caractéristiques des spots turbulents est regardée en détail. Les spots turbulents présentent de fortes similitudes avec ceux des écoulements supersoniques sur parois froides. Tout d'abord, en raison de la capacité thermique élevée du Novec, des tourbillons orientés dans le sens de la largeur sont présents près de la paroi au sein des spots turbulentes et la couche limite turbulente, comme dans le cadre des parois isothermes dans des écoulements d'air. De plus, une augmentation paradoxale d'effets de compressibilité est observée. Dans des écoulements en air, l'augmentation du nombre de Mach conduit à une diminution de l'angle d'étalement latéral des spots turbulents α. En Novec, cet angle α est encore davantage réduit et est comparable aux écoulements d'air supersoniques à paroi froide.

Chapitre 6 : Étude d'un écoulement transsonique de gaz dense au-dessus d'une configuration d'aube idéalisée

Dans ce chapitre, l'écoulement autour de la configuration complète de l'aube idéalisée est maintenant étudié. Pour limiter le coût de calcul comparée à une LES résolue à la paroi, coût très important à cause des nombres de Reynolds élevé, une approche hybride RANS/LES est sélectionnée. Cette approche utilise la méthode des équations de Navier-Stokes moyennées (RANS) pour modéliser les couches limites attachées et passe automatiquement à une approche LES dans les régions où la résolution de la grille est suffisante. Bien que la région modélisée RANS empêche une résolution précise de la transition de la couche limite, cela n'est pas être critique pour la configuration considérée, car la majeure partie de la couche limite est principalement turbulente en raison d'une transition juste après le bord d'attaque, comme mentionné au chapitre 5. En particulier, l'approche Delayed Detached Eddy Simulation (DDES) est sélectionnée car elle est spécialement conçu pour

accélérer la transition vers la turbulence résolue dans les couches de cisaillement séparées. Ainsi, cette stratégie de simulation permet de résoudre avec précision les dynamiques de sillage turbulent les plus importantes.

Les résultats obtenus pour le Novec sont comparés à ceux calculés pour l'air, afin de mettre en évidence le rôle de la complexité du fluide organique. Tout d'abord, les écoulements Novec présentent un exposant isentropique γ_{pv} inférieur à celui de l'air et sont détendus dans une région de gaz dense, ce qui entraîne un comportement opposé de la vitesse du son par rapport au comportement du gaz parfait. Dans les conditions thermodynamiques sélectionnées, aucun phénomène non idéal significatif n'est observé, et la topologie globale de l'écoulement est similaire à celle obtenue dans l'air. Ces conditions ont essentiellement un impact sur le rapport de pression maximal réalisable.

De plus, une étude approfondie du sillage instationnaire est réalisée. On observe que le nombre de Strouhal dépend principalement de M, mais aussi du nombre de Reynolds. De plus, en raison de la grande capacité thermique du Novec, le phénomène de séparation d'énergie est supprimé. En revanche, les fluctuations de pression et en particulier les ondes acoustiques sont renforcées.

Enfin, les pertes au sein de la configuration considérée sont étudiées. L'analyse des pertes montre qu'elles augmentent à mesure que γ_{pv} et le rapport de pression diminuent. La majorité des pertes se produisent dans la région du sillage, principalement sous l'effet de la pression de base, comme le montre la décomposition des pertes de Denton. Comparées aux simulations DES, les simulations RANS sous-estiment de manière significative la pression de base, conduisant à une erreur de 30% dans l'estimation des pertes au niveau du bord de fuite. Enfin, les simulations RANS instationnaires apportent une amélioration limitée par rapport aux simulations RANS stationnaires en raison de leur incapacité à capturer correctement l'instabilité du sillage.

Conclusion

Cette thèse vise à mieux comprendre les mécanismes physiques impliqués dans les processus de pertes au sein des écoulements de gaz denses étant dans des conditions représentatives des turbines ORC, notamment les pertes liées à la transition laminaire-turbulente de couche limite et lié au sillage au niveau du bord de fuite. Cet objectif est réalisé grâce à des simulations haute-fidélité, qui sont un outil clé pour affiner notre compréhension des phénomènes physiques impliqués dans les turbines ORC, afin d'obtenir à terme un meilleur rendement. Comme il s'agit d'une source importante de pertes, une grande partie du présent travail se concentre sur les couches limites du gaz dense et sur la transition induite par la turbulence extérieure à la couche limite, qui

représente le mécanisme de transition dominant dans les turbines et qui n'a pas encore été étudié dans un gaz dense. La thèse s'intéresse ensuite de manière plus générale aux pertes de profil, qui ne sont pas uniquement liées aux couches limites mais aussi au développement du sillage au bord de fuite et éventuellement aux chocs dans les détentes transsoniques. En particulier, le fluide considéré est le Novec649, identifié comme un bon candidat fluide de travail dans les systèmes ORC.

Dans les conditions de fonctionnement modérées considérées dans cette thèse, les écoulements de Novec sont caractérisés par des valeurs de la dérivée fondamentale de la dynamique des fluides inférieures à un et se produisent donc dans une région de gaz denses. Les couches limites de gaz dense ne sont que légèrement plus stables que l'air, à la fois dans les transitions naturelles et bypass, et les mécanismes de transition ne sont pas affectés. Des effets plus significatifs des gaz denses sont observés sur la configuration idéalisée des aubes, avec la diminution de la vitesse du son pendant la détente du Novec, ce qui conduit à un rapport de pression plus faible que celui de l'air. Les pertes de la turbine augmentent au fur et à mesure que les détentes se rapprochent des conditions non idéales.

La chaleur spécifique, qui est généralement élevée dans les vapeurs organiques complexes, a des effets plus importants sur les écoulements. La capacité thermique élevée du Novec conduit à la suppression de plusieurs effets compressibles observés sur les écoulements de gaz parfaits légers aux vitesses subsoniques et transsoniques considérées. Dans les couches limites entièrement turbulentes, en raison de la réduction significative de la surchauffe à la paroi, la distribution du coefficient de frottement est quasiment superposée aux références incompressibles et, même si de véritables effets de compressibilité sont néanmoins observés sur les quantités thermophysiques, les propriétés dynamiques sont similaires à celles des écoulements d'air à faible vitesse. La chaleur spécifique élevée du Novec supprime également les stries thermiques dans les couches limites Novec et, en particulier, le phénomène de séparation d'énergie est absent dans le sillage de l'aube utilisant de la vapeur de Novec. Une autre caractéristique intéressante des écoulements de Novec est que, si le mode thermique est supprimé, le mode acoustique est renforcé par rapport à l'air. Ce phénomène est observé par exemple au-dessus des couches limites turbulentes, mais aussi en aval du bord de fuite dans la région du sillage où les fluctuations de pression sont renforcées.

Une autre caractéristique importante des écoulements dans les ORC est qu'ils se produisent généralement à des nombres de Reynolds très élevés, en raison de la densité élevée des vapeurs organiques. Dans les transitions bypass typiques des turbines ORC, les grandes structures turbulentes interagissent donc avec une couche limite très fine. L'étude de transitions induites par la turbulence extérieure réalisée dans cette thèse révèle que, dans

de telles conditions, le scénario classique (croissance linéaire non modale de stries subissant des instabilités secondaires) peut être contourné par un mécanisme de réceptivité non linéaire (croissance non linéaire non modale de structures en forme de Λ, qui conduisent à la formation de spots turbulents). L'étude menée met en évidence l'influence de l'échelle intégrale longitudinale de la turbulence extérieure dans la compétition entre les deux différents mécanismes de transition. Le scénario alternatif entre dans la catégorie de la réceptivité non linéaire à des perturbations localisées intenses qui peut être pertinent pour d'autres scénarios de transition bypass rencontrés dans les turbomachines, par exemple lorsqu'il s'agit du processus de réceptivité autour du bord d'attaque épais [19] ou dans le cadre de transition induite par le sillage [20, 21, 22]. Outre les caractéristiques du bord d'attaque et de la turbulence extérieure, les forts gradients de pression favorables rencontrés dans les turbines peuvent également influencer la trajectoire de la transition. L'étude de la transition induite par la turbulence extérieure autour du bord d'attaque de l'aube idéalisée révèle que, dans ce cas, le gradient de pression favorable élevé empêche les structures en forme de Λ de participer à la transition et que la transition se produit via des mécanismes d'instabilités de stries et d'interactions de stries. La séparation d'échelle induite par les nombres de Reynolds élevé conduit à des structures turbulentes qui s'enroulent autour du grand bord d'attaque et qui s'organisent dans un arrangement latéral à grande échelle, en formant des clusters de petits tourbillons. Cet arrangement dans le sens de l'envergure module profondément la formation des stries laminaires et la propagation latéral des spots turbulentes en aval.

Ces conditions de nombre de Reynolds élevé ont longtemps été un obstacle à l'application de méthodes de haute fidélité dans la conception des ORC et les outils couramment utilisés sont principalement basés sur des méthodes RANS. L'étude de l'aube idéalisée révèle que la prédiction des pertes peut être largement sous-estimée dans les simulations RANS par rapport à une méthode plus haute-fidélité telle que l'approche DDES-SLA retenue pour cette configuration. Même si les caractéristiques globales de l'écoulement (topologie des chocs, quantités de sorties, ...) sont bien prises en compte dans les simulations RANS, le coefficient de pression du bord de fuite est cependant sévèrement sous-estimé par rapport à l'approche RANS-LES. Comme les pertes de sillage sont dominantes dans cette configuration transsonique, cela conduit à une erreur de 20% dans l'estimation du coefficient de pertes enthalpiques.

Contents

Chapter 1

Introduction and state of the art

1.1 Context and motivation

Organic Rankine Cycle (ORC) systems appear more and more as one of the solutions to answer the current energy and environmental challenges because of their significant potential for energy recovery [1]. ORCs are based on the classical thermodynamic cycle of Rankine, a closed-loop cycle generally realized by means of a compressor, an expander and heat exchangers (see Fig. 1.1 left), which has long been used to recover energy from heat sources. Instead of water, ORCs working fluids are complex organic compounds characterized by mild to high molecular complexity, moderate to large molecular weights and relatively low boiling temperatures [2]. The use of these organic fluids gives an extra degree of freedom to the thermodynamic cycle, allowing for the exploitation of lower temperature heat sources than achievable with water [1]. For instance, ORC are used to recover energy from renewable energy sources such as geothermal reservoirs, solar radiation and ocean thermal gradient, but also waste heat from industrial plants or from engine exhausts.

In thermodynamic conditions typical of ORC applications, the organic working fluids can operate in the so-called dense gas regime. Dense gases (DG) are usually defined as single-phase fluids, characterized by sufficiently complex molecules, working in pressure and temperature conditions of the same order of magnitude of their thermodynamic critical point (see, e.g., Guardone *et al.* [4] and references cited therein). At such conditions, real gas effects play a crucial role in the dynamic behavior of the fluid [5], in a manner that strongly depends on its molecular complexity and weight, which in turn determines the number of active vibrational degrees of freedom according to the fluid working temperature. To describe the gas dynamic behavior of fluids,

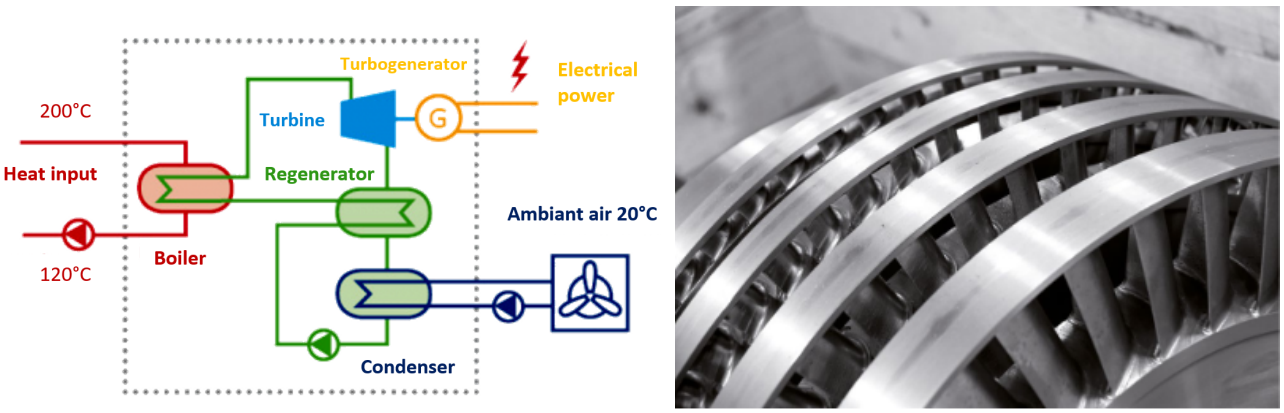

Figure 1.1: Left: Organic Rankine Cycle (adapted from Enertime website [3]). Right: Example of a multi-stage axial turbine (Enertime [3]).

Thompson [6] introduced the fundamental derivative of gas dynamics:

$$\Gamma := \frac{v^3}{2c^2}\left.\frac{\partial^2 p}{\partial v^2}\right|_s = 1 + \frac{\rho}{c}\left.\frac{\partial c}{\partial \rho}\right|_s, \tag{1.1}$$

where ρ is the density, $v = 1/\rho$ the specific volume, p the pressure, s the entropy, and $c = \sqrt{\partial p/\partial \rho|_s}$ the sound speed. The first equality in (1.1) shows that Γ is related to the curvature of isentropic lines in the p-v plane; according to the second definition, Γ is a measure of the rate of change of the speed of sound in isentropic transformations. A dense gas regime, defined by $\Gamma < 1$, implies $\partial c/\partial \rho|_s < 0$, meaning that the speed of sound increases in isentropic expansions and decreases in isentropic compressions, in contrast to the case of perfect gases, where:

$$\Gamma = \frac{\gamma + 1}{2}, \tag{1.2}$$

$\gamma = c_p/c_v$ being the ratio of the isobaric specific heat c_p to the isochoric specific heat c_v. For thermodynamic stability, γ is always greater than unity, hence $\Gamma > 1$ for perfect gases. On the contrary, heavy gases characterized by high c_v/R ratios (R being the gas constant), exhibit extended ranges of density and pressures in which Γ is less than unity. The most complex molecules, named Bethe–Zel'dovich–Thompson (BZT) fluids [7, 8, 6], are even characterized by thermodynamic range conditions where Γ becomes negative (the "inversion zone"), predicted to result in non-classical compressibility effects in the transonic and supersonic flow regimes. In the low-density limit, where the perfect gas behavior is recovered, the molecular complexity of the gas still plays a role, leading to a specific heat ratio γ very close to 1: for $\gamma \to 1$ isentropic transformations of ideal gases, for which the well known isentropic law of Laplace ($pv^\gamma = \text{const}$) is valid, also become isothermal ($pv = \text{const}$).

In most ORC, even though different alternatives of expanders exist [9], the working fluid is generally

expanded in a turbine (see Fig. 1.1 right). The latter component can be critical for the cycle efficiency and, with the goal of achieving consistently higher performance, it is of utmost importance to estimate the various loss mechanisms. The origins of losses within turbines are detailed in the review of Denton [10] . In the absence of heat transfer and non-equilibrium effects, entropy creation comes from viscous friction in the shear layers. In particular, considering the large proportion of walls, one major source of losses in turbines is often the boundary layers. These losses are influenced by the state of the boundary layer, i.e. laminar or turbulent, and its development. Being able to predict the laminar-turbulent transition of boundary layers is therefore very important, to know where the flow is likely to be turbulent or to separate as it will directly affect the estimated losses. Another important source of losses is the wake development, originating from free shear layers forming at the trailing-edge and directly affected by the state of the boundary layers separating off. As it can account for an important proportion of the profile losses [11], the correct prediction of the vortex shedding is also of primordial importance.

In the following sections, a state of the art of the key points identified concerning losses within ORC turbines is discussed. First, results from numerical and experimental dense gas boundary layers investigations are reported in section 1.2. Then, as it is expected to be the most dominant transition mechanism, a review on the freestream turbulence-induced transition phenomenon is given in section 1.3. Finally, an overview of research on ORC turbines losses, with a focus on high-fidelity simulations, is presented in section 1.4.

1.2 Dense gases boundary layers

Although the literature about boundary layers is extremely large, few studies have investigated boundary layers of dense gases or organic vapors. The first studies dealt with the laminar boundary layer using similarity solutions [23, 24, 25, 26]. Cramer *et al.* [23] compared similarity solutions for nitrogen N_2, modelled as a perfect gas, sulfur hexafluoride SF_6, used in heavy gas wind tunnels, and toluene, widespread in ORC turbomachinery, for freestream Mach numbers between 2 and 3. Kluwick [25] considered laminar boundary layers of nitrogen and two BZT fluids, PP11 (perfluoro-perhydrophenanthrene) and FC-71 (perfluoro-trihexylamine) at M=2. Cinnella & Congedo [27] performed numerical simulations for a lighter fluorocarbon (PP10) at M=0.9 and 2. In the case of N_2, dissipative effects cause a substantial temperature variation and the velocity profile deviates significantly from the incompressible Blasius solution. On the other hand, for all studied dense gases, temperature remains almost constant due to high heat capacity of the fluid. The isobaric heat capacity c_p can indeed become quite large in the neighborhood of the critical point [23]. This effect is also related to the molecular complexity of

heavy compounds. Kluwick [25] used the ratio of the specific heat at constant volume over the gas constant, c_v/R, to characterize the molecular complexity. He noted that the Eckert number (Ec), which is the ratio of the kinetic energy over the fluid enthalpy, is proportional to M^2 in the ideal gas limit, whereas it scales with $M^2 \times R/c_v$ for real gases. Due to the high molecular complexity, dissipation caused by internal friction and heat conduction can be neglected, even at relatively large supersonic Mach numbers. The temperature and the density are nearly constant across the boundary layer, and consequently, the velocity profiles for boundary layers of dense-gases nearly collapse on the incompressible profile. Chakravarthy [28] studied dense gas effects on linear instabilities of laminar boundary layers. Toluene vapor was selected at six Eckert numbers (which can be related to the Mach number). The linear stability theory (LST) shows that the boundary layer becomes more stable as the Eckert number increases, developing eventually no modal instabilities for $Ec > 0.15$. Gloerfelt *et al.* [29] performed a linear stability study for various dense gases which showed that Tollmien-Schlichting (TS) mode (first mode) is damped dramatically for a dense gas when the Mach number becomes supersonic. This is also the case for an ideal gas, but the mode gradually becomes non-viscous due to the presence of a generalized inflection point and remains unstable. For a dense gas, the large thermal capacity (large Eckert number) drastically reduces the heating at the wall (which is at the origin of the generalized inflection point) and the first mode ceases to exist. Furthermore, the second mode appearing for a Mach number above 4 is shifted toward high frequencies due to the reduced thickening of the boundary layer. It then takes on the characteristics of a supersonic mode.

The first scale-resolving simulations for wall-bounded flows of a dense gas were performed for the compressible channel flow. Sciacovelli, Cinnella & Gloerfelt [30] used direct numerical simulations (DNS) for a heavy fluorocarbon (PP11) and bulk Mach and Reynolds numbers between 1.5 and 3, and 3000 and 12000, respectively. They also observed a negligible friction heating and a liquid-like behavior for the viscosity. Despite the very weak temperature variations, strong density fluctuations are present due to the non-standard thermodynamic behavior (see Fig. 1.2). Density fluctuations are correlated with pressure ones, unlike the perfect gas, where the near-wall streaks correspond directly to high- and low-density fluid. A priori analyses of several RANS models based on these DNS databases was conducted by Sciacovelli, Cinnella & Gloerfelt [31]. If the modeled eddy viscosity behaves in the same manner as for air flows at similar conditions, the agreement with turbulent Prandtl number models is less conclusive due to the reduced thermal boundary layer. More recently, Chen *et al.* [32] performed DNS of turbulent channel flow for two organic gases, R1233zd(E) and MDM, two candidate working fluids for ORC systems, at conditions close to the supercritical region. The

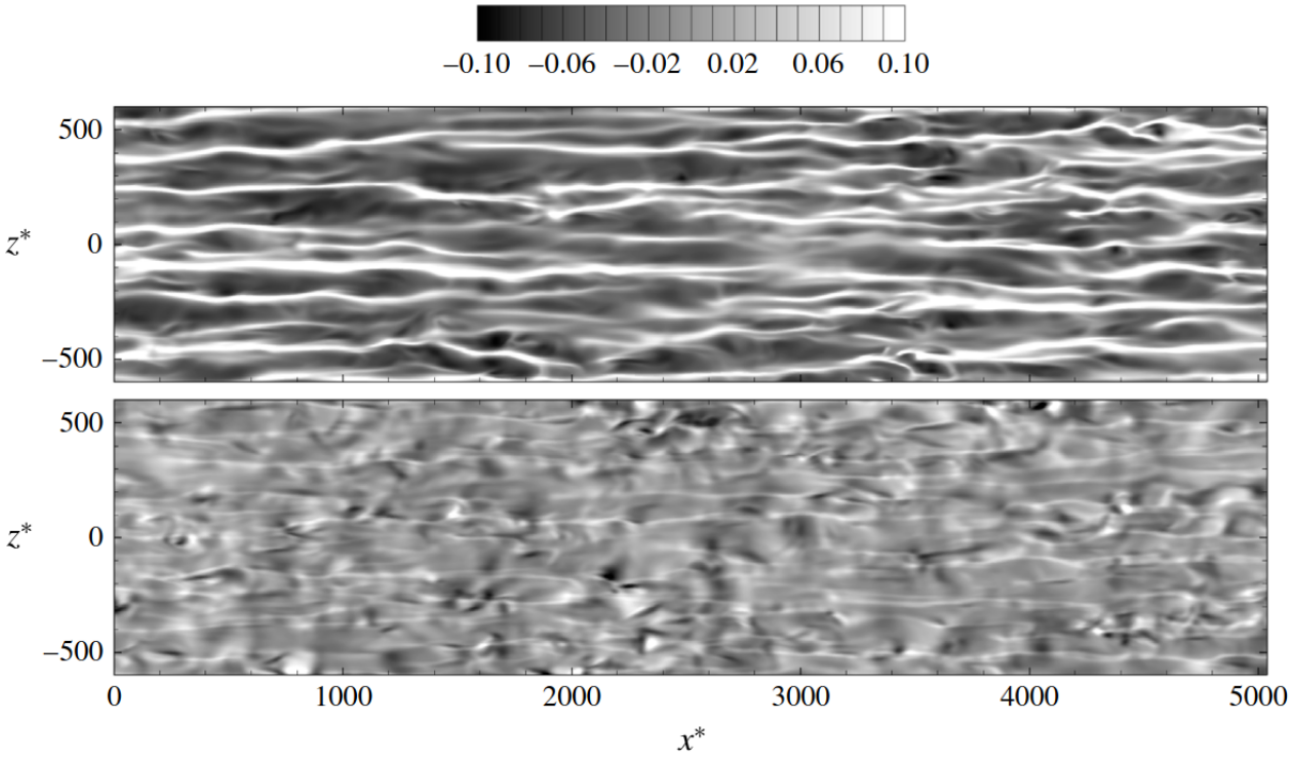

Figure 1.2: Density fluctuations near the wall for Air (top) and PP11 (bottom) at a bulk Mach number of 3 and a bulk Reynolds number of 3000 in the channel flow DNS of Sciacovelli *et al.* [30].

results show that real-gas effects can significantly affect the profiles of averaged thermodynamic properties, and the viscosity has a liquid-like variation, contrary to a perfect gas flow. The viscosity profile entails an increase of the Reynolds stresses and of the kinetic energy dissipation. An a priori evaluation of RANS models (k-ε and k-ω) indicated that theses models remain suitable for turbulence in denses gases. Giauque *et al.* [33] used the turbulent channel flow with the heavy fluorocarbon FC-70 to provide a priori analyses of subgrid-scale models for large-eddy simulations and showed that the subgrid-scale turbulent stress and pressure should be taken into account. The first DNS for a spatially developing boundary layer of a dense gas, namely PP11 at M=2.25 and 6, was carried out by Sciacovelli *et al.* [34]. The DNS of the laminar-to-turbulent transition was triggered by suction and blowing to investigate the fully turbulent state. As already observed for laminar boundary layers or turbulent channel flows, the mean velocity profiles are largely insensitive to the Mach number and very close to the incompressible case even at hypersonic speeds. The boundary layer structure is deeply modified compared to air and density variations are severely attenuated in the outer region of the dense gas boundary layer (see Fig. 1.3). The strongly non-ideal thermodynamic and transport-property behavior results

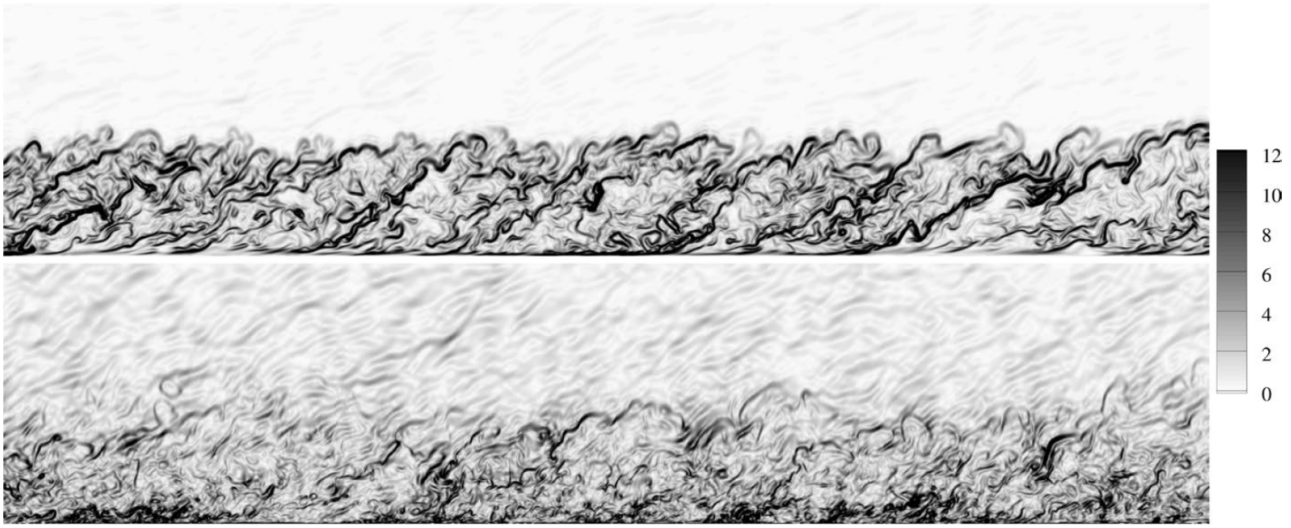

Figure 1.3: Numerical Schlieren in a spanwise plane for Air (top) and PP11 (bottom) at $M = 6$ in the highly-resolved LES of Sciacovelli *et al.* [34].

in unconventional distributions of the fluctuating thermo-physical quantities. In particular, dense-gas boundary layers exhibit significantly higher values of the fluctuating Mach number and velocity divergence, compared to high-Mach-number light-gas boundary layers at the same conditions. Using a blowing and suction at the wall to simulate a roughness, Yang *et al.* [35] investigated the non-ideal effects on the bypass transition in boundary layers for two dense gases in three operating conditions: in the dilute-gas region, near the saturation line and close to the critical region. Compared to air, the onset of transition is seen to be earlier for the dense gases, regardless of the flow conditions. The authors underlined that acoutics due to pressure fluctuations can affect turbulent energy transportation.

Recent years have seen renewed interest for estimating the dissipation due to turbulent boundary layers of dense gases. Similarity solutions for the laminar state and RANS models for the turbulent state were used in [36] to estimate the dissipation phenomena in the boundary layer. Various RANS models to simulate steady turbulent boundary layers are discussed in [37] for a siloxane fluid (MM) at M between 0.2 and 2.8. Pini and De Servi [38] investigated the entropy generation in laminar boundary layers of dense gases and proposed a reduced-order model (ROM) based on the boundary layer equations. Tosto *et al.* [39] used high-fidelity simulations with the 3DNS code to assess the ROM model. They carried out DNS of spatially developing boundary layers at M=0.9 for air and MM, in dilute– (case *iMM*) and dense-vapor conditions (case *niMM*), where the turbulent state is triggered using a numerical trip. The ROM [38], coupled with an algebraic turbulence model, gave a fair estimation of the dissipation rate. The shape factor H is 1.45 for *iMM* and 1.49 for *niMM*, close to the nominal

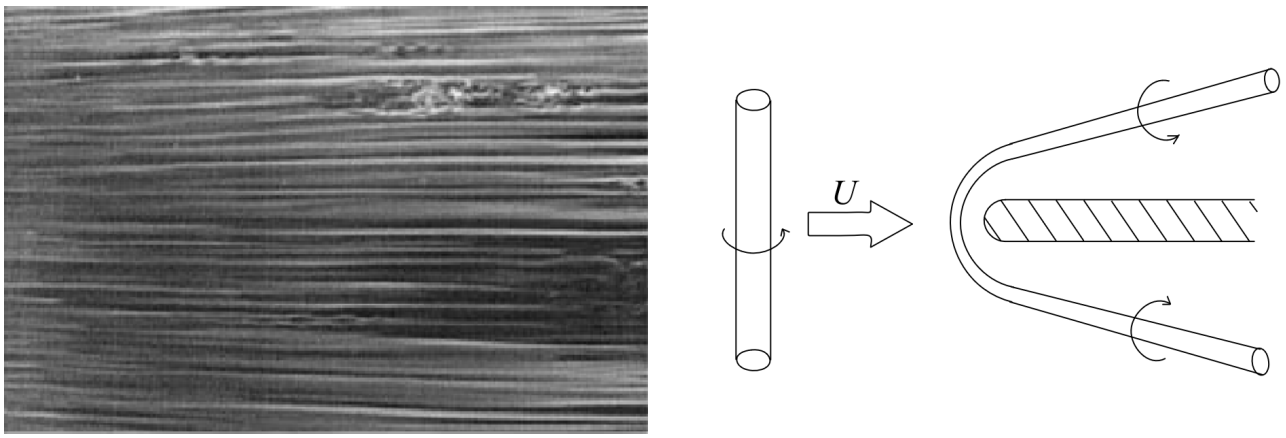

Figure 1.4: Left: Visualization of a FST-induced transition on a flat plate in the experiment of Matsubara & Alfredsson [40]. Right: Schematic view of the effect of leading edge through stretching of vortex tubes (from [19]).

value for an incompressible TBL, whereas H=1.84 for air due to the alteration of boundary layer thicknesses by friction heating. Another conclusion is that since dense gases are almost isothermal, the loss contribution due to irreversible heat transfer is negligible.

1.3 Freestream turbulence-induced transition of boundary layers

As discussed, the correct prediction of laminar-turbulent transition is of key importance to the performance of turbines, as it will affects the development of the blade boundary layers and where it may separate. In turbines, transition of the boundary layers induced by freestream turbulence (FST) is the most dominant mechanism due to the highly perturbed environment [41, 42]. Although the FST-induced transition has not yet been studied in dense gas boundary-layers (BL), the literature for air BL, in particular at low-speed, is abundant [43, 44]. When boundary layer flows are subjected to moderate or high levels of freestream turbulence (FST), the orderly route to turbulence through amplification and breakdown of linear instabilities can be bypassed. Through receptivity at the plate or blade leading edge, streamwise fluctuations are generated in the laminar boundary layer and evolve in the so-called Klebanoff streaks, which lift-up and eventually break down, producing a turbulent patch near the wall, called turbulent spots (see Fig. 1.4 left). These turbulent spots merge further downstream, until a fully turbulent boundary layer is obtained. This transition is particularly sensitive to the intensity of the freestream turbulence, generally defined as $T_u = \sqrt{(u'^2 + v'^2 + w'^2)/3}/U_\infty$, but the role of the disturbances scales, which can be estimated through the integral length scale, has also been highlighted.

1.3.1 Effects of the integral length scale on FST-induced transition

While it is clear that an increase of T_u, when keeping the other parameters constant, moves the transition upstream [45, 19, 46, 47, 48], the effect of FST integral length scale is less obvious. In the experiments of Jonas *et al.* [49] at $T_u = 3\%$, it was found that the final stages of transition occur earlier for FST with large-scale incoming structures whereas the extent of the transition region shortens with decreasing length scales. Brandt *et al.* [45] also reported in their numerical simulations that, for a fixed T_u, larger values of the integral length scale promotes earlier transition. Similar results were reported by Ovchinnikov *et al.* [50], Pinto & Lodato [46] or Muthu *et al.* [48]. More recently, the extensive experiments of Fransson & Shahinfar [47] showed two scenarios depending on the FST intensity: for low T_u ($\leq 2.45\%$), the transition was moved forward as L_f increased whereas the opposite was obtained with larger values of T_u ($\geq 2.8\%$).

Since streamwise laminar streaks are generally forerunners of the appearance of turbulent spots in most of FST-induced transitions, the role of the integral length scale on their characteristics is of the utmost importance. One key property of the streaks is their spanwise scale, which is related to the spanwise velocity gradient and thus could affect the streak destabilization. The spanwise distance between streaks was initially thought to be relatively independent of the FST conditions (see discussion in [47]). Klebanoff [51] observed in his experiments (reported in [52]) that the minima of two-point spanwise correlations of the streamwise velocity, corresponding to the average half spanwise wavelength of the streaks, were almost constant and seemed relatively independent of T_u. Kendall [53] estimated that the mean distance between low-speed and high-speed streaks was approximately equal to the BL thickness but was also similar to the lateral scale of the freestream turbulence. With FST scales approximately twice as big as Kendall [53], Westin *et al.* [54] found similar spanwise scales, thus inferring that the spanwise scales were weakly correlated to the FST conditions. Similar streaks spanwise distance were also found by Jacobs & Durbin [55]. Under variable FST intensity (1-6%), Matsubara & Alfredsson [40] measured a relatively constant value of $3\delta^*$ (δ^* being the displacement thickness in the transition region), confirming the previous observations. However, this asymptotic value was attained for some cases inside the turbulent boundary layer (TBL) and not in the transitional region. The spanwise scales found in the direct numerical simulations (DNS) of Brandt *et al.* [45], similar to that of Matsubara & Alfredsson [40], seemed to be only weakly affected by the FST scales, at least for Re_{L_f} between 750 and 2250, where Re_{L_f} is the Reynolds number based on the integral length scale. These observations may be due to the fact that relatively similar FST conditions were used in all cited studies. The experiments of Fransson & Alfredsson [56] were the first to report a significant change in streak spacing due to FST characteristics. Specifically, a significant increase in FST intensity was found to

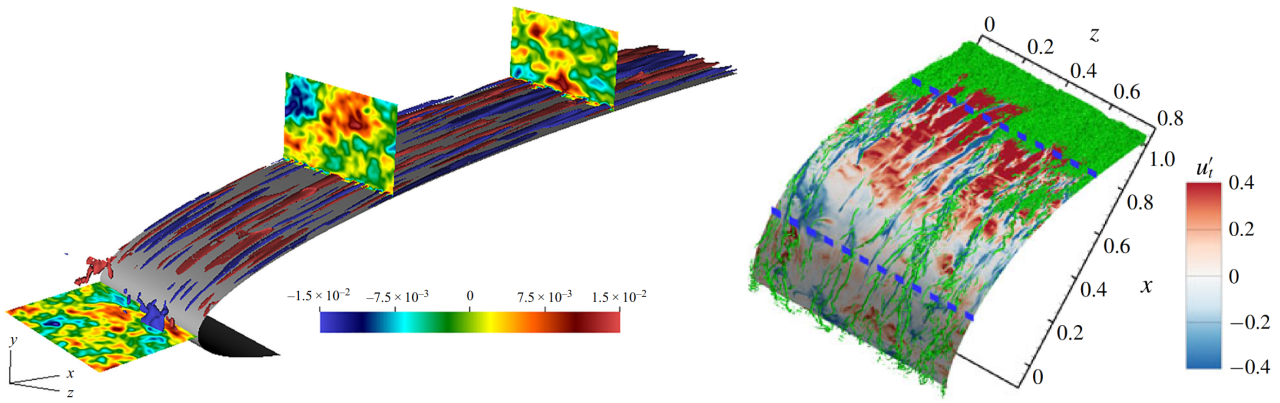

Figure 1.5: Left: Snapshot of streamwise velocity perturbation u_t' in a DNS of streaks growth around a NACA0008 wing under FST (from Faúndez Alarcón *et al.* [60]). Right: Snapshot of u_t' in a well-resolved LES of transition around LS89 turbine under relatively high FST intensity (from Zhao & Sandberg [59]).

reduce the spanwise distance between streaks. They also suggested that the FST scales play an important role in the spanwise scale selection process. Moreover, they observed that a reduction of the BL thickness by a factor of two left the streak spacing unchanged, demonstrating that the latter is not directly correlated with the former. Ovchinnikov *et al.* [57] used two different Re_{L_f} at comparable FST intensities in order to reproduce numerically the T3B experimental configuration [58]. They observed that the increase of the integral length scale leads to increased spanwise scales. Similarly, the LES of FST-induced transition over a turbine blade of Zhao & Sandberg [59] (see Fig. 1.5) showed that the streak spacing depends on the FST and is not directly connected to the BL thickness. Faúndez Alarcón *et al.* [60] used DNS to study FST transition on a NACA0008 wing (see Fig. 1.5), and found that the scales of the freestream vorticity play an important role in the induced streaks. The preferred spanwise wavenumbers are already set in the freestream turbulence, and are shown to correspond to that obtained with optimal disturbance theory (at least for low levels of turbulence intensity where the linear theory is applicable). Thanks to a comprehensive investigation over a wide range of T_u (1.8-6.2 %) and Re_{Lf} (6400-10000), Fransson & Shahinfar [47] demonstrated that the streak spacing was not correlated to T_u or L_f separately but rather to a combination of these two FST parameters. They introduced a Reynolds number, $Re_{FST} = Re_{L_f} \times T_u$, that reflects this double dependence, and proposed an empirical correlation for the streak spanwise scale.

1.3.2 Leading-edge effects

Another important parameter is the leading edge, whose effects on FST-induced transition has also been investigated in the past. While trying to establish a Blasius BL in their wind tunnel, Watmuff [61] observed a persistence of Klebanoff modes inside the BL due to vortices originating at the LE. Goldstein & Wundrow [62] showed that the LE caused vortex stretching (see Fig. 1.4 right), leading to the formation and enhancement of streamwise vortices which are essential in the formation of laminar streaks through the lift-up effect [63]. While studying the effects of free-stream turbulence on heat transfer at the stagnation point, Xiong & Lele [64] also observed strong streamwise vortices developing close to the LE and reported an increase of the turbulence intensity by approaching the LE, specifically for the spanwise fluctuations of velocity, in accordance with theoretical predictions of Goldstein & Wundrow [62]. Subsequently, Nagarajan et al. [19] noted that the wavepacket-like disturbances they observed were related to the localized streamwise vorticity generated at the LE. Due to the distortion of the FST by the LE, the level of tangential velocity fluctuations was lowered while the spanwise and wall-normal components were enhanced. Moreover, the amplification of streamwise vortices at the LE was promoted by greater T_u and blunter LE. Zhao & Sandberg [59] reported the same strengthening by increasing FST intensity. This strengthening was found to be sensitive to the integral length scale by Faúndez Alarcón et al. [60]. Ovchinnikov et al. [57] observed that higher wall-normal fluctuations at the LE of the plate resulted in higher levels of streamwise Reynolds stress inside the transitional BL, promoting the turbulent breakdown. An important parameter in these studies is the thickness of the leading edge related to the boundary layer. This can be characterized by forming a Reynolds number based on the half-thickness of the plate or the blade and the incoming velocity, which is equal to 470 in the study of Ovchinnikov et al. [57], between $5\,000$ and $8\,400$ in Nagarajan et al. [19], who considered flat plates with an elliptic LE. The value is increased to $21\,320$ in the DNS of Faúndez Alarcón et al. [60] for a thin airfoil and to approximately $65\,000$ in the LES of Zhao & Sandberg [59] for a stator blade with a round nose.

1.3.3 Turbulent spot precursors

A key feature in FST-induced transition is the generation of turbulent spots. In many situations, the turbulent spot precursors come from the destabilization of Klebanoff modes inside the BL. The main breakdown path is related to laminar streaks undergoing secondary instabilities. Andersson *et al.* [66] carried out secondary instability analyses of optimal streaks and found two different instability modes, namely the sinuous (anti-symmetric) and varicose (symmetric) mode. The sinuous and varicose modes, associated respectively

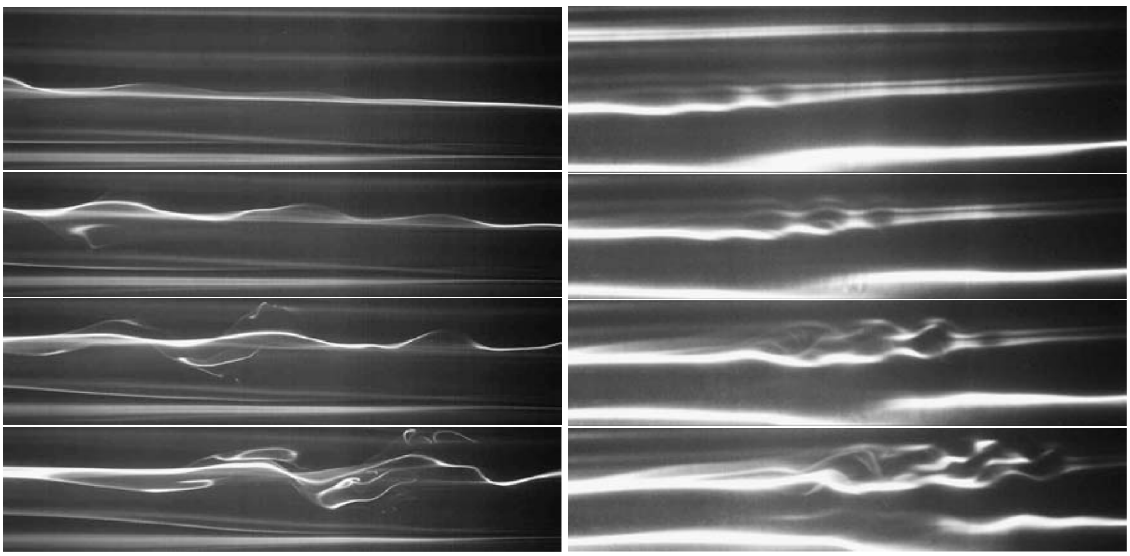

Figure 1.6: Dye visualization of streak breakdown on a low-speed streak: sinuous antisymmetric (left) and varicose symmetric (right) breakdown (from Mans [65]).

with spanwise and wall-normal mean velocity gradients, have been observed in numerous experiments and simulations (see Fig. 1.6 for experimental visualizations). In their experiments, Matsubara & Alfredsson [40] observed that the streak breakdowns can be associated with secondary instabilities. In a computational domain containing a single pair of streaks, Brandt & Henningson [67] simulated an antisymmetric instability leading to the streamwise streak breakdown in a zero-pressure gradient flat plate (ZPGFP) boundary layer. The DNS of Brandt *et al.* [45] described in details the varicose and sinuous instabilities of low-speed streaks and also suggested that the low-speed and high-speed streaks interactions are important to the breakdown. This was further assessed in Brandt & Lange [68], where sinuous and varicose breakdowns were produced directly due to streaks collisions and interactions, without any external disturbances. Mans [65] reported in his experimental work that the breakdown leading to turbulent spots was initiated by sinuous and varicose modes and that the critical amplitude of the latter was higher. The relevance of the sinuous secondary-instability mechanism for turbulent spots generation was further demonstrated by Schlatter *et al.* [69]. Hoepffner *et al.* [70] observed that the breakdown of subcritical streaks (with respect to the linear secondary-instability theory) can occur by non-modal transient growth and reported that the spanwise shear participates in the growth of both sinuous and varicose disturbances, whereas varicose perturbations are driven by the action of the wall-normal shear. In such cases, as noted by Durbin [71], secondary streak instability could therefore take the form of combined sinuous and varicose modes.

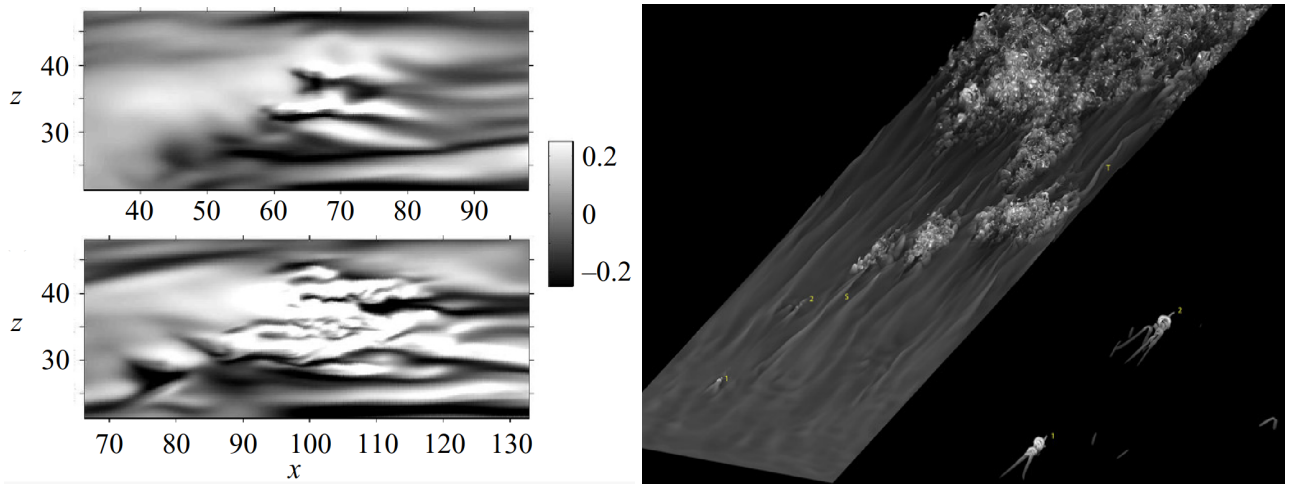

Figure 1.7: Left: group of low-speed Λ-shaped structures leading to turbulent spots in DNS of Ovchinnikov *et al.* [57]. Right: Δ-shaped low-speed patch observed by Wu *et al.* [76].

Including the leading edge of the flat plate in their simulations to reproduce the T3A and T3B benchmark cases [58], Nagarajan *et al.* [19] also observed that the transition occurs through low-speed streak secondary instabilities for sharp leading edge and low T_u but interestingly, with increasing FST intensity and bluntness, breakdown is initiated by wavepacket-like disturbances in the BL. Another type of streak instability was discovered by Vaughan & Zaki [72]. These authors studied secondary instability of idealized streaks, extending the work of Andersson *et al.* [66] to an unsteady base flow. They identified two unstable modes: an inner (varicose) and an outer instability, named after their vertical position inside the BL. The outer mode, which corresponds to the previously identified sinuous instability [66], can take the form of a combination of sinuous and varicose instabilities in the case of unsteady streaks. Even if they were not located on a low-speed streak, the near-wall wavepackets spot precursors reported by Nagarajan *et al.* [19] were linked to the inner mode described by Vaughan & Zaki [72]. Hack & Zaki [73] then compared in details secondary instabilities of streaks using DNS, either by directly tracking the streak inside the BL or by comparing with 2D linear analyses in a cross-section, confirming the theoretical conclusions of Vaughan & Zaki [72]. Nolan & Zaki [74] identified the inner instability in their simulations and demonstrated that this mode was promoted by strong adverse pressure gradient. Finally, Bose & Durbin [75] identified a helical inner mode in their simulations, resulting from the interaction between Tollmien–Schlichting (TS) waves and streaks.

In some other studies, the turbulent spots are not necessarily associated with streak destabilization. Using a similar numerical setup as Nagarajan *et al.* [19], but with an integral length scale three times larger, Ovchinnikov

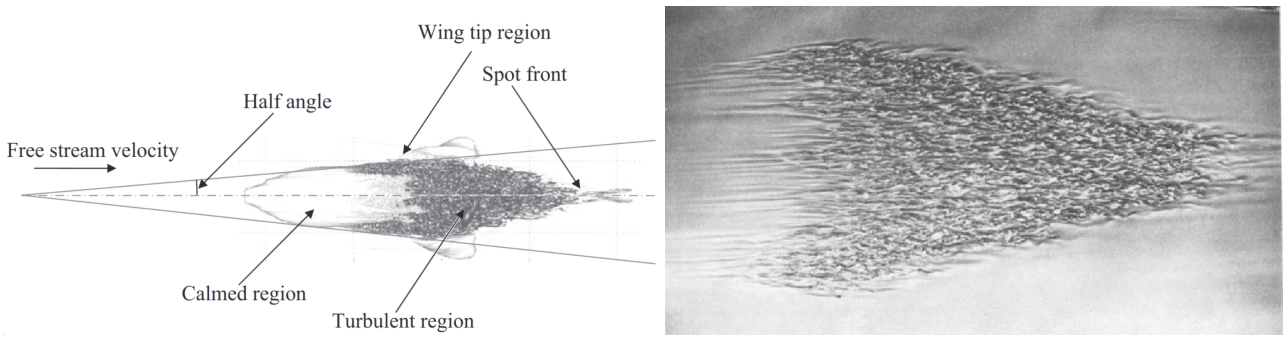

Figure 1.8: Left: Key features of a turbulent spot (from Redford *et al.* [78]). Right: Aluminium visualization of inner streaks for turbulent spots in the water experiment of Cantwell *et al.* [79].

et al. [57] found an alternative transition mechanism. While the transition was initiated by streak instabilities in their low-Re_{L_f} simulation, the authors reported that, for large-scale FST (high Re_{L_f}), the breakdown was driven by low-speed Λ-shaped structures that did not originate from TS waves and that were formed upstream of laminar streaks. Such low-speed Λ structures were associated with Λ-vortices, originating from spanwise vortex filament streched in the streamwise and wall-normal direction by the BL mean shear. Similarly, Wu *et al.* [76] observed that the same Λ-vortices formation mechanism was responsible for the turbulent spot formation in their DNS, and that the low-speed streaks forming downstream were not involved in turbulent breakdown. In a recent review about turbulent spots, Wu [77] reported that the paths to turbulent spot inception were likely to be classified in two categories: if $T_u \leq 2\%$, the breakdown occurs by laminar streaks instabilities, whereas, for $T_u > 2.5\%$, the breakdown is driven by oblique vortices interacting with a Δ-shaped low-speed patch underneath. As observed in Fig. 1.7, the Δ-shaped low-speed patch, shown in the supplementary movies, are analogous to the Λ low-speed structures reported in Ovchinnikov *et al.* [57], which appeared by varying the incoming turbulence scale only.

1.3.4 Turbulent spot characteristics

A further issue is to determine the influence of the transition path on the turbulent spot characteristics, detailed on Fig. 1.8 (left). The turbulent regions appearing in the boundary layer during FST-induced transition were first referred to as turbulent spots by Emmons [80]. Their key features are the front overhang, the trailing-edge calmed region, the wing-tip regions and the arrowhead shape, first identified with experimental visualizations [79, 81] (see Fig. 1.8). Turbulent spots characteristics in low-speed air flows under variable pressure gradient have been well documented (see for instance the experiments [82, 83] or the numerical study

[74]). Concerning high-subsonic and supersonic flows, Fischer [84] observed experimentally a dependence of the lateral spreading angle on the Mach number, where increasing the Mach number from 0 to 6 lead to a reduction of the spreading angle by a factor up to 4. In their DNS at $M = 2$, 4 and 6, Krishnan & Sandham [85] reported a similar trend. Jocksch & Kleiser [86] noted an equivalent behavior but also observed an influence of their initial Reynolds number on the growth rate of spots. Krishnan & Sandham [85] , Jocksch & Kleiser [86] and Redford *et al.* [78] reported at these supersonic speeds the presence of spanwise oriented vortices under the turbulent spots, linked to the supersonic mode (Mack mode). The characteristics of turbulent spots in high-speed air flows and in complex configurations is reviewed by Wu [77].

1.4 ORC turbines

As the working fluid in ORC systems is organic, the much smaller enthalpy decrease of an expanding vapor allows to design an expander with a lower rotational speed compared to air or water steam, for given power output [1]. Alternatively, this gives the possibility in ORC of building turbines with a reduced number of stages by increasing the level of load of each stage, without requiring high rotational speeds. To reduce production and maintenance cost, small-scale turbines are generally favored to expand organic fluids and, because of these small dimensions, ORC turbines tends to operate in transonic and supersonic regimes. Due to their molecularly complex structures, organic fluids operate in the dense-gas regime where the fundamental derivative of fluid dynamics Γ is lower than one, which results in an inverse behavior of the speed of sound compared to perfect gases: the speed of sound increases as the flow expands (see section 1.1). Therefore, transonic turbines expanding dense vapors reach critical chocking conditions at lower Mach numbers than those characterized by $\Gamma > 1$, leading to a lower pressure ratio at iso-geometry (Tosto *et al.* [87]). For weakly non-ideal conditions, the gas dynamics and the associated losses are mainly driven by the molecular complexity of the compound (Harinck *et al.* [5]) and the isentropic exponent, defined as $\gamma_{pv} = -\frac{v}{p}\left(\frac{\partial p}{\partial v}\right)_s$, where $v = 1/\rho$ is the specific volume and p is the pressure. The experimental study of Baumgartner *et al.* [88] showed that, for an exit Mach number M_2 greater than 0.9, the losses increase with decreasing isentropic exponent γ_{pv} due to the combined effect of shock loss within the blade passage and mixing loss downstream of the blade trailing edge (see Fig. 1.9). Furthermore, in the close proximity of the vapor–liquid saturation curve and critical point, the expansion is characterized by strong non-ideal effects. In addition to Γ and γ_{pv}, an important parameter to characterize the non-ideality of the flow is the ratio of relative Mach number variations to relative density variations at constant

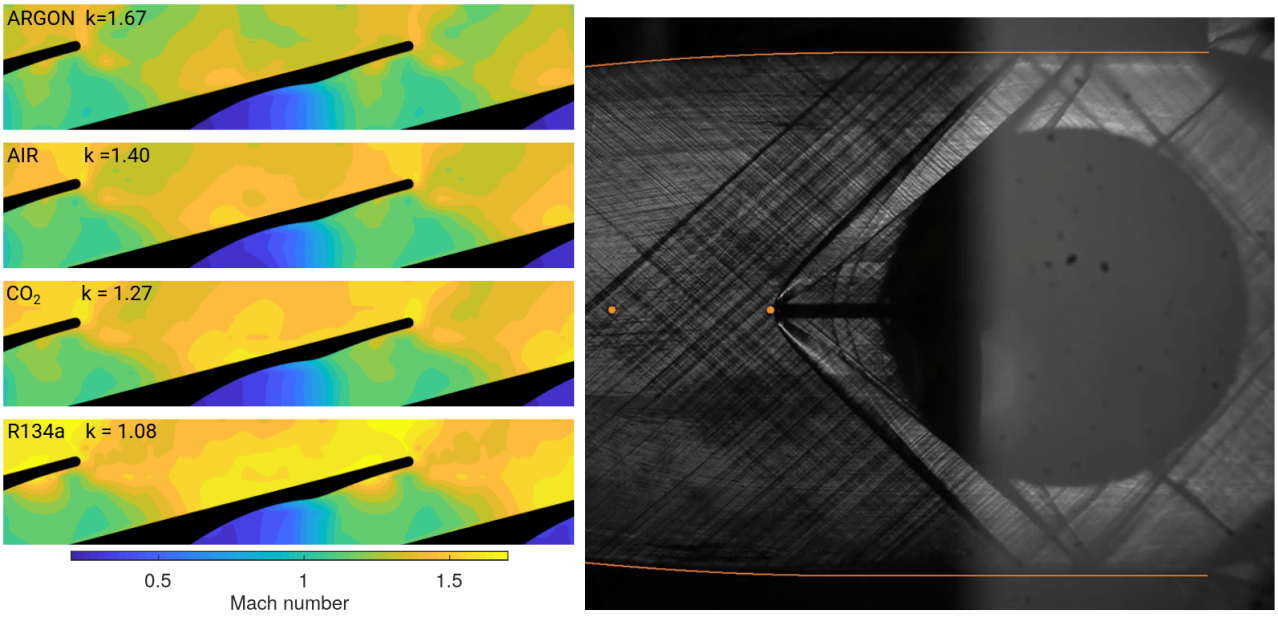

Figure 1.9: Left: Experimental investigation of isentropic exponent ($k = \gamma_{pv}$) influence on Mach number distributions (from Baumgärtner *et al.* [88]). Right: Schlieren vizualisation of shock system around a Pitot tube in a siloxane MM flow (from Conti *et al.* [94]).

entropy. In quasi-1D flow conditions this writes [89]:

$$\mathfrak{J} = \frac{\rho}{M}\left.\frac{\partial M}{\partial \rho}\right|_s = 1 - \Gamma - \frac{1}{M^2} \tag{1.3}$$

For a perfect gas, $\mathfrak{J} < 0$ at any point in the flow, and the Mach number, M, can only increase during an isentropic expansion. On the contrary, for a dense gas with $\Gamma < 1$ it is possible to identify flow conditions such that the Mach number decreases during an expansion as shown by Romei *et al.* [90]. An increased sensitivity to off-design conditions have also been reported by Romei *et al.* [91]. The most non-ideal flow conditions are obtained for BZT fluids ($\Gamma < 0$), which can exhibit for instance non-classical expansion and compression waves (Hoarau *et al.* [92], Vimercati *et al.* [93]).

Due to the combination of various mechanisms with a somehow contradictory influence, experimental and numerical databases are critical for improving turbine efficiency. Experimental data for non-ideal gas flows has been unavailable for a long time, or limited to global measurements of turbine performance (e.g. [95]), but significant progress has recently been realized in experimental facilities, as various teams developed test benches. A detailed review on the experimental techniques for non-ideal compressible flows was recently done by aus der Wiesche [96]. The majority of these facilities are blow-down wind tunnels, where only short-time statistics are possible [97, 98, 99]. Furthermore, most of the data produced to date are pressure measurements

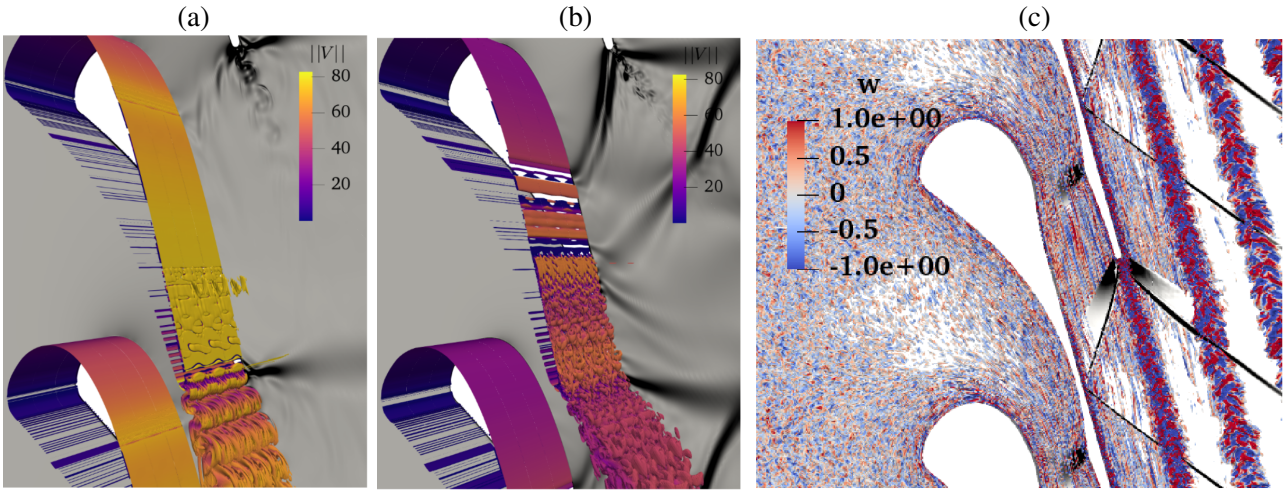

Figure 1.10: LES of LS89 turbine with PP11 for a subcritical (a) and transcritical (b) expansion (from Hoarau *et al.* [92]). LES of Baumgärtner's experiment (from Matar *et al.* [105]).

and visualizations of simplified flow configurations like nozzles [98], cylinders [94] (see Fig. 1.9) and diamond-shaped airfoil [100] with attached boundary layers, generally well captured by steady and inviscid flow models [101], provided that a suitable thermodynamic model of the gas is used. As the characteristic Reynolds numbers are very high (10^6–10^7), the measurement of near-wall flow quantities or temporal velocity signals is a formidable challenge. Recently, closed-loop wind tunnels [102, 103] have been built, allowing the measurement of long signals, e.g. for the generation of turbulence statistics [104]. Despite significant progress, the experiments remain difficult and limited, especially concerning fine details of laminar-to-turbulent transition and turbulent dynamics, and their interplay with non-ideal gas phenomena.

Concerning numerical databases, so-called scale resolving simulations, i.e. simulations resolving part or all of the turbulent flow dynamics, have gained more and more attention in turbomachinery analysis in the recent years because of their improved ability to bring insights into the intricate fluid dynamics and its connection to the generation of losses [42] with respect to lower fidelity models. These approaches, which include direct numerical simulations (DNS) or large-eddy simulations (LES), remain extremely challenging for ORC turbines due to their computational cost, although they have recently contributed to important advances in the understanding of turbulent flows of non-ideal gases [106]. Typical ORC turbines can exhibit outlet Reynolds numbers as high as 10 millions. Under such conditions, wall-resolved LES would require a computational mesh of roughly 100 billions points, which is currently extremely expensive even with advanced high-performance computing resources. On the other hand, Computational Fluid Dynamics (CFD) tools commonly used in

ORC design are mostly based on steady Reynolds-averaged Navier-Stokes (RANS) models, even if RANS is notoriously inaccurate for the prediction of several phenomena occurring in turbomachinery, such as laminar-to-turbulent transition, shock/boundary layer interaction, flow separation, and unsteady wakes. As reported by Sieverding & Manna [11], the wake region can account for a large part of the losses and needs to be properly captured. Contrary to gas turbines, for which high-fidelity simulations have been carried out for several years now as reported by Sandberg & Michelassi [42], scale resolving simulations of ORC turbines are much more recent. Durá Galiana & Wheeler [97] were the first to report simulations of ORC turbine cascades using higher-fidelity methods, with the aim to explore trailing edge loss mechanisms with a combined experimental and numerical study. Despite the rather coarse grid, LES captured total pressure profiles across the wake much more accurately than RANS, leading to significant differences in loss estimations. Coarse wall-resolved LES of a turbine stator using an organic working fluid (the fluorocarbon PP11) were presented by Hoarau *et al.* [92] for various thermodynamic conditions and pressure ratios. The exit Reynolds number was chosen in the range $1.13 \times 10^6 \div 2.26 \times 10^6$ to reduce the computational cost. In all cases, the flow was subjected to a very strong favorable pressure gradient, contributing to maintaining a laminar boundary layer over most of the blade surface. Boundary layer state played a dominant role in the complex shock/boundary layer interactions occurring in the trailing edge region, and could only be captured by LES, while RANS predicted excessively thick fully turbulent boundary layers. Such behavior was shown to have a profound effect on the predicted loss coefficients. Recently, the experimental investigation of Baumgärtner *et al.* [88] on a realistic ORC turbine blade was numerically reproduced in [105, 107]. To limit the computational effort, a simplified configuration corresponding to a 2D section extracted at the turbine shroud and extruded in the spanwise direction was investigated by Matar *et al.* [105] using wall-resolved LES. Due to the highly twisted 3D geometry, the 2D simulations showed discrepancies with the existing experimental measurements. However, the LES again highlighted the highly transitional nature of the blade boundary layers, despite the high exit Reynolds number of about 2 millions. As a consequence, fully turbulent RANS simulations yielded overly optimistic estimates of the loss coefficients. Giauque *et al.* [107] reduced the CPU cost to reproduce Baumgärtner's experiment [88] by using wall-modeled LES. This allowed the full configuration to be simulated including the upper and bottom walls, and the influence of the secondary vortices on the transition location and overall flow topology to be taken into account. The RANS calculations lead to higher losses than LES by $\sim 10\%$.

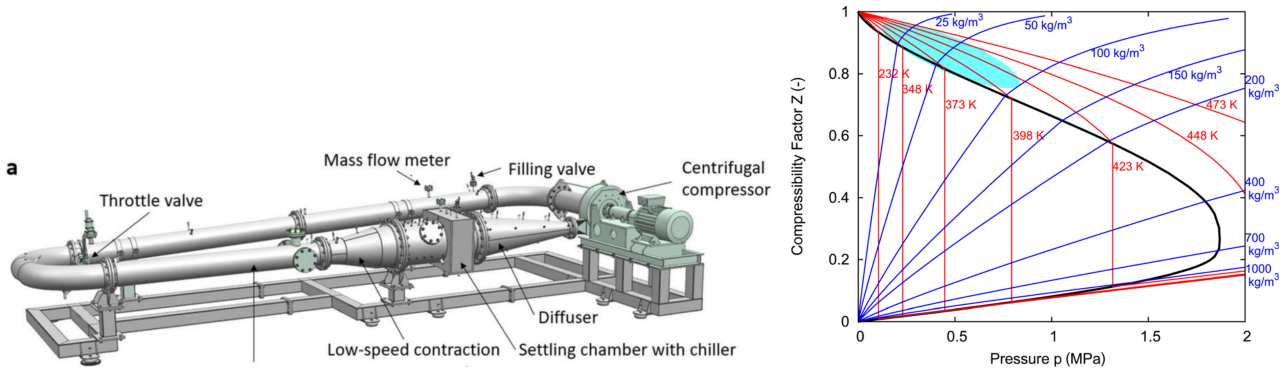

Figure 1.11: Left: Wind tunnel of the test facility CLOWT (from aus der Wiesche [96]). Right: Compressibility factor Z vs pressure for Novec649, with operability of the CLOWT in blue (from Reinker *et al.* [110]).

1.5 CLOWT experimental facility

The thesis is part of a Franco-German project with FH Muenster university, the ANR-DFG project REGAL-ORC (REal-GAs effects on loss mechanisms of ORC turbine flows). The project aims at conducting a joint experimental/numerical investigation of loss mechanisms in ORC turbine expanders. The numerical investigations are realized in France, at the Arts et Métiers Institute of Technology and Jean LeRond D'Alembert Institute. Concerning the experiments, a new facility has been built at Münster University in Germany, which consists of a pressurized closed-loop wind tunnel using Novec649 [102], Due to its low toxicity, flammability and environmental impact, Novec649 has been identified as a good candidate working fluid in ORC in replacement of chlorofluorocarbons (CFCs) and various other halogenated compounds, which contribute to ozone depletion [108, 109]. Compared to the organic vapor test facilities built by now, this wind tunnel operates in a continuous running mode, which allows for highly steady flow conditions, notably to study axial turbine blade cascades at high Reynolds numbers. The range of operating conditions of the CLOWT with $Novec^{TM}649$ are given in figure 1.12. The pressure can go up to 10 bars and the maximal temperature is around 180°C, and high subsonic to transonic flows can be established in the test section. The fundamental derivative of fluid dynamics Γ can be decreased up to 0.8. The turbulent intensity of the facility is ~ 0.1.

First experimental studies were performed on rotating cylinder Pitot tubes and hot-wire anemometers up to a Mach number of 0.7 and compared to numerical results previously reported in [111, 112] of URANS and LES. The simulations were compared with pressure measurements and Backward-Oriented Schlieren (BOS) visualizations, as well as Nusselt number measurements. Such comparisons represent the first-in-the-literature cross-validation of numerical models of flows dominated by viscous effects (flow separation, shock/boundary

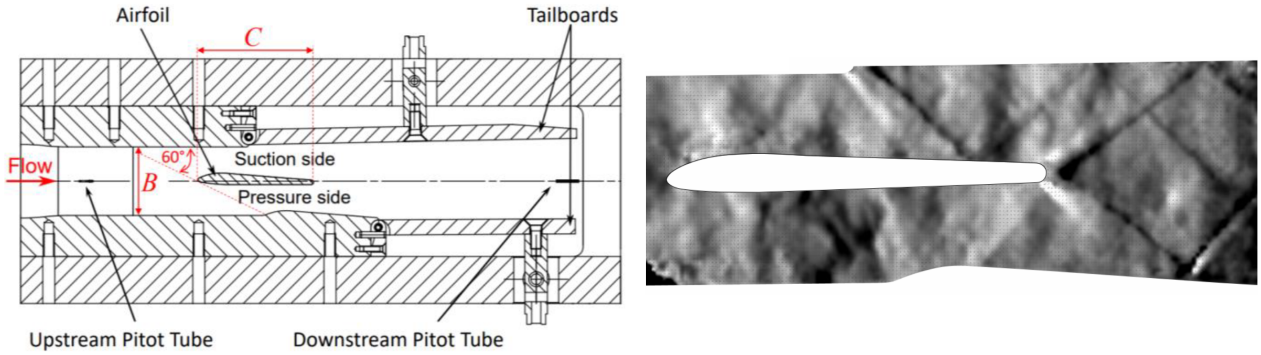

Figure 1.12: Experimental set-up (left) and BOS visualization (right) of the idealized blade vane configuration in Novec649 flow (from Hake *et al.* [115]).

layer and shock/wake interactions and unsteady wake dynamics) against experiments in the non-ideal flow regime. An experimental and numerical investigation of decaying HIT, reported here in Appendix A, was also performed in the facility (Hake *et al.* [113]). Recently, an experimental set-up of an idealized blade vane configuration was implemented in the CLOWT facility (see figure 1.12 left). While the profile lacks the typical curvature of most turbine blade profiles, it can be used as a test case to investigate fundamental phenomena such as tip gap flows in Passmann [114] or loss mechanisms with Novec649 in Hake *et al.* [115]. The blade was numerically investigated in the present thesis in Chapter 6. A preliminary BOS visualization of the idealized blade vane configuration is depicted in figure 1.12 (right).

1.6 Objectives and outline

In the present work, we investigate transition and loss mechanisms in ORC turbines by means of scale resolving simulations. In particular, the working fluid Novec649, used in the CLOWT facility, is considered. Specifically, the objectives of the thesis were:

1. First, we quantify real-gas effects on the development of a dense gas boundary layer at operating conditions representative of ORC applications. The latter provide a numerical reference of a Novec649 turbulent boundary layer, which is then used to assess our numerical strategy based on large-eddy simulations (LES) and implicit time integration.

2. Then, we study FST-induced transitions of a dense gas boundary layer in a canonical configuration, i.e. zero-pressure gradient flat plate configuration, under different FST conditions. In particular, we examine the influence of large-scale freestream disturbances on the transition.

3. Afterwards, we investigate the FST-induced transition in a more complex configuration, namely, a turbine leading edge, in order to understand the influence of leading edge receptivity and favorable pressure gradient on the transition.

4. Finally, we study the flow through an idealized turbine vane configuration to gain more insights in ORC turbines losses for non-ideal gases.

The thesis is organized as follows. In Chapter 2, the governing equations and numerical methods are described, and in particular the implementation and improvement of the implicit time strategy (see section 2.4). In Chapter 3, results of a reference DNS for transitional and fully turbulent state of Novec649 BL flow are presented and compared to LES. Chapter 4 presents various LES of FST-induced transitions on zero-pressure gradient BL of Novec649 under different FST conditions. To characterize the influence of the real gas on the transition, the simulations are compared with air BLs at low and high-subsonic conditions. In Chapter 5, LES results of FST-induced transition around a thick leading edge representative of turbine blades are discussed. Finally, in Chapter 6 the Novec649 flow in a dense gas regime around an idealized blade vane configuration is investigated by means of detached eddy simulations.

Chapter 2

Governing equations and numerical methods

2.1 Numerical solver MUSICAA

The simulations are performed using the in-house code MUSICAA (MUltiblock solver IN Computational AErodynamics and AEroacoustics), a well-validated, high-performance CPU numerical solver written in Fortran and parallelized with MPI library. The code solves the compressible Navier–Stokes equations and relies on a parallel multi-block strategy, alongside a coordinate transformation for curvilinear structured grids. To optimize computational and memory requirements, three sub-solvers are implemented: (i) for Cartesian grids, the Navier–Stokes equations are directly written in conservative form for Cartesian coordinates (x, y, z); (ii) for 2D curvilinear grids, (x, y) is transformed into (ξ, η), and the third direction, which corresponds generally to the spanwise direction z, is left unchanged (see section 2.2.1); (iii) for fully 3D curvilinear grids, (x, y, z) is transformed into (ξ, η, ζ) (see equations in [116]). The metrics for nonuniform grids are computed using the same finite-difference scheme as the one used for the discretization of fluxes (see section 2.3.1). In particular, great care is taken to ensure metrics commutation in 2D and metrics conservation in 3D, using the geometric conservation law (GCL) [117, 118]. In the present work, the Cartesian sub-solver is used in chapters 3 and 4 and the 2D curvilinear one is used in chapters 5 and 6.

In order to be able to study both perfect and real gas flows, the solver is equipped with several equation of state (EoS), given hereafter in ascending order of complexity: perfect gas EoS, van der Waals EoS, Peng-Robinson-Stryjek-Vera EoS [13], Martin-Hou EoS [119], Span-Wagner EoS [120] and reference NIST REFPROP EoS [121]. To supplement the EoS, several choices are available for the transport properties. The thermal conductivity can be modeled with Sutherland's law, a power law, Chung-Lee-Starling model [122, 123], Wen *et al.* model [124] or REFPROP model [121]. In addition to the constant Prandtl number law, the thermal

conductivity can be modeled using Chung-Lee-Starling and REFPROP model. The EoS and transport properties models used in the present work are presented in section 2.2 and are assessed for the thermodynamic conditions range considered along the thesis in section 3.2.

The finite-differences solver is equipped with various spatial and temporal schemes. Standard and Dispersion Relation Preserving spatial centered schemes [125, 126] are available up to the tenth-order. For explicit temporal integration, the solver allows the use of several Runge-Kutta schemes, such as also low-storage [16, 127] or optimized [127, 126] versions. The spatial and temporal schemes specifically used in the present work are detailed in section 2.3. During the thesis, a high-order Implicit Residual Smoothing (IRS) time integration strategy [17] was implemented in MUSICAA, along with some improvements. This point is thoroughly discussed in section 2.4.

The code is also relatively versatile in terms of boundary conditions. No-slip and slip wall conditions can be selected, in an adiabatic or isothermal formulation. For free boundary conditions, the radiation boundary conditions of Tam & Dong [128, 129] are available, along with the characteristic boundary conditions [130, 131, 132]. Recently, in order to tackle turbomachinery applications, inlet boundary condition based on real gas Riemann formulation [133, 134], in combination with a back pressure condition, were implemented. These boundary conditions can be supplemented with radial equilibrium and angular periodicity. Details about the boundary conditions used in the present work are provided in section 2.3.4. For inflow conditions, the solver is completed with different perturbation techniques (suction and blowing [34], instability waves [135], ...). Synthetic turbulence can also be introduced at the inlet through Random Fourier Modes (RFM), as described in section 2.3.4.3.

With the ability to perform Direct Numerical Simulations (DNS), Large-Eddy simulations (LES), or Reynolds-averaged Navier Stokes (RANS) simulations, MUSICAA is well-suited to address a broad range of applications. For LES, the subgrid scales (SGS) modeling in the solver can be realized either explicitly, for instance with a static or a dynamic Smagorinsky model which can be combined with a van Driest damping function for wall-bounded cases and with a multiscale model (small-small and large-small version), or with a similarity scale model, or it can be realized implicitly through the numerical dissipation [14]. RANS simulations can be performed either with the Spalart-Allmaras or the $k-\omega$ SST models. Recently, the solver has also been enhanced with the capability to conduct RANS-LES simulations with Delayed Detached Eddy Simulation (DDES), DDES-Shear Layer Adapted (DDES-SLA) and improved DDES (IDDES). The turbulence modeling strategies used within the scope of this research project are presented in section 2.3.5.

2.2 Governing equations

2.2.1 Flow equations

The compressible Navier–Stokes equations are written for a 2D curvilinear domain by using a coordinate transform. The physical space $(x,\ y)$ is mapped into a Cartesian regular computational space $(\xi,\ \eta)$ and the third direction, which corresponds in the following to the spanwise direction z, is left unchanged. By denoting $\mathbf{u} = (u, v, w)^T$ the velocity vector, ρ the density, p the pressure and E the specific total energy, the set of equations for the unknown vector $\mathbf{U} = (\rho, \rho u, \rho v, \rho w, \rho E)^T$ is given by:

$$\frac{\partial \mathbf{U}}{\partial t} + \frac{1}{J}\left(\frac{\partial \mathbf{F}_c}{\partial \xi} + \frac{\partial \mathbf{G}_c}{\partial \eta}\right) + \frac{\partial \mathbf{H}}{\partial z} = 0 \tag{2.1}$$

with $J = x_\xi y_\eta - y_\xi x_\eta$ the Jacobian of the coordinate transformation. The curvilinear fluxes are $\mathbf{F}_c = \mathbf{F}_c^e - \mathbf{F}_c^v$, $\mathbf{G}_c = \mathbf{G}_c^e - \mathbf{G}_c^v$, $\mathbf{H} = \mathbf{H}^e - \mathbf{H}^v$, where the inviscid (superscript e) and visco-thermal fluxes (superscript v) are given by:

$$\begin{aligned}
\mathbf{F}_c^e &= J\begin{pmatrix} \rho\Theta_\xi \\ \rho\mathbf{u}\Theta_\xi + p\nabla\xi \\ (\rho E + p)\Theta_\xi \end{pmatrix}, \quad \mathbf{G}_c^e = J\begin{pmatrix} \rho\Theta_\eta \\ \rho\mathbf{u}\Theta_\eta + p\nabla\eta \\ (\rho E + p)\Theta_\eta \end{pmatrix}, \quad \mathbf{H}^e = J\begin{pmatrix} \rho w \\ \rho w\mathbf{u} + p\nabla z \\ (\rho E + p)w \end{pmatrix}, \\
\mathbf{F}_c^v &= \begin{pmatrix} 0 \\ \boldsymbol{\tau}_\xi \\ \mathbf{u}\cdot\boldsymbol{\tau}_\xi - \mathbf{q}\cdot\nabla\xi \end{pmatrix}, \qquad \mathbf{G}_c^v = \begin{pmatrix} 0 \\ \boldsymbol{\tau}_\eta \\ \mathbf{u}\cdot\boldsymbol{\tau}_\eta - \mathbf{q}\cdot\nabla\eta \end{pmatrix}, \qquad \mathbf{H}^v = \begin{pmatrix} 0 \\ \boldsymbol{\tau}_z \\ \mathbf{u}\cdot\boldsymbol{\tau}_z - \mathbf{q}_z \end{pmatrix},
\end{aligned} \tag{2.2}$$

where $\Theta_\xi = \mathbf{u}\cdot\nabla\xi$ and $\Theta_\eta = \mathbf{u}\cdot\nabla\eta$ are the contravariant velocities. We have noted $\boldsymbol{\tau}_\xi = \mathscr{D}\cdot\nabla\xi$, $\boldsymbol{\tau}_\eta = \mathscr{D}\cdot\nabla\eta$, and $\boldsymbol{\tau}_z = \mathscr{D}\cdot\nabla z = \mathscr{D}\cdot(0,0,1)^T$, where $\mathscr{D}$ is the viscous stress tensor. The tensor $\mathscr{D}$ follows the Newtonian fluid constitutive relation, which gives:

$$\tau_{ij} = \mu\left(\frac{\partial u_i}{\partial x_j} + \frac{\partial u_j}{\partial x_i} - \frac{2}{3}\delta_{ij}\frac{\partial u_k}{\partial x_k}\right) \tag{2.3}$$

where $(u_1, u_2, u_3)^T = \mathbf{u}$ and δ_{ij} is the Kronecker symbol.

In the following, air is modeled as a perfect gas, thus satisfying $p = \rho RT$, with T the temperature and R the gas constant. For perfect gas flow, the specific total energy is $E = p/[(\gamma-1)\rho] + (u^2+v^2+w^2)/2$ with γ the ratio of specific heats. The heat flux components are modeled with Fourier's law, $\mathbf{q} = -\lambda\nabla T$. For perfect gas flows, the dynamic viscosity μ is approximated with Sutherland's law and the thermal conductivity λ is modeled by a constant Prandtl number (Pr) assumption. For dense gas conditions, μ and λ are also function of fluid density or pressure and modeled differently (see following section).

$\mathscr{M}$ [g/mol]	T_c [K]	p_c [MPa]	ρ_c [kg/m^3]	Z_c [-]	R_g [J/kg/K]	$c_{v,\infty}(T_c)$ [J/kg/K]	$\overline{\omega}$ [-]	$\overline{\xi}$ [Debye]
316.04	441.81	1.87	606.80	0.2650	26.308	975.96	0.471	0.43

Table 2.1: Main properties of Novec649 from [139]. $\mathscr{M}$ denotes the molar mass, Z the compressibility factor, R_g the individual gas constant, $c_{v,\infty}$ the ideal-gas specific heat at constant volume, $\overline{\omega}$ the acentric factor, $\overline{\xi}$ the dipole moment and subscript c is used for critical conditions.

2.2.2 Equation of State for Novec649

The fluid Novec649 considered in this thesis is the compound 1,1,1,2,2,4,5,5,5-nonafluoro-4-(trifluoromethyl)-3-pentanone, a perfluorinated ketone (chemical formula $C_6F_{12}O$) used as a working fluid in ORC, electronic cooling and fire suppression systems. Recent measurements [136, 137, 124, 138] have been made to characterise its thermo-physical properties. The values in Table 2.1 are those given by the manufacturer [139] and used in the NIST Refprop library [140]. The reference equation of state (EoS) in Refprop is based on experiments and modeling by McLinden *et al.* [136]. Specifically, a multiparameter functional form based on the Helmholtz free energy is calibrated for Novec649, with estimated errors lower than 0.1% for temperatures from 165 to 500 K and pressure up to 50 MPa. Additional measurements near the critical region were reported by Tanaka [137] and underlined some uncertainties in the definition of the critical point.

In the thesis, relatively dilute conditions for the vapor phase will be considered (see figure 2.1). A cubic EoS is chosen to reduce the overcost during the direct simulation integrations, namely the Peng-Robinson [12] EoS modified by Stryjek & Vera [13] (hereafter abbreviated as PRSV). It is given as:

$$p = \frac{R_g T}{v - b} - \frac{a\alpha(T)}{v^2 + 2bv - b^2}$$

where v is the specific volume and R_g the individual gas constant. By enforcing the critical-point conditions, the constants a, b are given by:

$$a = \underbrace{0.457235}_{a'} \frac{R_g^2 T_c^2}{p_c} \qquad b = \underbrace{0.077796}_{b'} \frac{R_g T_c}{p_c} \qquad \alpha(T) = \left[1 + K(1 - \sqrt{T_r})\right]^2$$

with $T_r = T/T_c$ the reduced temperature. In the Stryjek & Vera [13] modification, the parameter K is $K_0 + K_1(1 + \sqrt{T_r})(0.7 - T_r)$ with $K_0 = 0.378893 + 1.4897153\overline{\omega} - 0.17131848\overline{\omega}^2 + 0.196554\overline{\omega}^3$, $\overline{\omega}$ being the acentric factor. For $T_r > 0.7$, the authors suggest that $K_1 = 0$, which is the case for our applications ($T > 310$ K). For cubic EoS, the critical quantities cannot be set independently and, introducing the compressibility factor

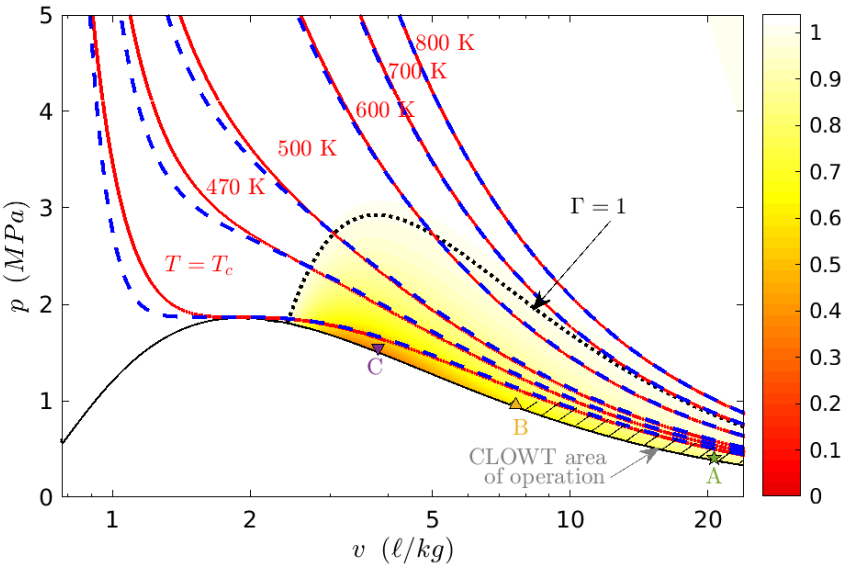

Figure 2.1: Clapeyron's diagram for Novec649. The thick black line represents the saturation curve and the thick dotted line marks the boundary of the dense-gas region ($\Gamma < 1$), where the colormap represents values of the fundamental derivative of gas dynamics Γ. Isothermal curves obtained with PRSV EoS (——) are compared with ones obtained with the reference EoS of REFPROP (– – –). The hatched area indicates the limits of operability of CLOWT facility, and the three selected operating conditions A, B and C are marked with symbols.

$Z_c = p_c/(R_g \rho_c T_c)$, the compatibility at critical condition yields

$$1 = \frac{1}{Z_c - b'} - \frac{a'}{Z_c^2 + 2b'Z_c - b'^2} \quad \Rightarrow \quad Z_c \approx 0.3112$$

Keeping reference values for T_c and p_c, the critical density is thus modified from its value in Table 2.1 as $\rho_c = 516.71$ kg/m^3.

For the calculation of caloric properties, the PRSV EoS is supplemented with a model for the ideal gas contribution to the specific heat at constant volume, represented by a power law of the form:

$$c_{v,\infty}(T) = c_{v,\infty}(T_c)\left(\frac{T}{T_c}\right)^n$$

where the exponent n is set at 0.405 and $c_{v,\infty}$ is given in Table 2.1. The caloric equation of state is then completely determined via the compatibility relation for the internal energy:

$$e = e_{ref} + \int_{T_{ref}}^{T} c_{v,\infty}(T')dT' - \int_{\rho_{ref}}^{\rho} \left[T \left.\frac{\partial p}{\partial T}\right|_{\rho} - p \right] \frac{d\rho'}{\rho'^2},$$

The isothermal curves calculated with the reference EoS of REFPROP and with PRSV Eos are compared in figure 2.1. A very good match is observed for dilute-gas conditions. The operation range of CLOWT wind

Condition	T [K]	ρ [kg/m^3]	Fluid models	p [MPa]	c [m/s]	Γ	μ [μ Pa.s]	λ [W/m/K]	Pr
Point A	*373.15*	*48.51*	PRSV-Chung	0.40	84.66	0.84	12.8	0.014	0.89
			REFPROP	0.40	84.66	-	18.3	0.017	1.05
Point B	*408.15*	*131.58*	PRSV-Chung	0.96	70.22	0.60	20.1	0.018	1.24
			REFPROP	0.96	70.12	-	26.0	0.021	1.43
Point C	*433.15*	*263.16*	PRSV-Chung	1.55	53.89	0.41	33.6	0.023	2.20
			REFPROP	1.55	53.42	-	35.9	0.026	2.37

Table 2.2: Thermophysical properties at selected operating points A, B, C. Numbers in italic are imposed.

tunnel at Muenster University, namely $p < 1$ MPa and $T < 453$ K [110], is indicated by the hatched region, which belongs to the dense-gas regime (fundamental derivative of gas dynamics, $\Gamma = 1 + \rho/c(\partial c/\partial \rho)_s < 1$, c being the sound speed and s the entropy). Three operating conditions are selected in the following studies. Point A corresponds to nominal conditions of the CLOWT facility, $p = 4$ bars and $T = 100°$C, and will be the operating point for the direct numerical simulations (DNS) and large-eddy simulations (LES) in chapters 3 and 4. Point B is chosen at the limits of operability of the CLOWT facility, which is still in the dilute-gas region. Finally, point C is close to the minimum of Γ, where greater non-ideal effects can be expected and will be used in chapter 6. Note that a minimum value of Γ of 0.35 is estimated using PRSV EoS, meaning that Novec649 is not a BZT fluid (characterized by a region with $\Gamma < 0$ in the vapor phase). The thermodynamic quantities obtained with PRSV and REFPROP are reported in Table 2.2. The difference is below 0.3% for p, T, ρ and up to 1% for the sound speed c at point C.

2.2.3 Transport properties for Novec649

Reference laws for Novec649 based on new measurements are implemented in the REFPROP library [140], namely the model of Wen *et al.* [124] for dynamic viscosity and the model of Perkins *et al.* [138] for thermal conductivity. In Wen *et al.* [124], the viscosity correlation is written as a sum of three contributions:

$$\mu(\rho, T) = \mu_0(T) + \mu_1(T)\rho + \Delta\mu(\rho, T) \tag{2.4}$$

where μ_0 is the dilute-gas limit viscosity deduced from Chapman-Enskog theory [123], $\mu_1(T)$ gives a density dependence of viscosity, following the work of Vogel *et al.* [141], and $\Delta\mu(\rho, T)$ is a residual term determined from an empirical fit based on measurements for the compressed liquid phase at pressures up to 40 MPa and a temperature range between 243 to 373 K. The estimated uncertainty of formula (2.4) is 2% in this region. Unfortunately, there are no measurements in the gas phase, for which an uncertainty of 10% is estimated [140].

In the present simulations, we use the viscosity model for dense gases of Chung, Lee & Starling [122] and Chung *et al.* [123], which is also based on a density-dependent correction of the Chapman-Enskog formula for pure substances and can be written as:

$$\mu(\rho,T) = \mu_0(T)[1/G_2 + A_6 Y] + \mu_p(\rho,T) \tag{2.5}$$

where the dilute-gas component μ_0 is given by

$$\mu_0 = 4.0785\times10^{-6}\frac{\sqrt{\mathscr{M}T}}{V_c^{2/3}\Omega^*}F_c \quad \text{with} \quad F_c = 1 - 0.2756\overline{\omega} + 0.059035\overline{\xi}_r^4 \tag{2.6}$$

$\overline{\xi}_r = 131.3\overline{\xi}/(V_cT_c)^{1/3}$ being the reduced dipole moment, V_c denotes the molar critical volume in cm^3/mol and $\mathscr{M}$ denotes the molar mass in g/mol. The dimensionless Lennard-Jones collision integral Ω^* is approximated using the empirical equation of Neufeld, Janzen & Aziz [142]:

$$\begin{aligned}\Omega^*(T^*) = {} & 1.16145(T^*)^{-0.14874} + 0.52487\mathrm{e}^{-0.7732T^*} + 2.16178\mathrm{e}^{-2.43787T^*} \\ & - 6.435\times10^{-4}(T^*)^{0.14874}\sin\left[18.0323(T^*)^{-0.7683} - 7.27371\right]\end{aligned} \tag{2.7}$$

with $T^* = 1.2593T/T_c$. A density dependence is introduced by the nonlinear function G_2:

$$G_2 = \frac{A_1[1-\exp(-A_4Y)]/Y + A_2G_1\exp(A_5Y) + A_3G_1}{A_1A_4 + A_2 + A_3}$$

with

$$Y = \frac{\rho}{6\rho_c}, \quad G_1 = \frac{1-0.5Y}{(1-Y)^3} \tag{2.8}$$

The third term in Eq.(2.5) is a correction that takes into account dense-gas effects:

$$\mu_p = 36.344\times10^{-7}\frac{\sqrt{\mathscr{M}T_c}}{V_c^{2/3}}A_7Y^2G_2\exp\left[A_8 + A_9(T^*)^{-1} + A_{10}(T^*)^{-2}\right]$$

The constants A_1-A_{10} are functions of the acentric factor $\overline{\omega}$ and reduced dipole moment $\overline{\xi}_r$:

$$A_i = a_0(i) + a_1(i)\overline{\omega} + a_2(i)\overline{\xi}_r^4, \qquad i\in\{1,..,10\}.$$

whose coefficients a_0, a_1 and a_2 are given in Chung *et al.* [123] and in appendix A of Sciacovelli *et al.* [30].

For the thermal conductivity λ, the correlation implemented in Refprop is that of Perkins *et al.* [138] based on measurements for vapor, liquid and supercritical fluid. It is made of three contributions:

$$\lambda(\rho,T) = \lambda_0(T) + \Delta\lambda_r(\rho,T) + \Delta\lambda_c(\rho,T) \tag{2.9}$$

A rational polynomial in reduced temperature T_r is used for the dilute-gas thermal conductivity λ_0 and a polynomial in temperature and density is fitted for the residual thermal conductivity $\Delta\lambda_r$. The last term $\Delta\lambda_c$ is used to describe the thermal conductivity enhancement in the critical region and relies on the crossover model of Olchowy & Sengers [143], which requires a model of viscosity (here the correlation of Wen *et al.* [124]), and an EoS for heat capacities and density derivatives (here EoS of McLinden *et al.* [136]).

In our calculations, the Chung-Lee-Starling model [122, 123] is used, which is written similarly as viscosity model (2.5):

$$\lambda(\rho,T) = \lambda_0(T)[1/H_2 + B_6 Y] + \lambda_p(\rho,T) \tag{2.10}$$

The dilute-gas contribution λ_0 is modeled as

$$\lambda_0 = 418.4 \times 7.452 \frac{\mu_0}{\mathscr{M}}\psi$$

where μ_0 is given by Eq.(2.6) and ψ is a modified Eucken-type correlation based on kinetic theory extended to polyatomic gases, where the contribution of internal degrees of freedom (rotational and vibrational) is added to translational degrees of freedom:

$$\psi = 1 + \alpha \frac{0.215 + 0.28288\alpha - 1.061\beta + 0.26665 Z_{\text{coll}}}{0.6366 + \beta Z_{\text{coll}} + 1.061\alpha\beta}$$

with a rotational coefficient $\alpha = c_{v,\infty}/R_g - 3/2$, a diffusion term β, empirically linked to the acentric factor as $\beta = 0.7862 - 0.7109\overline{\omega} + 1.3168\overline{\omega}^2$ and $Z_{\text{coll}} = 2 + 10.5T_r^2$ modeling the number of collisions required to interchange a quantum of rotational energy with translational energy. In the same way as the viscosity model, the dilute-gas contribution is weighted by a density-dependent nonlinear term H_2, given by:

$$H_2 = \frac{B_1[1 - \exp(-B_4 Y)]/Y + B_2 G_1 \exp(B_5 Y) + B_3 G_1}{B_1 B_4 + B_2 + B_3}$$

with Y and G_1 defined by Eq.(2.8). The third term in Eq.(2.5) is a dense-gas correction:

$$\lambda_p = 418.4 \times 3.039 \times 10^{-4} \frac{\sqrt{T_c/\mathscr{M}}}{V_c^{2/3}} B_7 Y^2 H_2 T_r^{1/2}$$

The constants B_1-B_7 are functions of the acentric factor $\overline{\omega}$ and reduced dipole moment $\overline{\xi}_r$:

$$B_i = b_0(i) + b_1(i)\overline{\omega} + b_2(i)\overline{\xi}_r^4, \qquad i \in \{1,..,7\}.$$

with coefficients b_0, b_1 and b_2 given in Chung *et al.* [123].

The transport properties calculated with Chung-Lee-Starling and Refprop models for selected operating conditions A, B, C are reported in Table 2.2. The difference for viscosity values decreases from 30% (point A) to 6% (point C). A difference of about 15% is noted for the thermal conductivity. Since the dilute-gas component $\mu_0(T)$ is the same in the models of Wen *et al.* [124] and Chung *et al.* [123], this means that the differences observed for the viscosity are due to the density dependence, even in the very dilute condition (point A). A posteriori validations for the laminar boundary layer are reported in section 3.2.

2.3 Numerical methods

2.3.1 Space discretization

We consider a system of conservation laws of the form

$$\frac{\partial w}{\partial t} + \sum_d \frac{\partial f_d(w)}{\partial x_d} = 0 \tag{2.11}$$

where d is the number of space dimensions, f_d is the flux function in the d^{th} direction, and x_d the corresponding space coordinate. The semi-discrete form of (2.11) is written as

$$w_t + \mathscr{R}(w) = 0\,, \tag{2.12}$$

$\mathscr{R}$ being the space approximation operator. In the present work, except if specified otherwise, we adopt a tenth-order central finite-difference (FD) scheme for the inviscid fluxes, and the viscous fluxes are discretized by fourth-order central FD scheme and integrated in the last substep of the time integration scheme (this choice is discussed in section 3.4.2). For a 1D problem on a uniform mesh of size Δx, $x_j = j\Delta x$ and the semi-discrete scheme in space reads:

$$(w_t)_j + \frac{(\delta \mathscr{F})_j}{\Delta x} = 0$$

where δ is the classical difference operator over one cell:

$$\delta(\bullet)_{j+\frac{1}{2}} = (\bullet)_{j+1} - (\bullet)_j \tag{2.13}$$

and the numerical inviscid flux $\mathscr{F}_{j+\frac{1}{2}}$ at cell interface $j+\frac{1}{2}$ is

$$\mathscr{F}_{j+\frac{1}{2}} = \left[\left(I - \frac{1}{6}\delta^2 + \frac{1}{30}\delta^4 - \frac{1}{140}\delta^6 + \frac{1}{1260}\delta^8\right)\mu f\right]_{j+\frac{1}{2}} \tag{2.14}$$

where f is the physical flux, and μ is the cell average operator $\mu(\bullet)_{j+\frac{1}{2}} = \frac{1}{2}\left((\bullet)_{j+1} + (\bullet)_j\right)$.

2.3.2 Dissipation strategy

Central difference methods are zero dissipative and prone to aliasing errors. Even starting with a smooth solution, nonlinearity can excite odd-even decoupling, and dissipation or filtering is needed to remove grid-to-grid oscillations. The latter are preferentially generated near the approximate physical boundary conditions and can arise due to the successive application of the first-order derivative operator in computing the derivatives of viscous fluxes. The problem is further complicated in the presence of sharp flow discontinuities, such as shocks, and in the context of large-eddy simulations. The unresolved modes introduce an aliasing error and have to be dissipated by adding some form of numerical dissipation or filtering. Alternative options are given by convective splitting strategies that ensure the exact conservation of physical quantities such as the kinetic energy or the entropy at the discrete level [144, 145, 146, 147], or by considering staggered arrangements of variables [148, 149, 150]. For strategies relying on unsplitted fluxes and colocated variables, the nature, amount and form of the numerical dissipation have a strong influence on the solution accuracy [14, 15].

A scalar artificial dissipation (AD) can be used (we omit here the shock-capturing term for simplicity). The approximation of flux derivatives is supplemented by a ninth-order dissipation term:

$$\mathscr{F}_{j+\frac{1}{2}} = \left[\left(I - \frac{1}{6}\delta^2 + \frac{1}{30}\delta^4 - \frac{1}{140}\delta^6 + \frac{1}{1260}\delta^8\right)\mu f - \mathscr{D}^{AD}\right]_{j+\frac{1}{2}}$$

with

$$\mathscr{D}^{AD}_{j+\frac{1}{2}} = \frac{1}{1260}(\lambda^e \delta^9 w)_{j+\frac{1}{2}} \tag{2.15}$$

where λ^e is the spectral radius of the inviscid flux Jacobian. The coefficient $1/1260$ is used by analogy with a ninth-order MUSCL scheme [17].

In this work, an alternative to artificial viscosity is selected and the numerical dissipation is provided with selective filtering (SF), as for instance in [14, 15]. Specifically, a filtered quantity w^*_j is computed by using a tenth-order centered filter built on an eleven-point stencil [151, 152] :

$$w^*_j = w_j - \chi_f \mathscr{D}^{SF}_j \quad \text{with} \quad \mathscr{D}^{SF}_j = \sum_{l=-5}^{5} d_l \, w_{j+l} \,, \tag{2.16}$$

with the coefficient χ_f ranging between 0 and 1. In the following, a value $\chi_f \in [0.1\,, 0.2]$ is used, so that a minimal amount of dissipation is introduced. The filter has symmetric coefficients d_l, so that it is nondispersive. The connection with artificial dissipation has been clearly highlighted by Edoh *et al.* [153] (see also [154, 155]), who showed that the performance of explicit AD and SF are similar.

Both methods adjust the amount of dissipation to the mesh size Δx. One pitfall of the filtering approach is that it does not take into account the time step Δt, and for very small time steps (or Courant-Friedrichs-Lewy (CFL) numbers), the repeated application of the filter can lead to an overdissipation. A simple trick proposed in [153] to overcome this artefact is to replace χ_f by

$$\min\{\chi_f, \mathrm{CFL}_{\mathrm{local}}\}, \tag{2.17}$$

where $\mathrm{CFL}_{\mathrm{local}}$ is based on the spectral radius of inviscid fluxes at the considered point and in the considered direction. Another possibility not explored in this work is the temporally consistent filter based on viscous scaling proposed by [156]. We will see that selective filtering independent on Δt has also some advantages in the context of IRS time advancement in section 2.4.

For transonic or supersonic configurations (Chapter 6), the filter is equipped with a shock capturing method. The high-order selective filtering scheme is combined with a lower-order term activated in proximity of flow discontinuities based on a shock sensor. The filter therefore writes:

$$w_j^* = w_j - \frac{(\delta \mathscr{D}^{SC})_j}{\Delta x} \quad \text{with} \quad \mathscr{D}^{SC}_{j+\frac{1}{2}} = [\epsilon_2 \delta w + \epsilon_{10} \delta^9 w]_{j+\frac{1}{2}} \tag{2.18}$$

where $\epsilon_{2,j+\frac{1}{2}} = \chi_f^{sc} \max(\phi_j, \phi_{j+1})$ and $\epsilon_{10,j+\frac{1}{2}} = \max(0, k_{10} - \frac{1}{105}\epsilon_{2,j+\frac{1}{2}})$, with χ_f^{sc} the filtering coefficient associated with the low-order term and $k_{10} = \chi_f/1260$. In practice, χ_f^{sc} is taken of the same order of magnitude as χ_f. The low-order filter is activated based on a combination between Ducros (term I) [157] and a pressure-based (term II) shock sensors:

$$\phi_j = \underbrace{\frac{(\nabla.\mathbf{u})^2}{(\nabla.\mathbf{u})^2 + |\nabla \times \mathbf{u}|^2 + e_s}}_{\mathrm{I}} \times \underbrace{\left| \frac{p_{j+1} - 2p_j + p_{j-1}}{\omega_s \times \mathscr{P} + (1-\omega_s)\mathscr{P}_{TVD}} \right|}_{\mathrm{II}} \tag{2.19}$$

with e_s a small positive value (10^{-16}) to avoid division by zero in term I. The pressure-based shock sensor used is constructed as a combination of the Jameson pressure-based shock sensor [16], $\mathscr{P} = (p_{j+1} + 2p_j + p_{j-1})$, and a total variation diminishing (TVD)-like formulation, $\mathscr{P}_{TVD} = |p_{j+1} - p_j| + |p_j - p_{j-1}|$. It was first introduced by Swanson & Turkel [158] to give more dissipation near shocks and prevent the occurrence of spurious oscillations near shocks. The switch ω_s is set to 0.5.

2.3.3 Time discretization

The baseline time-stepping procedure is the explicit four-stage low-storage Runge–Kutta (RK4) of Jameson *et al.* [16], which may be written as:

$$\begin{cases} w^{(0)} = w^n \\ \Delta w^{(k)} = -\alpha_k \Delta t \mathscr{R}(w^{(k-1)}), \quad k = 1, ..., s \\ w^{n+1} = w^{(s)} \end{cases} \tag{2.20}$$

where w^n is the numerical solution at time $n\Delta t$, $\Delta w^{(k)} = w^{(k)} - w^{(0)}$ is the solution increment at the k-th RK stage, s=4 is the number of stages and α_k are the scheme coefficients (α_1=1/4, α_2=1/3, α_3=1/2, α_4=1). Its order of accuracy is equal to four for linear equations and reduces down to two for nonlinear problems. When coupled with the tenth-order centered approximation, RK4 is stable under a CFL condition:

$$\text{CFL} = \frac{\Delta t \lambda_e}{\Delta x} \lessapprox 1.598$$

where the spectral radius of the inviscid flux Jacobians, λ_e, is the sum of the velocity magnitude U and the sound speed c. For a viscous problem, RK4 has also to satisfy a viscous stability condition:

$$\frac{\Delta t \lambda_v}{\Delta x^2} \lessapprox 0.696$$

where λ_v is the spectral radius of viscous flux Jacobians. In practice, the time step is taken as the minimum time step given by the CFL condition and the viscous condition (also called Fourier criterion). When solving compressible Navier–Stokes equations, the CFL criterion is more restrictive due to the contribution of the sound speed to the definition of the CFL, except for very low Mach numbers and fine grids. However, using time steps larger than those allowed by the CFL condition in partially implicit time integration methods can still lead to the violation of the Fourier criterion (see discussion in section 5.6 in [116]).

2.3.4 Boundary conditions

For wall boundary conditions, the no-slip condition $u = v = w = 0$ is enforced together with the nullity of the normal pressure gradient $\partial p/\partial n = 0$. The temperature is also prescribed from the nullity of normal temperature gradient $\partial T/\partial n = 0$ for adiabatic walls, so that all variables are imposed. The FD scheme is kept centered and reduced down to second order near walls. In the different 3D simulations tackled in the following, periodicity is enforced in the third direction. Outlet boundary conditions are systematically complemented with grid stretching and a Laplacian filter to damp exiting flow structures and avoid reflections. Tam & Dong inflow

boundary condition is described in section 2.3.4.1. Details on Riemann invariant boundary condition, used for turbomachinery applications in the present thesis, are given in section 2.3.4.2. Finally, the synthetic inflow strategy retained in the present thesis is presented in section 2.3.4.3.

2.3.4.1 Tam & Dong inflow boundary condition

From chapters 3 to 5, the radiation boundary conditions of Tam & Dong [128], using a far-field solution of the sound waves, are applied at the free boundaries of the computational domains. The governing equations are consequently changed in the few first planes parallel to the boundary. Since periodic boundary conditions are applied for the lateral boundaries, we choose to use a 3-D cylindrical formulation:

$$\left(\frac{1}{V_g}\frac{\partial}{\partial t}+\frac{\partial}{\partial r}+\frac{1}{r}\right)\begin{bmatrix}\rho-\bar{\rho}\\ \mathbf{u}-\bar{\mathbf{u}}\\ p-\bar{p}\end{bmatrix} = 0 \tag{2.21}$$

where V_g denotes the group velocity of acoustic waves:

$$V_g = \bar{\mathbf{u}}.\mathbf{e_r}+\sqrt{\bar{c}^2-(\bar{\mathbf{u}}.\mathbf{e}_\theta)^2} \quad \text{with} \quad \begin{cases}\mathbf{e_r}=(\cos\theta,\sin\theta)\\ \mathbf{e}_\theta=(-\sin\theta,\cos\theta)\end{cases}$$

The radiation conditions are expressed in the polar coordinates $(r,\ \theta)$, which requires the choice of a radiation center. The exact location of the radiation center is not very important if the boundaries are sufficiently far [129]. In chapter 3, the perturbations imposed at the inflow corresponds to the oblique instability waves (see details in [135]) and the location of the radiation center is chosen at the wall close to the inflow condition at (x,y)=(0.5 mm,0). In chapter 4 and 5, a synthetic flowfield based on Random Fourier Modes (RFM) is added at the inflow (see section 2.3.4.3) and, to allow the correct introduction of the freestream turbulence, the location of the radiation center is chosen close to the inlet and variable along y, in order to remain parallel to the inlet boundary condition.

For an inflow boundary, Tam [129] has proposed to replace the radiation condition by the modified system :

$$\left(\frac{1}{V_g}\frac{\partial}{\partial t}+\frac{\partial}{\partial r}+\frac{1}{r}\right)\begin{bmatrix}\rho-\bar{\rho}\\ \mathbf{u}-\bar{\mathbf{u}}\\ p-\bar{p}\end{bmatrix} = \left(\frac{1}{V_g}\frac{\partial}{\partial t}+\frac{\partial}{\partial r}+\frac{1}{r}\right)\begin{bmatrix}\rho_{in}\\ \mathbf{u}_{in}\\ p_{in}\end{bmatrix} \tag{2.22}$$

where $(\rho_{in},\ \mathbf{u}_{in},\ p_{in})$ are the density, velocity vector, and pressure fluctuations to be imposed at the inflow. In the formulas, the mean quantities, denoted with an overbar, are computed during the simulation. The sound speed is obtained from the real-gas equation of state (PRSV in the present case). The next step is to add the increments written for the primitive variables to the ones for the conservative variables. For that purpose, we

use the same procedure used by [132] to extend characteristic boundary conditions. Namely, the time derivative of the internal energy e is

$$\frac{\partial e}{\partial t} = \left(\frac{\partial e}{\partial \rho}\right)_p \frac{\partial \rho}{\partial t} + \left(\frac{\partial e}{\partial p}\right)_\rho \frac{\partial p}{\partial t} \tag{2.23}$$

with

$$\left(\frac{\partial e}{\partial \rho}\right)_p = \frac{1}{\rho}\left(\frac{p}{\rho} - \frac{c_p}{\alpha_v}\right) \quad \text{and} \quad \left(\frac{\partial e}{\partial p}\right)_\rho = \frac{c_p}{\alpha_v}\frac{1}{\rho c^2} \tag{2.24}$$

where the specific heat at constant pressure c_p, the isobaric expansion coefficient α_v , and the sound speed c are computed from the equation of state. The time derivatives of the conservatives variables are thus $\partial\rho/\partial t$ and

$$\frac{\partial \rho u_i}{\partial t} = u_i \frac{\partial \rho}{\partial t} + \rho \frac{\partial u_i}{\partial t} \tag{2.25}$$

$$\frac{\partial \rho E}{\partial t} = \frac{c_p}{\alpha_v}\left(\frac{1}{c^2}\frac{\partial p}{\partial t} + \frac{\partial \rho}{\partial t}\right) + \left(E + \frac{p}{\rho}\right)\frac{\partial \rho}{\partial t} + \rho u_j \frac{\partial u_j}{\partial t} \tag{2.26}$$

In the following test-cases, at free boundaries, non-reflecting Tam and Dong's conditions [128] are applied on the first 5 rows of cells. One-sided 7 point-stencil FD schemes [128] are applied for derivatives normal to borders, and the resulting discretized terms are added to the increments.

2.3.4.2 Riemann invariant boundary condition

For turbomachinery applications, velocity direction, total enthalpy H_0 and entropy s_0 are imposed at inlet boundary condition. To do that, we rely on the conservation of the outgoing Riemann invariant:

$$\mathrm{R} = p_i - (\rho c)_m u_{n,i} = p_b - (\rho c)_m u_{n,b} \tag{2.27}$$

where subscripts i and b are for the interior point and boundary point, respectively, and where u_n denotes the inlet velocity normal to the boundary condition, p is the pressure and $(\rho c)_m$ is the product of the density and sound speed at the interface of the interior and boundary points. Using a Newton method, the boundary temperature T_b is computed from the total stagnation enthalpy $H_0(s_0, T)$. With PRSV EoS, a second Newton loop inside the first one is necessary to determine one other thermodynamic variable (pressure or density) based on the entropy $s_0(T, \rho)$. Only a few iterations are necessary to converge the Newton loops. The conservative variables are then updated based on the calculated thermodynamic variables and the Riemann invariant, using $u_{n,b} = (p_b - \mathrm{R})/(\rho c)_m$.

A back pressure condition is used at the outlet boundary. In subsonic conditions, a target pressure is used to impose a given pressure ratio through the turbine cascade whereas, in supersonic conditions, the pressure is directly extrapolated from the interior points.

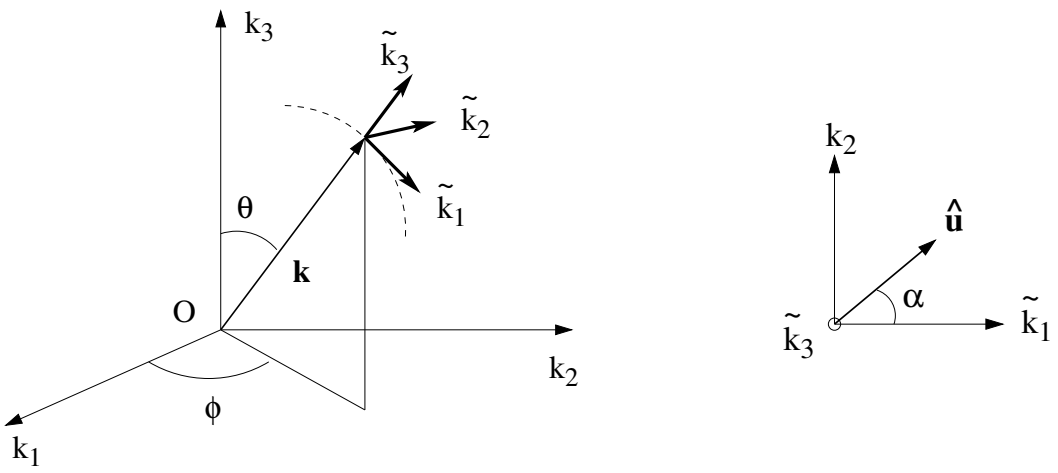

Figure 2.2: Local frame ($\tilde{\mathbf{k}}_1$, $\tilde{\mathbf{k}}_2$, $\tilde{\mathbf{k}}_3$) in the k-space, and representation of the Fourier component $\hat{\mathbf{u}}_a$.

2.3.4.3 Inlet synthetic turbulence

To create unsteady, stochastic inlet conditions, we use a synthetic flowfield based on Random Fourier Modes (RFM), in the form derived in the Stochastic Noise Generation and Radiation (SNGR) model [159, 160]. Some extensions of the RFM have been proposed by Smirnov *et al.*[161] and Batten *et al.*[162], to take into account the anisotropy of wall turbulence. For homogeneous turbulence, the 3-D Fourier transform in space of the fluctuating velocity field can be defined as:

$$\mathbf{u}'(\mathbf{x}) = \int \hat{\mathbf{u}}(\mathbf{k}) e^{i\mathbf{k}.\mathbf{x}}\, d\mathbf{k} \tag{2.28}$$

A straightforward application of the incompressibility condition yields $\hat{\mathbf{u}}(\mathbf{k}).\mathbf{k} = 0$, *i.e.* the Fourier component $\hat{\mathbf{u}}(\mathbf{k})$ must be perpendicular to the wavenumber vector $\mathbf{k}$. Here we choose a fluctuating velocity field as :

$$\mathbf{u}'(\mathbf{x}) = \int 2\hat{\mathbf{u}}_a \cos(\mathbf{k}.\mathbf{x})\, d\mathbf{k} \tag{2.29}$$

The wavenumber $\mathbf{k}$ is plotted in the k-space in fig. 2.2. Introducing the local frame ($\tilde{\mathbf{k}}_1$, $\tilde{\mathbf{k}}_2$, $\tilde{\mathbf{k}}_3$) corresponding to the spherical coordinates (k, θ, ϕ), since $\tilde{\mathbf{k}}_3$ is aligned with $\mathbf{k}$, the normality condition deduced from the continuity constraint indicates that the vector $\hat{\mathbf{u}}_a$ is necessarily in the plane ($\tilde{\mathbf{k}}_1$, $\tilde{\mathbf{k}}_2$). In this frame, we note $\hat{\mathbf{u}}_a = \hat{u}\,\mathbf{a} = \hat{u}(\cos\alpha, \sin\alpha)$, with the angle α defined on the right of Fig. 2.2.

The turbulent inlet field is generated as the sum of N independent RFM. The amplitudes $\hat{u}_n$ are not random, but are determined from the turbulent kinetic energy spectrum. The fluctuating velocity field is then expressed as a

Fourier serie :

$$\mathbf{u}'(\mathbf{x},t) = \sum_{n=1}^{N} 2\hat{u}_n \cos(\mathbf{k}_n.(\mathbf{x}-\overline{\mathbf{u}}t) + \omega_n t + \psi_n)\mathbf{a}_n \tag{2.30}$$

where $\psi_n, \mathbf{k}_n, \mathbf{a}_n$ are random variables with given probability density functions. Isotropy is obtained by choosing the random variables in the following way. For each mode, the wavenumber vector $\mathbf{k}$ is picked on a sphere of radius k. In the Cartesian coordinate system, the three unit vectors of the local frame are :

$$\tilde{\mathbf{k}}_1 = \begin{pmatrix} \cos\theta\cos\phi \\ \cos\theta\sin\phi \\ -\sin\theta \end{pmatrix} \quad \tilde{\mathbf{k}}_2 = \begin{pmatrix} -\sin\phi \\ \cos\phi \\ 0 \end{pmatrix} \quad \tilde{\mathbf{k}}_3 = \begin{pmatrix} \sin\theta\cos\phi \\ \sin\theta\sin\phi \\ \cos\theta \end{pmatrix} \tag{2.31}$$

The wavenumber vector is simply $\mathbf{k} = k\tilde{\mathbf{k}}_3$, and the isotropy requires that:

$$\frac{dS}{4\pi k^2} = \frac{k\sin\theta d\phi k d\theta}{4\pi k^2} = p(\theta)d\theta p(\phi)d\phi \tag{2.32}$$

The probability density functions are taken to be $p(\theta)$=$\sin\theta/2$ and $p(\phi)$=$1/(2\pi)$. The unit vector $\mathbf{a}_n$ is:

$$\mathbf{a}_n = \cos\alpha\,\tilde{\mathbf{k}}_1 + \sin\alpha\,\tilde{\mathbf{k}}_2 = \begin{pmatrix} \cos\alpha\cos\theta\cos\phi - \sin\alpha\sin\phi \\ \cos\alpha\cos\theta\sin\phi + \sin\alpha\cos\phi \\ -\cos\alpha\sin\theta \end{pmatrix} \tag{2.33}$$

α being distributed uniformly between 0 and 2π, thus $p(\alpha)$=$1/(2\pi)$. The turbulent kinetic energy is given by:

$$\bar{k} = \frac{\overline{u_i' u_j'}}{2} = \frac{1}{2}\sum_{n=1}^{N} \hat{u}_n^2 \tag{2.34}$$

The amplitudes of the modes are determined from the turbulent kinetic energy spectrum with $\hat{u}_n = \sqrt{2E(k_n)\Delta k_n}$. The wavenumber $k_n = \|\mathbf{k}_n\| = \exp\left[\ln k_1 + (n-1)\Delta k\right]$ is discretized using a logarithmic distribution $\Delta k_n = (\ln k_{max} - \ln k_{min})/(N-1)$, to correctly represent the turbulent energy spectrum for low wavenumbers as well as for larger ones. k_{min} and k_{max} are the minimum and maximum mode wavenumbers, respectively. The turbulent kinetic energy spectrum is modeled by a von Kármán spectrum with Saffman viscous dissipation function and a bottleneck correction [163]:

$$E(k) = 1.453\frac{(u_{rms})^2 k^4/k_e^5}{\exp(17/6\log(1+(k/k_e)^2)} \times \exp\left(-1.5c_K(k\eta)^2\right) \times \left[(1+0.522\left(\frac{1}{\pi}\arctan(10\log_{10}(k\eta)+12.58)+\frac{1}{2}\right)\right] \tag{2.35}$$

with $k_e = 0.747/L_f$, $c_K = 1.613$ and η the Kolmogorov viscous scale. An unfrozen turbulent field is obtained by incorporating the convection velocity $\overline{\mathbf{u}}$ and the pulsation ω_n, accounting for the temporal evolution of the

perturbations. In the present simulations (chapters 4 and 5), $N = 100$ and ω_n is deduced from Kolmogorov's theory with $\omega_n = \epsilon^{1/3} k_n^{2/3}$, ϵ being the dissipation rate. The synthetic turbulence injection strategy based on RFM is assessed in Appendix B against the freestream turbulence (FST) evolution of the incompressible T3A experiment [58], with spatial HIT simulations. In particular, the choice $N = 100$ and grid resolution criteria are justified.

2.3.5 Turbulence modeling

2.3.5.1 Sub-grid scale modeling

In the following, a brief description of the two SGS modeling approach used in the present work is given.

Smagorinsky model (SM): In the Smagorinsky model, the deviatoric part of the subgrid-scale (SGS) tensor is modeled as $\tau_{ij}^d = \tau_{ij} - 1/3\tau_{kk}\delta_{ij} = -2\rho\nu_t S_{ij}$, where S_{ij} is the resolved strain rate tensor and ν_t is the turbulent eddy viscosity, defined as:

$$\nu_t = C_S^2 \Delta_c^2 (2S_{ij}S_{ij})^{1/2} \tag{2.36}$$

where $\Delta_c = (\Delta x \Delta y \Delta z)^{1/3}$ and C_S is the Smagorinsky constant. Moreover, the isotropic part of the SGS tensor τ_{ij} is modeled, according to Yoshizawa [164], by $\tau_{kk} = 2C_I \rho \Delta_c^2 (2S_{ij}S_{ij})^{1/2}$, where $C_I = 0.066$ [165]. The characteristic length scale Δ_c can be weighted near the walls to perform wall-bounded flows using the classical formulation of the van Driest damping function [166] or a more advanced formulations (e.g., [167]).

Regularization term (RT): In this approach, no explicit SGS model is used and the dissipative effect of the subgrid motions is mimicked through a regularization procedure. Several authors propose the use of hyperviscosity [168, 169] or spectral vanishing viscosity [170] concepts to provide sufficient dissipation at the smallest scales without recourse to an explicit model. The regularization can also originate directly from the numerical procedure, as in MILES (monotonically-integrated LES), where the dissipative part of the numerical scheme constitutes an implicit model [171, 172]. Following this idea, a methodology combining low-dissipation schemes with the use a high-order filtering has been developed by Stolz *et al.* [173], Rizzetta *et al.* [174], or Bogey & Bailly [175]. In the present study, the selective filter (2.16), defined as part of the numerical discretization, acts as the regularization term. It also provides a smooth defiltering by removing the fluctuations at wavenumbers greater than the finite-difference scheme resolvability. As demonstrated by Mathew *et al.* [176], the effect of the Approximate Deconvolution Model (ADM) is globally similar to the convolution with an explicit filter.

The effect of SGS motions is taken into account implicitly in the high-wavenumber range thanks to the smooth truncations of the filter and finite-difference schemes in the wavenumber space. When the selective filter is used alone, the strategy is referred to as RT (for Regularization Term). Such a procedure does not imply any additional cost for the explicit computation of SGS terms.

While performing well-resolved LES of the Taylor-Green-vortex and supersonic boundary layers with several SGS strategies, Aubard *et al* [14] demonstrated that the RT approach was the best approach, both in terms of accuracy and computational cost. Gloerfelt & Cinnella [15] further assessed this on the periodic hills case and showed that the dissipative part of the numerical discretization plays a much more crucial role than SGS modeling. Thus, within the scope of this research project, the RT approach is selected to perform the LES, combined with a high-order filtering strategy and well-refined computational mesh. The only exception is for the investigation of the Novec649 decaying turbulence presented in Appendix A, where the SM model is used.

2.3.5.2 RANS modeling

In this work, all the RANS simulations are performed with the one-transport-equation model of Spalart and Allmaras [177], based on the following transport equation for the turbulence-related variable $\tilde{\nu}$:

$$\frac{\partial \tilde{\nu}}{\partial t} + u_i \frac{\partial \tilde{\nu}}{\partial x_i} - \frac{1}{\sigma} \frac{\partial}{\partial x_i} \left((\nu + \tilde{\nu}) \frac{\partial \tilde{\nu}}{\partial x_i} \right) = \Psi + \Pi - \Phi \tag{2.37}$$

where Ψ, Π and Φ are the diffusion, production, and destruction terms, respectively, and $\sigma = 2/3$ The baseline equation [177] is implemented with Crivellini's correction [178], to ensure that ν_t remains always positive, yielding:

$$\nu_t = f_{v1} \max(0, \tilde{\nu}) \tag{2.38}$$

were $f_{v1} = \chi^3/(\chi^3 + C_{v1})$, $\chi = \tilde{\nu}/\nu$ and $C_{v1} = 7.1$. For details about source terms, the reader is referred to [178]. In particular, the difference between the production and the destruction terms is function of a length scale l_{RANS} taken as the distance to the nearest wall d_w.

Computing the dynamic turbulent viscosity $\mu_t = \nu_t \rho$, the viscous stress tensor τ_{ij} is constructed as:

$$\tau_{ij} = (\mu + \mu_t) \left(\frac{\partial u_i}{\partial x_j} + \frac{\partial u_j}{\partial x_i} - \frac{2}{3} \delta_{ij} \frac{\partial u_k}{\partial x_k} \right) \tag{2.39}$$

The contribution of the RANS model to the heat flux is modeled by a constant Prandtl number (Pr) assumption.

2.3.5.3 RANS-LES approach

In situations where we desire to resolve part of the spatio-temporal scales in some regions of the flow while keeping a reduced computational cost w.r.t. LES, an appealing strategy is represented by so called hybrid RANS-LES models. involves coupling RANS models with LES resolution. The RANS-LES approach selected in the present work is based on the Detached Eddy Simulation strategy introduced by Spalart *et al.* [179]. One advantage of this method lies in its ease of implementation, especially when combined with the Spalart-Allmaras model. A detailed review on the evolution of DES can be found in [180] and, concerning more recent developments, in [181]. DES approaches switch between RANS and LES regions through the turbulence model length scale l_{RANS}, to deactivate RANS modeling in the resolved regions of the flow. In the original version DES [179], l_{RANS} is replaced by another length scale l_{DES} defined as:

$$l_{DES} = \min(l_{RANS}, C_{DES}\Delta_{sls}) \tag{2.40}$$

where C_{DES} is 0.65, and Δ_{sls} is the subgrid length scale, which is taken as the local maximum cell dimension. A drawback of the method is that it is highly mesh dependent and the gray area between RANS and LES can arise in the boundary layer at the location where the turbulence is not resolved and needs to be modeled. This was corrected in the Delayed DES version [182] where the length scale is taken as:

$$l_{DDES} = l_{RANS} - f_d \max(0, l_{RANS} - \Psi C_{DES}\Delta_{sls}) \tag{2.41}$$

with Ψ a low-Re correction and f_d a delaying function computed as $f_d = 1 - \tanh([8r_d]^3)$ with:

$$r_d = \frac{\nu + \nu_t}{(\frac{\partial u_i}{\partial x_j}\frac{\partial u_i}{\partial x_j})^{\frac{1}{2}}\kappa^2 {d_w}^2}$$

with the von Kármán constant κ taken as 0.41. This shielding function ensure that RANS mode remains activated in attached boundary layers. The term Ψ is introduced to avoid a drastic reduction in eddy viscosity values in low Reynolds regions or with excessive grid refinement (see eq. (4.3.4) in [182]).

The choice of Δ_{sls} as the local maximum cell dimension was demonstrated to damp the K-H instability waves in the case of separated shear layers. To accelerate the transition to turbulence in separated shear layers, Shur *et al* [183] introduced the Shear Layer Adapted (SLA) subgrid length scale Δ_{SLA} which, in combination with the DDES approach, was shown to improve this behavior. In the DDES-SLA approach, the length scale therefore becomes:

$$l_{DDES-SLA} = l_{RANS} - f_d \max(0, l_{RANS} - \Psi C_{DES}\Delta_{SLA}) \tag{2.42}$$

An expression for Δ_{SLA} is provided in [183]. For details about the implementation, the reader is referred to [184]. The two different DDES versions are assessed on a turbomachine configuration in Appendix D and, as the DDES-SLA approach improves wake predictions compared to unsteady RANS and DDES, the DDES-SLA method is retained in Chapter 6.

2.4 Improvement of a high-order implicit temporal integration strategy

In DNS and LES of turbulent flows and aeroacoustics, in order to maintain numerical accuracy and due to the time scales comparable to the spatial scales, the CFL number is close to unity and generally explicit time integration schemes, such as Runge-Kutta or Adams-Bashforth schemes, are used. The limit is then dictated by the physics rather than the numerical stability. However, in the presence of solid boundaries, thin turbulent boundary layers develop along the walls, requiring the use of very small mesh sizes. In such a situation, stability constraints of explicit schemes impose time steps much smaller than the characteristic time of viscosity-dominated turbulent structures near the wall, despite the physics allowing CFL of the order of 10 [185]. In the incompressible regime, if the stability limit is dictated by a viscous criterion, an implicit scheme can remove the limit at the price of the solution of a linear system. If the cost is moderate, the algorithm remains efficient. For the compressible Navier–Stokes equations the implicit treatment of the convective fluxed necessitates the solution of nonlinear systems. If a high-accurate time integration is chosen, such as implicit Runge–Kutta schemes or linear multistep methods (Adams-Moulton or Backward Differentiation Formula schemes), the overhead may outweigh the benefits of increasing the time step beyond the CFL limit.

One way to relax the severe stability limitations of explicit schemes without going to the trouble of fully implicit ones, is the use of residual smoothing techniques. These consist in running the simulations with a CFL number higher than the maximum value allowed by the explicit scheme in use, and redistributing errors in the residuals over neighboring cells by applying an explicit or implicit smoothing operator. Explicit residual smoothing, discussed in [186] and [187] in the case of second-order accurate smoothing operators, does not allow significant increases in CFL, limiting the potential gains over an unsmoothed explicit scheme. Implicit Residual Smoothing (IRS) is a technique originally introduced to speed-up convergence to steady-state solutions. In fact, as shown in [17, 188], this technique can be extended to high order and can accurately simulate unsteady flow at CFL between 5 and 10 at a moderate overhead. IRS may be one order of magnitude cheaper than a fully implicit method where the nonlinear system is solved to strict tolerance. In the context of compressible flow simulations, IRS was introduced at a time when computing power essentially only allowed the calculation

of steady-state solutions. A relatively accurate (second-order) implicit phase was constructed by Lerat and coworkers [189, 190, 191, 192] by simplifying a Lax-Wendroff-type implicit scheme. Based on second-order central differencing, it acts as a Laplacian smoother to accelerate convergence. The implicit phase of Lerat et al. bears a strong resemblance to the implicit phase introduced later by Jameson and coworkers [186, 193] to smooth/filter the solution. A fully implicit version using the approximate Jacobian of the residual instead of a scalar smoothing coefficient was proposed in [194] in the context of multigrid acceleration for steady solutions of Navier–Stokes equations, and requires the inversion of a block matrix using approximate splitting. IRS was used in several computational fluid dynamics (CFD) codes to speed-up convergence of steady Euler and Navier–Stokes calculations in conjunction with multigrid algorithms [195, 196, 197, 198, 199]. A fourth-order accurate version (IRS4) was introduced in [17] and applied to the LES and DNS of selected geometrically simple flow configurations. A finite-volume multi-domain formulation was discussed in [188] and shown to be efficient for LES in turbomachinery in conjunction with a third-order accurate spatial scheme. The fourth-order IRS relies on a bi-Laplacian filter to damp high-frequency modes of the residual, which leads to the solution of pentadiagonal systems for each space direction and Runge–Kutta stage. Thanks to the efficient inversion of scalar pentadiagonal matrices, the extra computational cost associated with the implicit operator was shown to remain much lower than standard implicit schemes at least for the considered configurations. As discussed in section 2.4.4, a multi-domain implementation can require simplifications of the implicit matrix that may hinder robustness. Furthermore, the numerical dissipation properties of the implicit scheme are also modified and may lead to reduced numerical stability in conjunction with higher-order schemes, such as the tenth-order-accurate scheme considered along the thesis.

In this section, the improvements proposed to the IRS4 are presented. The principle of IRS and its interpretation in Fourier space are presented in sections 2.4.1 and 2.4.2. In section 2.4.3, a detailed study of the numerical dissipation is carried out, and a selective filtering strategy on the solution variables is introduced to ensure the correct damping of small scales at high CFL numbers. Finally, the numerical properties of boundary and interface treatment, which is critical for DNS and LES on massively parallel computers, is presented in section 2.4.4.

2.4.1 Principle of Implicit Residual Smoothing

In the original developments by Lerat and coworkers [189, 190, 191, 192], an implicit phase was proposed for a general class of three-point schemes using an approximate Lax-Wendroff-like implicit operator. Starting

from the 2D Euler equations, written as:

$$w_t + f(w)_x + g(w)_y = 0$$

and denoting $A = \partial f/\partial w$ and $B = \partial g/\partial w$ the Jacobian matrices, the complete implicit phase is:

$$\Delta w + \theta\frac{\Delta t^2}{2}\left\{\left[A^2(\Delta w)_x + AB(\Delta w)_y\right]_x + \left[BA(\Delta w)_x + B^2(\Delta w)_y\right]_y\right\} = \Delta w^{expl}$$

where Δw is the solution increment and Δw^{expl} represents the explicit phase (e.g., $\Delta w^{expl} = -\frac{(\delta \mathcal{F})_j}{\Delta x}$ for a 1D inviscid problem). It is unconditionally stable for $\theta \leq -1/2$. A first simplification consists in the suppression of cross-derivative terms:

$$\Delta w + \theta\frac{\Delta t^2}{2}\left\{\left[A^2(\Delta w)_x\right]_x + \left[B^2(\Delta w)_y\right]_y\right\} = \Delta w^{expl}$$

An approximate factorization per spatial direction is then used, yielding:

$$\begin{cases} \Delta w^* + \theta\frac{\Delta t^2}{2}\left[A^2(\Delta w^*)_x\right]_x = \Delta w^{expl} \\ \Delta w + \theta\frac{\Delta t^2}{2}\left[B^2(\Delta w)_y\right]_y = \Delta w^* \end{cases}$$

The preceding relations are further simplified by replacing the Jacobian matrices by their spectral radius ρ:

$$\begin{cases} \Delta w^* + \theta\frac{\Delta t^2}{2}\left[\rho(A)^2(\Delta w^*)_x\right]_x = \Delta w^{expl} \\ \Delta w + \theta\frac{\Delta t^2}{2}\left[\rho(B)^2(\Delta w)_y\right]_y = \Delta w^* \end{cases}$$

After discretization by second-order central differences, the implicit operator $\mathcal{J}$ for each direction reads:

$$\mathcal{J} = 1 - \theta_2\left(\frac{\Delta t}{\Delta x}\right)^2 \delta(\lambda^e{}^2\delta) \tag{2.43}$$

where δ is the differencing operator (2.13), λ^e denotes the spectral radius of the flux Jacobians in each direction and $\theta_2 \geq 0$ is the value of the coefficient for the second-order scheme. With such a scheme, a scalar tridiagonal system must be solved for each space dimension. A similar implicit operator was used by Jameson & Baker [186] to increase the CFL number of an explicit Runge–Kutta time-stepping scheme for steady problems. The so-called "implicit residual smoothing" is applied at each RK stage as:

$$\begin{cases} w^{(0)} = w^n \\ \mathcal{J}\Delta w^{(k)} = -\alpha_k \Delta t \mathcal{R}(w^{(k-1)}), \quad k = 1, ..., s \\ w^{n+1} = w^{(s)} \end{cases} \tag{2.44}$$

where w^n is the solution vector at time iteration n and the implicit operator $\mathcal{J}$ of Jameson & Baker (JB) reads:

$$\mathcal{J}_{JB} = 1 - \varepsilon\left(\frac{\Delta t}{\Delta x}\right)^2 \delta^2 \quad \text{with} \quad \varepsilon \geq \frac{1}{4}\left[\left(\frac{\text{CFL}}{\text{CFL}^{expl}}\right)^2 - 1\right]$$

with ε a constant parameter that depends on the maximum allowable CFL of the underlying explicit scheme and the desired CFL in the implicit procedure. Note that, in the context of steady state computations using multigrid smoothers, alternative formulations of ε as a function of the CFL have been proposed in the literature [193, 200]. The $\mathscr{J}_{JB}$ operator has only first-order accuracy [201], whereas the Lax-Wendroff IRS operator (2.43) maintains second-order accuracy, and is then noted IRS2. The IRS2 was used in conjunction with RK time stepping by Cinnella & Lerat [202]. An extension to fourth-order (IRS4) was first proposed by Cinnella and Content [17], by keeping the same form of the operator (2.43) but replacing the Laplacian smoothing by a bi-Laplacian smoothing:

$$\mathscr{J} = 1 + \theta_4 \left(\frac{\Delta t}{\Delta x}\right)^4 \delta(\lambda^{e\,4}\delta^3)\,, \tag{2.45}$$

which implies the resolution of a pentadiagonal system for each space direction. IRS4 is unconditionally stable for $\theta_4 \gtrapprox 0.0023$ (see § 2.4.4.2). We use the value $\theta_4 = 0.0025$ in the following. The additional error introduced by the IRS4 operator with respect to the explicit scheme takes the form [17]:

$$-\frac{1}{12}\theta_4 \Delta t^4 \lambda^{e\,4} \frac{\partial^5 f_d^e}{\partial x^5} + \mathcal{O}(\Delta t^4) \tag{2.46}$$

with f_d^e the inviscid flux in the considered direction d. Being proportional to an odd derivative, this error has a dispersive nature. As the RK scheme is second-order in general, the additional error coming from the IRS4 is expected to have a negligible influence on the overall accuracy of the baseline time scheme.

2.4.2 Interpretation in Fourier space

The main idea of IRS is to stabilize the scheme by smoothing the residuals with a Laplacian filter (IRS2) or a bi-Laplacian filter (IRS4). The IRS operator acts on the difference scheme by contracting its support and thus relaxes the restriction on the time step imposed by the CFL condition. This behavior can be easily interpreted using Fourier symbols of the operators (denoted with $\widehat{\bullet}$). Fourier analysis also provides a simple means of determining errors produced by the discretization in absence of boundary conditions.

The amplification factor of the RK4 scheme is found to be:

$$\widehat{g}(\zeta) = 1 + \zeta + \zeta^2/2 + \zeta^3/6 + \zeta^4/24\,, \quad \zeta \in \mathbb{C} \tag{2.47}$$

The stability region can be represented in the complex plane. The black line in Fig.2.3 marks the stability boundary ($|\widehat{g}(\zeta)| = 1$). The gray color area denotes the unstable region ($|\widehat{g}(\zeta)| > 1$). Consider the linear scalar advection problem

$$w_t + a w_x = 0 \quad (a > 0) \tag{2.48}$$

The locus of the finite differences (FD) operator (2.14) is given by :

$$\widehat{\mathscr{R}}(k\Delta x) = \frac{2\,i\,a}{\Delta x}\sin\left(\frac{k\Delta x}{2}\right)\cos\left(\frac{k\Delta x}{2}\right)\left[1+\frac{2}{3}\sin^3\left(\frac{k\Delta x}{2}\right)+\frac{8}{15}\sin^5\left(\frac{k\Delta x}{2}\right)+\frac{16}{35}\sin^7\left(\frac{k\Delta x}{2}\right)+\frac{128}{315}\sin^9\left(\frac{k\Delta x}{2}\right)\right] \tag{2.49}$$

with $i=\sqrt{-1}$ and $k\Delta x$ the reduced wavenumber. The space discretization is nondissipative and its locus lies on the imaginary axis. The Fourier symbol of the artificial dissipation operator (2.15) is given by:

$$\widehat{\mathscr{D}}^{AD}(k\Delta x) = \frac{a}{\Delta x}\frac{256}{315}\sin^{10}\left(\frac{k\Delta x}{2}\right) \tag{2.50}$$

and its locus lies on the real axis. In order for the discrete scheme to be stable, the locus of the spatial operator $(-\widehat{\mathscr{R}}+\widehat{\mathscr{D}}^{AD})$ must remain within the stability region of the RK integration scheme, as shown in Fig.2.3a. As the CFL increases, the locus will expand and ultimately exit the stability region, as exemplified in Fig.2.3(b-f).

The IRS smoothing in Eq.(2.44) corresponds to a modification of the Fourier symbol of the spatial operator, which becomes $(-\widehat{\mathscr{R}}+\widehat{\mathscr{D}}^{AD})/\widehat{\mathscr{F}}$, where the Fourier symbol of IRS4 reads:

$$\widehat{\mathscr{F}} = 1+16\,\theta_4\mathrm{CFL}^4\sin^4\left(\frac{k\Delta x}{2}\right) \tag{2.51}$$

The modified locii for IRS4 are plotted in Fig.2.3 for CFL=1 to 6. The IRS operator contracts the spatial locus, which is flattened on the imaginary axis due to the dispersive nature of the IRS operator. This also implies that, as the CFL increases, the dissipation error decreases and tends to zero.

2.4.3 Von Neumann stability

To better understand the role of the numerical dissipation in combination with IRS smoothing, a Von Neumann stability analysis is conducted. In the linear scalar case of a transport equation (2.48), the RK algorithm is developed as :

$$w_j^{n+1} = w_j^n + \sum_{s=1}^{4}\gamma_s\Delta t^s\frac{\partial^s w_j^n}{\partial t^s}+\ldots \quad \text{where} \quad \gamma_s = \prod_{q=4-s+1}^{4}\alpha_q \tag{2.52}$$

with w_j^n is the solution at grid index j and time iteration n. By applying a Fourier transform to (2.52), we write the amplification factor for the discretized equation without numerical dissipation as :

$$\widehat{\mathscr{G}}^0 = \frac{\hat{w}_j^{n+1}}{\hat{w}_j^n} = 1-\sum_{s=1}^{4}\gamma_s\sigma^s\widehat{\mathscr{R}}^s \tag{2.53}$$

where $\sigma = a\Delta t/\Delta x$ is the CFL number. Introducing artificial dissipation, the amplification factor becomes:

$$\widehat{\mathscr{G}}^{AD} = 1-\sum_{s=1}^{4}\gamma_s\sigma^s\left(\widehat{\mathscr{R}}-\widehat{\mathscr{D}}^{AD}\right)^s \tag{2.54}$$

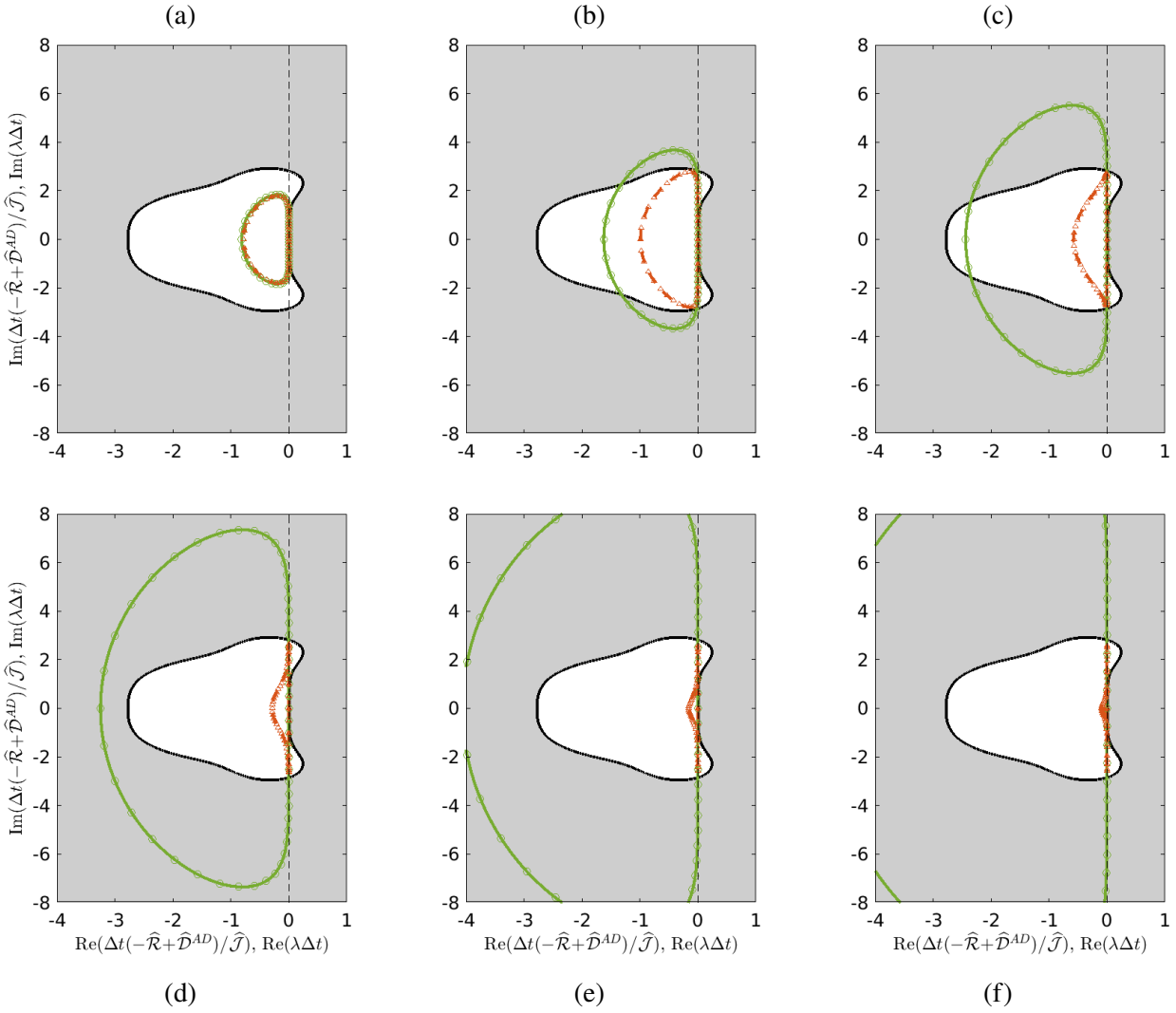

Figure 2.3: Stability region of the RK4 (white) and locus of the spatial operator with IRS4 smoothing (red) and without (explicit, green), obtained from the Fourier symbols (lines) and the operator's eigenvalues $\lambda\Delta t$ (symbols). From left to right and top to bottom, CFL=1, 2, 3, 4, 5 and 6.

On the other hand, the filtering operation (2.16), applied at the last RK stage, corresponds to a convolution operation in physical space, so that the amplification factor after filtering is multiplied by $1 - \chi_f \widehat{\mathscr{D}}^{SF}$:

$$\widehat{\mathscr{G}}^{SF} = \left(1 - \sum_{s=1}^{4} \gamma_s \sigma^s \widehat{\mathscr{R}}^s\right)\left(1 - \widehat{\mathscr{D}}^{SF}\right) \tag{2.55}$$

where the Fourier symbol of SF is obtained by applying a Fourier transform to (2.16) :

$$\widehat{\mathscr{D}}^{SF}(k\Delta x) = \chi_f \left(d_0 + \sum_{l=1}^{5} 2d_l \cos(lk\Delta x)\right) = \chi_f \sin^{10}\left(\frac{k\Delta x}{2}\right) \tag{2.56}$$

Note that, for $a/\Delta x = 1$, the Fourier symbol of the tenth-order filter is the same as the one of the ninth-order artificial dissipation when chosing $\chi_f = 256/315$. The role of the numerical dissipation is displayed in Fig.2.4 for CFL numbers between 1 and 15. We first focus on the base scheme without stabilization in Fig.2.4(a). For the selected value of the IRS4 coefficient (θ_4=0.0025), it is apparent that the scheme remains always stable. At CFL=1, we observe a damping in the mid-wavenumber range, which depends on the coupled effects of the RK and FD schemes. For higher values of the CFL, the IRS4 operator acts and a double damping peak is visible, which moves toward low wavenumbers as CFL increases. Damping vanishes at smallest scales ($k\Delta x \approx \pi$), which highlights the need for additional high-wavenumber dissipation. Figure 2.4(b) shows the amplification factors with artificial dissipation. Since it is added to the spatial operator, its effect is coupled with the temporal scheme, which leads to the non-monotonic behavior for CFL 1 and 2. For high values of CFL, the contractive character of the IRS4 operator dramatically reduces the dissipation, which could also have been inferred from Fig.2.3. As a consequence, for CFL $\gtrapprox 10$, almost no dissipation is applied near the grid cut-off ($k\Delta x \approx \pi$), so that grid-to-grid oscillations can remain undamped and pollute the solution or become unstable. In Fig.2.4(c), the selective filtering is applied with a coefficient $\chi_f = 256/315$, so that the amount of damping is similar to that of AD without IRS. As expected, the spectral characteristics are a combination of the base scheme and the filter response. In particular, the damping at $k\Delta x \approx \pi$ remains the same independently of the CFL value. The fact that the stabilization is independent of the base scheme gives the greater robustness of RK4-IRS4 implementation, notably for high values of CFL, since the filter will continue to dissipate the modes not resolved by the grid. That is why, in the following, the results are obtained with the base scheme supplemented by the selective filtering.

Since the IRS operator essentially introduces a dispersive error, it is also interesting to look at the relative phase error $\phi + \sigma k\Delta x$ in Fig.2.5. Since the dissipation term is non dispersive, this quantity is due uniquely to the centered difference operator (2.14). The striking point in Fig.2.5(a) is that IRS4 damages the phase in

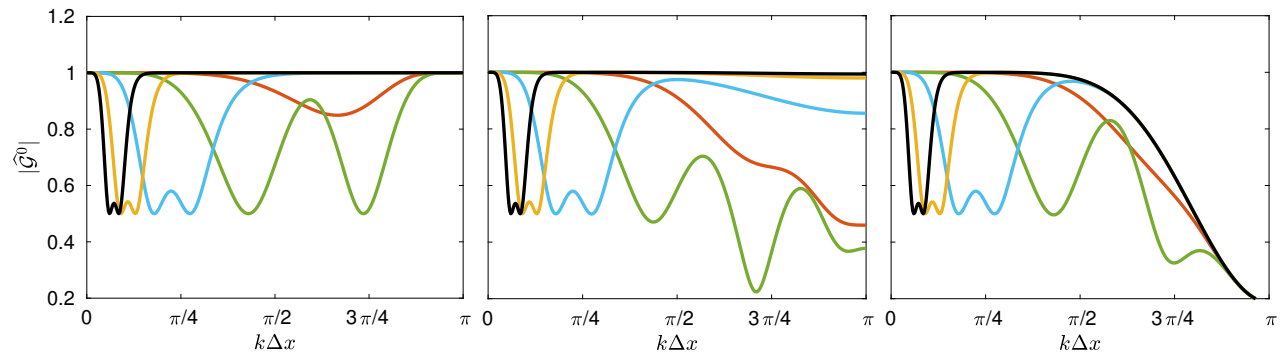

Figure 2.4: Amplification factors for the centered spatial operator (a), supplemented by artificial dissipation (b) or by selective filtering (c) for increasing CFL numbers, CFL=1 (——), 2 (——), 5 (——), 10 (——), 15 (——).

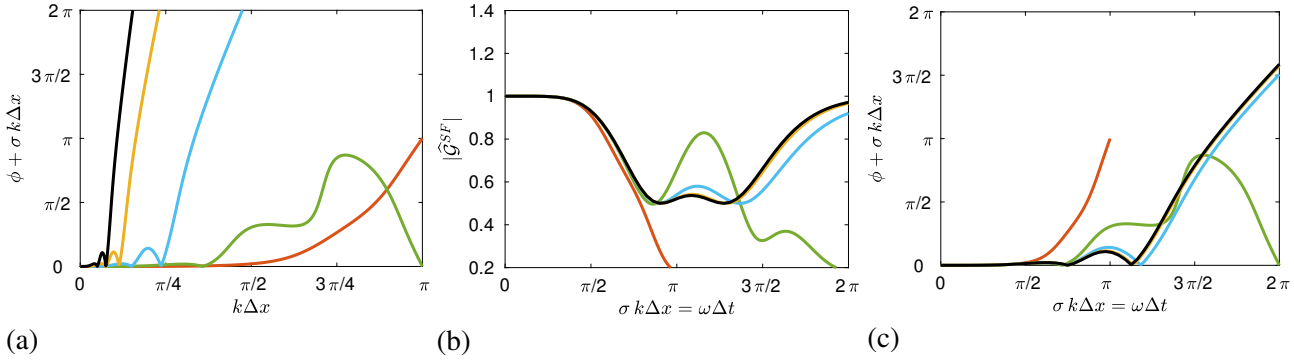

Figure 2.5: Spectral properties of IRS4 operator: relative phase error (a), damping factor versus $\omega\Delta t$ (b), and phase error versus $\omega\Delta t$ (c) for increasing CFL numbers, CFL=1 (——), 2 (——), 5 (——), 10 (——), 15 (——).

proportion to the CFL rise. Such a representation would suggest that dispersion errors are unacceptable for CFL greater than 5. However, the analysis would be only valid for a regular grid with constant Δx. In practice, grid points are clustered near wall boundaries, and high values of the CFL (5 or greater) are located at these particular points due to the small Δx. From another point of view, we can also look at the spectral properties relative to a fixed time step Δt, which is done in Fig.2.5(b) and (c) for the amplification factor and the phase respectively by multiplying the abscissa by the CFL number σ. For the advection equation, $\omega = k\, a$, and $\sigma\, k\Delta x = \omega\Delta t$. In this representation, it is clear that the base scheme spectral properties are preserved in proportion to the CFL number up to $\omega\Delta t = \pi/2$, i.e. if the time signal is discretized by four or more time steps.

2.4.4 Boundary conditions and multi-domain interface treatment

The preceding analysis is valid for an infinite computational domain or a domain with periodic conditions. The modification of the spatial operator close to boundaries will affect both stability and numerical errors. For

this reason, the stability analysis in the following will be carried out with the method of lines [203]. For the linear scalar wave problem (2.48), spatial discretization on a grid with m points yields

$$\frac{\partial \mathbf{w}_m}{\partial t} = -\mathbf{R}_{m,m}\mathbf{w}_m$$

where $\mathbf{w}_m$ is the numerical solution vector, of size m and $\mathbf{R}_{m,m}$ is the matrix associated to the spatial operator $\mathscr{R}$. By taking the Fourier transform of this expression, with $\mathbf{w}_m = \hat{\mathbf{w}}_m e^{\lambda t}$, we obtain the following eigenvalue problem :

$$(a\mathbf{R}_{m,m})\hat{\mathbf{w}}_m = -\lambda\hat{\mathbf{w}}_m \tag{2.57}$$

2.4.4.1 Periodic boundary condition

Writing the IRS scheme at the k^{th} RK stage in matrix-vector form

$$\mathbf{J}_{m,m}\Delta\mathbf{w}_m^{(k)} = -\alpha_k\Delta t\,\mathbf{R}_{m,m}\mathbf{w}_m^{(k-1)}$$

the IRS4 operator leads to the inversion of a pentadiagonal matrix $\mathbf{J}_{m,m}$ per direction at each Runge–Kutta stage. For periodic boundary conditions, the periodic matrix $\mathbf{J}_{\mathrm{p}_{m,m}}$ reads:

$$\mathbf{J}_{\mathrm{p}_{m,m}} = \begin{pmatrix} \gamma & \alpha & \beta & 0 & \cdots & \cdots & \cdots & 0 & \beta & \alpha \\ \alpha & \gamma & \alpha & \beta & 0 & \cdots & \cdots & \cdots & 0 & \beta \\ \beta & \alpha & \gamma & \alpha & \beta & 0 & \cdots & \cdots & \vdots & 0 \\ 0 & \beta & \alpha & \gamma & \alpha & \beta & 0 & \cdots & \vdots & \vdots \\ \vdots & \ddots & \ddots & \ddots & \ddots & \ddots & \ddots & \ddots & \ddots & \vdots \\ 0 & \cdots & 0 & \beta & \alpha & \gamma & \alpha & \beta & \cdots & \vdots \\ \vdots & \ddots & \ddots & \ddots & \ddots & \ddots & \ddots & \ddots & \ddots & \vdots \\ 0 & \cdots & \cdots & \cdots & 0 & \beta & \alpha & \gamma & \alpha & \beta \\ \beta & 0 & \cdots & \cdots & \cdots & 0 & \beta & \alpha & \gamma & \alpha \\ \alpha & \beta & 0 & \cdots & \cdots & \cdots & 0 & \beta & \alpha & \gamma \end{pmatrix} \tag{2.58}$$

with $\beta = \theta_4 \mathrm{CFL}^4$, $\alpha = -4\beta$ and $\gamma = 1 + 6\beta$. The eigenvalue problem (2.57) then becomes:

$$(\mathbf{J}_{m,m}^{-1}\mathbf{R}_{m,m})\hat{\mathbf{w}}_m = -\lambda\hat{\mathbf{w}}_m \tag{2.59}$$

For periodic boundary conditions, as expected, the solutions from the eigenvalue problem (2.59) with IRS4 matrix $\mathbf{J}_{\mathrm{p}_{m,m}}$ perfectly match the locus of the Fourier symbol $\widehat{\mathscr{R}}/\widehat{\mathscr{F}}$, as seen in Fig.2.3 for CFL 1 to 6.

2.4.4.2 Physical boundary conditions

Near boundaries of the computational domain it is necessary to modify the IRS4 matrix. In Ref.[17], the pentadiagonal matrix is simply truncated, which gives matrix $\mathbf{J_1}_{m,m}$:

$$\mathbf{J_1}_{m,m} = \begin{pmatrix} \gamma & \alpha & \beta & 0 & \cdots & \cdots & \cdots & 0 \\ \alpha & \gamma & \alpha & \beta & \ddots & \cdots & \cdots & 0 \\ \beta & \alpha & \gamma & \alpha & \beta & \ddots & \cdots & 0 \\ 0 & \beta & \alpha & \gamma & \alpha & \beta & \ddots & \vdots \\ \vdots & \ddots & \ddots & \ddots & \ddots & \ddots & \ddots & 0 \\ 0 & \cdots & \ddots & \beta & \alpha & \gamma & \alpha & \beta \\ 0 & \cdots & \cdots & \ddots & \beta & \alpha & \gamma & \alpha \\ 0 & \cdots & \cdots & \cdots & 0 & \beta & \alpha & \gamma \end{pmatrix}, \tag{2.60}$$

To gain some robustness in the FD implementation, we have chosen to reduce IRS order near boundaries. The second to last row of nodes is smoothed with IRS2 operator of Eq.(2.43) and the one-sided IRS1 operator [198] is used at the boundary points, yielding matrix $\mathbf{J_2}_{m,m}$:

$$\mathbf{J_2}_{m,m} = \begin{pmatrix} \gamma_1 & \alpha_1 & 0 & \cdots & \cdots & \cdots & \cdots & 0 \\ \alpha_2 & \gamma_2 & \alpha_2 & 0 & \cdots & \cdots & \cdots & 0 \\ \beta & \alpha & \gamma & \alpha & \beta & 0 & \cdots & 0 \\ 0 & \beta & \alpha & \gamma & \alpha & \beta & \ddots & \vdots \\ \vdots & \ddots & \ddots & \ddots & \ddots & \ddots & \ddots & 0 \\ 0 & \cdots & 0 & \beta & \alpha & \gamma & \alpha & \beta \\ 0 & \cdots & \cdots & \cdots & 0 & \alpha_2 & \gamma_2 & \alpha_2 \\ 0 & \cdots & \cdots & \cdots & \cdots & 0 & \alpha_1 & \gamma_1 \end{pmatrix} \tag{2.61}$$

with coefficients $\alpha_2 = -\theta_2 \mathrm{CFL}^2$ and $\gamma_2 = 1 - 2\alpha_2$ for IRS2, and $\alpha_1 = \pm\theta_1 \mathrm{CFL}$, $\gamma_1 = 1 - \alpha_1$ for IRS1 operator, which is defined as:

$$\begin{cases} \mathcal{J}_{IRS1^+} = 1 - \theta_1 \dfrac{\Delta t}{\Delta x} \lambda^e \delta^+ & \text{for a left boundary} \\ \\ \mathcal{J}_{IRS1^-} = 1 + \theta_1 \dfrac{\Delta t}{\Delta x} \lambda^e \delta^- & \text{for a right boundary} \end{cases} \tag{2.62}$$

with δ^+, δ^- the upward and backward difference operator respectively. The Fourier symbol of IRS1 and IRS2 are given by:

$$\begin{cases} \widehat{\mathcal{J}}_{IRS1^+} = 1 + 2\,\theta_1 \mathrm{CFL} \left[\sin^2\left(\dfrac{k\Delta x}{2}\right) - i \cos\left(\dfrac{k\Delta x}{2}\right) \sin\left(\dfrac{k\Delta x}{2}\right) \right] \\ \widehat{\mathcal{J}}_{IRS2} = 1 + 4\,\theta_2 \mathrm{CFL}^2 \sin^2\left(\dfrac{k\Delta x}{2}\right) \end{cases} \tag{2.63}$$

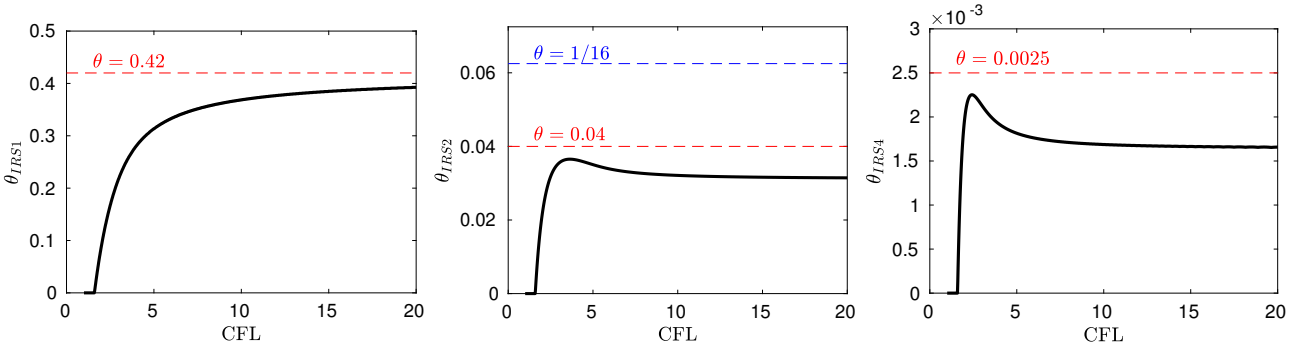

Figure 2.6: Numerical determination of smoothing parameter θ ensuring unconditional stability for the 1D advection problem: IRS1 (left), IRS2 (center) and IRS4 (right).

To determine the coefficients θ ensuring the unconditional stability of the different IRS operators, a numerical search is performed for the 1D scalar problem. The results are plotted in Fig.2.6. For IRS1, we set the value $\theta_1 = 0.42$. A theoretical value for IRS2 of 1/16 was obtained analytically in [204, 202]. In the following, we use the value $\theta_2 = 0.04$, for which the numerical stability is ensured. For IRS4, the distribution of θ_4 as function of CFL follows the same trend as IRS2 with a peak around CFL=2, where the contractive effect of IRS operator is not yet large. We set the value $\theta_4 = 0.0025$ in the applications.

For a Dirichlet boundary condition, the method of lines is applied with the matrix $\mathbf{J_2}_{m,m}$ and centered schemes with reduced-stencil schemes near boundaries in the spatial operator matrix. The solution increments are imposed at the left boundary so that the corresponding first row and first column are suppressed in the matrices [205]. A simple extrapolation is used at the right boundary. The eigenvalues for m=200, plotted in Fig.2.7 for CFL 2, 5 and 10, show that the locii are significantly modified compared to the old treatment using the truncated matrix $\mathbf{J_1}_{m,m}$. In particular, for the highest CFL value, the use of a reduced stencil IRS operator appears more dissipative, whereas the close-up view in the inset of Fig.2.7 (right) indicates that some eigenvalues can excite weak instabilities with the truncated version. However, using IRS2 and IRS1 coefficients on the borders, all the eigenvalues have a negative real part so that the linear problem has non growing solutions.

2.4.4.3 Interface treatment in multi-domain calculations

The different strategies of parallelisation for the linear system resolution: The parallel implementation of IRS is crucial for the efficiency of the method. As we have seen, IRS4 leads to the inversion of a pentadiagonal matrix per mesh direction at each Runge–Kutta step. As the number of linear systems to solve is proportional to the number of implicited directions and to the number of points in that direction, the computational cost

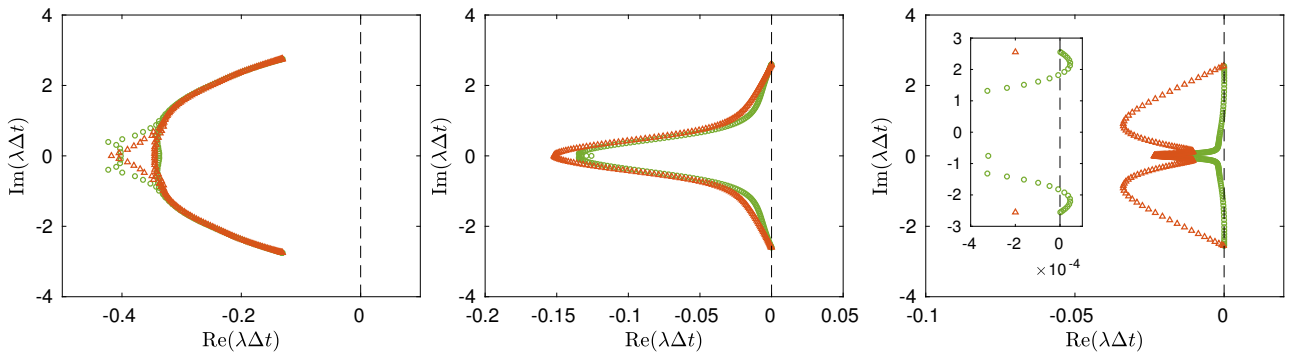

Figure 2.7: Eigenvalue spectrum with the method of lines for Dirichlet boundary condition using IRS matrix $\mathbf{J}_{2_{m,m}}$ (△) and $\mathbf{J}_{1_{m,m}}$ (○): CFL=2 (left), CFL=5 (center) and CFL=10 (right).

can be important. Efficient algorithms, such as Thomas' algorithm or cyclic reduction, exist to solve small-banded matrices on scalar computers. They are based on a first forward sweep, during which new coefficients are computed, and then a backward substitution to compute the solution. Unfortunately, such algorithms are hard to parallelize efficiently, even if a large body of literature has tackled this problem, mostly for tridiagonal systems. Strategies based on the redistribution of data between processors [206] or Thomas-pipelined algorithms [207] are better suited for distributed memory architectures, but they lack efficiency due to a large number of communications for the former, and to idle time for the second. Some methods are based on the divide-and-conquer algorithm, where successive transformations are used to divide the original problem over the computing cores. The tridiagonal and banded-matrix solvers available in the ScaLapack library [208] propose an MPI implementation. We have tested the banded-matrix routines of ScaLapack to solve the pentadiagonal systems but the overhead is prohibitive, amounting to approximately 220% with respect to the explicit solver . More complex algorithms, such as Spike, [209] have been proposed to reduce the cost. Even if the scalability has been improved, notably for large band matrices on distributed memory or with GPU processors, the cost remains high for pentadiagonal systems. We have also tested the recent PaScal_tdma library [210], which proposes an optimized parallel cyclic reduction method for tridiagonal matrices. The overhead is more reasonable (approximately 30% when few processors per implicit directions are used), but its does not scale well to large number of processors (the overhead increases up to 150% when using about 30 processors per direction); furthermore, the library is not applicable to pentadiagonal matrices. Last but not least, even if each block is individually structured, complex multiblock grids can lead to globally unstructured topologies (see for instance test cases 5.7 to 5.10). In that case, the definition of global linear systems distributed across all blocks is not possible.

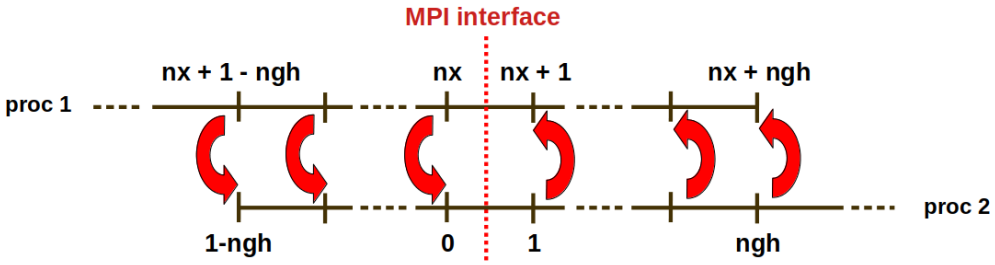

Figure 2.8: Schematic of the ghost-point strategy adopted for the parallel implementation of IRS.

Note that the aim here is to relax CFL constrains in compressible DNS and LES, but anyway the maximum allowable time step will be limited by the need of resolving the smallest time scales in the simulation. As shown in Section 5.4, values of CFL of 5 to 10 can then be used for compressible DNS without affecting or reducing the physical time accuracy. Such values are much smaller than those used in steady state simulations ($O(100)$ or more). It is then of the utmost importance that the matrix inversion associated with the implicit treatment is as cheap as possible. For that reason, in the following we extend IRS to parallel and multiblock configurations by solving approximate systems on each subdomains and by truncating the global system to generate local independent linear systems for each processors. Some studies discuss the multi-domain extension for IRS implicitation but are generally restricted to steady problems. Borel and Roux [211] used a Schwarz iterative method for overlapping domain decomposition. They studied the influence of the thickness of the overlap and found an optimal efficiency for an overlapping of L_0=2CFL+1 cells. Lerat and Wu [212] proposed a time-lagging interface condition, where the interface values are fixed at the previous time step. They showed how to obtain a stable and conservative condition. Wu and Zou [213] further analyzed this interface treatment and found an optimal overlap L_0=CFL for steady problems. They extended the time-lagging method to unsteady problem by using an overlapping L_0=2CFL+1 points. In Ref.[188], a strategy based on the use of an overlap between blocks was studied by defining halos of ghost points, which is a popular strategy to implement compact FD schemes [214]. It was shown that adding ghost points at the interfaces can limit the error generated by the truncation. This strategy is pursued in the present study.

The ghost-point strategy Layers of ghost cells are used to make mesh blocks independent and reduce the required number of parallel communications. They are filled using the solution increments computed in the neighboring subdomain at the previous RK stage, as schematized in figure 2.8.

In Ref.[17, 188], the IRS operator is simply set equal to the identity for the last two rows, which means

that the two outside ghost cells are advanced explicitly in time, while the right-hand sides are communicated from the neighboring block. In the present implementation, the coefficients for the two first/last rows in the IRS matrix are those of IRS1 and IRS2 operators. For an interior subdomain, the IRS4 matrix is thus $J_{2m+\text{ngh},m+\text{ngh}}$ as defined in Eq.(2.61) where m is replaced by m + ngh, ngh being the number of ghost cells. Note that the eleven-point stencil base schemes already necessitates five rows of ghost points in each direction, so that we use at least ngh=5. This results in the inversion of a $(m + \text{ngh}) \times (m + \text{ngh})$ pentadiagonal matrix per direction on each mesh block, which introduces an overhead. The part due to parallel communications is rather small, and a good parallel scalability is observed for blocks of approximately 50^3 points. The strategy may however suffer from a lack of robustness when using high values of CFL numbers (greater than about 10). To illustrate this point, the scalar advection (2.48) is solved for a domain $0 < x < 1$ discretized by 600 points. A 1D Gaussian hump, defined as $w(x, 0) = \exp(-500(x - 0.5)^2)$, is initially located at the middle of the domain and advected periodically to its starting position 10 times at CFL=5. The results are reported in Fig.2.9 using two solutions: the true periodic solution, *i.e.* IRS matrix is $\mathbf{J}_{\mathrm{p}m,m}$ of Eq.(2.58), and the approximate ghost-point solution, *i.e.* IRS matrix $\mathbf{J}_{2m+\text{ngh},m+\text{ngh}}$ of Eq.(2.61). The number of grid points has been chosen so that the periodic hump is correctly advected (some oscillations due to dispersion are visible on its left foot). Then ghost points are used at the left and right boundaries, which can represent the connection with other MPI domains or blocks (note that periodicity is treated as communications by MPI library). Using the nominal number of ghost cells, ngh=5 (first row of Fig.2.9), a numerical instability is observed after 10 turnovers and the simulation blows up rapidly. Using an extended number of ghost cells, ngh=11 (bottom row of Fig.2.9), the solution is in perfect agreement with the periodic one. The corresponding eigenspectra are plotted on the right. Two unstable modes are clearly visible for ngh=5 and almost disappear for ngh=11 (weak instabilities with a positive imaginary part of the order of 10^{-9} are present). In fact, numerical waves should not travel at a distance (in terms of the number of mesh points) larger than the one determined by the CFL number at each time step.

Additionally, the above-mentioned simplifications can introduce an error in the interface region. Such an error can be reduced by increasing the number of ghost cells from 5 on each side of the domain to a given integer ngh, so that a reasonable tradeoff between cost and accuracy has to be found. Previous analyses by Wu and Zou [213] for a time-lagging interface condition suggest that "since the CFL number is based on the maximum wave speed (eigenvalue), it is natural that a local perturbation (due to time-lagging) of the scheme will travel at a distance, in terms of the number of mesh points, no larger than the CFL number at each time step." An optimal overlapping width of 2CFL+1 would enable to contain the error in the overlapping region. As

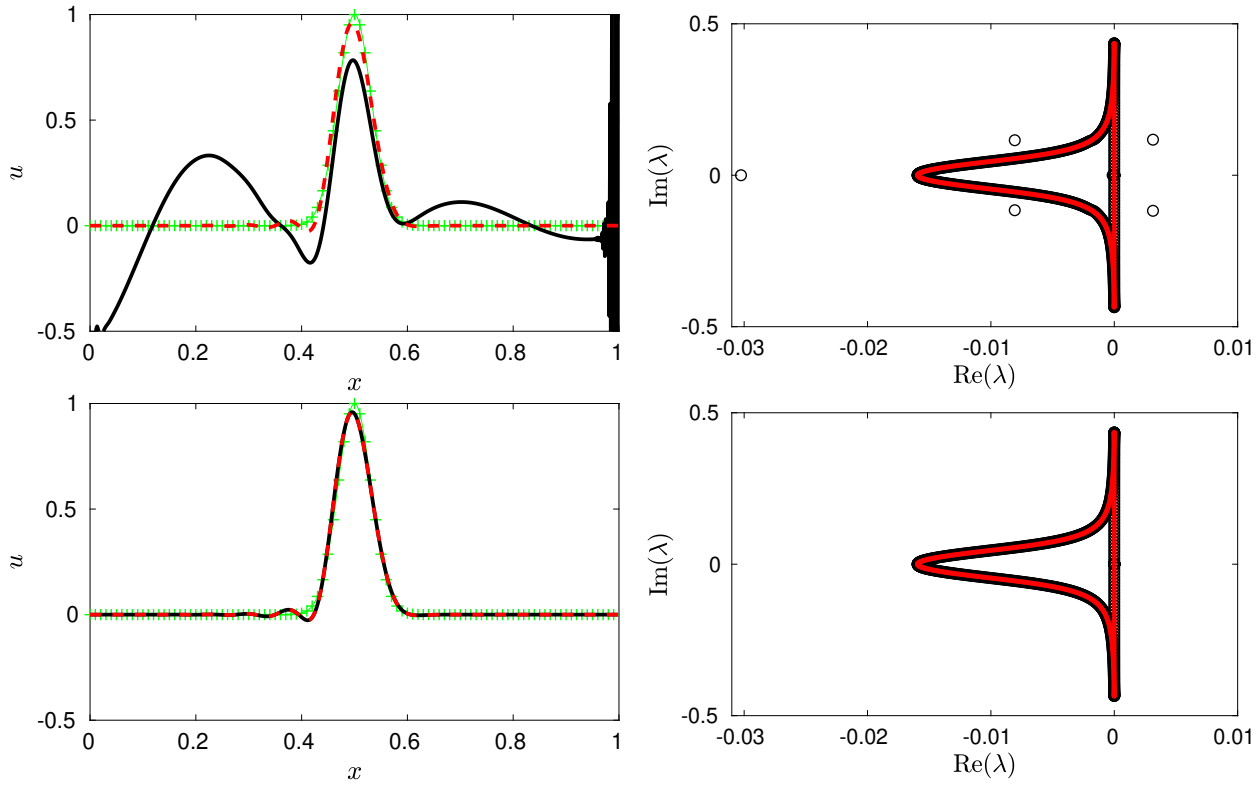

Figure 2.9: Scalar advection of a Gaussian hump: On the left, the solutions after 10 turnovers at CFL=5 using true periodic conditions (– – –) and the approximate conditions with ghost points (——) are compared to the initial (exact) solution (++). The corresponding eigenspectrum is given on the right with red symbols for the periodic problem et black symbols for the ghost-point problem. For top figures, ngh=5 and for bottom figures, ngh=11.

a consequence, the overlapping method using ghost points should maintain the order of accuracy of the interior scheme if ngh≈2CFL+1. This point will be investigated in § 2.5.1 for a vortex advection problem. In practice, all following applications are run on parallel computers. The maximum CFL is tested for each interface and the number of ghost points is set to $\max(5,2\text{CFL}+1)$. Generally, high CFL region are located near wall boundaries and few interfaces are concerned by the ghost-point extension.

2.4.5 Implementation in MUSICAA solver

In Cartesian coordinates, the multi-dimensional IRS4 operator writes:

$$\mathcal{J} = \left(1+\theta_4\left(\frac{\Delta t}{\Delta x}\right)^4 \delta_x(\lambda_x^{e\,4}\delta_x^3)\right)\left(1+\theta_4\left(\frac{\Delta t}{\Delta y}\right)^4 \delta_y(\lambda_y^{e\,4}\delta_y^3)\right)\left(1+\theta_4\left(\frac{\Delta t}{\Delta z}\right)^4 \delta_z(\lambda_z^{e\,4}\delta_z^3)\right) \tag{2.64}$$

where the directional spectral radius of the inviscid Jacobian matrix are $\lambda_x^e = |u|+c$, $\lambda_y^e = |v|+c$ and $\lambda_z^e = |w|+c$, c being the local sound speed. The subscript of the difference operator δ denotes the grid direction in which it is applied. Using 2D coordinate transform $(\xi,\eta,z) \rightarrow (x,y,z)$, the IRS4 operator is written as:

$$\mathcal{J} = \left(1+\theta_4\left(\frac{\Delta t}{\Delta \xi}\right)^4 \delta_\xi(\lambda_{\xi\eta}^{e\,4}\delta_\xi^3)\right)\left(1+\theta_4\left(\frac{\Delta t}{\Delta \eta}\right)^4 \delta_\eta(\lambda_{\xi\eta}^{e\,4}\delta_\eta^3)\right)\left(1+\theta_4\left(\frac{\Delta t}{\Delta z}\right)^4 \delta_z(\lambda_z^{e\,4}\delta_z^3)\right) \tag{2.65}$$

noting that the transformed coordinates (ξ,η) correspond to a unitary Cartesian grid ($\Delta\xi = \Delta\eta = 1$). Since the transformed directions are coupled, a single spectral radius is used for (ξ,η)-directions (in the spirit of Pulliam [215] for artificial dissipation):

$$\lambda_{\xi\eta}^e = \sqrt{\Theta_\xi^2+\Theta_\eta^2} + c\sqrt{\nabla\xi^2+\nabla\eta^2}\,, \tag{2.66}$$

The nominal implicit residual smoothing coefficients are $\theta_1 = 0.42$, $\theta_2 = 0.04$ and $\theta_4 = 0.0025$. The number of ghost cells ngh required in domain interfaces and the switch (2.17) for the filtering coefficient are based on the local CFL, defined for 2D curvilinear grids as

$$\text{CFL}_{\text{local},i} = \Delta t(\Theta_\xi + c\nabla\xi); \quad \text{CFL}_{\text{local},j} = \Delta t(\Theta_\eta + c\nabla\eta); \quad \text{CFL}_{\text{local},k} = \frac{\Delta t}{\Delta z}(w+c)$$

where i, j, k denote the three directions. For wall boundary condition, the increment is zero for IRS matrix at the wall points.

2.5 Validation of IRS4 time implicitation

The numerical solver, in particular the implicitation strategy, is assessed in the following on a few canonical test cases.

2.5.1 Vortex advection test case

As noted earlier, the major issue in multi-domain computations is the treatment of interfaces between domains. In the present work, communication between adjacent meshes is conducted through finite-size overlaps. Their effect on solution accuracy and stability is investigated initially for the unsteady inviscid flow generated by a vortex convected by a uniform flow with freestream Mach number $M = U_\infty/c = 0.5$. The initial condition is determined from Taylor's theoretical vortex model:

$$\begin{cases} u = U_\infty + A\dfrac{y}{\Delta y}\exp(\alpha R^2) \\ v = -A\dfrac{x}{\Delta x}\exp(\alpha R^2) \\ p = p_\infty - \rho_\infty \dfrac{A^2}{4\alpha\Delta x\Delta y}\exp(2\alpha R^2) \end{cases} \tag{2.67}$$

where $R = \sqrt{(x-x_0)^2 + (y-y_0)^2}$ with $(x_0, y_0) = (-30, 0)$ the initial vortex position, using a reference length $L = 1$ m. The vortex strength is $A = 5$ and $\alpha = -\ln 2/b^2$, where the Gaussian half-width is set to $b = 4$. The computational domain $-100 < x < 100$, $-100 < y < 100$ is discretized by $N \times N$ uniformly spaced points, and periodic conditions are enforced in both directions. The grid is subdivided into four equally sized subdomains. The vortex, initially located on the interface $y = 0$, is advected from left to right during 100 time units L/U_∞, crossing the interface located at $x = 0$. The L_2-norm of the error with respect to the analytical solution is first used to assess the solver accuracy. The first series of runs, reported on the left of Fig.2.10, uses low CFL values between 0.02 and 1 with explicit time marching and deliberately coarse grids ranging between $N = 50$ to 300 to distinguish the accuracy of the spatial scheme. A slope of 2.5 in the log-log plot is obtained at CFL=1 and a very small time step has to be used to approach the spatial scheme accuracy. A slope of 7 is obtained for CFL=0.02. This first series shows that the temporal error rapidly dominates for this advection case.

In the second series of runs (middle plot of Fig.2.10), the IRS4 solver is used for large CFL numbers between 1 and 10 on fine grids ($N = 200$ to 1600) to highlight temporal integration errors. At CFL=1, the second-order accuracy of RK4 for nonlinear problems is recovered, and the slope slightly increases for higher CFL. The error saturates for the coarsest grids and CFL 8 to 10, since the error level is very high and the vortex is severely damaged during its advection.

Finally in the right subfigure of Fig.2.10, error logarithm is plotted as function of logarithm of Δt for the grid 400×400 and CFL ranging from 0.1 to 10 with IRS4 smoothing. Up to CFL 1.2 the error is the same as the one obtained with the explicit solver (black circles) and the solution is second-order accurate. For higher values, a steeper slope of 4 is observed since the advection error rapidly rises when coarsening the mesh. By

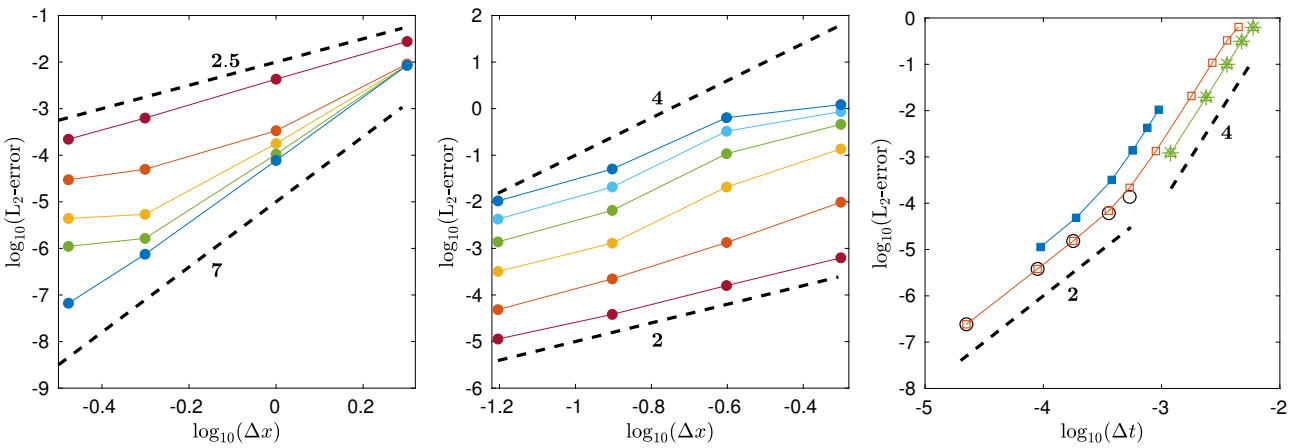

Figure 2.10: Vortex advection: L_2-norm of the error with respect to the analytical solution. Left, error of the explicit solver as a function of the mesh size Δx (grids 50×50, 100×100, 200×200, 300×300) for small CFL numbers (●,1; ●,0.5; ●,0.1;●,0.1; ●,0.02). Middle, error of the IRS4 solver as a function of the mesh size Δx (grids 200×200, 400×400, 800×800, 1600×1600) for large CFL numbers (●,1; ●,2; ●,4;●,6; ●,8; ●,10). Right, error as a function of the time step Δt: explicit solver (○) and IRS4 solver (□) for the grid 400×400 on 4 blocks at M=0.5; IRS4 solver on grid 400×400 at M=0.1 on 4 blocks (△) and 1 block (∗); IRS4 solver on grid 1600×1600 at M=0.5 (■).

reproducing the same numerical experiment with a very fine grid ($N = 1600$) for CFL 1, 2, 4, 6, 8, 10 (filled squares), it is clear that the change of slope is due to the difficulty to advect information with large time steps. A last test for the large CFL values is realized with $N = 400$ for a lower Mach number, $M = 0.1$. The error levels are the same as the ones obtained for $M = 0.5$. For these runs, a single domain was also used, which does not change the measured error, meaning that the errors are not related to the interface treatment.

In the preceding tests, the number of ghost cells for the MPI domain overlaps has been set to 2CFL+1. The influence of the number of ghost cells is illustrated in Fig.2.11 for $N = 1600$ and CFL=10. We report the iso-contours of the fluctuating pressure field, obtained by varying the number of ghost cells from 6 to 18. Intense spurious noise is generated when 6 ghost cells are used (note that the simulation blows up for 5 ghost cells). The spurious acoustic pulse and the vertical and horizontal oscillations developing at the interfaces are reduced for 9 ghost cells and are almost absent when 18 ghost cells are used (the theoretical value is 2CFL+1=21).

2.5.2 DNS of turbulent channel flow

The increased stability achieved through IRS4 smoothing is particularly beneficial for the simulation of wall-bounded turbulent flows, where very small mesh sizes are required near the wall to capture the stiff velocity gradient and predict the wall friction accurately. Therefore, the case now investigated is the turbulent channel flow at Reynolds number $Re_\tau = (\rho_w u_\tau H_m)/\mu_w = 180$, based on the friction velocity u_τ, the channel half-height H_m

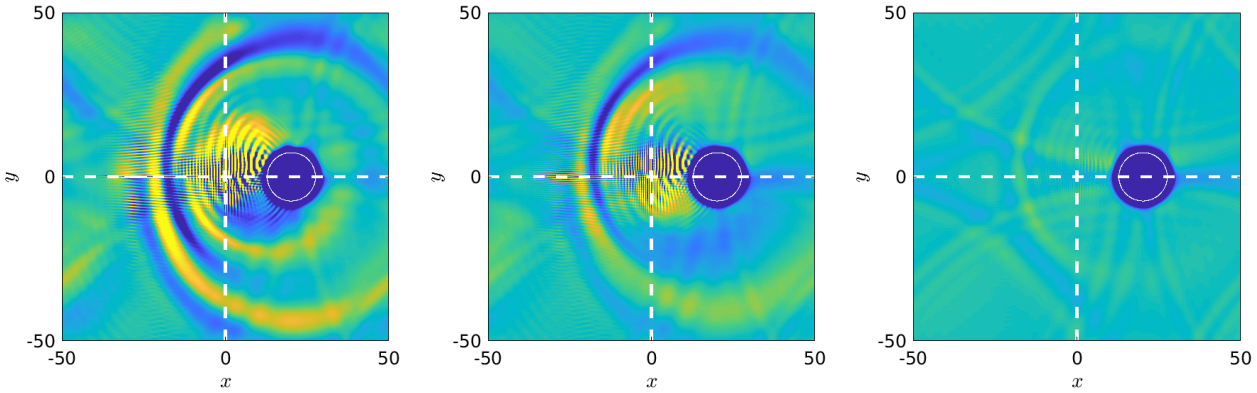

Figure 2.11: Vortex advection: maps of fluctuating pressure (between ±5 Pa, and 1 white contour for -100 Pa identifying the vortex core) on the grid 1600×1600 and CFL=10 using 6 (left), 9 (center) and 18 (right) ghost points. The white dashed lines mark the domain interfaces.

and the wall density and viscosity ρ_w and μ_w, respectively. The computational domain of $4\pi H_m \times 2H_m \times 2\pi H_m$ is discretized with a grid $192 \times 180 \times 160$, uniformly spaced in the homogeneous directions x and z and clustered at the wall in the wall-normal direction y. This leads to a DNS resolution of $\Delta x^+ = 11.9$, $\Delta z^+ = 7.1$, $\Delta y_w^+ = 0.8$ and $\Delta y_c^+ = 4$, where the subscripts w and c are used to denote the wall and centerline resolutions, respectively. Isothermal no-slip conditions are applied at the walls and periodicity conditions along the streamwise and spanwise directions. The Mach number is set to $M = 0.3$ and the simulations are parallelized on 80 cores. For the implicit cases, IRS4 is applied in the wall-normal direction only, and the number of ghost points used for the IRS4 at the MPI interfaces is set to 5, i.e. the minimum required by the scheme stencil. Results using an explicit time integration with a global time step Δt_{expl} are compared with IRS4-accelerated simulations using time steps ranging from $4\Delta t_{expl}$ to $7\Delta t_{expl}$ (see Table 2.3).

Case	Δt^+	Nb iterations	$\frac{t_{\text{cpu,expl}}}{t_{\text{cpu}}}$	time/it	Legend
EXPL CFL=1	1.05×10^{-2}	750 000	1.0	1.0	·····
IRS4 CFL=4	4.21×10^{-2}	187 000	3.30	1.18	- - -
IRS4 CFL=5	5.26×10^{-2}	150 000	4.06	1.18	- · - ·
IRS4 CFL=6	6.31×10^{-2}	125 000	5.08	1.18	- · - · ▽
IRS4 CFL=7	7.36×10^{-2}	110 000	5.93	1.18	- · - · ○

Table 2.3: Numerical parameters and computational performance of turbulent channel flow simulations with and without IRS4.

In the explicit case, the maximum CFL number is chosen equal to 1 to ensure stability throughout the simulation. Choi & Moin [216] studied the effects of the computational time step on the numerical solutions for an incompressible turbulent channel flow at $Re_\tau = 180$ using a fully implicit method. Up to Δt^+=0.4, no

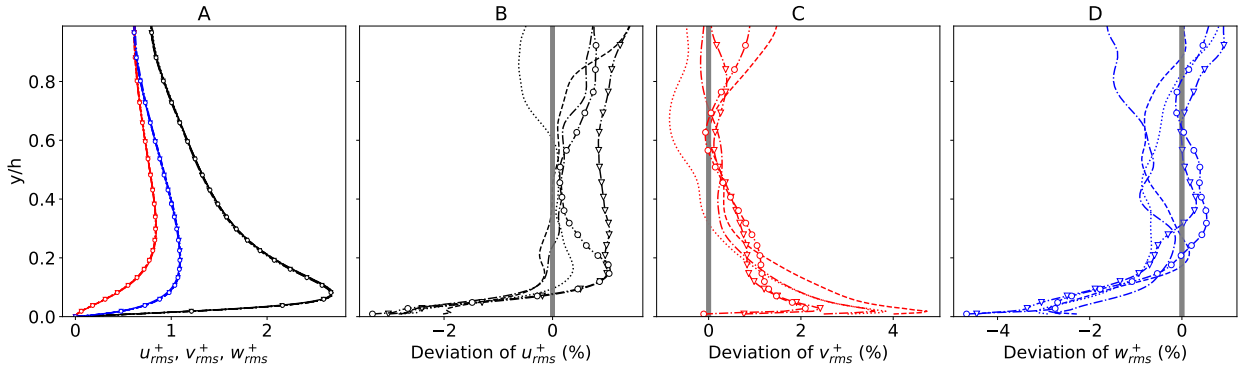

Figure 2.12: Turbulent channel flow: comparison of the rms velocities profiles (u^+_{rms}, v^+_{rms} and w^+_{rms}) with the Vreman & Kuerten (——) reference [217] for the explicit and IRS4 time integration cases. Line legends in Table 2.3.

significant deterioration of turbulence statistics was observed. For the case IRS4 CFL=7, which corresponds to the highest CFL used here, the time step is equal to 0.0736, well below the limit found in [216], so we expect the physical time step to have little impact on the accuracy of the solution. This allows to observe the influence of additional numerical errors introduced by the IRS4 on the solution quality. For all implicit cases, the total number of iterations used to reach a statistically converged solution corresponds to the total number of iterations of case EXPL divided by CFL, so that the statistics are collected over the same physical time interval for all cases. Comparisons of the computational cost for the explicit and implicit cases show that applying IRS4 in the wall-normal direction represents an overhead of 18% per iteration. However, the total number of iterations being reduced proportionally to the CFL in use, the total computation time is reduced. For instance a reduction by a factor 4.06 is obtained for CFL=5, and a factor 5.93 is found for CFL=7.

Figure 2.12 shows numerical solution for the various cases at stake. These are compared to the reference solution of Vreman & Kuerten [217], obtained with an incompressible solver based on spectral method and a very fine grid. The root-mean-square (rms) velocities profiles are plotted in Figure 2.12(A) along with the reference solution and we observe a very good agreement for all cases. To highlight differences, the relative deviations from the reference are plotted Fig.2.12(B, C and D). These are defined as $\mathrm{dev}(u^+_{i,rms}) = (u^+_{i,rms,\mathrm{VK}} - u^+_{i,rms})/u^+_{i,rms,\mathrm{VK}}$ with $u^+_{i,rms,\mathrm{VK}}$ the solution of Vreman & Kuerten for the i-th velocity component. Except for points close to the wall, deviations are below 1% for all cases. Moreover, the application of the IRS4 does not lead to any noticeable increase of the relative deviation. For an accumulation of statistics on an equivalent duration, we observe a good convergence of second-order statistics with a reduced computational cost when applying IRS4. For simulations that require a longer time to converge statistics or to obtain higher-order statistics, introducing

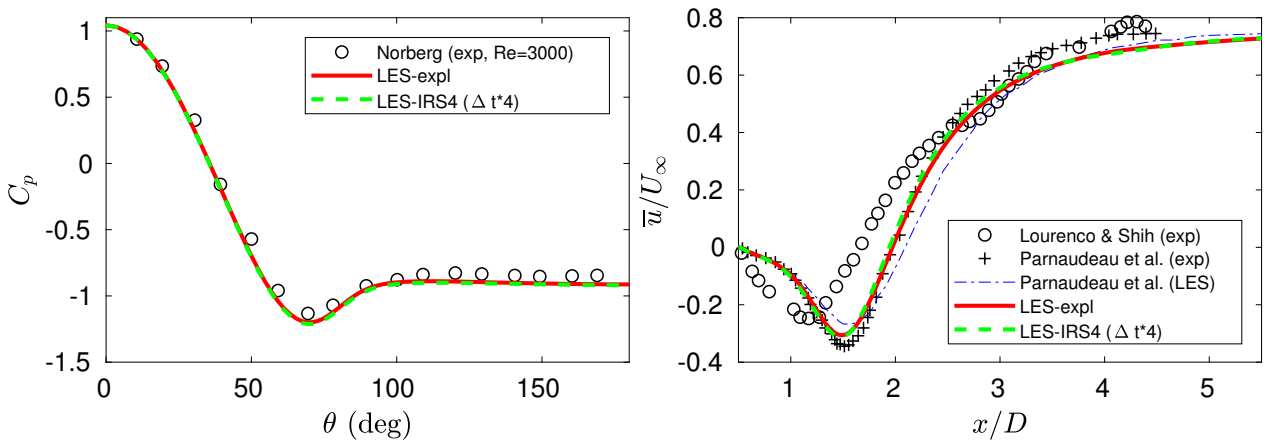

Figure 2.13: Flow past a cylinder at $Re_D = 3900$: pressure coefficient on cylinder wall, compared to Norberg's experiments [220] (left), and evolution of mean streamwise velocity along the wake centerline (right), compared to experiments of Lourenco and Shih [221] and Parnaudeau *et al.* [218].

IRS4 acceleration is therefore particularly beneficial.

2.5.3 Turbulent flow past a cylinder at Re_D=3900

We now investigate the performance of IRS4 on curvilinear grids. The IRS4 method is applied to the flow past a circular cylinder at $Re_D = 3900$ based on the diameter D, and at $M = 0.3$, which is a common benchmark case for curvilinear geometries [218, 219]. The simulation is performed on a multi-block H-O-H grid topology with approximatively 10 millions points parallelized on 102 processors. 270 points are used around the cylinder with a first mesh size of $0.002\times D$, 96 points are used in the spanwise direction to discretize $2D$ and the wake extent is discretized by 405 points. Non-reflecting Tam & Dong's conditions are applied at free boundaries and a sponge zone is added at the outlet boundary. An explicit simulation is started from the initial field described in the AS1 benchmark case [219] during 500 000 iterations with a nondimensional time step $\Delta t U_\infty/D = 4.55\times10^{-4}$. The explicit calculation is then run for 500 000 and statistics are accumulated. Afterwards, three implicit simulations with IRS4 are run by multiplying the time step by 2, 3, 4 and dividing the number of iterations by the same amount. The IRS4 smoothing is applied in the ξ and η-directions; the number of ghost cells in MPI interfaces is ngh=5.

The distributions of the pressure coefficient, $C_p = (\overline{p} - p_\infty)/(\frac{1}{2}\rho_\infty U_\infty^2)$, are superimposed for the explicit and implicit simulations in Fig.2.13 (left). The evolution of the mean velocity along the wake centerline, in Fig.2.13 (right), gives a good idea about the flow topology. In particular, the zero-crossing yields the mean recirculation length. The same values are obtained for both LES-expl and LES-IRS4 in good agreement with the

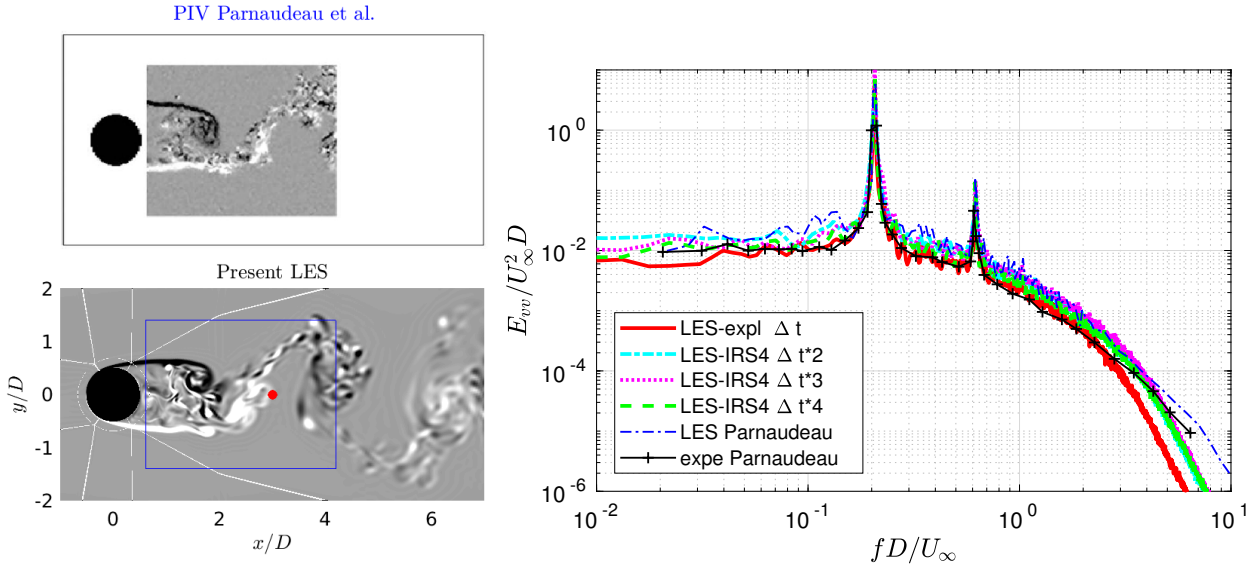

Figure 2.14: Flow past a cylinder at $Re_D = 3900$: map of the spanwise vorticity $\omega_z D/U_\infty$ compared to PIV measurements of Parnaudeau *et al.* [218] on the left, and power spectra of the normal velocity fluctuations at the location $(x, y) = (3D, 0)$ (marked by a red point in the vorticity snapshot).

measurements of Parnaudeau *et al.* [218]. The older experiments of Lourenco and Shih [221] gave a significantly shorter bubble. In fact, for $Re_D = 3900$, the cylinder flow corresponds to the shear-layer instability regime, where the transition to turbulence occurs in the separated shear layers [222]. This regime is characterized by a great sensitivity of the recirculation length to details of flow conditions, or numerical parameters for simulations [223, 224]. For instance, Lehmkuhl *et al.* [223] performed simulations over a very long time and showed some intermittency between short- and long-bubble flow topologies. In the present study, the long-bubble regime is captured but it remains highly dependent on the numerical setup.

The spanwise vorticity in the mid-plane in Fig.2.14 (left) highlights the instabilities in the two shear layers. At the particular instant shown in the pictures, the top shear layer becomes unstable and rolls up to form a primary vortex near the end of the recirculating region. A small vortex resulting from the shear-layer instability is visible near the end of the bottom shear layer. The alternate vortex shedding from the two shear layers then forms the von Kármán street. The shedding frequency can be estimated from normal velocity spectra along the wake centerline. The spectra at x/D=3 for the present explicit and implicit simulations are compared in Fig.2.14 (right) with the experimental and numerical results from Parnaudeau *et al.* [218]. Power spectral densities are estimated with an autoregressive method for 6 shedding cycles. The velocity signal is recorded every 50 iterations for the explicit case and every 10 iterations for IRS4 cases, yielding a sampling frequency $f_s D/U_\infty$ of 44, 110,

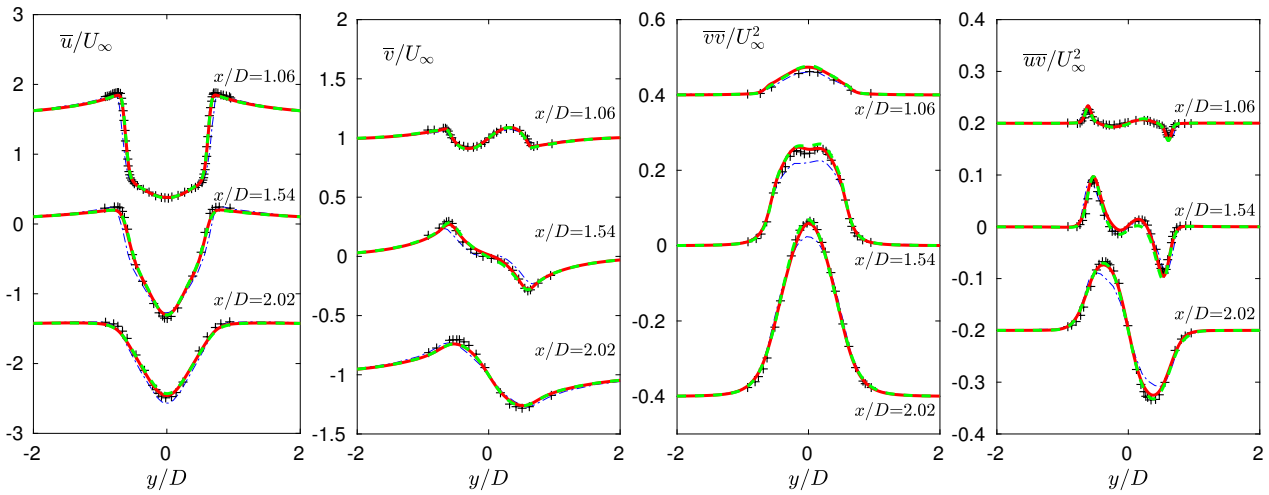

Figure 2.15: Flow past a cylinder at $Re_D = 3900$: mean velocity and turbulent intensities profiles for the explicit (——) and implicit IRS4 (– – –) LES, compared to experiment (++) and LES () of Parnaudeau *et al.* [218].

73 and 55 for Δt, $2\Delta t$, $3\Delta t$ and $4\Delta t$, respectively. The corresponding frequency resolution is 0.0044, 0.0055, 0.0044 and 0.0044, and the peak Strouhal number 0.207, 0.209, 0.207 and 0.207 for the increasing timesteps, in good agreement with the experimental value, St=0.208. Time-averaged fields, computed over the same physical duration, are shown in Fig.2.15. The explicit and the implicit case with $4\Delta t$ are almost superimposed and in very good agreement with the experiments. The overhead introduced by IRS4 is approximately 20% per direction, leading to overall savings in CPU time, due to the increased CFL, of 1.44, 2.16 and 2.98, respectively.

Chapter Summary

The governing equations and the numerical methods used in the present thesis are presented, along with some validation test cases. In particular, the implementation and improvement of a high-order implicit time integration strategy is described.

In-house finite-differences (FD) MUSICAA solver:

- Parallel multi-block strategy with curvilinear structured grids, for ideal or real gas flows.
- Performs DNS, LES, RANS and DDES for simple to moderately complex configurations.

Governing equations:

- Flow equations: compressible Navier-Stokes equations.
- Fluid modeling: Peng-Robinson-Stryjek-Vera cubic equation of state combined with Chung-Lee-Starling model for the transport properties.

Numerical methods:

- Discretization: high-order centered scheme (inviscid: 10^{th}-order / viscous: 4^{th}-order).
- Time integration: Runge-Kutta 4 combined with fourth-order implicit residual smoothing.
- Dissipation strategy: 10^{th}-order selective filtering with shock capturing device.
- Explicit filter acts as an implicit subgrid-scales model in LES.
- RANS (Spalart-Allmaras model) & DDES-SLA approaches are also used.
- No-slip walls, non-reflecting & turbomachinery boundary conditions (BC).

Fourth-order Implicit Residual Smoothing 4 (IRS4):

- Principle: bi-Laplacian smoothing applied at each RK stage, leading to the inversion of a pentadiagonal system per implicit direction.
- Use of explicit filtering after the implicit steps to cope with underdissipation at high CFL.
- Extension to curvilinear grids using high-order coordinate transforms.
- Parallel and multi-block implementation, optimal overlap region with 2CFL+1 ghost points.
- Substantial computational time savings: CFL up to 5-10, overcost of 15 to 20% per implicited direction and per time step leading to acceleration factors of 3 to 5 w.r.t. explicit time integration.

Chapter 3

High-subsonic boundary-layer flows of an organic vapor

In this chapter, we present DNS and LES studies of Novec649 boundary-layer (BL) flows at conditions representative of CLOWT facility and ORC applications. One important motivation is to carry out a reference DNS for the spatial development of a boundary layer and quantify real-gas effects in realistic conditions. In particular, a modal transition is performed from a pair of oblique modes, determined from a preliminary linear stability study realized in [18]. Then, LES are performed on the same configuration to assess our numerical strategy, notably the implicit time integration. In additional LES, we also vary the amplitude and frequency of oblique modes inducing the natural transition in order to determine when an equilibrium turbulent state is reached. The chapter is organized as follows. The numerical methods and thermodynamic conditions are succinctly recalled in section 3.1. At realistic and more non-ideal conditions, laminar boundary layers at $M = 0.9$ and their linear stability are discussed in section 3.2. Section 3.3 reports DNS results for transitional and fully turbulent states of a Novec649 boundary-layer flow at M=0.9, T_∞=100°C and p_∞=4 bars. The influence of the excitation parameters used to realize the modal transition are discussed in section 3.4 using LES.

3.1 Numerical methods and operating conditions

3.1.1 Numerical methods

As described in Chapter 2, the compressible Navier-Stokes equations are solved using the MUSICAA solver. They are supplemented with the Peng-Robinson-Stryjek-Vera (PRSV) equation of state [13] and the Chung-Lee-Starling model [123] for the transport properties. The inviscid fluxes are discretized by means of 10th-order

Condition	T [K]	ρ [kg/m^3]	Fluid models	p [MPa]	c [m/s]	Γ	μ [μ Pa.s]	λ [W/m/K]	Pr
Point A	*373.15*	*48.51*	PRSV-Chung	0.40	84.66	0.84	12.8	0.014	0.89
			REFPROP	0.40	84.66	-	18.3	0.017	1.05
Point B	*408.15*	*131.58*	PRSV-Chung	0.96	70.22	0.60	20.1	0.018	1.24
			REFPROP	0.96	70.12	-	26.0	0.021	1.43
Point C	*433.15*	*263.16*	PRSV-Chung	1.55	53.89	0.41	33.6	0.023	2.20
			REFPROP	1.55	53.42	-	35.9	0.026	2.37

Table 3.1: Thermophysical properties at selected operating points A, B, C. Numbers in italic are imposed.

centered differences whereas 4th-order finite differences are used for the visco-thermal fluxes. The scheme is supplemented with a tenth-order selective filtering to eliminate grid-to-grid unresolved oscillations. A four-stage low-storage Runge Kutta algorithm is used for time integration, and is combined with a fourth-order implicit residual smooting (IRS4) method in LES (section 3.4). The IRS4 is applied in the y-direction only, allowing CFL∼4 at the wall for an overcost of 15% and resulting in an overall CPU cost reduction of a factor 3.5. Periodicity is enforced in the spanwise direction and adiabatic no-slip conditions are applied at the wall. Non-reflecting Tam and Dong's conditions are imposed at the inlet, top and outflow boundaries. A sponge zone combining grid stretching and a Laplacian filter is added at the outlet.

3.1.2 Operating conditions

The thermodynamic conditions selected correspond to the operating points already presented in section 2.2.1 and reported here in table 3.1 for ease of reading. In particular, point A corresponds to nominal conditions of the CLOWT facility, point B is chosen at the limits of operability of the CLOWT facility, which is still in the dilute-gas region, and point C is close to the minimum of Γ. These three operating conditions are investigated in section 3.2. Then, point A is selected for the direct numerical simulations (DNS) and large-eddy simulations (LES) in sections 3.3 and 3.4.

3.2 Laminar boundary layers of Novec649

The similarity solutions for a zero-pressure-gradient compressible laminar boundary layer are computed for the three operating points A, B and C defined in table 3.1 and a Mach number M=0.9. The results are given in figure 3.1 and table 3.2. The similarity solutions obtained with the Peng-Robinson-Stryjek-Vera (PRSV)

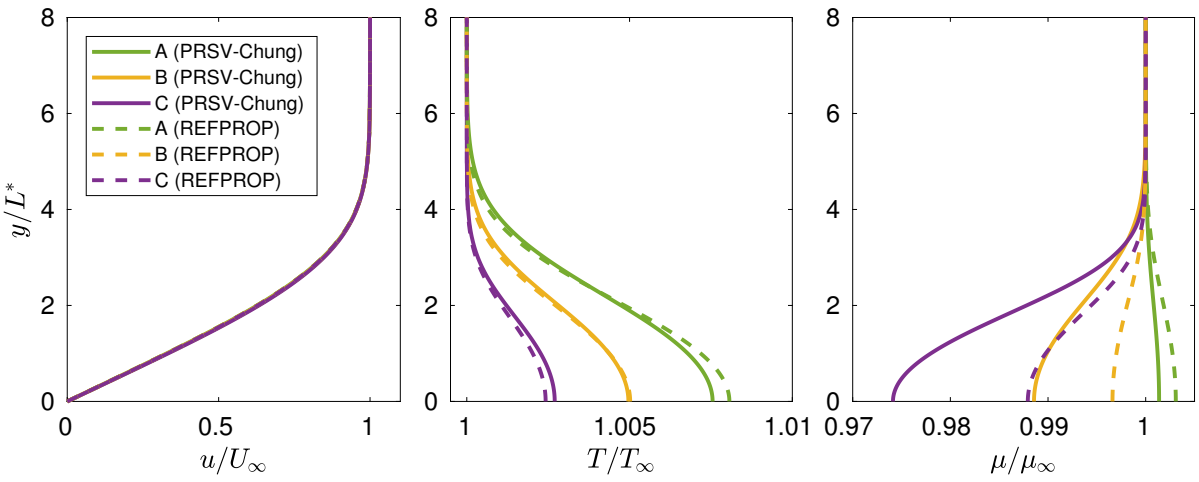

Figure 3.1: Influence of operating conditions on a laminar boundary layer at M=0.9. Nondimensional streamwise velocity, temperature and viscosity: similarity solutions using PRSV/Chung-Lee-Starling (solid lines) and REFPROP laws (dashed lines).

EoS and Chung-Lee-Starling transport properties are compared to the ones for the reference laws available in REFPROP. The velocity profiles are all matching, meaning that the operating conditions and/or the fluid models have a weak influence. Small deviations are observed for the temperature profiles in figure 3.1. The wall temperature, reported in table 3.2, is slightly underestimated (-0.05%) for point A and overestimated for point C (+0.023%). Greater discrepancies are visible for the dynamic viscosity profiles, as already discussed in section 2.2. The maximum deviation for point A is 1.4%. It is worth noting that a gas-like behavior (increasing viscosity with increasing temperature) is obtained for the more dilute condition C, whereas viscosity follows a liquid-like behavior for the two other points (more pronounced for point C, close to the minimum of Γ). This behavior is captured by both fluid models. At the high subsonic Mach number under consideration (M=0.9) the friction heating is negligible (less than 1%) due to the high heat capacity of Novec649. For comparison, temperature variations of 14% are obtained in air for this Mach number. As a consequence, the thickening factor $\delta^*/L^* \approx 1.74$ is very close to the incompressible value of 1.72, where δ^* denotes the displacement thickness and L^* the Blasius length scale $\sqrt{\mu_\infty x/(\rho_\infty U_\infty)}$.

A 2D linear stability analysis was conducted by Gloerfelt in [18]. The local stability analysis is based on the linearized compressible Navier-Stokes equations written in Cartesian coordinates. The local assumption imposes that the base flow is a function of the crossflow dimension y solely. The latter is obtained from the similarity solution of a zero-pressure-gradient compressible laminar boundary layer generalized to fluids governed by an arbitrary EoS [29]. The differential eigenvalue problem is solved using the Chebyshev collocation

Condition	T [K]	ρ [kg/m^3]	Fluid models	T_w/T_∞	μ_w/μ_∞	Γ_w	δ^*/L^*
Point A	*373.15*	*48.51*	PRSV-Chung	1.0076	1.0014	0.85	1.743
			REFPROP	1.0081	1.0031	-	1.746
Point B	*408.15*	*131.58*	PRSV-Chung	1.0050	0.989	0.62	1.737
			REFPROP	1.0050	0.997	-	1.746
Point C	*433.15*	*263.16*	PRSV-Chung	1.0027	0.974	0.46	1.732
			REFPROP	1.0024	0.988	-	1.744

Table 3.2: Influence of operating conditions on a laminar boundary layer at M=0.9. Properties at points A, B, C from similarity solutions.

method (see [135, 29] for details about the stability solver and its extension to dense gases). Three-dimensional spatial modes are searched with a real angular frequency ω and a complex wavenumber $\mathbf{k} = \alpha\mathbf{e}_x + \beta\mathbf{e}_z$. The streamwise component of the wavenumber is a complex number, $\alpha = \alpha_r + i\alpha_i$, where α_i thus represents the amplification factor. The spanwise component β defines the wave angle $\Psi = \arctan(\beta/\alpha_r)$. In the following, only linear stability results for the three operating conditions are given. For a discussion about the influence of the Mach number on the linear stability, the reader is referred to [18].

First, the influence of the fluid models on the development of unstable modes in the laminar boundary layer is reported. The neutral curves obtained for PRSV/Chung and REFPROP models are almost matching in figure 3.2. The amplification factor obtained at $Re_{L^*} = 2000$ is plotted in the left panel, and only the close-up view in the inset shows weak variations, with slightly more unstable waves for dilute conditions and for REFPROP models with respect to PRSV/Chung models. The deviations for the maximum amplification are always lower than 1%.

The linear stability analysis was also carried out to determine the most unstable oblique modes at M=0.9, which will be used to trigger transition towards the turbulent regime in the following. Neutral curves are displayed in figure 3.3(a) for wave angle between 0 (2D) and 50°. The 2D waves are the most unstable since the flow is subsonic but, for low values of Ψ, the 3D modes are almost as unstable as their 2D counterpart, notably for low frequencies. In the following study, we have chosen $\Psi = 30°$ for the oblique modes (red dashed curve in the figure). Figure 3.3(b) shows the amplification rate $\alpha_i L^*$ bounded by the neutral curve (negative values denote unstable waves) using the non-dimensional frequency $F = \omega\mu_\infty/(\rho_\infty {U_\infty}^2)$. Since $\omega L^*/U_\infty = Re_{L^*}F$, the path followed by DNS and LES simulations are represented by horizontal lines. For instance, the nominal DNS and LES calculations will start at $Re_{L^*} = 1000$ with an angular frequency $\omega L^*/U_\infty = 0.02$, corresponding to the green dashed line $F = 2 \times 10^{-5}$. Two other frequencies will also be examined, namely $\omega L^*/U_\infty = 0.024$

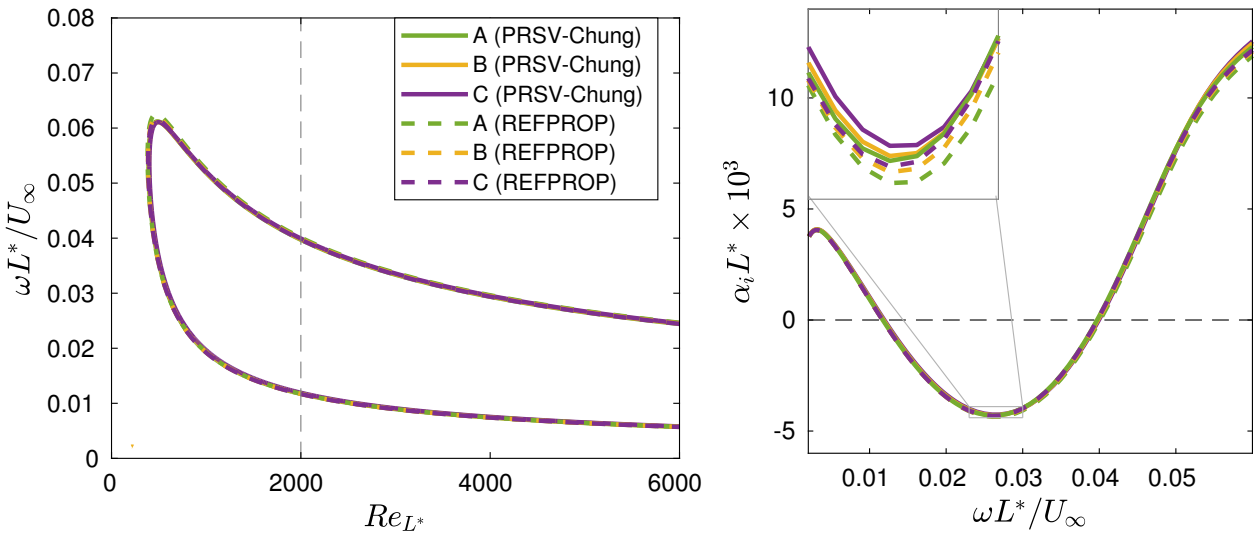

Figure 3.2: Influence of operating conditions on instabilities at M=0.9. Neutral curves on the left and growth rate at $Re_{L^*} = 2000$ on the right for various base flows: similarity solutions using PRSV/Chung-Lee-Starling (solid lines) and REFPROP laws (dashed lines).

(blue dashed line) and $\omega L^*/U_\infty = 0.04$ (magenta dashed line). Finally, the neutral curve obtained for air (with stagnation temperature and pressure of 305 K and 0.819 atm respectively) is plotted with dotted line for comparison. The shape and the stability bounds are relatively similar (due to the very close velocity profile) but the Novec649 boundary layer is slightly more stable.

The development of two-dimensional Tollmien-Schlichting-like instabilities at M=0.9 is simulated using the DNS code for various initial wave amplitudes. The computational domain is discretized by 2000×400 points, with $\Delta x = 4 \times 10^{-6}$ m and $\Delta y_w = 10^{-7}$ m. The inlet plane corresponds to $Re_{L^*} = 1000$, where 2D instabilities from LST are imposed at an angular frequency $\omega_0 L^*/U_\infty$=0.02. The mode obtained from LST has a wavenumber $\alpha_r L^* = 0.06486$ and a growth rate $\alpha_i L^* = -2.7 \times 10^{-4}$ (almost neutral). The wavelength of the perturbation $\lambda_x = 2\pi/\alpha_r = 96.87 L^*$ is discretized by $84\Delta x$. Since the DNS results will be Fourier transformed in time to get the harmonic contribution at the forcing frequency, the time step is fixed as $\Delta t = 2\pi/\omega_0/23000$, yielding a Courant-Friedrichs-Lewy (CFL) number of approximately 1. At such conditions, the simulations are conducted using an explicit time stepping. First, a precursor calculation of 1 500 000 iterations without the excitation is run to generate the base flow. When nondimensionalized with freestream quantities (subscript ∞) and the Blasius length scale L^*, perfectly autosimilar profiles are obtained in figure 3.4 in excellent agreement with the similarity solution.

The simulation is then run for 500 000 iterations with the LST eigenfunctions for u, v, p, ρ and T imposed in

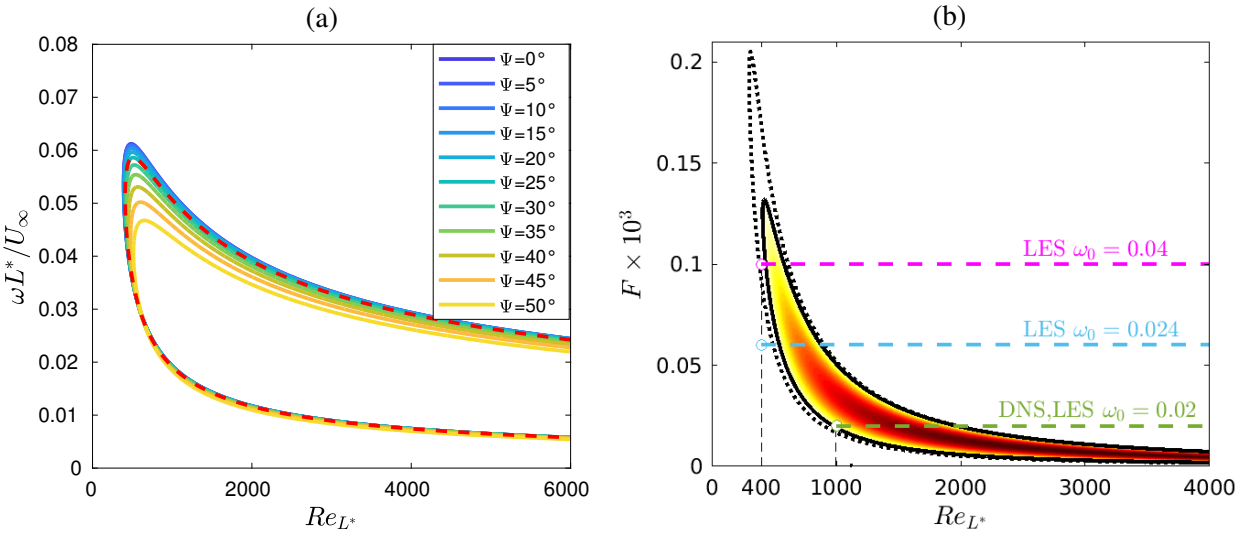

Figure 3.3: Oblique modes at $M = 0.9$: (a) Neutral curves for various values of the wave angle Ψ. The selected values $\Psi = 30°$ corresponds to the red dashes. (b) F-Re map of amplification rate at $\Psi = 30°$ for Novec649 (——) and for air (·····). The DNS and LES simulation paths are shown with horizontal dashed lines.

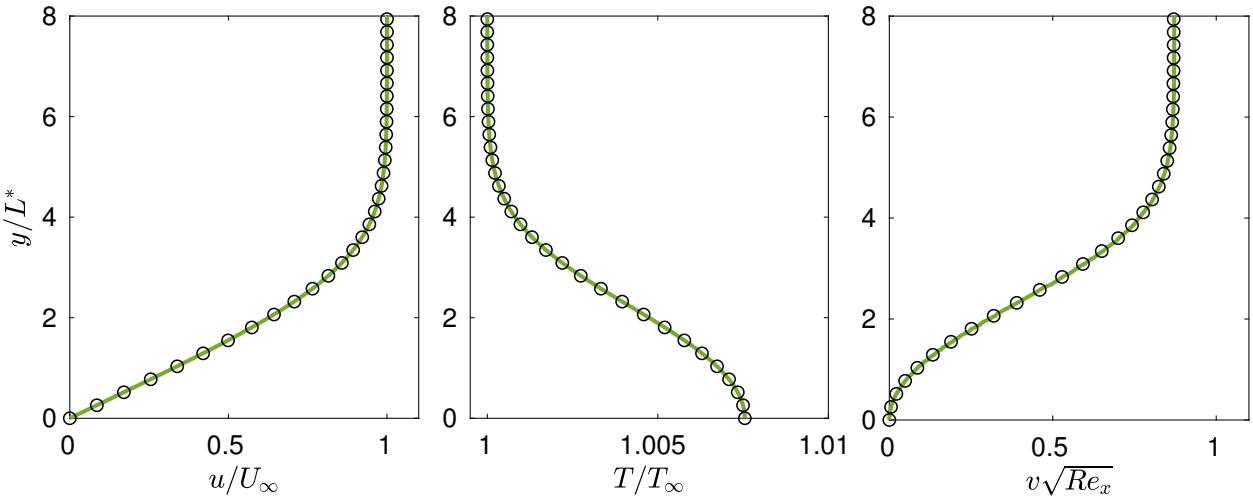

Figure 3.4: Laminar boundary layer of Novec649 at M=0.9. Nondimensional streamwise velocity, temperature and wall-normal velocity: DNS profiles (——) compared to similarity solutions using PRSV/Chung-Lee-Starling (○).

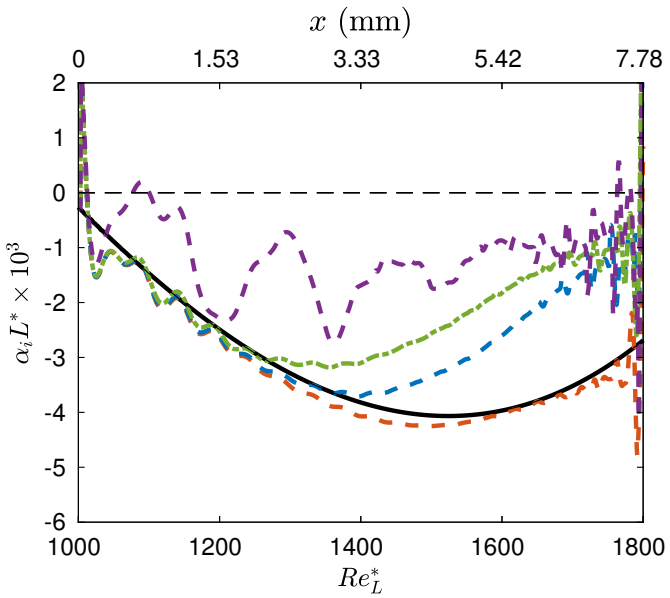

Figure 3.5: Growth rate from DNS of 2D TS waves with various amplitudes ($\varepsilon_0/U_\infty = 10^{-4}$ - - -; 5×10^{-4} - - -; 10^{-3} - · - ·; 5×10^{-3} - - -) compared to LST (——).

the Tam & Dong inflow condition [135]. Since the stability analysis is linear, we need to prescribe an amplitude for the inlet perturbations. We select four values from $\varepsilon_0 = 10^{-4}U_\infty$, which ensures that the disturbance stays in the linear regime, up to $\varepsilon_0 = 5\times10^{-3}U_\infty$. The results are stored for the last 23000 iterations every 100, which corresponds to one period. The amplitude $A_1(x)$ of the Fourier transform of the wall pressure at the fundamental frequency is used to compute the spatial growth rate as $\alpha_i = -d\left[\ln(A_1(x))\right]/dx$. Figure 3.5 shows the streamwise evolution of the computed growth rate compared to LST results as a function of Blasius Reynolds number (bottom scale) and distance x (top scale). After slight oscillations due to the adaptation of the inflow boundary condition, the growth rate for $\varepsilon_0 = 10^{-4}U_\infty$ is in fair agreement with the LST results all along the computational box. The maximum growth rate computed from DNS is slightly higher, which can be attributed to non-parallel effects ignored in the LST. As the forcing amplitude is increased, the growth rate deviates more and more rapidly from the LST curve, highlighting the onset of non linearities that saturate earlier the unstable mode. At the highest value ($\varepsilon_0 = 5\times10^{-3}U_\infty$), the saturation is almost immediate and strong oscillations of α_i are visible. The amplitude and phase of the DNS modes for $\varepsilon_0/U_\infty = 10^{-4}$ and 10^{-3} are compared in figure 3.6 to LST at the location $Re_{L^*} = 1200$. The profiles for both amplitudes match perfectly and the modulus and phase of the simulated waves are in fair agreement with LST. Once again, the discrepancies can be attributed to non parallel effects present in DNS but not to the chosen forcing amplitude. These preliminary results also validate the use of the DNS code to simulate the linear development of instabilities.

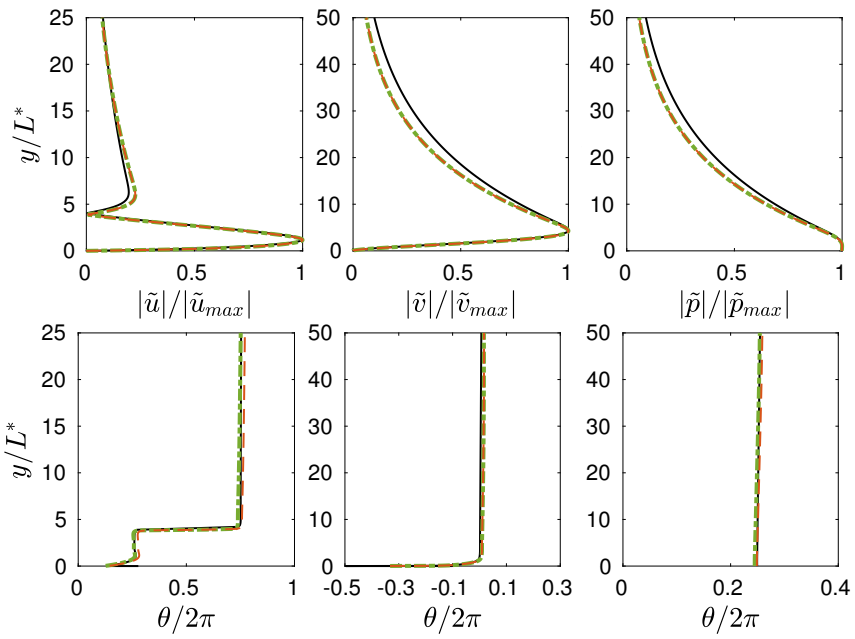

Figure 3.6: Amplitude (top row) and phase (bottom row) at $Re_{L^*} = 1200$ of the streamwise velocity, wall-normal velocity and pressure disturbances from DNS of 2D TS waves ($\varepsilon_0/U_\infty = 10^{-4}$ – – –; 10^{-3} - · - · -) compared to LST (——).

3.3 DNS of a turbulent boundary-layer flow of Novec649 at M=0.9

3.3.1 DNS setup

The study of boundary layer modal transition from the laminar to the fully turbulent regime in Novec649 is first carried out by means of DNS. The thermodynamic operating conditions correspond to the nominal case in section 3.2, namely a freestream temperature T=100°C and pressure p=4 bars, and the Mach number is M=0.9, representative of the CLOWT facility. To induce a relatively rapid transition, a pair of unstable oblique modes, determined in the previous section, are entered with an amplitude $\varepsilon_0 = 10^{-3}U_\infty$. At the inlet, where the Reynolds number is Re_{L^*}=1000, oblique waves skewed by 30° with respect to the mean-flow direction are imposed at a nondimensional angular frequency $\omega_0 L^*/U_\infty$=0.02. The spanwise extent is taken equal to one wavelength of the input modes, $\lambda_z = 2\pi/\beta_0$, with the spanwise wavenumber $\beta_0 = 0.04L^*$. The path followed by the DNS is shown with the green dashed line in figure 3.3.

A grid of $9000 \times 400 \times 1000$ points (3.6 billions) is used, yielding a DNS resolution with mesh sizes in wall units ($\Delta x_i^+ = \Delta x_i u_\tau/\nu$, u_τ being the friction velocity and ν the kinematic viscosity) equal to Δx^+=15.7-12.9 in the streamwise direction, Δz^+=7.7-6.3 in the spanwise direction, and Δy_w^+=0.78-0.64 at the wall and Δy_e^+=12.2-

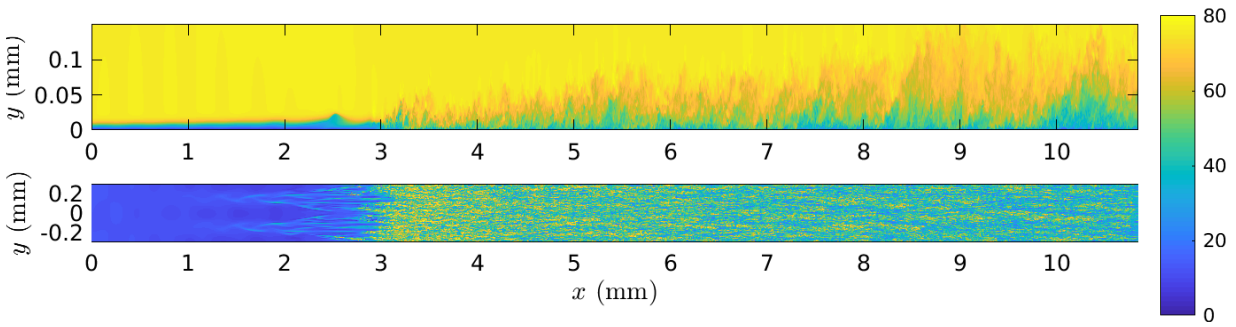

Figure 3.7: Instantaneous views of the streamwise velocity (m/s) in the plane $z = 0$ (top) and in the plane $y^+ \approx 15$ (bottom).

10.7 at the boundary-layer edge over the turbulent region. The simulation is run for 500 000 iterations with a maximum CFL=1 and the explicit Runge–Kutta time stepping, and then statistics are collected during 450 000 iterations. The overall cost is approximately 5 millions CPU hours on 18 000 CascadeLake cores.

3.3.2 Oblique breadown

A snapshot of the DNS is shown in figure 3.7. The axes are kept dimensional and the portion of the flat plate simulated is just over a centimeter long (the experiments in CLOWT facility will use a plate of 6 cm). Transition to turbulence is seen to occur 3 mm from the plate leading edge and boundary layer thickness is of the order of one tenth of millimeter. Measurements would thus be very challenging, especially as the high density of Novec649 precludes the use of miniaturized hot wire.

A three-dimensional view of the transitional region is reported in figure 3.8. A checkerboard pattern is visible just after the inlet due to the interaction of the two initial oblique waves with opposite angles (see also figure 3.20 in section 3.4). Further downstream, the initial oblique modes $(\omega/\omega_0,\beta/\beta_0)$=(1,±1) grow slowly. From 2D results of figure 3.5, the onset of nonlinear saturation due to the forcing amplitude is expected to occur after x=2 mm. In 3D, the λ_2-criterion clearly shows saturated vortices as early as x=1 mm, meaning that the forcing amplitude is not directly responsible for the early nonlinear energy transfer between modes. Using a two-dimensional t-z Fourier transform of the streamwise velocity component in the horizontal plane y=0.0013 mm, the development of the $(\omega/\omega_0,\beta/\beta_0)$ modes is obtained in figure 3.9. Initially, the only present mode is (1,±1) but the first streak mode (0,2) rapidly emerges near x=0.5 mm and dominates after x=0.7 mm. This mode is represented by isocontours of the fluctuating streamwise velocity in the 3D view of figure 3.8, which correspond to laminar streaks of opposite sign, visible from x=1 mm with the selected isocontour level.

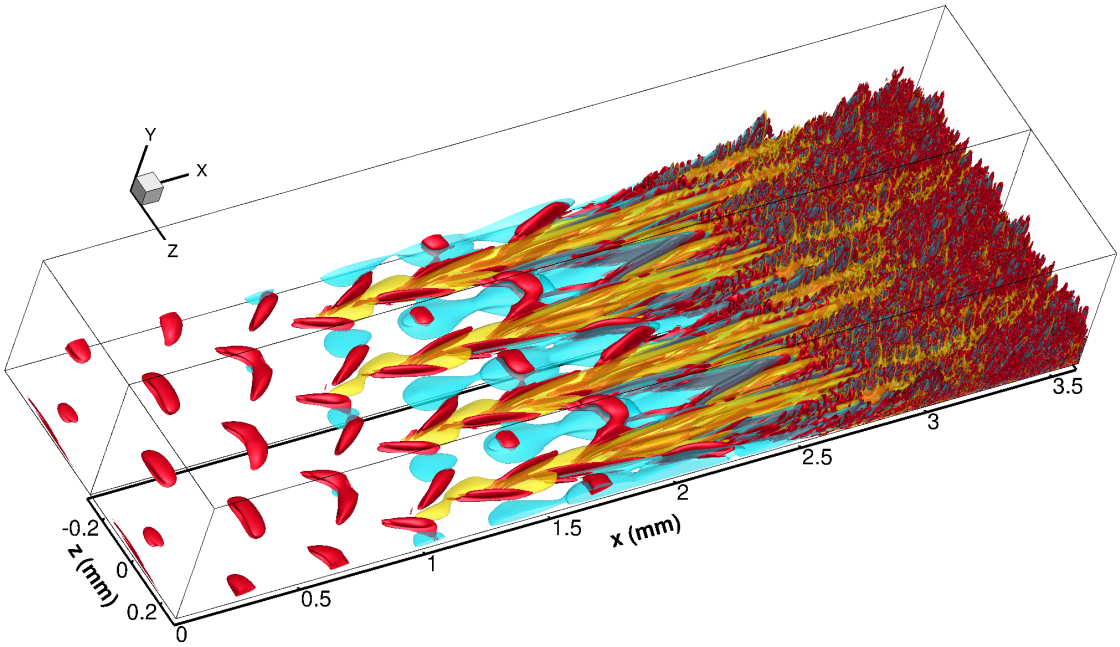

Figure 3.8: Instantaneous view of the transitional region: two isocontours of the fluctuating longitudinal velocity (u'=0.05 m/s in yellow and u'=-0.05 m/s in blue) and one isocontour of λ_2-criterion ($\lambda_2\delta^2_{1,in}/U^2_\infty$=$-1.26\times10^{-8}$ in red). The domain is duplicated in the spanwise direction.

The latter are modulated by the checkerboard pattern in their early development. The mode (1,3), resulting from nonlinear interactions with the fundamental oblique waves, reaches a large amplitude at x=1 mm. Nonlinearities then rapidly develop with the eruption of streak harmonics (0,4) and (0,6). These wavelength doublings are better identified on top views of the fluctuating velocity (see figures 3.20 or 3.30 in section 3.4)). This first phase is very similar to the observations for oblique transition from the literature [225, 226, 135]. The low-speed streaks have a sinuous evolution and the appearance of high frequencies due to transient growth leads rapidly to turbulence.

3.3.3 Fully turbulent state

The evolution of the skin friction coefficient $C_f = \tau_w/(\frac{1}{2}\rho_\infty U_\infty)$ is plotted in figure 3.10(a) with the wall shear stress evaluated as $\tau_w = \overline{\mu}_w(\partial\overline{u}/\partial y)_w$. The friction coefficient departs rapidly from the laminar correlation and is found to be in very good agreement with incompressible DNS databases [227, 228] further downstream, meaning that a canonical zero-pressure-gradient turbulent boundary layer is obtained for a range of Reynolds number Re_θ, based on momentum thickness, between approximately 1500 and 5000. Almost no overshoot of the friction coefficient is observed here, which is reminiscent to the FST-induced bypass transition of Wu &

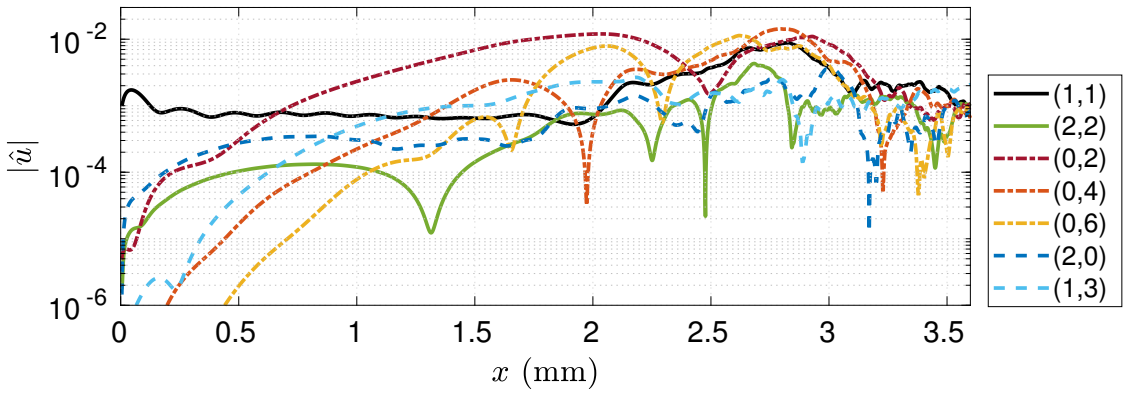

Figure 3.9: Streamwise evolution of Fourier components with frequency and spanwise wavenumber (ω/ω_0,β/β_0) for the streamwise velocity at y=0.0013 mm.

Moin [228], even if the Reynolds number of transition is larger since the inlet Reynolds number is relatively high. A similar zero-pressure-gradient boundary layer at M=0.9 in air would correspond to smaller values of C_f due to friction heating effects, as illustrated by the data from Wenzel *et al.* [229]. This effects can be physically interpreted as an incompressible C_f-distribution that is stretched by compressibility and viscosity effects. For the dense gas, since the wall temperature differs by less than 1%, compressibility effects on the mean flow are almost absent.

Figures 3.10(b) and 3.11 show the mean streamwise velocity profiles $\overline{u}^+ = \overline{u}/u_\tau$ and turbulent intensities $u^+_{i,rms} = u_{i,rms}/u_\tau$ (where u_i is either the streamwise u, wall-normal v or transverse w components of the velocity vector and the friction velocity is $u_\tau = \sqrt{\tau_w/\overline{\rho}_w}$) for various streamwise stations. The profiles are in good agreement with the incompressible database of Schlatter & Örlü [227] at the same values of Re_θ. Slight deviations can be seen for the first station, where the Novec649 boundary layer has not yet reached a perfect turbulent equilibrium.

The turbulent kinetic energy (TKE) budget, written in the compressible regime, is reported in figure 3.12. The main terms of the budget are the production term $\left(-\overline{\rho u_i'' u_j''}\frac{\partial \widetilde{u}_i}{\partial x_j}\right)$, the turbulent transport term $\left(-\frac{1}{2}\frac{\partial}{\partial x_j}\overline{\rho u_i''^2 u_j''} - \frac{\partial}{\partial x_j}\overline{p' u_i'}\right)$, the viscous diffusion term $\left(\frac{\partial}{\partial x_j}\overline{u_i' \tau_{ij}}\right)$, and the viscous dissipation term $\left(-\overline{\tau_{ij}\frac{\partial u_i'}{\partial x_j}}\right)$. Here the compressible form [230] is implemented with $\overline{(\cdot)}$ the Reynolds average and $\widetilde{(\cdot)}$ the Favre average; prime quantities are Reynolds fluctuations and double prime Favre fluctuations. Note that Reynolds and Favre averaging provide essentially the same results at the present Mach number, with velocity statistics very close to the incompressible ones. These terms, normalized by $\overline{\rho}_w u_\tau^4/\overline{\nu}_w$, are in very good agreement with incompressible DNS databases at $Re_\theta \approx 4000$.

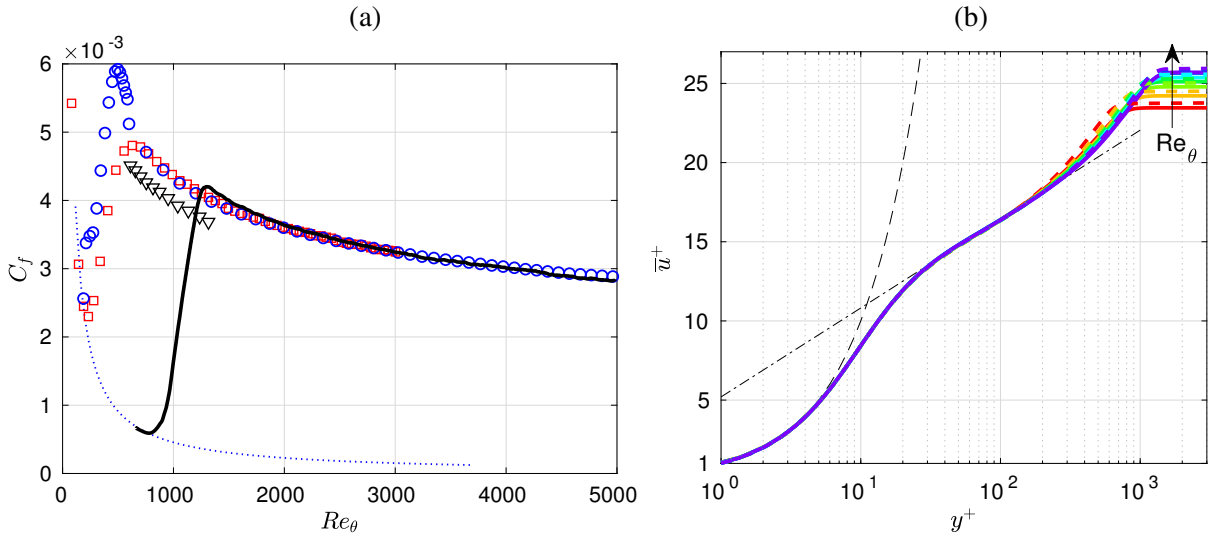

Figure 3.10: (a) Skin friction coefficient: present DNS (——); incompressible DNS of Schlatter & Örlü [227] (○); DNS of bypass transition of Wu & Moin [228] (□); compressible DNS of Wenzel *et al.* [229] at M=0.85 (▽); laminar Blasius correlation $0.664/\sqrt{Re_x}$ (·····). (b) Mean streamwise velocity at Re_θ=2000, 2540, 3030, 3270, 3630, 3970, 4060 (solid lines from red to blue) compared to DNS results of Schlatter & Örlü [227] (dashed lines) at the same Re_θ.

In figure 3.13, premultiplied spanwise energy spectra are shown for the streamwise velocity at Re_θ=2435 and 4963. An invariant maximum is found at a wall distance of y^+=12 with a wavelength λ_z^+=120, corresponding to near-wall turbulent streaks. These values are the same as those observed for incompressible boundary layer [232, 233]. For sufficiently high Reynolds numbers, a second peak emerges due to the presence of large scales in the outer region, whose location and wavelengths scaled in outer units are $y \approx 0.13\delta$ and $\lambda_z \approx 0.7\delta$, respectively. The emergence of large-scale motions is also present in the temporal spectra of figure 3.14. To obtain spectral information, the temporal signal, made of 9000 samples recorded every $50\Delta t_{\mathrm{DNS}}$, is transformed in Fourier space using the spectral estimator of Capon [234] and the Welch method with Hann windowing and 4 overlapping segments. The frequency resolution is 22.3 kHz. Contour plots of the premultiplied temporal spectra for two values of the Reynolds number show that a broad range of temporal frequencies are excited with dominant activity for $\lambda_t U_\infty/\delta$ between 1 and 3 in the near-wall region ($y^+ \approx 15$). As the Reynolds is increased, spectral level are more intense for large wavelengths in the outer region ($y > 0.1\delta$), indicating the presence of longer lasting structures. Using a Taylor's hypothesis, this indicates the presence of elongated large-scale motions. Using a convection velocity $U_c = 0.7U_\infty$, the temporal scales $\lambda_t U_\infty/\delta \sim 10$ would correspond to streamwise wavelengths of the order of 7δ, in fair agreement with measurements by Hutchins & Marusic [235] in low-speed air boundary layers.

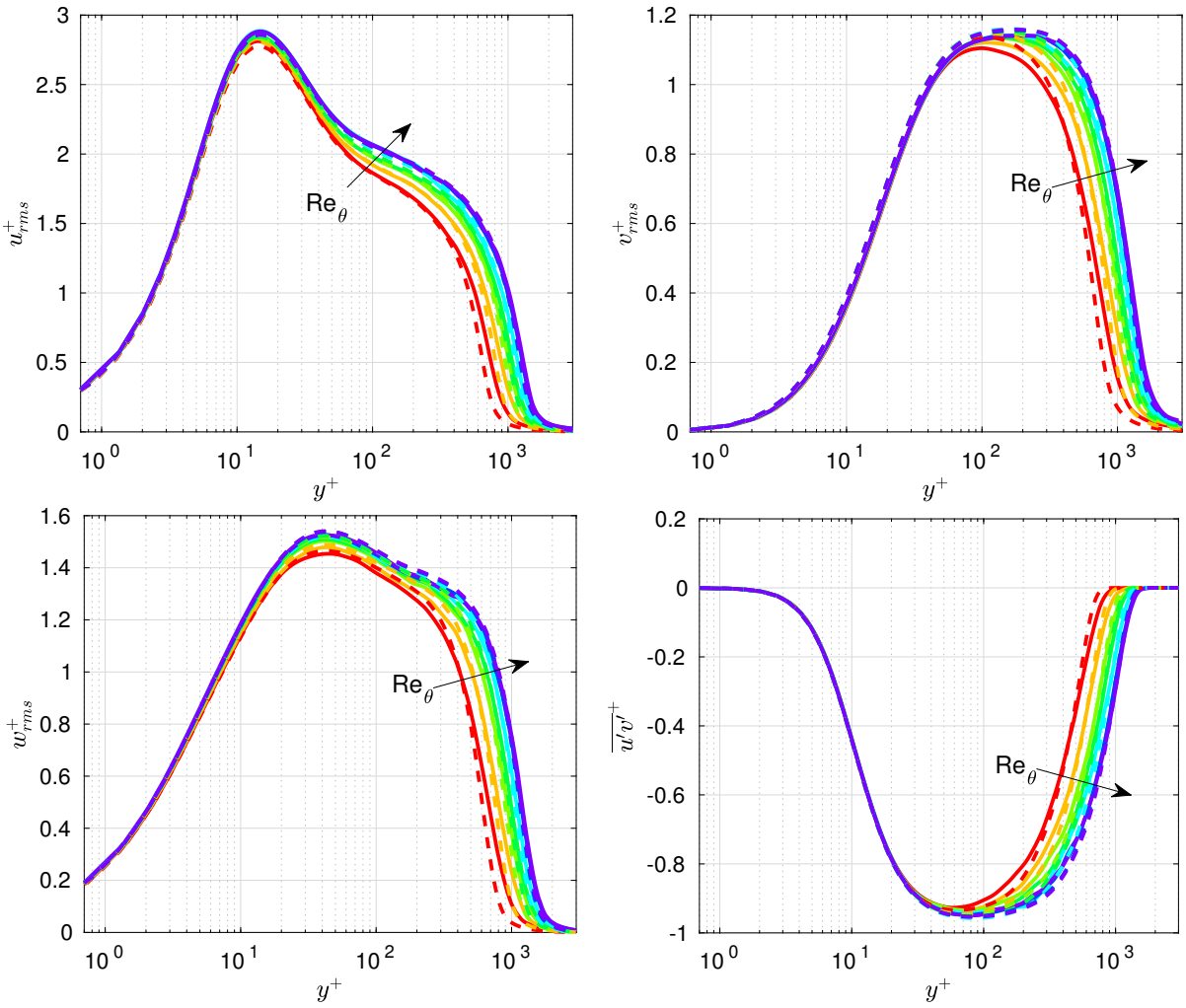

Figure 3.11: Turbulent intensity profiles at Re_θ=2000, 2540, 3030, 3270, 3630, 3970, 4060 (solid lines from red to blue) compared to Schlatter & Örlü [227] (dashed lines).

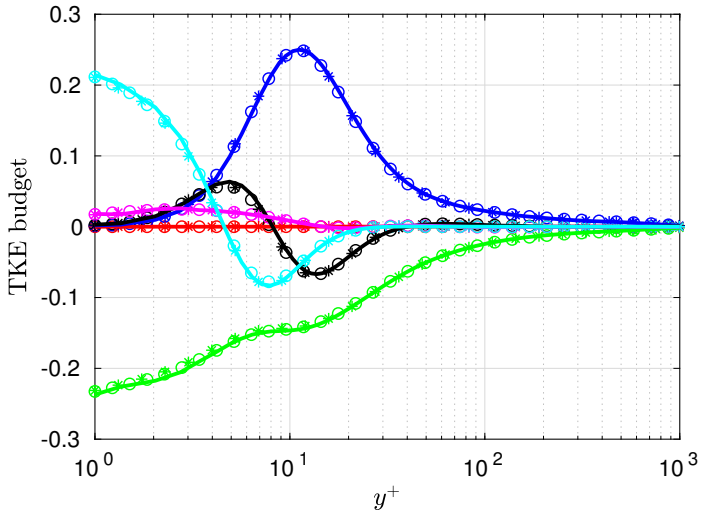

Figure 3.12: Turbulent kinetic energy budget: production (——); turbulent transport(——); viscous diffusion (——); viscous dissipation (——); pressure-dilation + pressure diffusion (——); mean flow convection(——). Solid lines denote the present DNS at Re_θ=4060 compared to incompressible DNS of Schlatter & Örlü [227] at Re_θ=4060 (○) and Sillero, Jimenez & Moser [231] at Re_θ=4000 (∗).

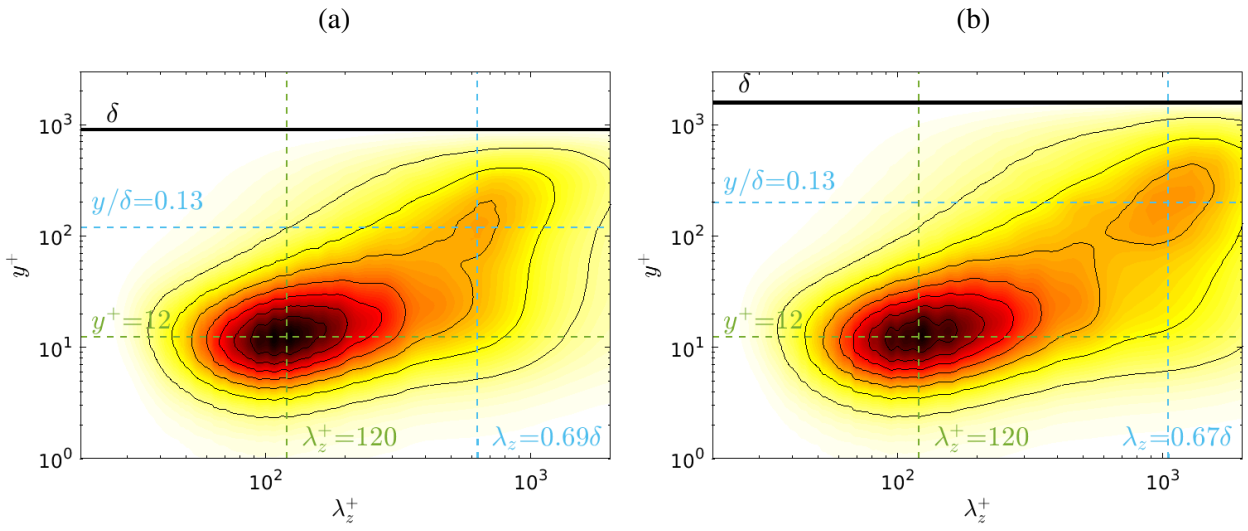

Figure 3.13: Premultiplied spanwise spectra $k_z E_{uu}(k_z)/u_\tau^2$ of streamwise velocity u at Re_θ=2435 (a) and Re_θ=4963 (b). Contours between 0 and 4 with spacing 0.5.

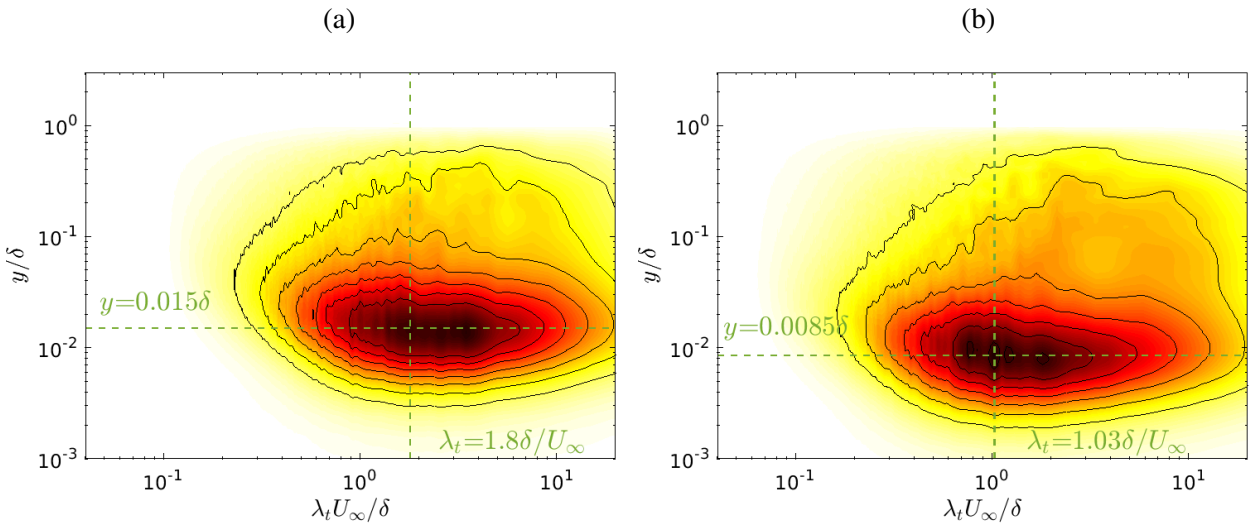

Figure 3.14: Premultiplied temporal spectra $\omega E_{uu}(\omega)/u_\tau^2$ of streamwise velocity u at Re_θ=2435 (a) and Re_θ=4963 (b). Contour between 0.5 and 2.5 with spacing 0.3.

As a first conclusion, velocity statistics for the turbulent boundary layer of Novec649 are very close to their incompressible counterparts despite the high-subsonic Mach number. Compressibility effects that are clearly visible in air at M=0.85 [229] are almost absent here due to the high molecular complexity of the compound that induces a high specific heat and reduces considerably temperature variations. Higher-order statistics, such as TKE budget, and turbulent scales, deduced from a spectral analysis, are also in very good agreement with low-speed boundary layers in air.

3.3.4 Statistics of thermo-physical properties

Wall-normal profiles of the time- and span-averaged pressure, temperature and density are reported in figure 3.15 for successive stations in the turbulent boundary layer. To highlight similarities and differences with air flows, the compressible results of Wenzel *et al.* [229] at a close Mach number (M=0.85) have been added and rescaled for comparison (by a factor given in the figure legend). The small pressure drop at the edge of the boundary layer is similar to what is observed in air (note that the last station in [229] corresponds to a lower Reynolds number than the first turbulent profile for Novec649; see black triangles in figure 3.10a). The shape of temperature and density deviations from their edge value are similar with air but the levels are drastically reduced. This is more pronounced for mean temperature variations (with a reduction by a factor 17 with respect to air) than for density profiles, which vary inversely and are reduced by 9. Due to these weak variations, the pressure fluctuations across the boundary layer, in figure 3.16, follow very well the incompressible turbulent

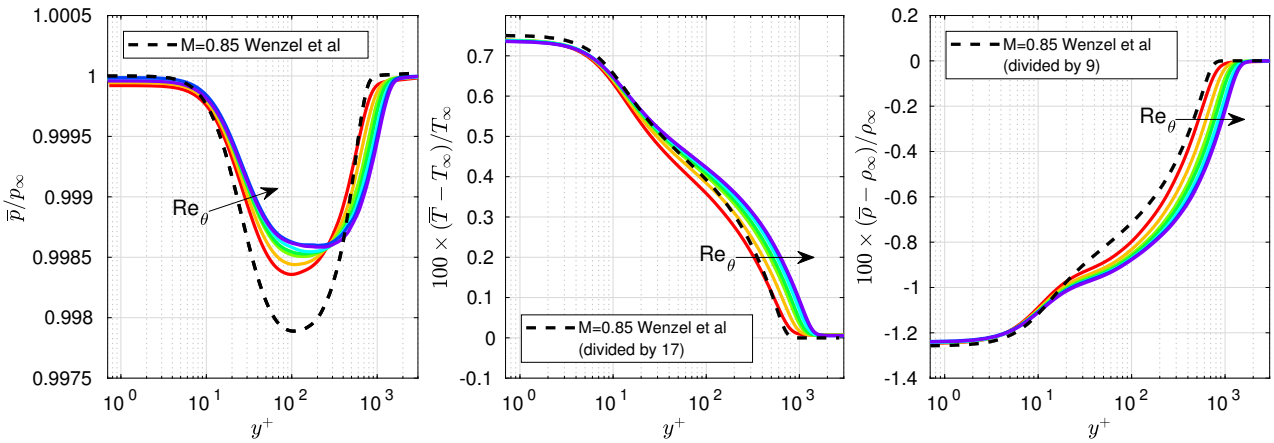

Figure 3.15: Mean profiles of thermodynamic quantities: pressure, temperature and density (from left to right) at Re_θ=2000, 2540, 3030, 3270, 3630, 3970, 4060 (solid lines from red to blue) compared to DNS of Wenzel *et al.* [229] for air at M=0.85, Re_τ=671(– – –).

boundary layer data of Schlatter & Örlü [227]. The temperature fluctuations are very low (of the order of 10^{-3}). Their vertical variations is very similar to what is expected in air but the levels are reduced by a factor 13. On the contrary, density fluctuations keep the same order of variations as air flow but the distribution is different. For dense gas flows, they are highly correlated with pressure fluctuations [30]. This behavior can be deduced from the equation of state, by differentiating and approximating differential terms by rms fluctuations:

$$dp = \left(\frac{\partial p}{\partial \rho}\right)_T d\rho + \left(\frac{\partial p}{\partial T}\right)_\rho dT \;\Rightarrow\; \frac{\rho_{rms}}{\overline{\rho}} \approx \frac{1}{\overline{\rho}} \left[p_{rms} - \left(\frac{\partial p}{\partial T}\right)_\rho T_{rms} \right] \Big/ \left(\frac{\partial p}{\partial \rho}\right)_T$$

Since T_{rms} is very small, the density fluctuations can be approximated by $p_{rms}/(\partial p/\partial \rho)_T$, which is further approximated as p_{rms}/c^2, using the definition of the sound speed $c^2 = (\partial p/\partial \rho)_s$ (thus replacing the partial derivative at constant T by the same partial derivative at constant entropy s, an approximation valid in the limit of $c_p \to \infty$). The approximated distribution (dotted line in figure 3.16) reproduces reasonably well the fluctuating density distribution.

Important deviations arise for the mean dynamic viscosity profiles in figure 3.17 (left panel) with respect to results obtained in air at a similar Mach number. The levels in Novec649 are severely reduced (factor of 75) and the profile trends do not follow the one of the mean temperature. The kinematic viscosity ($\overline{\nu} = \overline{\mu/\rho}$) evolves similarly as air results. It is thus correlated with temperature variations, showing that the variations of $\overline{\mu}$ are related to the peculiar behavior of the density, being correlated with pressure. The high reduction factor for $\overline{\mu}$ is approximately the combination of the reduction factors for $\overline{\nu}$ and $\overline{\rho}$, and explains a posteriori why a velocity scaling law, such as the one of van Driest, is not necessary for dense gases. Finally, the right panel

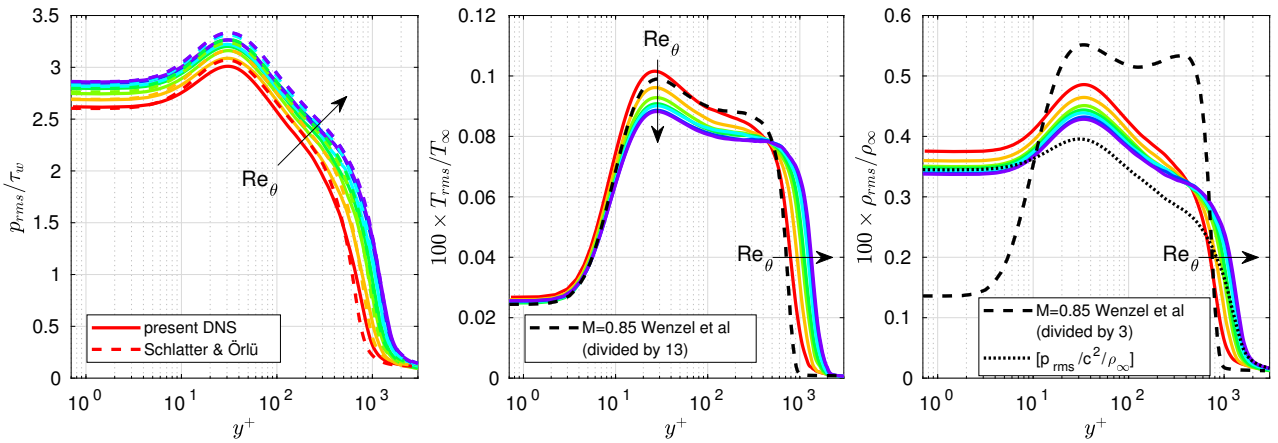

Figure 3.16: Profiles of fluctuating thermodynamic quantities: pressure, temperature and density (from left to right) at Re_θ=2000, 2540, 3030, 3270, 3630, 3970, 4060 (solid lines from red to blue). Pressure fluctuations are compared to incompressible DNS of Schlatter & Örlü [227] at the same Reynolds numbers (dashed lines); rescaled temperature and density profiles at Re_τ=671 from DNS of Wenzel *et al.* [229] in air at M=0.85 (- - -).

	T	ρ	c	$h-h_\infty$	$s-s_\infty$	c_p	c_v	Pr	Γ
	[K]	[kg/m^3]	[m/s]	[J]	[J/K]	[J/K]	[J/K]		
edge value	373.15	48.59	84.64	0	0	969.4	915.6	0.891	0.844
wall value	375.9	47.99	85.41	2650	7	971	918.2	0.885	0.851
max rms	0.38	0.23	0.125	365	1	0.315	0.365	0.0012	0.0012

Table 3.3: Averaged variations of some thermodynamic quantities.

of figure 3.17 shows the variations of the mean fundamental derivative of gas dynamics ($\overline{\Gamma}$). Its value remains lower than one (dense gas regime) across the entire boundary layer; see also table 3.3. In this table, dimensional averaged variations between the wall and the edge of the boundary layer are given. Small deviations of the thermodynamic quantities are noticed, even if the enthalpy variation is large due to the excitation of internal degrees of freedom.

The heat exhanges are very important in the context of turbine flows, which is the final objective of the present research. For incompressible laminar boundary layer, the similarity of the momentum and energy equation (Reynolds analogy) allows one to relate diffusive transport of momentum and heat. For two-dimensional flow, adiabatic wall and zero pressure gradient, the Crocco-Busemann relation implies that the total enthalpy $\mathscr{H} = h + (1/2)u^2$ is constant across the boundary layer under the assumption $Pr = 1$. The Crocco relation

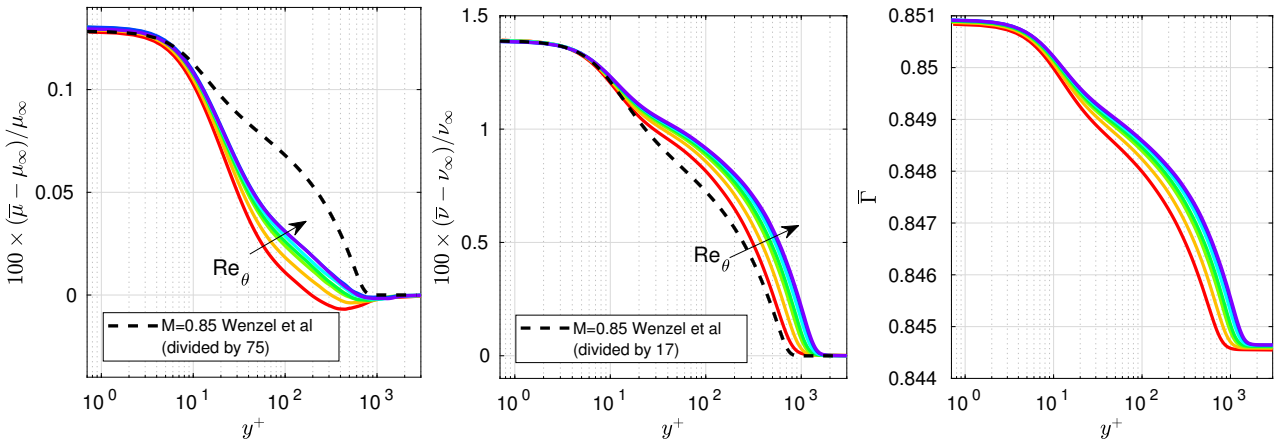

Figure 3.17: Mean profiles of dynamic ($\overline{\mu}$), kinematic ($\overline{\nu}$) viscosities and fundamental derivative of gas dynamics ($\overline{\Gamma}$) (from left to right) at Re_θ=2000, 2540, 3030, 3270, 3630, 3970, 4060 (solid lines from red to blue).

establishes a link between the local values of velocity and enthalpy:

$$h_{\text{Crocco}}(y) \approx h_w - (h_w - h_\infty)\left(\frac{\overline{u}(y)}{U_\infty}\right)^2 \tag{3.1}$$

and, for a calorically perfect gas, second Joule's law ($h = C_p T$) yields:

$$T_{\text{Crocco}}(y) \approx T_w - (T_w - T_\infty)\left(\frac{\overline{u}(y)}{U_\infty}\right)^2 \tag{3.2}$$

Figure 3.18(a) indicates that these approximations are in very good agreement with the DNS turbulent field. The good match for T means that a relation $h = \hat{c}_p T$ holds (but $\hat{c}_p \approx h_\infty/T_\infty$ is not equal to $\overline{c_p}$).

Figure 3.18(b) shows the recovery factor, defined as

$$r = \frac{h_{aw} - h_\infty}{\frac{1}{2}U_\infty^2} \tag{3.3}$$

with h_{aw} the adiabatic wall enthalpy, which corresponds to the present wall condition. For laminar boundary layers, an approximate theoretical value for $r = \sqrt{Pr}$ can be deduced from self-similar boundary-layer approximation with constant property flow. In the present simulation, the Prandtl number is almost constant (see table 3.3) and equal to 0.89, leading to $r_{\text{lam}} \approx 0.943$ (dashed red line in figure 3.18b) in very good agreement with DNS values. After a peak in the transition region, the recovery factor decreases to an approximate constant value in the turbulent region. For comparison, the approximate formula given by van Driest [236]

$$r = Pr_t\left[1 + \frac{2}{\kappa}\sqrt{\frac{C_f}{2}}(1 - Pr_t)\left[\frac{\pi^2}{6} + \frac{3}{2}(1 - Pr_t)\right] + 25\frac{C_f}{2}\left\{\left(\frac{Pr}{Pr_t} - 1\right)\right.\right.$$
$$\left.\left. + 2\ln\left[1 + \frac{5}{6}\left(\frac{Pr}{Pr_t} + 1\right)\right] + \ln 6 \cdot \ln\left[1 + \frac{7}{8}\left(\frac{Pr}{Pr_t} - 1\right)\right] - \ln 6 \cdot \ln\left[1 + \frac{1}{4}\left(\frac{Pr}{Pr_t} - 1\right)\right]\right\}\right] \tag{3.4}$$

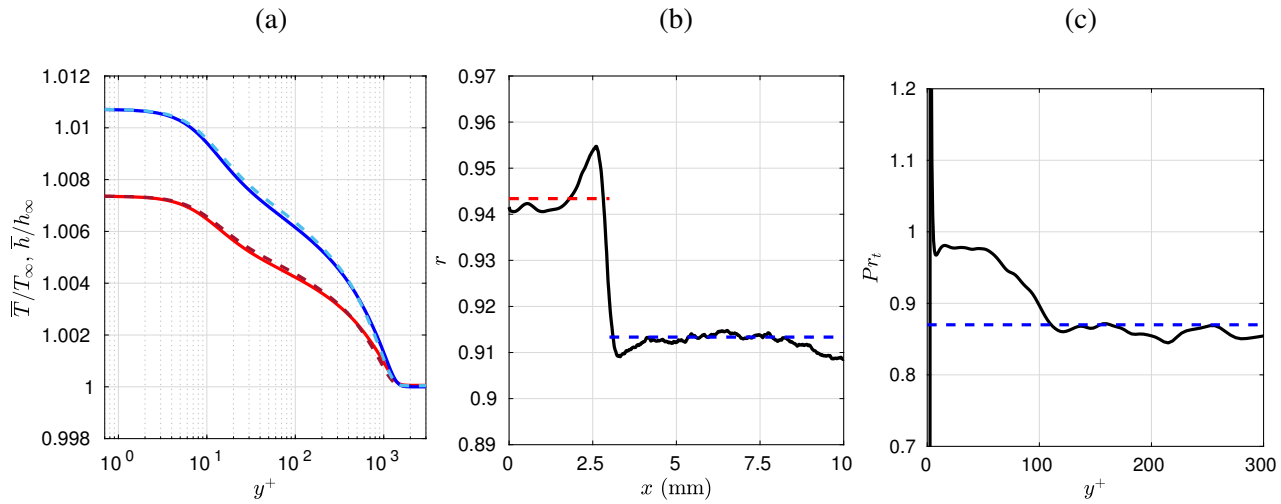

Figure 3.18: (a) Crocco's laws compared to mean profiles at Re_θ=4060: $\overline{h}/h_\infty$ (DNS ——; Eq.(3.1) - - -) and $\overline{T}/T_\infty$ (DNS ——; Eq.(3.2) - - -); (b) Recovery factor (3.3) from DNS (——) and approximate correlations for laminar ($\sqrt{Pr}$, - - -) and turbulent states (Eq.(3.4), - - -); (c) Turbulent Prandtl number from DNS (——) and Pr_t=0.87 (- - -).

where Pr_t is the turbulent Prandtl number, yields r_{turb}=0.913 for $Pr_t = 0.87$, represented by the dashed blue line in figure 3.18b, in very good agreement with the DNS value. The turbulent Prandtl number can be estimated directly from the DNS as

$$Pr_t \approx \frac{\overline{\rho u' v'}}{\partial \overline{u}/\partial y} \times \frac{\partial \overline{h}/\partial y}{\overline{\rho v' h'}}$$

and is plotted in figure 3.18(c). The value of 0.87 (dashed blue line) found in the region $100 < y^+ < 300$ is in fair agreement with the value used in Eq.(3.4). Values closer to one are found near the wall, where a singularity is observed at $y = 0$ due to the vanishing thermal fluctuations at the wall. Note that the smaller value obtained for the turbulent recovery factor with respect to the laminar one is the opposite to what is observed for air. This is simply due to the greater value of Pr (0.89 in Novec649 and 0.71 in air), which strongly depends on the operating conditions for a dense gas (see table 3.1). Furthermore, the definition of the recovery factor is sometimes given as $r = (T_{aw} - T_\infty)/(T_{0,\infty} - T_\infty)$, $T_{0,\infty}$ being the stagnation temperature in the freestream. This definition is only valid for an ideal gas, for which $T_0 = T_\infty[1 + (\gamma - 1)M_\infty^2/2]$. For a real gas, the stagnation temperature can be calculated with the Newton–Raphson algorithm based on the conservation of total enthalpy and entropy. We obtain $T_{0,\infty}$=378.96 K in the freestream, which would yield $r_{\text{lam}} \approx 0.484$ and $r_{\text{turb}} \approx 0.474$, far from the expected values.

Compressibility effects are further highlighted in figure 3.19. In panel a, profiles of the fluctuating Mach number, $M_{rms} = (\overline{u_i'^2/c^2})^{1/2}$, and of the turbulent Mach number, $M_t = (\overline{u_i'^2})^{1/2}/\overline{c}$, are plotted for successive

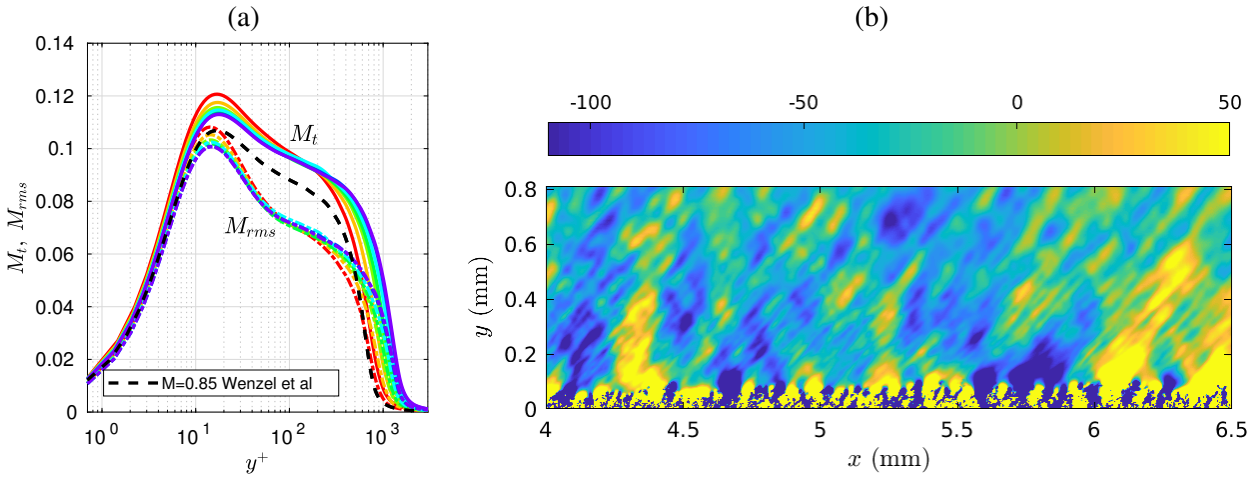

Figure 3.19: (a) Profiles of fluctuating (M_{rms}) and turbulent (M_t) Mach numbers at Re_θ=2000, 2540, 3030, 3270, 3630, 3970, 4060 (solid lines from red to blue) compared to M_t from Wenzel *et al.* [229] in air at M=0.85, Re_τ=671 (– – –); (b) snapshot of fluctuating pressure field in the median plane (levels ±80 Pa).

streamwise locations. These quantities constitute a good measure of the turbulent compressibility effects. Morkovin [237] suggested that turbulence is only weakly affected by compressibility if $M_{rms} < 0.2$. For the current subsonic Mach number (M=0.9), the maximum values are M_{rms}=0.11 and M_t=0.12, meaning that a weak influence of compressibility on velocity statistics is expected. Nevertheless, it is worth noting that the turbulent Mach number obtained for the dense gas is of the same order of magnitude as in air. The profile of Wenzel *et al.* [229] obtained in air at M=0.85 and for a smaller Reynolds number shows lower values than the ones encountered in Novec649 at the highest Reynolds number, suggesting that the fluctuations in Mach number are even greater for Novec649. Such a result was also obtained by Sciacovelli *et al.* [30] and Chen *et al.* [32] for turbulent channel flows of PP11. The levels of dilatation fluctuations can be inferred by the acoustic field radiated by the turbulent boundary layer, which can be directly obtained in our DNS (figure 3.19b). The maximum amplitude of pressure waves is of the order of 100 Pa, which of the same order or even greater than the values obtained in a direct computation of turbulent boundary layer noise in air by Gloerfelt & Margnat [238]. Interestingly, the wave fronts in air and Novec649 are very similar, dominated by Doppler effects due to the high subsonic Mach number. Even if temperature fluctuations are absorbed by the internal degrees of freedom of the complex molecules (or equivalently due to the high heat capacity of the gas), genuine compressibility effects are thus present in the dense-gas flow.

3.4 LES study of the transition influence on the turbulent boundary layer

In this section, the influence of the laminar-to-turbulent transition on the fully turbulent state is investigated by varying the excitation characteristics (amplitude and frequency of the oblique modes). Some studies (for example [239, 240, 241, 242]) have shown that an equilibrium turbulent boundary layer is reached only for sufficiently large Reynolds numbers. The low-speed experiments of Erm & Joubert [239] using different tripping devices showed that the evolutions of some integral quantities, such as shape factor, skin friction or wake parameter, become independent of excitation for $Re_\theta > 2175$. A similar study conducted numerically by Schlatter & Örlü [241] concluded that turbulent profiles and integral quantities agree well for both inner and outer layer for $Re_\theta > 2000$. These authors showed that when the numerical tripping is realized at a high Reynolds number, a long transient is neccessary before the fully turbulent state is reached. Marusic *et al* [242] found in their experiments that the effects of the trip can be significant, with non-equilibrium effects persisting up to $Re_\theta > 10000$ for over-stimulated conditions. Castillo & Johansson [240] even questioned whether an asymptotic state exists for statistics such as wall-normal stresses. Another important conclusion from previous studies is that the recovery length required for the statistics to become independent of the inlet conditions is not dependent on the order of the statistic, and mean flow quantities, such as ratios of boundary layer thicknesses and friction coefficient, are good indicators to ascertain whether a canonical boundary layer is reached. Given the relatively large Reynolds number necessary to trigger unstable oblique modes in Novec649, we investigated memory loss of inlet conditions and whether a canonical turbulent state is obtained.

3.4.1 LES setup

Large-eddy simulations (LES) are performed to assess the influence of the excitation parameters on the turbulent state. Significant gains in computational cost can be achieved by relaxing the space and time discretisations, which will also be useful for the following chapters of this thesis. A grid of $3000 \times 360 \times 660$ points is designed by doubling the streamwise spacing and reducing by one third the streamwise extent of the computational domain. The new resolution in wall units is Δx^+=29-27, Δz^+=11-10, Δy^+_w=0.798-0.9 and Δy^+_e=12-17 at the wall and at the boundary-layer edge, respectively. The effect of subgrid-scale motions is taken into account implicitly through the explicit filter (used as part of the numerical discretization) that removes subfilter scales and provides a selective regularization. This implicit modeling strategy has been shown to be effective [15] and avoids the computational overhead introduced by the explicit subgrid-scale models. LES

case (line style)	$\frac{\omega_0 L^*}{U_\infty}$	Re_{0,L^*}	ε_0/U_∞ $\times 10^{-3}$	$\beta_0 L^*$	CFL	N_x	N_y	N_z	L_x	L_y	L_z mm (λ_z)
DNS (——)	0.02	1000	1	0.037	1	9000	400	1000	10.8	0.92	0.59 (1)
LES-expl (– – –)	0.02	1000	1	0.037	1	3000	360	660	7.29	0.71	0.59 (1)
LES-IRS (– · – ·)	0.02	1000	1	0.037	4	3000	360	660	7.29	0.71	0.59 (1)
LES-LA (——)	0.02	1000	0.1	0.037	4	3000	360	660	7.29	0.71	0.59 (1)
LES-HA (– – –)	0.02	1000	5	0.037	4	3000	360	660	7.29	0.71	0.59 (1)
LES-MF (——)	0.024	400	1	0.040	4	3000	360	500	7.29	0.71	0.44 (2)
LES-HF (– – –)	0.04	400	1	0.060	4	3000	360	660	7.29	0.71	0.58 (4)

Table 3.4: Summary of simulations: excitation parameters with subscript 0, timestep and computational domain (box lengths L_x, L_y and L_z in mm).

simulations with higher and lower levels of filtering amplitude (not shown for brevity) have been performed to check if the filtering procedure does change the results. A first LES is conducted in the same condition as the DNS with a maximum CFL number of 1, which is close to the stability limit of the explicit four-step low-storage Runge-Kutta in use (hereafter referred to as LES-expl). The maximum allowable time step is thus dictated by the first cell height above the wall and is very small compared to the physical constraints to resolve in time the evolution of smallest scales. The use of an implicit integration scheme may overcome this limitation at the price of an increased computational cost per step and/or the introduction of numerical errors. The use of a fourth-order implicit residual smoothing scheme (IRS4) has been shown to be a good compromise introducing weak dispersion errors for moderate CFL numbers and a small overcost [17, 116]. A second LES (LES-IRS) is then performed by applying IRS4 in the wall-normal direction only. The overcost is due essentially to the parallel resolution of a pentadiagonal system with variable coefficients at each Runge–Kutta step, and is found to be approximately 15% for our code. A maximum CFL of 4 is used, resulting in computation time reduction by a factor 3.5. Our LES strategy is first validated against DNS results in section 3.4.2. The reduced-cost LES setup is then used to explore the effects of the excitation parameters on the laminar-turbulent transition and on the equilibrium character of the turbulent state. A summary of the various simulations is given in table 3.4. Note that the transverse sizes expressed in terms of the boundary layer thickness at the end of the computational domain are L_y=8.2δ_{end} and L_z=5.2δ_{end} for the DNS, and L_y=9.3δ_{end} and L_z=7.7δ_{end} for the LES, meaning that the boundary layer is not confined [243].

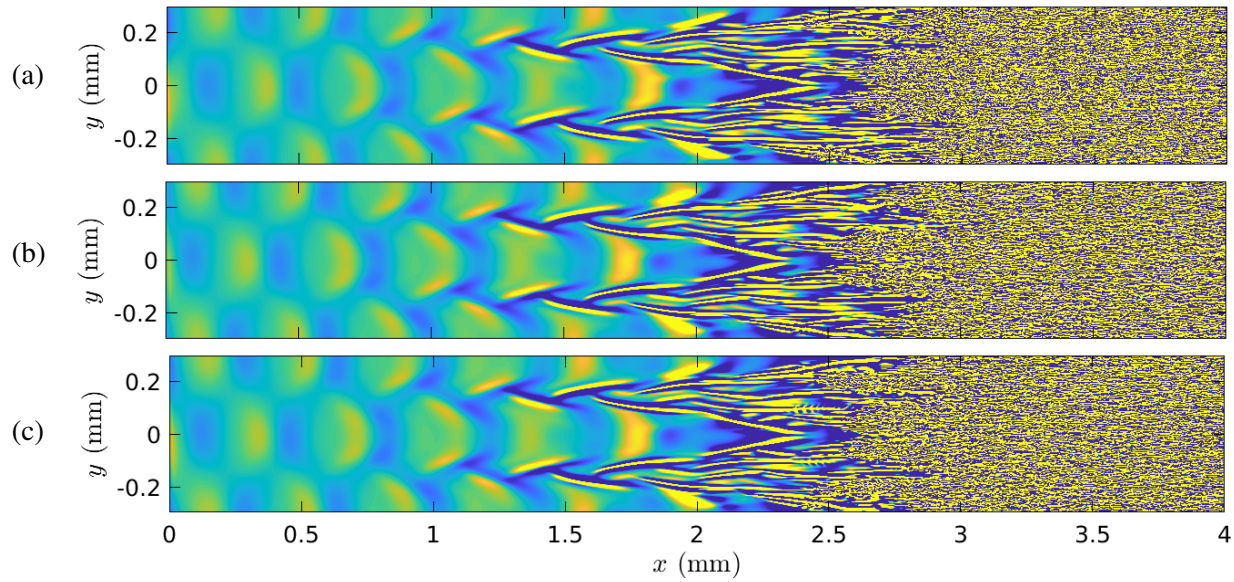

Figure 3.20: Snapshots of the wall-normal velocity fluctuations at $y^+ \approx 15$: DNS (a), LES-expl (b), LES-IRS (c) excited at $\omega L^*/U_\infty$=0.02, Re_{L^*}=1000, ε_0/U_∞=10^{-3}. Levels ±0.05 m/s.

3.4.2 Validation of LES resolution and implicit time-advancement

The case LES-expl, realized with the same setup as the DNS except for the grid, illustrates the influence of the grid on the solution quality. LES-IRS uses the same numerical parameters except for the time-step, which is multiplied by 4. The global cost saving with respect to DNS is more than a factor 20 for LES-IRS. A first qualitative comparison is provided in figure 3.20, where instantaneous top views of the wall-normal velocity fluctuations are plotted in the transition region. At first glance, the patterns are similar, confirming the ability of LES-expl and LES-IRS to reproduce the transition location and the flow structures observed in the DNS. The low-speed streaks have a sinuous evolution with several wavelength doublings, leading to the generation of high-frequency disturbances that break down into turbulence.

The C_f distributions for the LES calculations in figure 3.21(a) are in very good agreement with the DNS. In particular, the location of the transition is well reproduced and a turbulent state is reached with Re_θ=3270 at the end of the computational domain (since the longitudinal extent has been reduced in LES setup). The ratios of the boundary layer thicknesses (δ) over the displacement (δ^*) and momentum (θ) thicknesses, in figure 3.21(b), are good indicators of the equilibrium character [241]. These ratios match the ones from DNS only at the end of the LES domain and substantial variations are seen in the early turbulent state ($1500 < Re_\theta < 2000$), more pronounced for LES-expl than LES-IRS. The shape factors H, in figure 3.21(c), confirm that equilibrium

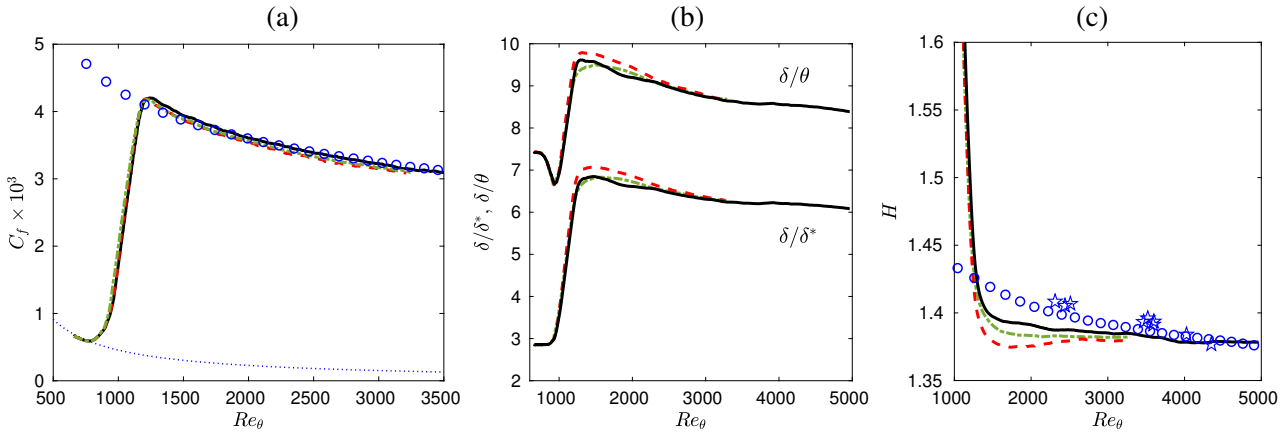

Figure 3.21: Skin friction coefficient (a), ratios of boundary layer thicknesses (b) and shape factor (c): DNS (——); LES-expl (– – –); LES-IRS (– · – · –); DNS (○) and experiments (★) of Schlatter & Örlü [227].

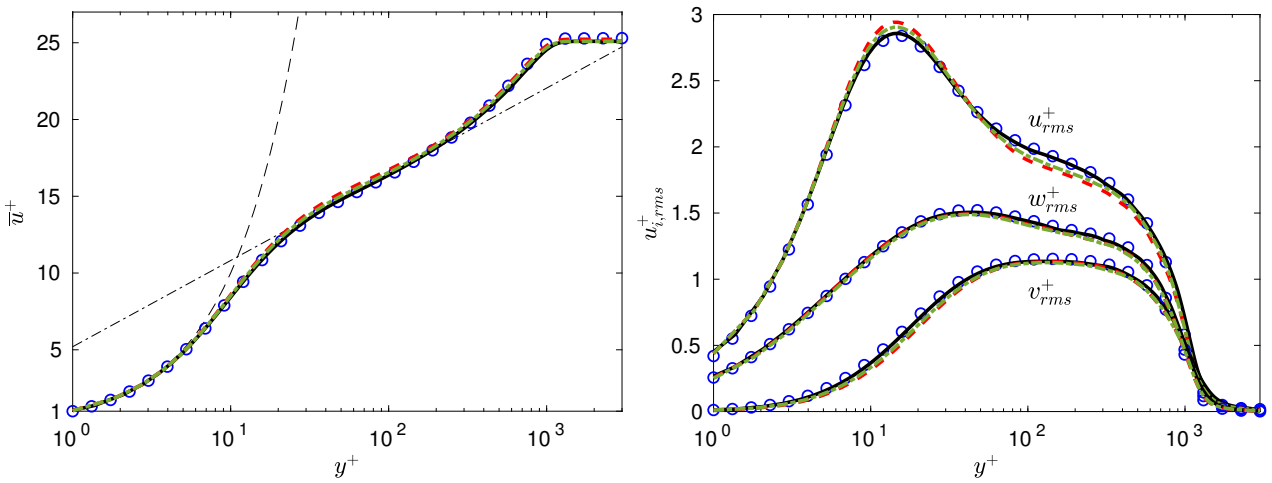

Figure 3.22: Mean streamwise velocity and turbulent intensity profiles at Re_θ=3270: DNS (——); LES-expl (– – –); LES-IRS (– · – · –); DNS of Schlatter & Örlü [227] (○).

is reached for $Re_\theta \approx 3000$. Downstream, the agreement of dense-gas results with incompressible DNS and experiments of Schlatter & Örlü [241] is good. The mean streamwise velocity and turbulent intensity profiles at this Reynolds number are compared in figure 3.22. A good agreement with the present DNS and the incompressible data is observed, with a slight underestimation of turbulent intensities, which is common with LES resolution. Once again, the profiles for LES-expl and LES-IRS are almost matching, validating the use of the implicit time advancement.

A more sensitive quantity is the fluctuating vorticity, reported in figure 3.23, where the three components normalized by ν/u_τ^2 are plotted for DNS and LES cases. For the x-component, a local minimum is observed

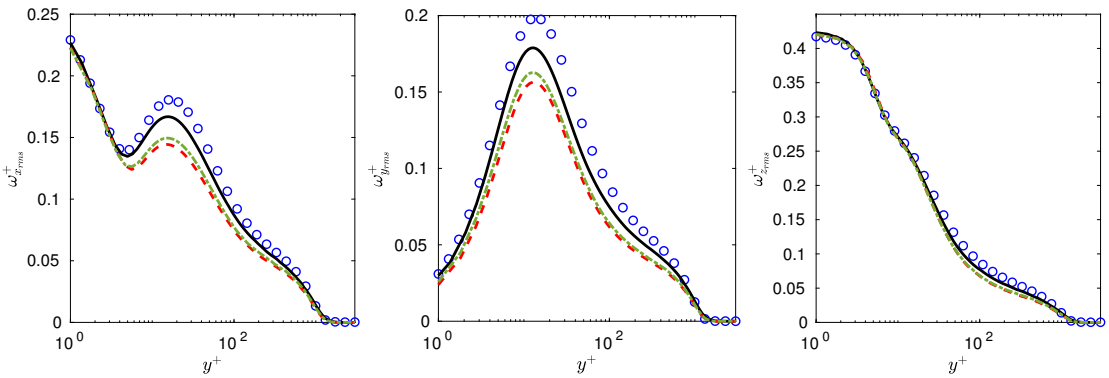

Figure 3.23: R.m.s. of vorticity fluctuation components for x-, y- and z-directions: DNS (——); LES-expl (– – –); LES-IRS (– · – · –); DNS of Schlatter & Örlü [227] (○).

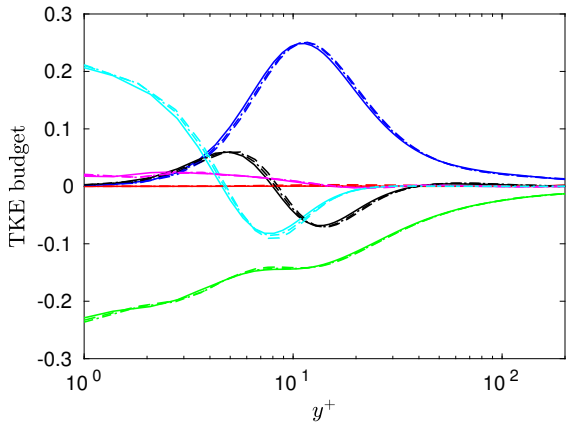

Figure 3.24: Turbulent kinetic energy budget at Re_θ=3270 for DNS (——), LES-expl (– – –) and LES-IRS (– · – · –). The same color legend as figure 3.12 is used.

at $y^+ \approx 5$ followed by local maximum at $y^+ \approx 15$, which can be attributed to near-wall streamwise vortices [244]. The peak levels are lower for the LES and the local minimum is closer to 5.5. The underestimation of fluctuating vorticity magnitude is also visible on the y-component, due to the unresolved small scales. However, for the more intense component $\omega^+_{z,rms}$ the discrepances are negligibly small. Finally, only slight discrepancies are noted for the TKE budget in figure 3.24, meaning that high-order statistics from LES at the end of the computational domain agrees well with DNS results.

To investigate in more detail the influence of spatial and temporal resolutions, spanwise and temporal premultiplied spectra of the streamwise velocity fluctuations at Re_θ=3270 are reported in figure 3.25. As expected, the premultiplied spanwise spectra exhibit an earlier cut-off for the two LES, due to coarser spanwise resolution. Interestingly, we observe a better resolution of LES-IRS with respect to LES-expl at the small

scales. This is a consequence of the lower numerical dissipation introduced in LES-IRS, because high-order filtering is applied less frequently over the integration interval, due to the larger time step. Similar results are obtained for the temporal spectra. The sizes of the main turbulent scales (indicated by vertical gray lines) are well reproduced. The fact that an earlier cutoff also appears in the temporal spectra means that the LES cut-off is governed by streamwise resolution and not by time resolution. Even for LES-IRS, with a time step multiplied by 4, the streamwise resolution remains the limiting one. The smoother slope of the spectral roll-off at high frequencies for LES-IRS with respect to LES-expl can be explained by the dispersion properties of the IRS operator (see section 2.4). The good agreement with the DNS gives good confidence in the LES strategy based on regularization filtering, and further validates the use of the IRS4 implicit treatment.

Finally, two supplementary LES are performed using the same numerical set-up as LES-IRS, to validate choices made in section 2. In the first one, namely LES-IRS-inc, the filtering is applied and added to increments before residual smoothing, a strategy which has been shown to affect scheme stability by significantly reducing dissipation for high frequencies at $CFL \geq 10$ in section 2.4.3. The second one (LES-IRS4-visc) is performed by integrating the viscous terms at each RK substep, to assess the choice to integrate the viscous terms in the last RK substep as presented in section 2.4.5. The temporal spectra for the two supplementary LES (LES-IRS-inc and LES-IRS-visc) are compared with LES-IRS in Fig.3.25 (right). Symbols have been added but the spectra are almost undistinguishable. This validates two issues: (i) filtering before or after the smoothing operation has no impact on the results but only on the stability, where filtering after smoothing is preferable to avoid that the contractive effect of IRS suppresses the necessary numerical dissipation; (ii) integrating viscous terms at the last RK step does not change the results (at least for problems not fully dominated by viscous effects) and allows a substantial reduction of computing time.

3.4.3 Influence of the forcing amplitude

We have seen in section 3.2 for the 2D simulations of the TS mode that the computed growth rate starts to deviate from the LST result for $\varepsilon_0 = 5 \times 10^{-4} U_\infty$. Since the nominal value has been set to 10^{-3}, two LES simulations with a lower amplitude ($\varepsilon_0 = 10^{-4} U_\infty$) and a higher amplitude ($\varepsilon_0 = 5 \times 10^{-3} U_\infty$) are carried out, hereafter referred to as LES-LA and LES-HA, respectively. All other numerical parameters are the same as LES-IRS. The transition pattern is illustrated by instantaneous top views of the wall-normal velocity fluctuations in figure 3.26. The transition is delayed by reducing the amplitude and occurs at x=6 mm (domain length is 7.3 mm). On the contrary, the forcing amplitude multiplied by 5 induces an earlier transition and the most

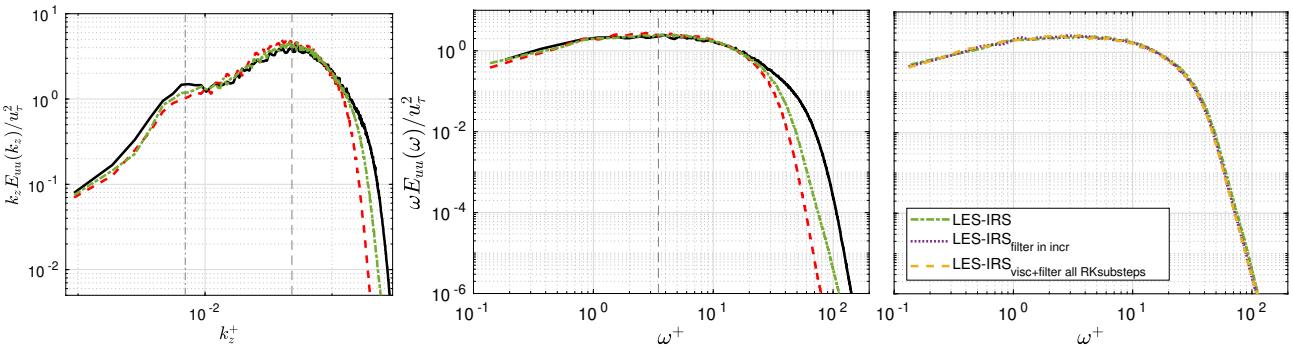

Figure 3.25: Premultiplied spanwise (left) and temporal (middle,right) spectra of the streamwise velocity fluctuations for the turbulent boundary layer at Re_θ=3270 at y^+=15: DNS (——); LES-expl (– – –); LES-IRS (– · – · –).

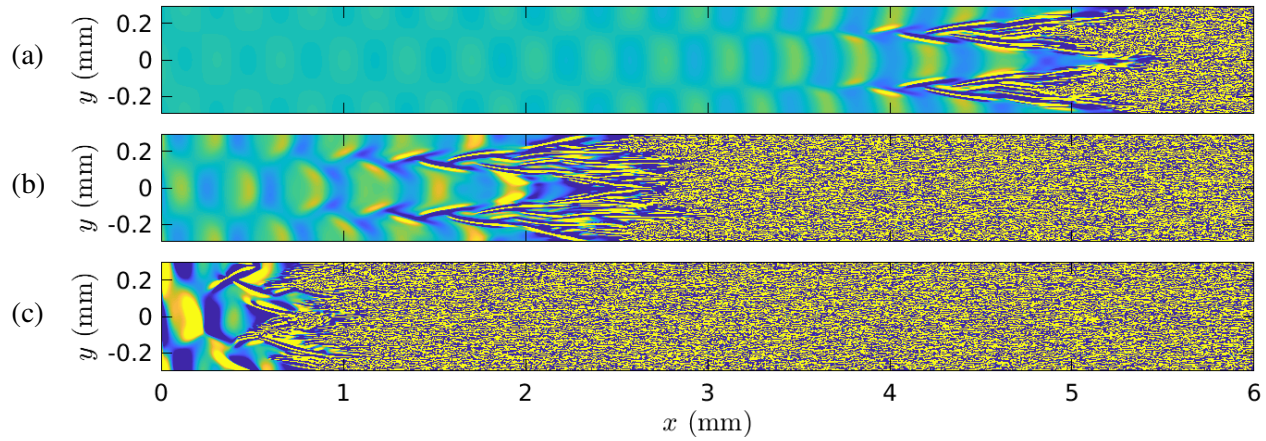

Figure 3.26: Snapshots of the wall-normal velocity fluctuations at $y^+ \approx 15$ for $\omega_0 L^*/U_\infty$=0.02 and Re_{0,L^*}=1000: LES-LA (a) with $\varepsilon_0 = 10^{-4}U_\infty$, LES-IRS (b) with $\varepsilon_0 = 10^{-3}U_\infty$, LES-HA (c) with $\varepsilon_0 = 5 \times 10^{-3}U_\infty$. Levels ± 0.05 m/s.

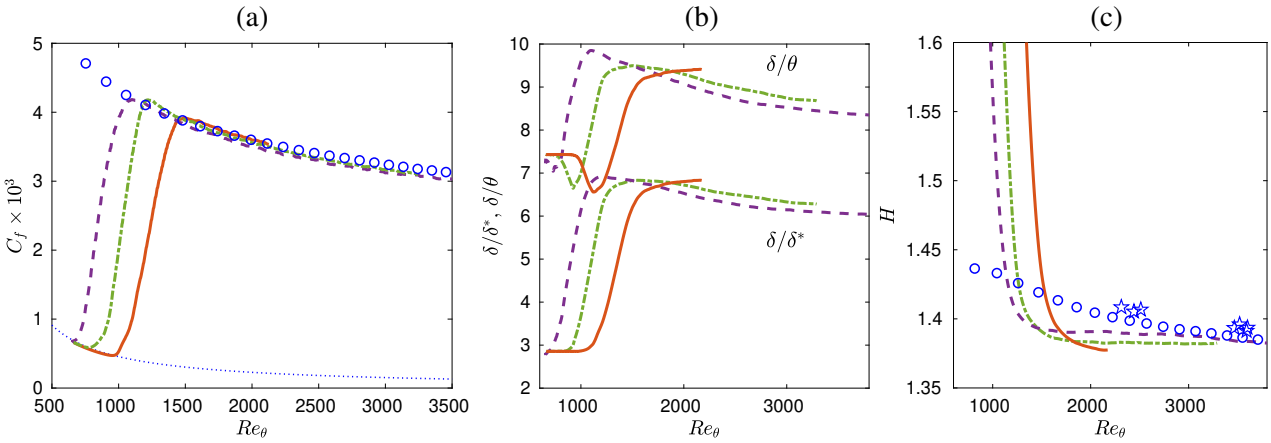

Figure 3.27: Skin friction coefficient (a), ratios of boundary layer thicknesses (b) and shape factor (c) for $\omega_0 L^*/U_\infty = 0.02$, $Re_{0,L^*} = 1000$: LES-LA $\varepsilon_0 = 10^{-4}U_\infty$ (——); LES-IRS $\varepsilon_0 = 10^{-3}U_\infty$ (– · – ·); LES-HA $\varepsilon_0 = 5 \times 10^{-3}U_\infty$ (– – –); DNS (○) and experiments (★) of Schlatter & Örlü [227].

striking feature is the distorted wave pattern, indicating that nonlinear effects arise in the early development stage (which was also the case in 2D, see figure 3.5). The sudden turbulent breakdown appears before the formation of well-defined streaks.

The faster transition with increasing forcing amplitude is also observed in figure 3.27. The reference turbulent state for the friction coefficient in panel a, represented here by the incompressible DNS of Schlatter & Örlü [227], is reached with no overshoot for all cases. The value of friction at the end of the computational domain is slightly higher as the forcing intensity diminishes. The ratios of boundary layer thicknesses and the shape factor in panels b and c indicate that the equilibrium is hardly achieved for $Re_\theta < 3000$. The maximum Reynolds number is approximately 2000 using the lowest amplitude. These results indicate that the discrepancies are not due to non linear generation of vortical structures due to high-amplitude forcing but to the long recovery length required to lose memory of transitional structures.

To get further insights on the slight discrepancies for the mean skin friction, we use a decomposition into physical phenomena. Several decompositions have been proposed in the literature. The first one is the Fukagata-Iwamoto-Kasagi (FIK) identity [245], based on a threefold repeated integration of the streamwise momentum equation, extended to compressible wall-bounded flows by Gomez, Flutet & Sagaut [246]. Renard & Deck [247] (RD) underlined some pitfalls about the interpretation of FIK for spatially developing boundary layer and proposed another decomposition based on the mean streamwise kinetic-energy equation in an absolute reference frame. The RD identity was generalized for compressible channel flows by Li *et al.* [248] and extended to compressible boundary layers by Fan, Li & Pirozzoli [249]. Zhang & Xia [250] and Wenzel, Gibis

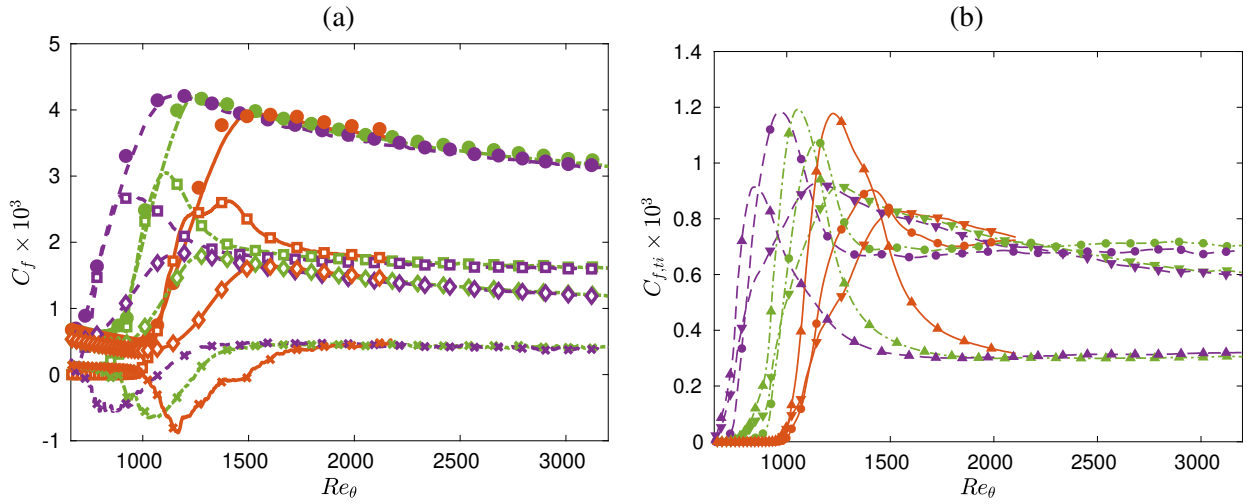

Figure 3.28: Skin friction decomposition for LES-LA (——), LES-IRS (– · – ·) and LES-HA (– – –). (a) RD decomposition: direct C_f evaluation (lines); sum of the three contributions (bullets); $C_{f,v}$ (lines with open diamond symbols); $C_{f,t}$ (lines with open square symbols); $C_{f,x}$ (lines with cross symbols). (b) decomposition of $C_{f,t}$ in three layers: inner layer (lines with downward triangles); log layer (lines with bullets); outer layer (lines with upward triangles).

& Kloker [251] noticed that the FIK identity based on a twofold integration can overcome the limitations of the original FIK decomposition and has the advantage of being applicable to the heat-transfer decomposition (see also [252]). Both RD and twofold-integrated FIK have been applied to the present dataset but only the RD decomposition is presented here for brevity. Assuming a no-slip wall, homogeneity in the spanwise direction and no body force, the RD identity writes

$$C_f = \underbrace{\frac{2}{\rho_\infty U_\infty^3}\int_0^\delta \overline{\tau}_{xy}\frac{\partial \tilde{u}}{\partial y}\mathrm{d}y}_{C_{f,v}} + \underbrace{\frac{2}{\rho_\infty U_\infty^3}\int_0^\delta -\overline{\rho u'' v''}\frac{\partial \tilde{u}}{\partial y}\mathrm{d}y}_{C_{f,t}} + \underbrace{\frac{2}{\rho_\infty U_\infty^3}\int_0^\delta (\tilde{u}-U_\infty)\left[\overline{\rho}\left(\tilde{u}\frac{\partial \tilde{u}}{\partial x}+\tilde{v}\frac{\partial \tilde{u}}{\partial y}\right)-\frac{\partial}{\partial x}\left(\overline{\tau}_{xx}-\overline{\rho}\widetilde{u''u''}-\overline{p}\right)\right]\mathrm{d}y}_{C_{f,x}} \tag{3.5}$$

Note that we choose δ for the upper integration limit [247, 249, 252]. $C_{f,v}$ and $C_{f,t}$ represent the contributions of the mean-field dissipation and the dissipation due to the Reynolds stresses, respectively, whereas $C_{f,x}$ accounts for the boundary layer spatial growth and includes the effects of streamwise heterogeneity. Figure 3.28(a) shows that the sum of the terms (bullets) reproduces fairly well the mean friction computed directly for all simulations. In the turbulent region, the dominant contribution is the turbulent term $C_{f,t}$ (from 48% at Re_θ=2000 to 51% at Re_θ=3200), followed by the viscous component $C_{f,v}$ (from 41% at Re_θ=2000 to 38% at Re_θ=3200) in fair

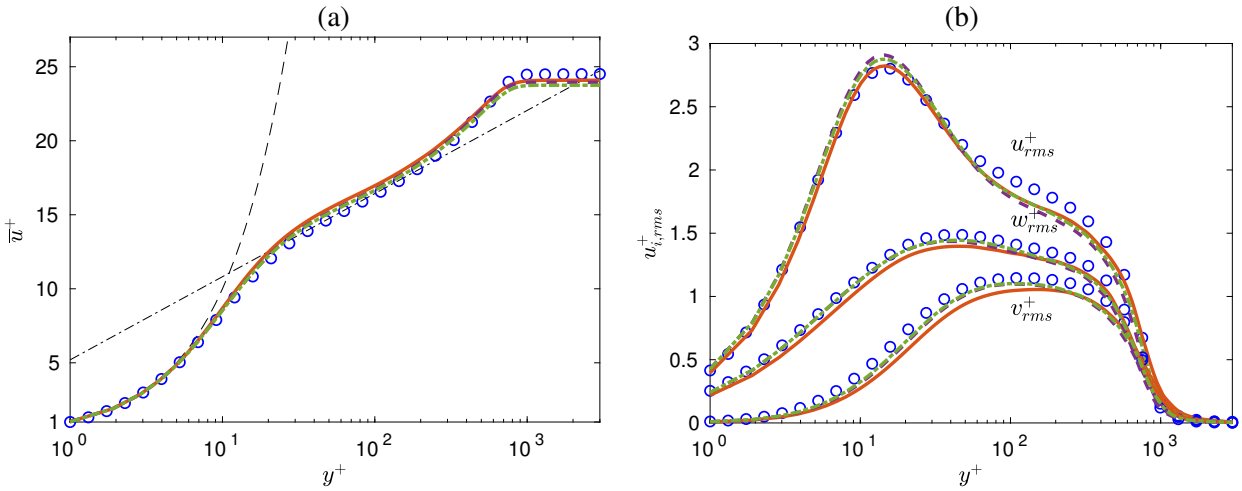

Figure 3.29: Mean streamwise velocity and turbulent intensity profiles at Re_θ=2000: LES-LA $\varepsilon_0 = 10^{-4}U_\infty$ (——); LES-IRS $\varepsilon_0 = 10^{-3}U_\infty$ (– · – ·); LES-HA $\varepsilon_0 = 5\times10^{-3}U_\infty$ (– – –); DNS of Schlatter & Örlü [227] (○).

agreement with results obtained for incompressible or supersonic boundary layers in air [249]. The overshoot of $C_{f,t}$ during transition is compensated by the growth term $C_{f,x}$. A good collapse of each contributions for the various forcing amplitudes is obtained for $Re_\theta \gtrapprox 2000$. A further decomposition of the main term, $C_{f,t}$, into three subregions is shown in figure 3.28(b): inner layer ($0 < y^+ < 30$), log layer (between $y^+ = 30$ and $y = 0.3\delta$) and outer layer ($0.3\delta < y < \delta$), as in Fan, Li & Pirozzoli [249]. The slight discrepancies observed for mean skin friction are mostly visible for the inner and log layers. The outer layer contributions require a longer length to stabilize on an almost constant plateau and indicates that the lowest amplitude case, LES-LA, is still transitional. An increasing (respectively decreasing) trend for the log (respectively inner) layer is observed, with a crossing at $Re_\theta \approx 2200$, corresponding to $Re_\tau \approx 840$. This can be interpreted by the generation of large scales at high Reynolds numbers and is in fair agreement with the results in Fan, Li & Pirozzoli [249], who found a crossing at $Re_\tau \approx 650$ for an incompressible boundary layer and at $Re_\tau \approx 780$ for a supersonic boundary layer at M=2.

Finally, the mean streamwise velocity and turbulent intensities profiles are reported in figure 3.29 at $Re_\theta = 2000$, which is close to the maximum Reynolds number reached by LES-LA. The deviations that are observed are associated to the fact that a canonical turbulent state is not yet reached.

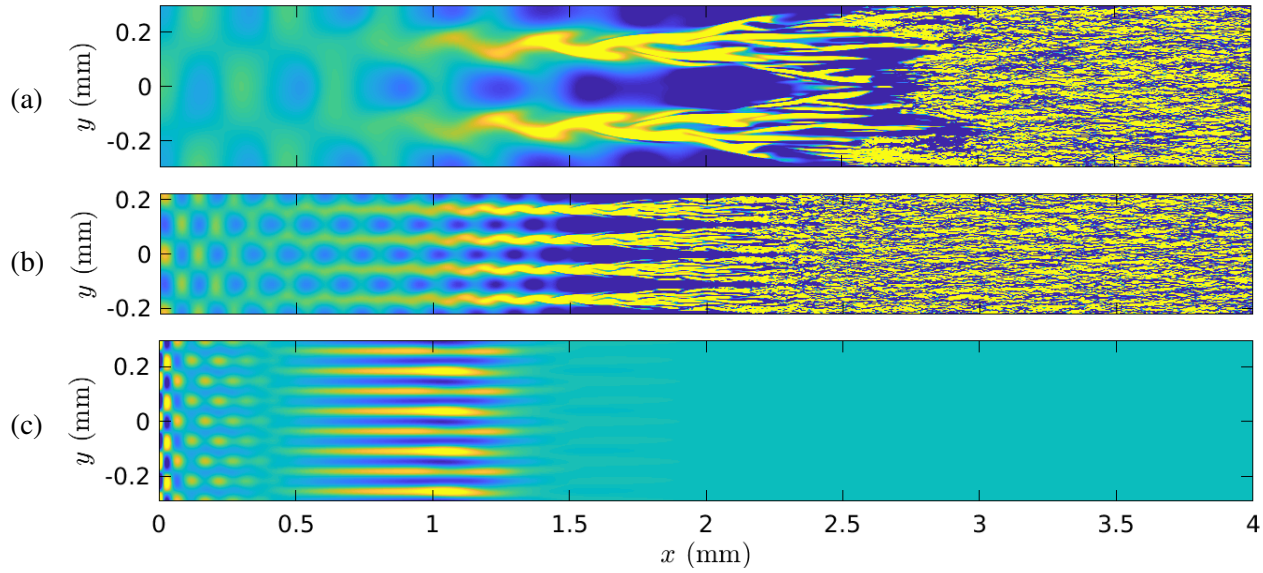

Figure 3.30: Snapshots of the streamwise velocity fluctuations at $y^+ \approx 15$: LES-IRS (a) excited at $\omega_0 L^*/U_\infty$=0.02, Re_{0,L^*}=1000, LES-MF (b) excited at $\omega_0 L^*/U_\infty$=0.024, Re_{0,L^*}=400, LES-HF (c) excited at $\omega_0 L^*/U_\infty$=0.04, Re_{0,L^*}=400. Levels between ±3 m/s (except panel c ±0.3 m/s).

3.4.4 Influence of the forcing frequency

The study on the influence of numerical tripping by Schlatter & Örlü [241] revealed that the recovery length increases if the excitation is introduced at a high Reynolds number (Re_θ=1500). In the computed cases, the inlet Reynolds number is Re_{0,L^*}=1000, corresponding to $Re_\theta \approx 700$. In order to decrease the initial Reynolds number, the excitation frequency must be increased. Two additional LES are carried out with Re_{0,L^*}=400: mid-frequency case (LES-MF) at $\omega_0 L^*/U_\infty$=0.024 (blue path in figure 3.3) and high-frequency case (LES-HF) at $\omega_0 L^*/U_\infty$=0.04 (magenta path in figure 3.3). Instantaneous top views of the streamwise velocity fluctuations in the transition region are shown in figure 3.30. Note that the spanwise width of the domain has changed to include an integer number of wavelengths (see table 3.4). For the case LES-MF (panel b), the low-speed streaks evolve on a longer distance (relative to the disturbance wavelength) and transition due to a streak secondary instability, so that strips of turbulence are generated and eventually merge. The earlier onset of turbulence with respect to LES-IRS can be interpreted by the presence of smaller structures (due to the higher frequency excitation) that gives rise more rapidly to the high-frequency breakdown. When the angular frequency is doubled to 0.04 (panel c), the oblique waves are weakly unstable and the breakdown to turbulence is not observed in the computational box. Very weak streaks (color levels are divided by 10) can be observed due to the nonlinear generation of a streamwise vortex by the two oblique waves. Since the extent of the unstable region is reduced

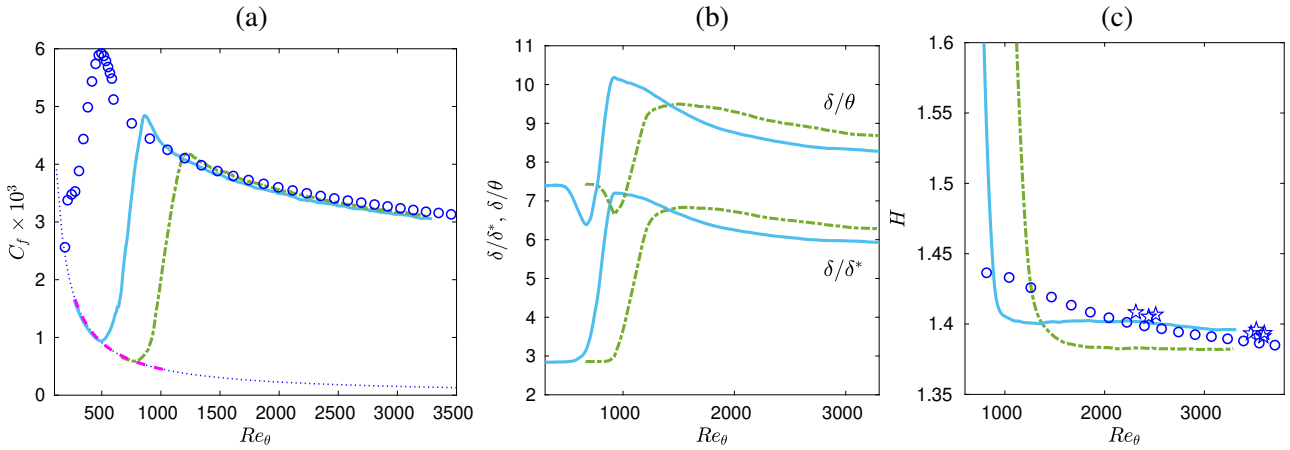

Figure 3.31: Skin friction coefficient (a), ratios of boundary layer thicknesses (b) and shape factor (c): LES-IRS $\omega_0 L^*/U_\infty = 0.02$, $Re_{0,L^*} = 1000$ (- · - ·); LES-MF $\omega_0 L^*/U_\infty = 0.024$, $Re_{0,L^*} = 400$ (——); LES-HF $\omega_0 L^*/U_\infty = 0.04$, $Re_{0,L^*} = 400$ (- - -); DNS (○) and experiments (★) of Schlatter & Örlü [227].

with respect to air at high frequencies (see figure 3.3), it is possible that an air flow excited at the same frequency may transition.

The mean skin friction and ratios of boundary layer thicknesses are reported in figure 3.31. For LES-HF, the friction coefficient (panel a) is matching with the laminar correlation. The earlier transition for LES-MF comes with a small overshoot. The value in the turbulent region is close to the nominal case LES-IRS, with a small underestimation. The ratios δ/δ^* and δ/θ stabilize on a lower value for LES-MF (panel b) and the shape factor is higher (panel c). The latter reaches more rapidly an equilibrium state in better agreement with incompressible data. The skin friction is decomposed using RD identity in figure 3.32(a) and the dominant term $C_{f,t}$ is integrated over three wall-normal layers in figure 3.32(b). The slight underestimation for the higher forcing frequency is mostly associated with the viscous contribution $C_{f,v}$ at the wall. The small differences appearing when the turbulent term $C_{f,t}$ is decomposed in layers are compensated between the innner/log layers and the outer layer. The pseudo-equilibrium is clearly achieved earlier for LES-MF case. The presence of an overshoot for LES-MF can be related to more intense transitional structures that persist in the turbulent region.

Finally, Figure 3.33 shows that the mean velocity and turbulent intensity profiles close to the end of the domain are almost superimposed for all cases, showing that the non-equilibrium effects due to the laminar-turbulent transition affect these quantities weakly.

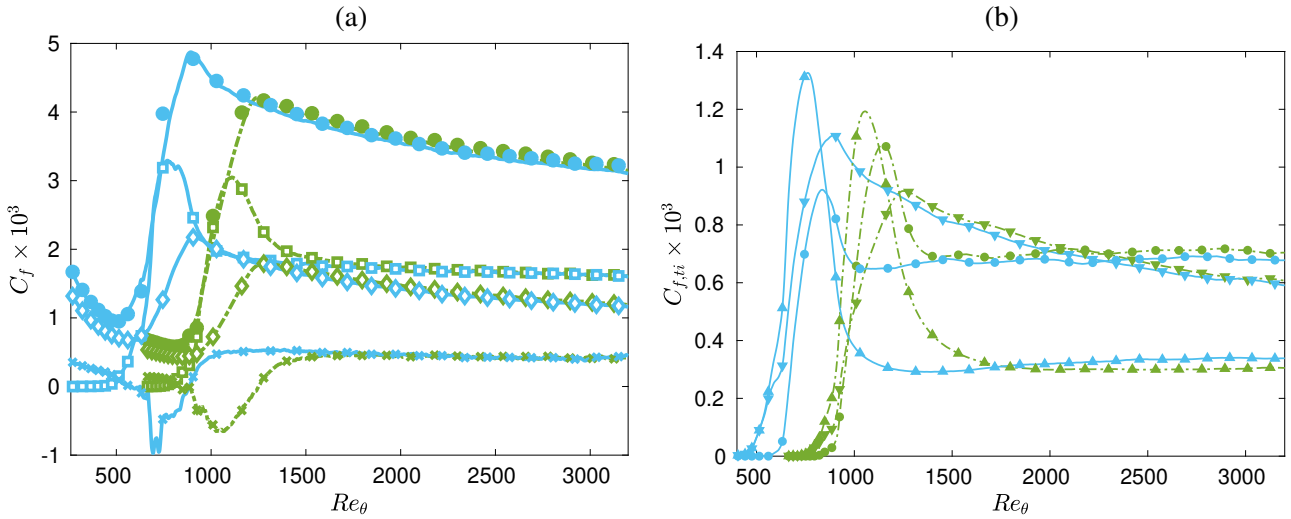

Figure 3.32: Skin friction decomposition for LES-IRS (- - -) and LES-MF (——). (a) RD decomposition: direct C_f evaluation (lines); sum of the three contributions (bullets); $C_{f,v}$ (lines with open diamond symbols); $C_{f,t}$ (lines with open square symbols); $C_{f,x}$ (lines with crosses). (b) decomposition of $C_{f,t}$ in three layers: inner layer (lines with downward triangles); log layer (lines with bullets); outer layer (lines with upward triangles).

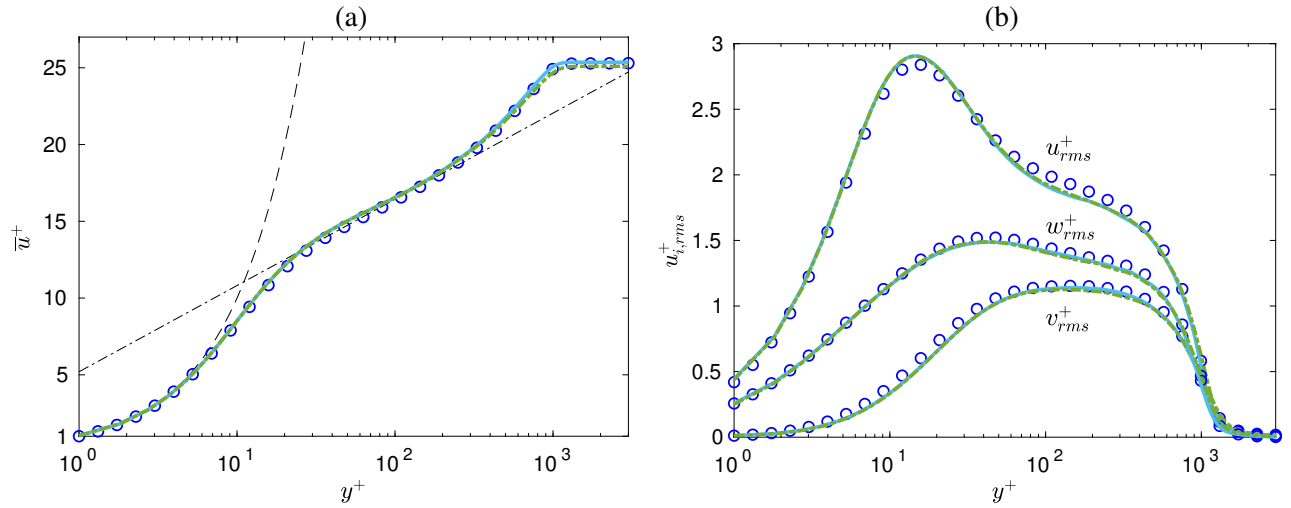

Figure 3.33: Mean streamwise velocity and turbulent intensity profiles at Re_θ=3270: LES-IRS $\omega_0 L^*/U_\infty$ = 0.02, Re_{0,L^*} = 1000 (- - -); LES-MF $\omega_0 L^*/U_\infty$ = 0.024, Re_{0,L^*} = 400 (——); DNS of Schlatter & Örlü [227] (○).

Chapter Summary

Laminar and turbulent boundary-layer (TBL) flows of the organic vapor Novec649 are studied using DNS and LES. The numerical study aims at providing a reference for the turbulent state of a Novec zero-pressure-gradient flat-plate boundary layer at M=0.9, a freestream temperature T_∞=100°C and pressure p_∞=4 bars.

Laminar boundary layers:

- Flow solver (PRSV cubic EoS and Chung-Lee-Starling model) provides thermodynamic quantities in good agreement with reference laws.
- Larger discrepancies are observed for transport properties, with deviations of $\sim 15-30\%$, but the wall-normal distribution of thermo-physical properties is well reproduced. Since variations of viscosity are very weak, they do not affect BL computations.
- Compared to Refprop, fluid models do not influence the development of unstable modes.

Reference DNS of fully turbulent state up to $Re_\theta = 5000$:

- Transition triggered by oblique modes with angle of 30°, almost as unstable as 2D modes.
- Despite $M = 0.9$, Novec's TBL dynamical behavior is close to incompressible databases for air flows.
- Genuine compressibility effects are nevertheless observed on thermo-physical quantities.
- The thermal mode is drastically damped and the acoustic mode is reinforced.

Validation of LES strategy and investigation of transition influence on TBL:

- Wall-resolved LES closely match with DNS, validating the grid resolution selected.
- Due to less frequent filtering, Implicit LES strategy with IRS4 outperforms the explicit approach, with a CPU speed-up of ~ 3.5. Filtering after IRS4 operator has no impact on the result while strengthening the IRS stability.
- Integrating viscous terms at each or at the last RK substep has no impact on the results.
- The influence of forcing parameters is assessed with additional LES. As $Re_{\theta,in}$ is relatively high, memory effects persist in TBL. Small discrepancies observed in TBL by varying forcing parameters are due to history of transition, as revealed by C_f decomposition.
- An approximate equilibrium state is obtained for $Re_\theta \gtrapprox 3000$.

Chapter 4

Influence of large-scale freestream turbulence on bypass transition in air and organic vapor flows

In this chapter, the freestream turbulence (FST) induced transition in zero-pressure gradient flat-plate boundary layers is investigated by means of large-eddy simulations. In particular, we are interested in investigating the influence of high integral length scales (L_f) on the bypass transition for different turbulent intensities (T_u), with specific focus on configurations of interest for ORC turbomachinery. Therefore, the flow conditions for Novec649 boundary layer are selected as representative of the CLOWT wind tunnel (M=0.9, temperature of 100 °C, pressure of 4 bars). A direct comparison with air flows in low and high-subsonic conditions (M=0.1 and 0.9 respectively) is performed to sort out dense-gas and compressibility effects on the FST-induced transition. The chapter is organized as follows. The numerical setups are described in section 4.1. The effects of changing FST properties (L_f and T_u), of the gas nature (air versus Novec649) and of compressibility (M=0.1 and 0.9) are highlighted in section 4.2. The influence of the FST properties, and in particular the integral length scale, on the laminar streaks is investigated in section 4.3. Two competing transition scenarios are analyzed and discussed in section 4.4, namely the destabilisation of laminar streaks and the generation of Λ-vortices close to the inlet. Finally, the influence of FST on the turbulent boundary layer is analyzed in section 4.5. Appendix C give further implementation details and validation cases.

Gas	M_∞	U_∞ [m/s]	c_∞ [m/s]	p_∞ [bars]	T_∞ [°C]	ρ_∞ [kg/m^3]	μ_∞ [Pa.s]	Γ_∞	δ^*_{in} [μm]
Air	0.1	34.6	346.1	1.01	25	1.18	1.8371×10^{-5}	1.2	79
	0.9	311.5	346.1	1.01	25	1.18	1.8371×10^{-5}	1.2	9.5
Novec	0.9	76.2	84.7	4.0	100	48.5	1.2835×10^{-5}	0.84	0.61

Table 4.1: Thermodynamic and aerodynamic freestream conditions (subscript ∞): M denotes the Mach number, U the velocity, c the sound speed, p the pressure, T the temperature, ρ the density, μ the dynamic viscosity and Γ the fundamental derivative of gas dynamics.

4.1 Flow configuration and numerical setup

4.1.1 Operating conditions

The operating conditions are given in table 4.1. The selected configuration for Novec649 vapor is the same as the DNS and LES of Chapter 3 and corresponds to nominal operating condition of the CLOWT facility [110]. Two flow speeds are chosen for simulations with air: a low subsonic one (M=0.1) to reproduce an incompressible-like case and a high subsonic speed (M=0.9), corresponding to the Mach number used for Novec. At the conditions chosen for Novec, the fundamental derivative of gas dynamics Γ has a value below one, meaning that the flow operates in the dense-gas thermodynamic region, as often encountered in ORC applications.

4.1.2 Numerical set-up

As described in Chapter 2, the compressible Navier-Stokes equations are solved using MUSICAA solver. They are supplemented with the Peng-Robinson-Stryjek-Vera (PRSV) equation of state [13] and the Chung-Lee-Starling model [123] for the transport properties for Novec vapor. The ideal gas law and Sutherland's model are used for air flows. The inviscid fluxes are discretised by means of 10th-order centered differences whereas 4th-order finite differences are used for the visco-thermal fluxes, and a 10th-order selective filtering is applied. A four-stage low-storage Runge Kutta algorithm is used for time integration, combined with a fourth-order implicit residual smooting (IRS4) method. The IRS4 is applied in the y-direction, allowing CFL$\sim$5 at the wall for an overcost of 15% and resulting in an overall CPU cost reduction of a factor 4. Periodicity is enforced in the spanwise direction and adiabatic no-slip conditions are applied at the wall. The non-reflecting conditions of Tam & Dong [128] are imposed at the inlet, top and outflow boundaries. Finally, a sponge zone combining

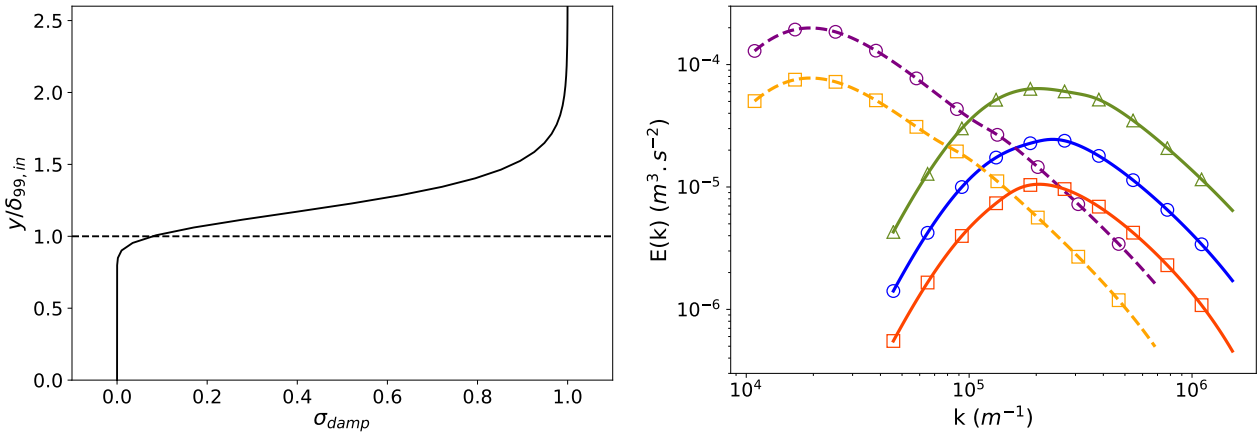

Figure 4.1: Damping function σ_{damp} (left), identical among cases, and initial kinetic energy spectra (right) for the inlet synthetic turbulence. Low L_f (——), high L_f (- - -) and T_u=2.5% (□), 4% (○) and 6.6% (△).

grid stretching and a Laplacian filter is added at the oulet.

To create turbulent inlet conditions, we use a synthetic flowfield based on Random Fourier Modes (RFM), as described in section 2.3.4.3. In particular, this stochastic velocity is windowed by a van Driest-type damping function to mimick the exponential damping of continuous Orr-Sommerfeld modes in the boundary layer. We use the function proposed by Pinto & Lodato [46], defined as:

$$\sigma_{\text{damp}}(y) = (1 - \exp(-y/(0.137 \times h)))^{1000} \tag{4.1}$$

where h corresponds to the height where the coefficient is equal to 0.5 and needs to be prescribed by the user. The synthetic turbulence is also damped at the upper corner of the inlet to prevent it from being injected too close to the upper boundary condition. The T3A benchmark case [58] is used in appendix C.1 to validate the strategy based on synthetic turbulence. In particular, the injection height h is a free parameter that can influence the precise location of transition. Nonetheless, FST-induced transition is well reproduced as long as the turbulence is injected above $\delta_{99,in}$. Thereafter, h is kept equal to $1.21\delta_{99,in}$, for all cases (see figure 4.1 left).

Simulations are initialised with similarity solutions of the compressible laminar boundary layer with zero pressure gradient. The Reynolds number at the inlet is taken as $Re_{x,in} = 10^4$. In the Novec cases, five different FST conditions are analysed. For the lowest value of the integral length scale (hereafter referred to as 'Low-L_f'), three turbulent intensities (2.5, 4 and 6.6%) are tested. The 'High-L_f' cases consider an integral length scale multiplied by a factor of ten for two values of $T_{u,in}$ (2.5 and 4%). For simulations in air, the low-L_f and high-L_f cases are reproduced at T_u=4% for two values of the Mach number (0.1 and 0.9). The

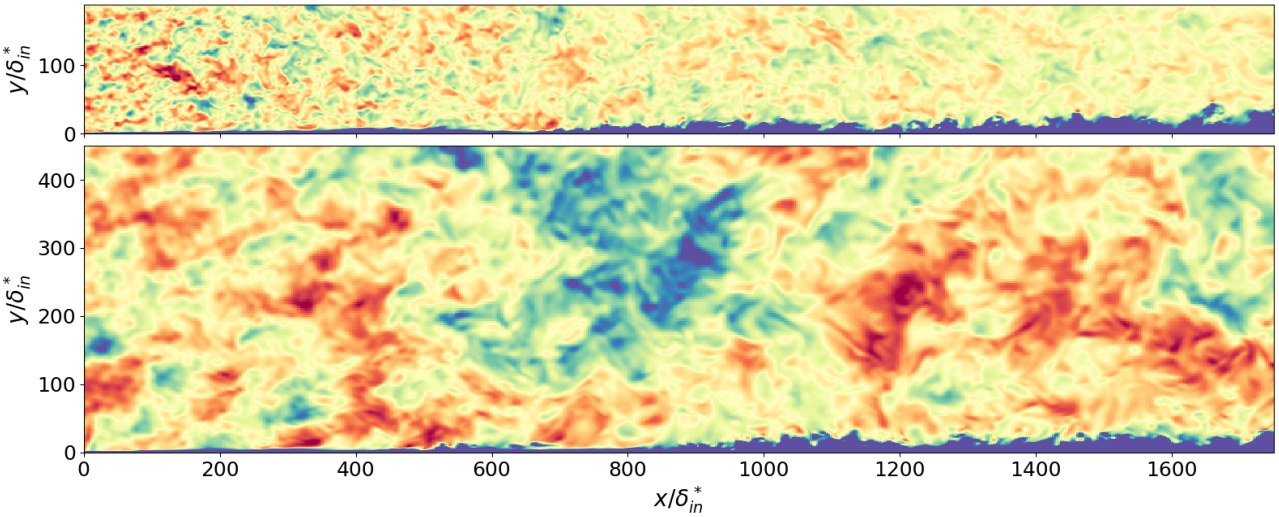

Figure 4.2: Snapshot of the streamwise velocity in the mid-span plane. Colorscale between $0.9U_\infty$ (blue) and $1.1U_\infty$ (red) for low L_f (top) and high L_f (bottom) Novec cases at T_u=4 %. For the high L_f-high L_f case, only half of the domain height is shown.

different LES simulations are summarised in the table 4.2, with the corresponding grids and line legends. For the low-L_f cases, the Reynolds number based on the integral length scale, Re_{L_f}, is the same as the one used to reproduce the T3A experiment in appendix C.1, and it is of similar magnitude to that used in most published FST transition experiments [65, 253] and simulations [45, 19, 46]. The effective integral length scale L_f at the inlet is determined by integration of the temporal autocorrelation function f of the velocity signal:

$$L_f = U_\infty \int_0^t f(\tau) d\tau \tag{4.2}$$

where the upper limit of integration is set as the first zero crossing of f [254]. For the high-L_f cases, the target value $Re_{L_f,t}$ has been multiplied by ten to investigate the effect of large incoming disturbances. The calculated value is $Re_{L_f,c} \sim 14000$, corresponding in the end to a factor of seven. The differences in turbulent scales are clearly visible in figure 4.2. Following Fransson & Shahinfar [47], we also introduce a FST Reynolds number, $Re_{FST} = T_u \times Re_{Lf}$, given in table 4.2.

The computational grid resolution needs to comply with two major constraints. The first one concerns the resolution of the near-wall boundary layer flow, for which a target resolution in wall units $\Delta x^+ \times \Delta y^+_w \times \Delta z^+ \sim 30 \times 1.0 \times 11$ has been determined in Chapter 3. The second constraint is the resolution of the freestream disturbances, which is driven by the values of the RFM wavenumber bounds, k_{min} and k_{max}. The resolution constraint are based on a parametric study of spatial HIT, detailed in Appendix B. k_{min} is such that the crossflow

Case	Flow	$Tu_{,in}$ (%)	$Re_{L_f,t}$ Theo.	$Re_{L_f,c}$ Calc.	Re_{FST} Calc.	Points $N_x \times N_y \times N_z$	Resolution $\Delta x^+ \times \Delta y_w^+ \times \Delta z^+$	Legend
Low L_f-Low Tu	Novec	2.5	1728	2150	54	1410×280×400	9×0.7×8	
High L_f-Low Tu	Novec	2.5	17280	13600	340	1800×480×800	27×0.9×10	
Low L_f-High Tu	Novec	4.0	1728	1950	78	1280×280×400	13×1.0×11	
	Air0.1	4.0	1728	2200	88	1410×280×400	13×1.0×11	
	Air0.9	4.0	1728	2100	84	1410×280×400	11×0.8×9	
High L_f-High Tu	Novec	4.0	17280	13250	530	1800×480×800	28×0.9×10	
	Air0.1	4.0	17280	14350	574	704×480×800	26×0.9×10	
	Air0.9	4.0	17280	14000	560	704×480×800	21×0.8×9	
Low L_f-vHigh Tu	Novec	6.6	1728	1850	122	4096×320×400	14×1.0×11	

Table 4.2: Computational grid and FST properties of the simulations.

dimensions L_y and L_z are at least $\sim 10L_f$ for the high-L_f cases. The obtained L_z is halved in the low-L_f simulations, yielding $L_z \sim 50L_f$. We then choose $k_{max} \geq 7k_{L_f}$, which gives a maximal value for the grid spacings to accurately resolve the injected modes (based on the resolvability limit of the current numerical scheme). The resulting resolutions given in table 4.2 are typical of wall-resolved LES. The streamwise resolution $\Delta x^+ \sim$ 13-14 for the low-L_f cases is dictated by the freestream turbulence, as shown by the inlet spectra in figure 4.1 (right). On the contrary, when the integral length scale is relatively large, the near-wall resolution constraint is more restrictive and the streamwise spacing is $\Delta x^+ \sim$ 27-28. These resolutions have been shown to be sufficient to accurately capture a modal transition and the fully turbulent state of the boundary layer (see Chapter 3). To make sure that the receptivity to freestream turbulence is not affected by grid resolution, the high L_f-high Tu case at M=0.9 in air has been simulated on a grid with a DNS resolution ($\Delta x^+ \times \Delta y_w^+ \times \Delta z^+ \sim 10.5 \times 0.8 \times 4.3$), keeping the same wavenumber bounds as the LES. Although transition occurs a bit earlier (as also observed, e.g., in Sayadi & Moin [255]), the results, reported in appendix C.2, remain close to DNS in the transitional region, which validates the present LES resolution. Furthermore, a second DNS has been performed with k_{max} increased to match the limit imposed by the DNS grid to investigate the influence of an increase of the high-frequency content of the freestream turbulence on the breakdown. The results are perfectly matching the first DNS, validating the choice $k_{max} \geq 7k_{L_f}$ used for LES study. The sensitivity to the choice of k_{min} has also been checked in Appendix C.3.

After the initial transient has been discarded, span- and time-averaged quantities are collected over 70 000 time steps for the cases at M=0.9 and 300 000 time steps for the ones at M=0.1. The evolutions of the averaged FST intensity are compared for the five Novec cases in figure 4.3 (left). As expected, when L_f is increased,

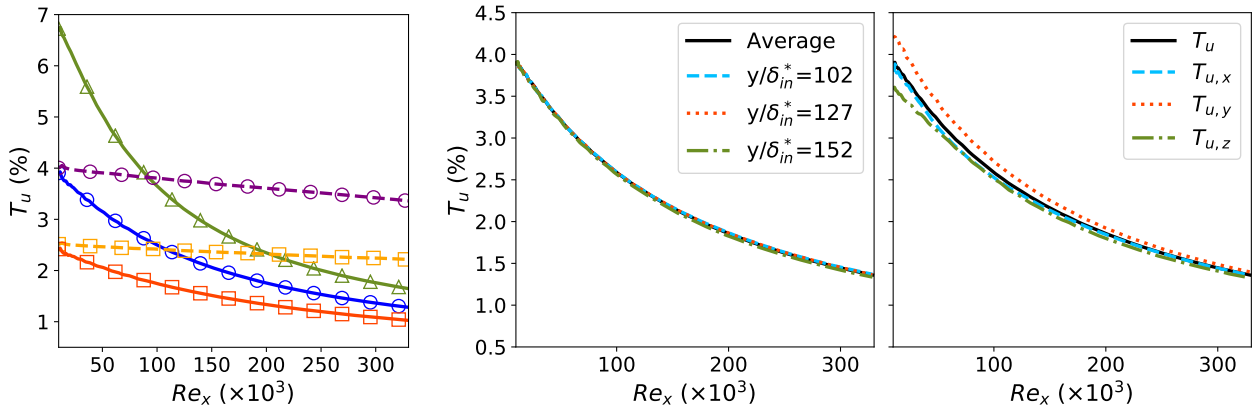

Figure 4.3: Evolution of the turbulence intensity for the different Novec cases (left): low L_f (——), high L_f (– – –) and T_u=2.5% (□), 4% (○) and 6.6% (△).
FST homogeneity (middle) and isotropy (right) of Novec low L_f-high T_u case. $T_u = \sqrt{(u'^2 + v'^2 + w'^2)/3}/U_\infty$; $T_{u,x} = \sqrt{u'^2}/U_\infty$; $T_{u,y} = \sqrt{v'^2}/U_\infty$; $T_{u,z} = \sqrt{w'^2}/U_\infty$.

the decay slope of the FST evolution is decreased. Therefore, in the high-L_f cases, the turbulence intensity remains greater than 3% and 2% for the high- and low-T_u cases, respectively, whereas the turbulence intensities for the low-L_f cases are rapidly below 2%. In order to estimate the homogeneity of the FST, T_u evolutions are plotted in figure 4.3 (middle) at three wall-normal locations in the freestream and compared to the averaged one for the low L_f-high T_u Novec case. The curves match perfectly, meaning that a good homogeneity is obtained for the injected synthetic turbulence. Furthermore, to assess the turbulence isotropy, T_u evolutions for the three velocity components are reported in figure 4.3 (right). Slight discrepancies can be observed close to the inlet, but they are relatively small and the FST can be considered as nearly isotropic.

4.2 Influence of flow conditions on transition location

First, the influence of the freestream turbulence characteristics on the bypass transition is analysed for the organic vapor flows. Then, for T_u=4%, the Novec BLs are compared to air flows in an incompressible-like (M=0.1) and compressible (M=0.9) configuration in order to quantify dense-gas and compressibility effects on the FST-induced transitions.

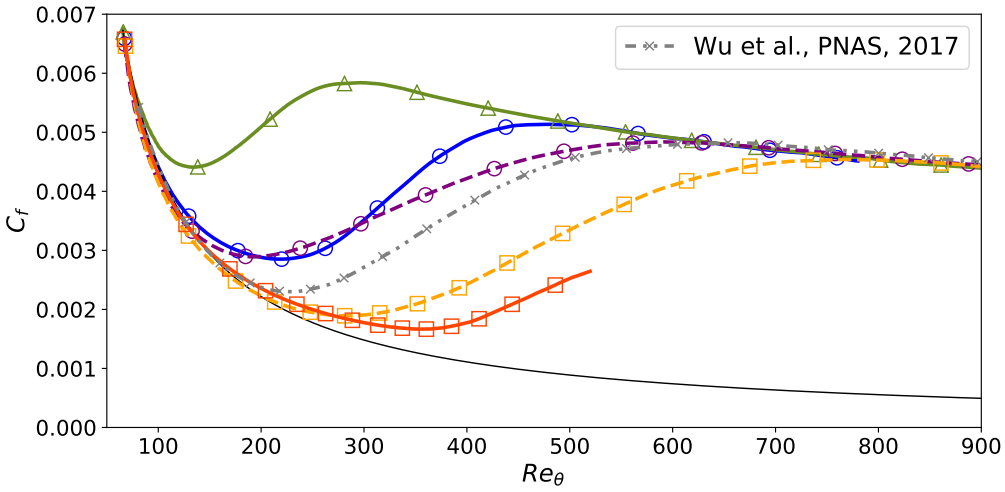

Figure 4.4: Distribution of the friction coefficient for the different cases with Novec vapor: Low L_f (——), high L_f (– – –) and T_u=2.5% (□), 4% (○) and 6.6% (△). Laminar correlation $C_{f,lam} = 0.664/\sqrt{Re_x}$ (——).

4.2.1 Influence of FST characteristics

The friction coefficient evolutions in the dense-gas BLs are reported in figure 4.4. All the flows transition to a fully turbulent state in the computational domain, except for the low L_f-low T_u case. As expected, an increase of the inlet turbulence intensity always leads to a faster onset and termination of the transition, for both high- and low-L_f cases. Similarly to Fransson & Shahinfar [47], a twofold effect is observed by changing L_f. For T_u=2.5%, an increase of the integral length scale moves the transition location upstream whereas, for T_u=4%, an increase of L_f delays the transition. For T_u=4%, the slope of the C_f rise in the transition region with a high L_f is smoother than with a low L_f, so that, even if the transition onset occurs earlier, the end of the transition region is shifted downstream. It is worth noting that the slopes of the C_f rise are similar for the low L_f-high T_u and vHigh T_u cases, whereas they are slightly different in the high-L_f cases.

The streamwise evolutions of the maximum of u_{rms}, in figure 4.5 (left), are often correlated with the streak growth. For the low L_f-high T_u case, a fast increase of $u_{rms,max}$ is observed in the pre-transitional region, *i.e.* prior to the minimum of skin friction (at $Re_\theta \approx 220$), and can be associated with the transient energy growth in the early streak development. The growth rate then slows down before a secondary growth phase yields the peak at approximately three-quarters of the transition region. This peak is associated with the eruption of turbulent spots [74]. A slower growth of $u_{rms,max}$ in the pre-transitional region is obtained for the low L_f-low T_u BL, in accordance with the lower FST intensity. An inflection point is visible near $Re_\theta \sim 120$ for the low-L_f

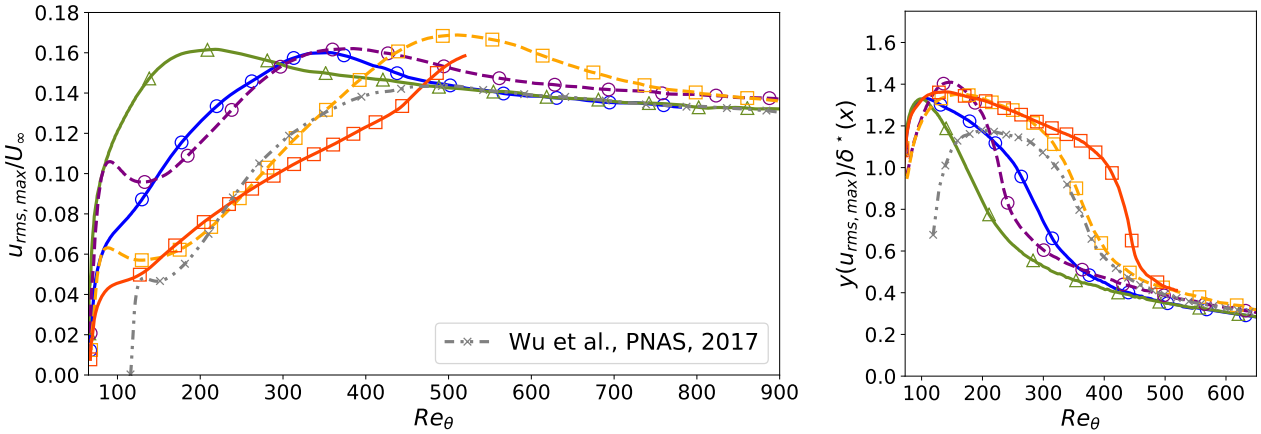

Figure 4.5: Evolution of $u_{rms,max}/U_\infty$ (left) and its height $y(u_{rms,max})/\delta^*$ (right). Low L_f (——), high L_f (– – –) and T_u=2.5% (□), 4% (○) and 6.6% (△).

cases with T_u=2.5% and 4%, which is not directly related to the growth of laminar streaks but rather to an other receptivity mechanism. For the low-L_f case with T_u=6.6%, the growth is so fast that no inflection is noticeable before the main peak. For the high-L_f cases, a first peak is visible in the pre-transitional region, just prior to the location of the inflection point of the low-L_f cases. This first local maximum is not linked to the laminar streak growth, and is also present in the results extracted from the database of Wu *et al.* [76]. In their simulation, HIT is injected at a height equal to $15\delta_{99,in}$ with an inlet Re_θ of 80, explaining the offset with our curves. As their simulation was characterized by the appearance of low-speed Λ-shaped structures prior to laminar streaks, the early secondary peak can be associated with the growth of these structures, which could also be present in the high-L_f simulations. In figure 4.5 (right), the height at which the maximum of u_{rms} is approximately the same between the cases. The location $y(u_{rms,max})$ moves from values around 1.2-1.4δ^* in the pre-transitional region, as predicted by the optimal perturbation theory [256, 257], towards a low level in the TBL, associated to the near-wall turbulent streaks. The evolutions are also in agreement with low-speed airflow results of Wu *et al.* [76], except for a slightly lower altitude in the laminar region.

Instantaneous top views of the streamwise velocity fluctuations at $y/\delta_{99,in}$=1.1 are shown in figure 4.6, using the same streamwise and spanwise extents to provide an overview of the structures present inside the BL and a first qualitative comparison of the Klebanoff streaks. The streak formation and the presence of turbulent spots are clearly revealed for each case, except for the case of T_u=6.6% which is highly disturbed. A first important observation is that the scales associated with Klebanoff modes are different between the low-L_f and high-L_f cases. At constant L_f, the spanwise distribution of the laminar streaks is also affected, to a lesser degree, by the

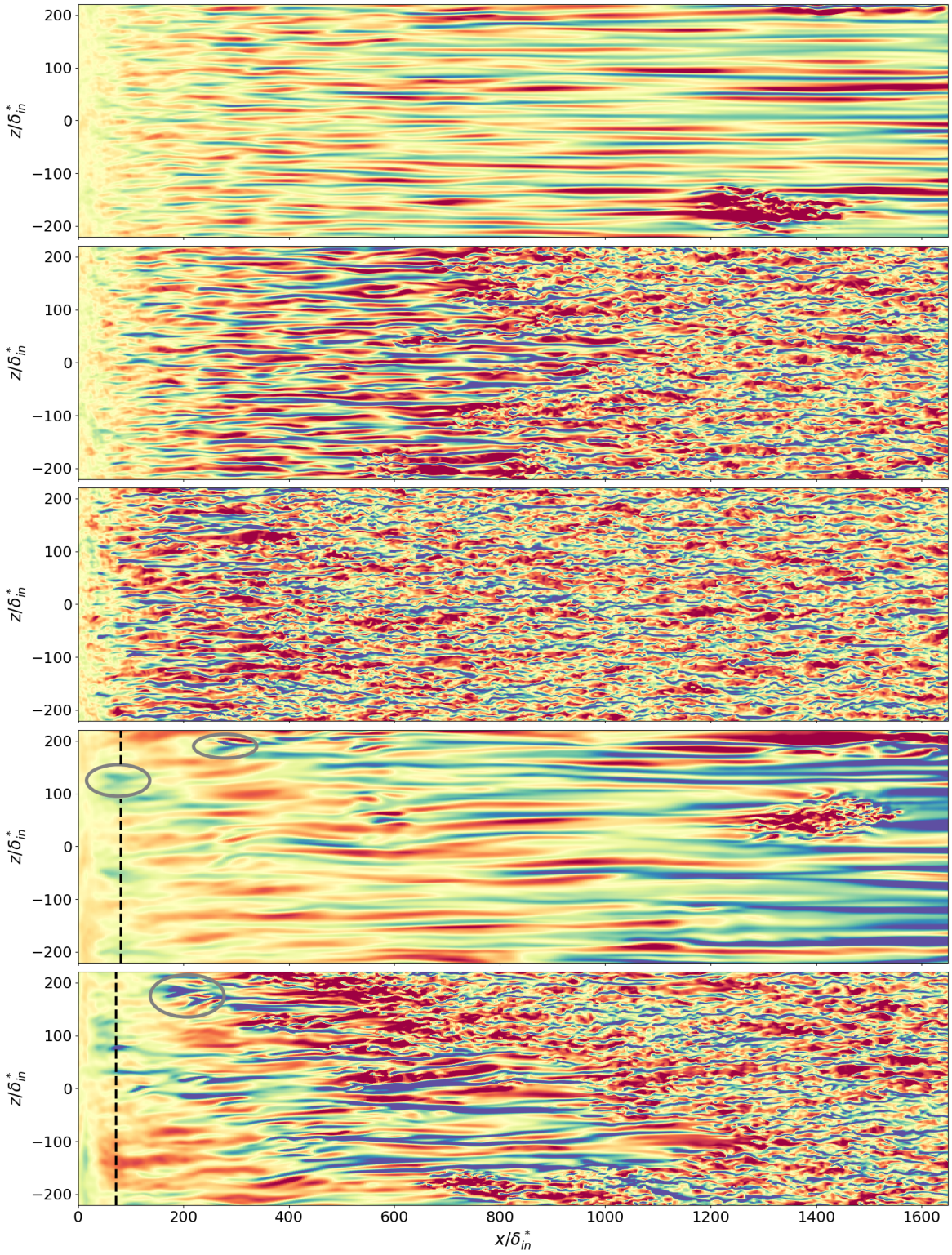

Figure 4.6: Instantaneous streamwise fluctuations in a wall-normal plane at $y/\delta^*_{in} = 3.1$. The values are plotted between $-0.2U_\infty$ (blue) and $0.2U_\infty$ (red). From top to bottom: low L_f cases (T_u= 2.5%, 4% and 6.6%) and high L_f cases (T_u=2.5% and 4%). The vertical dashed lines mark the location where Re_θ=100. Some occurences of Λ-shaped structures are marked by gray circles.

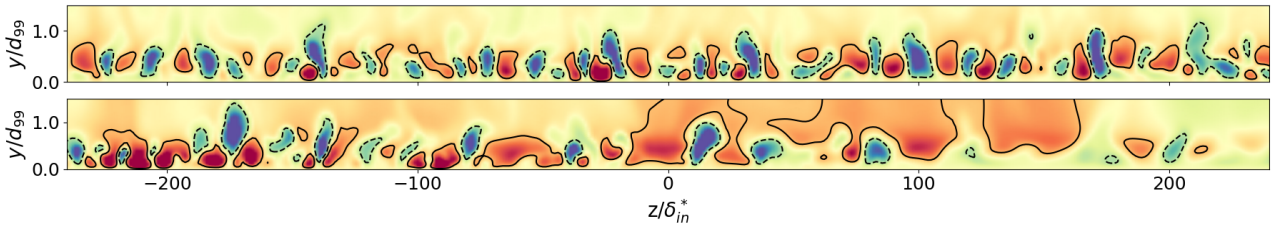

Figure 4.7: Streamwise fluctuations in a plane yz at the location of $C_{f,min}$ in the low L_f-high T_u (top) and high L_f-high T_u (bottom) Novec cases. To emphasize the streaks, the values are averaged in time over 5 consecutive planes. The y-axis is stretched by a factor of two compared to the z-axis. The colorscale is between $-0.3U_\infty$ (blue) and $0.3U_\infty$ (red), and 2 contours are marked with lines: $0.1U_\infty$ (solid) and $-0.1U_\infty$ (dashed).

FST intensity, in particular for the low-L_f BLs. In the low L_f-low T_u case, the spanwise scale of the Klebanoff modes increase as the boundary layer thickens. Moreover, the presence of low-speed Λ-shaped structures is clearly revealed in the instantaneous snapshots for the high-L_f cases, as highlighted by the gray circles in the figure. These Λ-shaped structures bear strong resemblance with the quasi-periodic spanwise structures described by Ovchinnikov *et al.* [57] and the Δ-shaped structures in Wu *et al.* [76]. As in Ovchinnikov *et al.* [57], they are located prior to laminar streaks. For T_u=2.5%, a Λ structure begins to emerge at the location $(x/\delta^*_{in}, z/\delta^*_{in})$ =(75, 125), around Re_θ=100 where the first peak was identified in figure 4.5. For the low-L_f cases, the visualisations do not reveal similar structures near the inlet. Differences in spanwise distribution of the laminar streaks are further observed on the yz-slices of the streamwise fluctuations of the T_u=4% Novec cases in figure 4.7. Larger spanwise distribution are observed in the high-L_f simulation compared to the low L_f simulation. The case also exhibits a wide variety of scales, for instance between left and right of the bottom panel, whereas the scales remain more constant in the low L_f case. Furthermore, the edge of the boundary layer in the high-L_f LES is blurred by the large disturbances present over it, with sporadic high-speed streaks connected to the FST.

4.2.2 Compressibility and dense-gas effects

For T_u=4%, additional simulations are carried out at the same conditions (same resolution) with air at Mach numbers M=0.1 and 0.9. Thus, the study allows to shed further light on the possible role of compressibility in FST-induced transition, which has been discussed only in relatively few studies. Specifically, Klebanoff streaks were found to be slightly stabilized in compressible boundary layer due to enhanced temperature fluctuations and reduced streamwise velocity fluctuations [258, 259]. This conclusion was also obtained by applying the optimal perturbation theory to compressible BL (Tumin & Reshotko [260]), showing that the threshold to destabilize

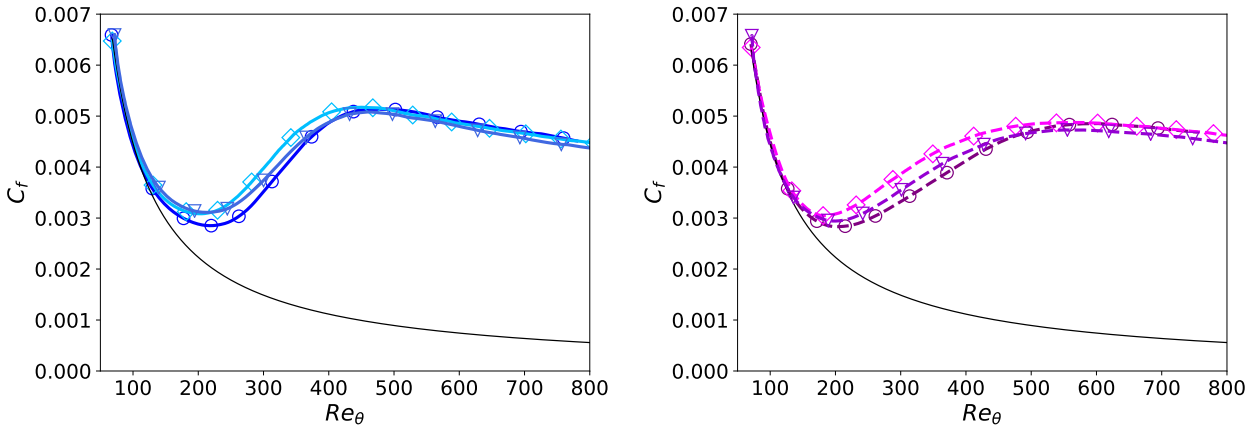

Figure 4.8: Distribution of the friction coefficient for the low L_f-high T_u (left) and high L_f-high T_u (right) cases for Novec at M=0.9 (○) and for air at M=0.1 (◇) and 0.9 (▽). Laminar correlation $C_{f,lam} = 0.664/\sqrt{Re_x}$ (——).

laminar streaks is increased. The onset of bypass transition is thus delayed by increasing the Mach number (Ohno *et al.* [261]).

The friction coefficient evolutions, displayed in figure 4.8, show the same trend for low (left panel) and high (right panel) integral length scale. First, comparing air BLs at the two flow speeds, an increase of the Mach number tends to slightly delay the transition and reduces the friction value in the turbulent state due to the friction heating at the wall. As reported by Marensi *et al.* [259] or Ohno *et al.* [261], temperature fluctuations are enhanced by compressibility and streamwise velocity fluctuations consequently reduced. This can be seen in figure 4.9, where thermal streaks present in the air BL at M=0.9 (left subfigure) have an intensity $T_{rms,max}$ ($\sim 3\%T_\infty$) significantly higher than at M=0.1 (right subfigure). Note that thermal fluctuations for the dense-gas flow at M=0.9 are very low due the high thermal capacity of the organic vapor. As a consequence, the C_f levels of Novec simulations in the fully turbulent state collapse on the ones of air BLs at M=0.1 or of incompressible simulations (as noted in Chapter 3). However, the C_f curves of Novec simulations in the transitional region show that the use of an organic vapor delays the transition even more than the effects of compressibility. This can be explained by the excitation of internal degrees of freedom of the complex Novec molecules, that further reduces streamwise velocity fluctuations. This stabilising effect is of the same nature as that due to the increase in thermal fluctuations, but is more significant. It was also noted in the BL stability of Gloerfelt *et al.* [18], where the neutral curve for Novec at M=0.9 is contained in the one for the same BL in air. The evolutions of $u_{rms,max}$ for low and high L_f are reported in the left and right parts of figure 4.10, respectively. The hierarchy

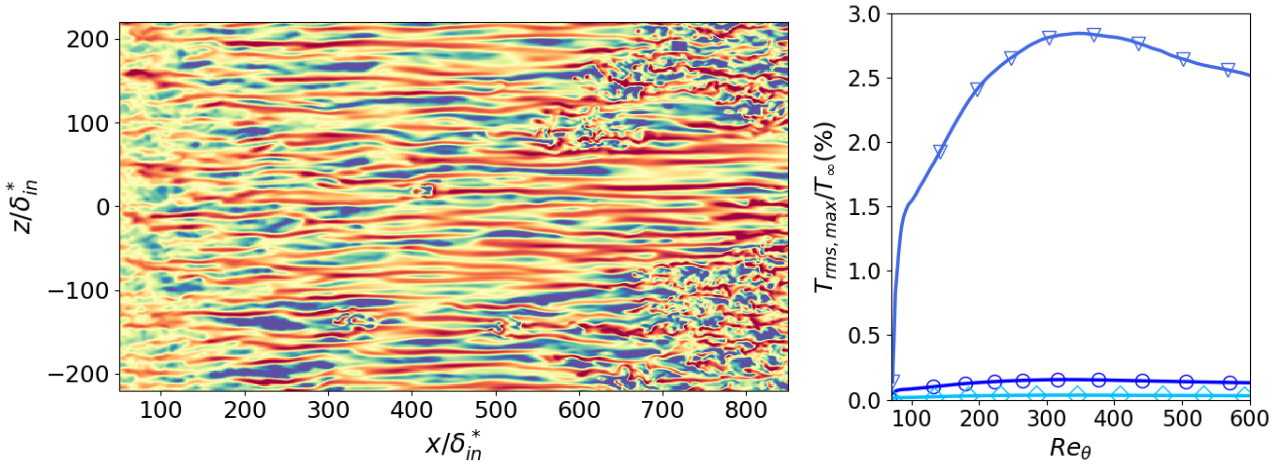

Figure 4.9: Left: Instantaneous temperature fluctuations T'/T_∞ between -5% (blue) and 5% (red) at y/δ^*_{in}=3.1 in the low L_f-high T_u air M=0.9 case. Right: Evolution of $T_{rms,max}/T_\infty$ for the low L_f-high T_u cases for Novec at M=0.9 (○) and for air at M=0.1 (◇) and 0.9 (▽).

observed for transition onset is respected, that is velocity fluctuations in air at M=0.1 are slightly reduced in air at M=0.9 and further reduced in Novec at M=0.9 for both FST length scales. The curves are however very close to each other for a given L_f meaning that the compressibility and real-gas effects are present but secondary compared to the effects of the FST length scale. It can be concluded that the observations made in § 4.2.1 about the influence of L_f on transition is the same in the air and organic vapor flows.

The similarities between the various flows is further shown by the instantaneous views of u' in a wall-normal plane in figure 4.11 (supplementary movies are available online). At a given freestream L_f, the laminar streaks retains at first sight similar spanwise distribution and are weakly affected by compressibility or real-gas effects (this will be quantified in section 4.4.1). For high L_f cases, the same Λ-shaped structures are observed in air flows, meaning that their presence is linked to the FST characteristics rather than dense-gas or compressibility effects. Overall, at the selected thermodynamic conditions, the FST-induced transition is only slightly modified by the high-subsonic regime or the organic vapor thermo-physical properties.

4.3 Laminar streak analysis

An in-depth analysis is carried out on the Klebanoff modes, essential in the transition phenomenon. Spanwise two-point correlations and spectral analysis are used to estimate their spanwise lengthscale. A laminar-turbulent discrimination is then applied to obtained streak statistics in the laminar region.

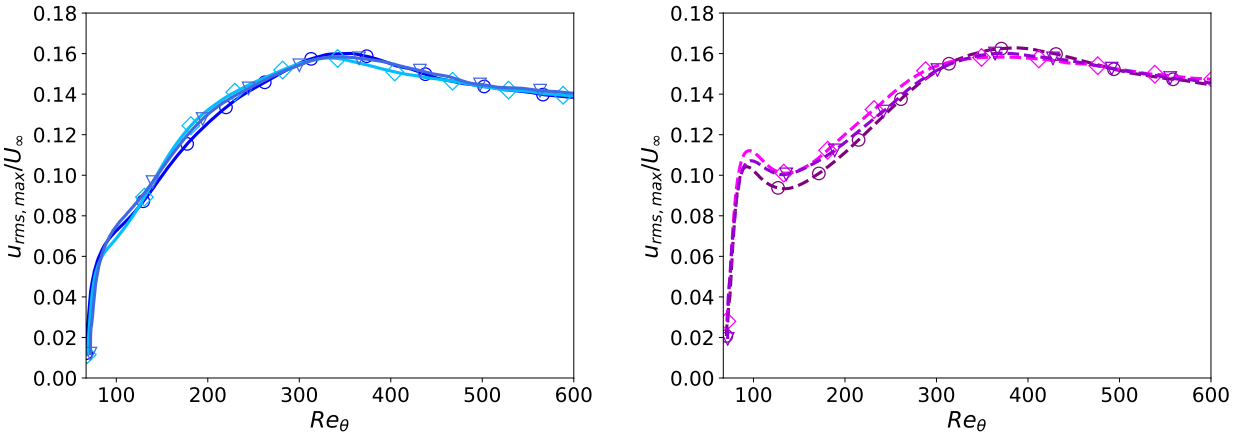

Figure 4.10: Evolution of $u_{rms,max}/U_\infty$ for the low L_f-high T_u (left) and high L_f-high T_u (right) cases for Novec at M=0.9 (○) and for air at M=0.1 (◇) and 0.9 (▽).

4.3.1 Spanwise correlations

As some variability in the spanwise sizes of the laminar streaks was observed in figures 4.6 and 4.7, the influence of the FST characteristics on their spanwise scale is investigated. The distance l_z which corresponds to a minimum of the spanwise correlation of the streamwise velocity, R_{uu}, can be related to the half spanwise wavelength of the streaks [47]. R_{uu} is evaluated in the transitional region at the height of the maximum u_{rms} and time averaged. For instance, R_{uu} profiles between Re_θ=67 and 710 are plotted in figure 4.12 for the low L_f-high T_u Novec case at the location of $u_{rms,max}$ in the BL. In this case, the minimum of the correlation functions evolves from l_z=12 at the inlet to 8.5 in the TBL.

The evolution of $\lambda_z = 2l_z$ for the Novec cases, estimated using a cubic interpolation, is reported in figure 4.13 (left). Some important differences between the cases are observed during transition, before all the curves tend to similar values in the TBL, except for the low L_f-low T_u case which does not fully transition in the domain. In particular, the latter case exhibits a significant increase in λ_z from the inlet, with a spanwise scale eventually larger than the high L_f-high T_u case. Figure 4.13 (right) compares the Novec cases with air flows at M=0.1 and 0.9 for T_u=4%. The results show that a similar spanwise scale is achieved for a given L_f, indicating that compressibility and dense-gas effects are of secondary importance.

As the minima of the correlation functions vary greatly across the transitional boundary layer for the different cases, the region considered for the evaluation of λ_z is restricted between the location of $C_{f,min}$ and the location at 60% between $C_{f,min}$ and $C_{f,max}$. This region includes the locations where the intermittency function γ_{peak}

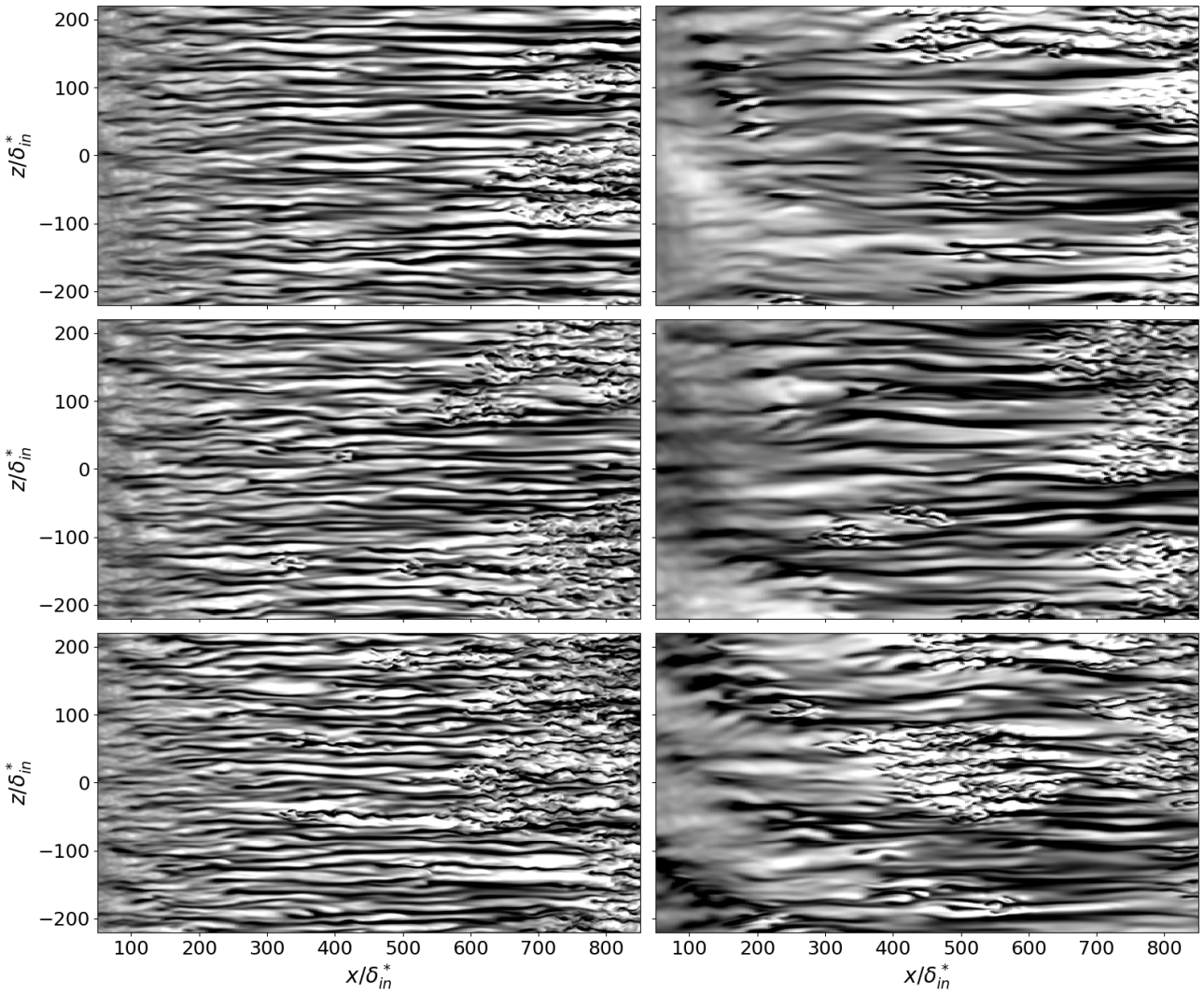

Figure 4.11: Comparison of air and Novec transitional flows at T_u=4% with the low L_f (left column) and high L_f (right column): Novec, Air M=0.1 and Air M=0.9 from top to bottom. Instantaneous streamwise fluctuations in a wall-normal plane at y/δ^*_{in}=3.1 are plotted between $-0.2U_\infty$ (black) and $0.2U_\infty$ (white).

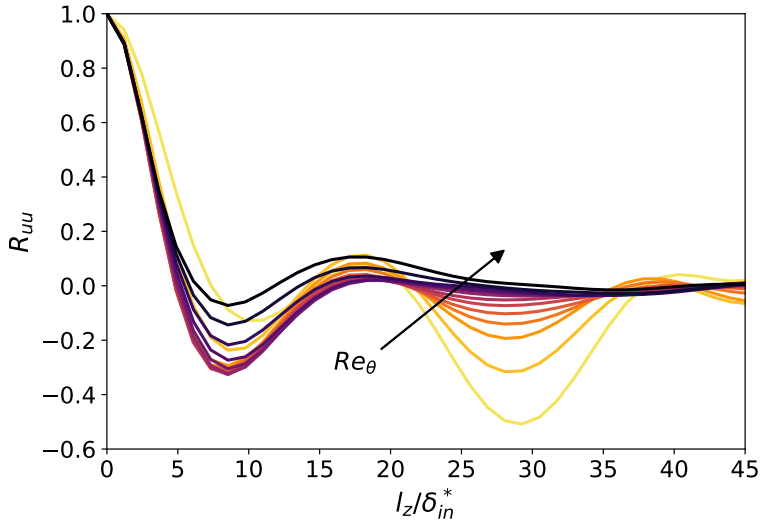

Figure 4.12: Spanwise correlation function of the streamwise velocity in the low L_f-high T_u Novec case (from light yellow to dark purple for Re_θ from 67 to 734).

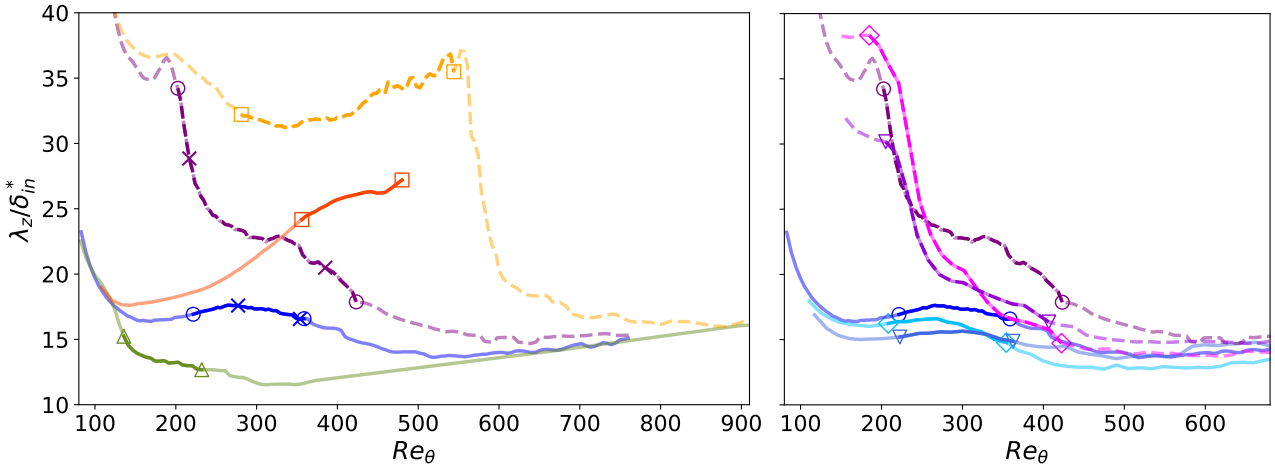

Figure 4.13: Evolution of spanwise wavelength of the streamwise streaks in the transitional region for the Novec cases (left) and comparison between Novec and Air cases at T_u=4% (right): Low L_f (——) and high L_f (- - -) at T_u=2.5% (□), 4% (○) and 6.6% (△) for Novec cases, and T_u=4% in Air at M=0.1 (◇) and 0.9 (▽). The colors are lighter outside the transition region between $C_{f,min}$ and 60% of $C_{f,max} - C_{f,min}$. In the left plot, crosses denote the position γ_{peak}=0.1 and 0.5 for the Novec cases at T_u=4%.

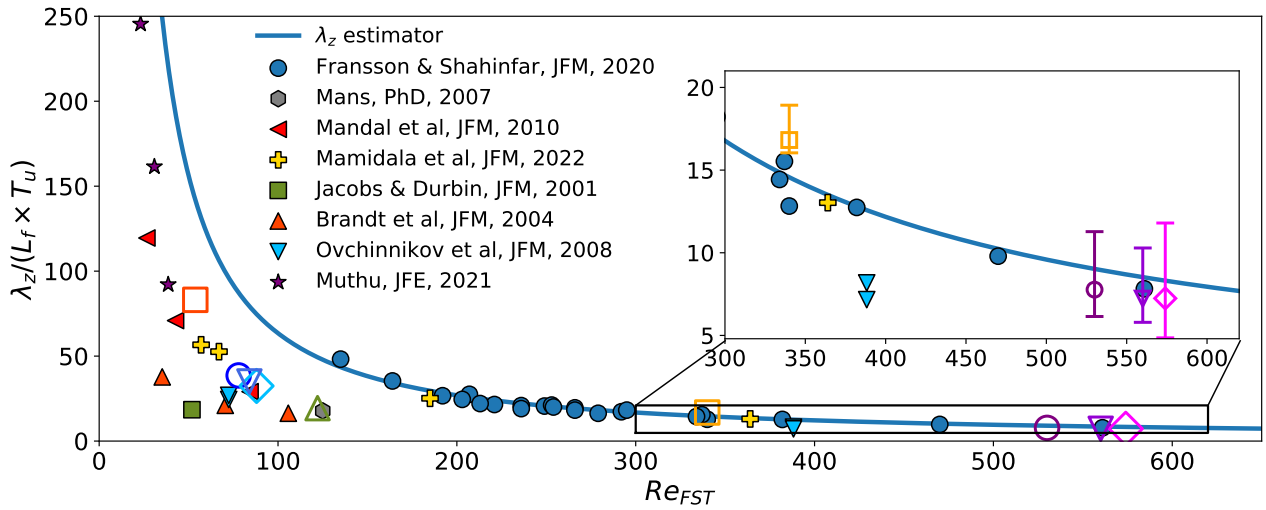

Figure 4.14: Spanwise wavelength of the streamwise streaks as a function of Re_{FST}. Novec: low L_f-low T_u (□), low L_f-high T_u (○), low L_f-vHigh T_u (△), high L_f-low T_u (□), and high L_f-high T_u (○) cases. At T_u=4%, Air M=0.1 for low L_f (◇) and high L_f (◇) cases and Air M=0.9 for low L_f (▽) and high L_f (▽) cases. Regarding the literature results, λ_z was either directly available [47, 262, 65, 55, 45, 57] or evaluated from R_{uu} profiles [253, 48]. The vertical bars in the inset show the variability in the transition region.

is 10% and 50% for the T_u=4% cases (see section 4.3.3 for the definition of γ_{peak}), as used in Fransson & Shahinfar [47]. Along this region, the spanwise distance between streaks remains relatively constant, except for the high L_f-high T_u case which exhibits significant variations due to the appearance of Λ-shaped structures prior to the laminar streaks. The hierarchy between the different cases is more apparent when restricted to this region. At constant L_f, an increase of T_u leads to a decrease of λ_z, as in Fransson *et al.* [56]. Inversely, at constant T_u, an increase of L_f leads to an increase of λ_z. Fransson & Shahinfar [47] showed that λ_z does not vary monotonically with T_u and L_f, but rather with a combination of these two FST parameters. They proposed an empirical correlation for the spanwise length, which was fitted to their extensive database and was given by:

$$\lambda_{z,FS} = L_f \, T_u \left(\mathscr{D}_1 \, Re_{FST}^{-1/\sqrt{2}} + \mathscr{D}_2 \right)^2 \tag{4.3}$$

with $(\mathscr{D}_1, \mathscr{D}_2)$=(186, 0.8) to match at ±10% the measured values. The estimator $\lambda_{z,FS}$ is plotted as a function of $Re_{FST} = T_u \times Re_{L_f}$ in figure 4.14, along with the experimental results of Fransson & Shahinfar [47] at Re_{FST} between 135 and 561 (evaluated at an intermittency level γ_{peak} of 10%). The measurements from Mamidala *et al.* [262], which contain lower Re_{FST} values (down to 57) and were obtained with a similar experimental setup to that used by Fransson & Shahinfar [47], are also reported. The mean values of λ_z along the evaluation region in the current simulations are also displayed. As noted earlier, the length scale varies with x for the high L_f-high

T_u cases, so to observe its influence on the results, λ_z values are plotted with their variations in the inset. Values from other experimental or numerical studies of FST-induced transition are also reported. In the high-Re_{FST} range shown in the zoomed view in figure 4.14, even taking into account the large λ_z variations, the present high-L_f results are in good agreement with the estimator $\lambda_{z,FS}$ for incompressible-like air flows but also for the air and organic vapor BLs at M=0.9. The results of Ovchinnikov *et al.* [57] are also in a fair agreement ($\sim -35\%$), showing that the estimator works well for large Re_{FST}, at least for the data considered. The majority of data in the literature is concentrated around lower Re_{FST} (≤ 150) and lower Re_{L_f} (≤ 3000). In this region, containing only one point from Fransson & Shahinfar's data, the comparison is less convincing. The increase of $\lambda_z/(L_f \times T_u)$ as Re_{FST} decreases is correctly captured by the estimator, but λ_z values predicted by (4.3) are twice the spanwise distance obtained in our low L_f cases. Our results are however in good agreement with the more recent experiment of Mamidala *et al.* [262]. Despite some scatter in the results from the literature, the general trend indicates that the correlation is less accurate for low Re_{FST}.

4.3.2 Spanwise spectra

To study in more detail the differences observed for the spanwise wavelengths in the previous section, a spectral analysis is carried out, focusing on the two T_u=4% Novec cases. Spanwise spectra can give additional information about the variability of streak spacing along the transitional region. In figure 4.15, premultiplied spanwise power spectral densities of the streamwise velocity are shown at different stations between the inlet and the position where the intermittency, which corresponds to the probability of the flow to being turbulent (see section 4.3.3), is equal to 0.5. The spectra are estimated at the position of $u_{rms,max}$ inside the BL. Close to the inlet, the energy inside the BL is very low, as the receptivity process just began. Several peaks are identified with vertical lines on the spectra. The spanwise wavelength evolution of the streamwise streaks identified in the previous section is also reported in transparent green. Clearly, the peaks associated with the vertical lines with square symbols correspond to the spanwise distance between streaks in the two cases. Energy distributes among surrounding wavelengths as Re_θ increases. Another peak at a higher wavelength is identified (marked by vertical lines with crosses), which is not associated with streak spacing but seems related to the value of L_f. In the high L_f case, this peak, located around λ_z/δ^*_{in}=160, is particularly dominant close to the inlet (at the second station) before decreasing further downstream. Looking at the bottom panel of figure 4.6 and the right panel of figure 4.11, Λ-shaped structures at the inlet spaced by approximately 100 to 200 δ^*_{in} can indeed be observed.

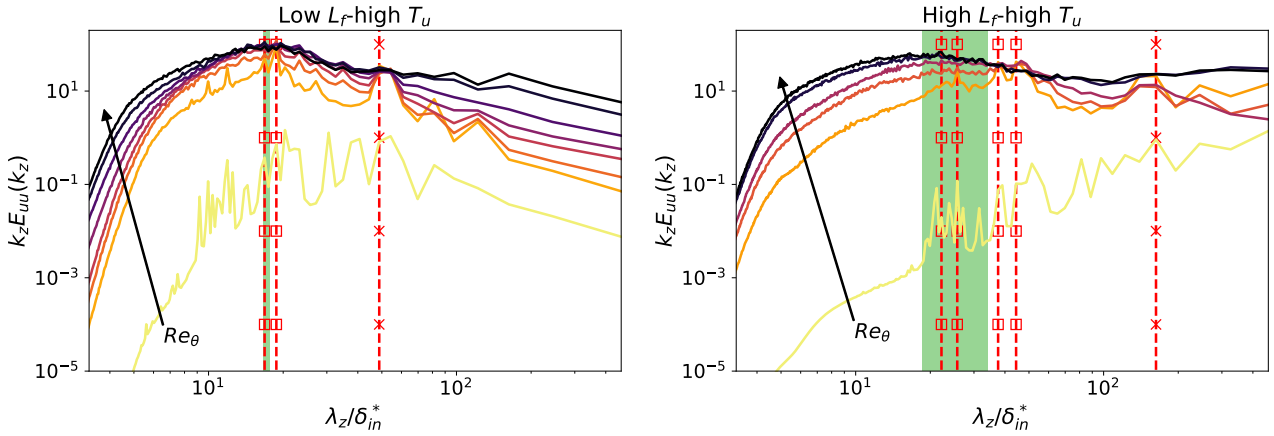

Figure 4.15: Premultiplied spanwise spectra $k_z E_{uu}(\lambda_z)$ at equally spaced streamwise position between the inlet and station where the intermittency $\gamma_{peak} = 50\%$ (from light yellow to dark purple for increasing Re_θ). - - -: dominant peaks at low (□) and high (x) λ_z. The evolution of spanwise wavelength of the streamwise streaks between $C_{f,min}$ and 60% of $C_{f,max} - C_{f,min}$ displayed in figure 4.13 is reported in transparent green. The definition for γ_{peak} is provided in section 4.3.3.

The streamwise evolutions of selected wavelengths, corresponding to the peaks identified in the spectra, are reported in figure 4.16. For the two cases, the initial dominant wavelength changes to a lower value with distance downstream. In particular, for the high L_f case, the dominant wavelength is reduced by a factor of two between the inlet and $\gamma = 50\%$, as the BL is populated with new laminar streaks. Moreover, the higher wavelength peak identified in figure 4.15 (magenta solid line) reaches a maximum around $Re_\theta \sim 90$ and decays further downstream. The initial peak observed for $u_{rms,max}$ in the high L_f-low T_u case is clearly correlated to the presence of Λ-shaped structures in the inlet region of the high L_f-low T_u case, and this wavelength dominates other modes close to the inlet. This is more ambiguous for the inflection point in the low L_f-low T_u case (figure 4.5 left), as no similar Λ structures were observed in this case. This point is tackled in section 4.4.2.

4.3.3 Laminar-turbulent discrimination

In order to separate the contributions of the laminar streaks from the turbulent ones and to identify the appearance of turbulent spots (section 4.4.3), a laminar-turbulent discrimination is applied over the transitional region. As in section 4.3.2, we focus on the two T_u=4% Novec cases to specifically observe the influence of the integral length scale. The discrimination algorithm is adapted from Durovic [263] and applied on volume snapshots, allowing the spatial separation into laminar and turbulent regions in the boundary layer. We first

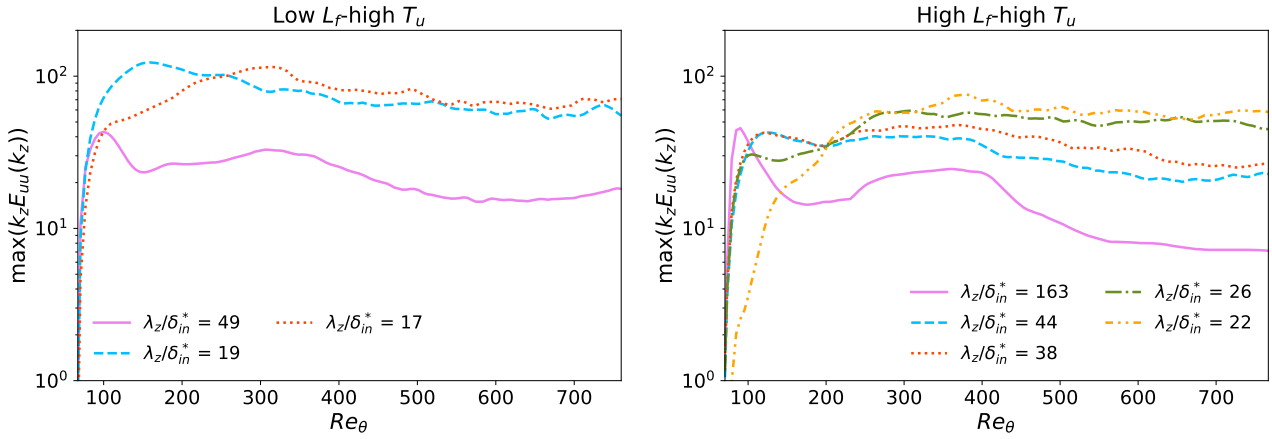

Figure 4.16: Evolution of the dominant wavelengths λ_z (marked by red vertical dashed lines in figure 4.15) between inlet and station where γ_{peak}=50%.

interpolate the field on a coarser mesh, reducing by a factor two the number of points in the spanwise and wall-normal directions. The number of points in the streamwise direction is divided by two only for the low-L_f simulations, so that similar resolution is obtained on the interpolated grid for all cases. The interpolation acts as a low-pass filter, in addition to reducing the cost of the procedure. For each wall-normal plane of a volume snapshot, the 2D scalar field of the spanwise velocity fluctuations w', noted $s_{w'}(\mathbf{x})$, is first used to define $s_{extr,w'}$ containing the local extrema of w'. The same extraction is realized for the wall-normal velocity fluctuations v' to obtain $s_{extr,v'}$. A 3D scalar field $s_{extr,3D}$ is reconstructed from the 2D extractions s_{extr}=$s_{extr,v'}$+$s_{extr,w'}$, and a smoothing S is applied on it. As the distance from the extrema increase, $S(\mathbf{x})$ decreases exponentially. Therefore, the smoothing is applied over a cubic domain D^3 restricted to the locations where $S(\mathbf{x}) \leq 0.025$, limiting the computational cost. An extrema density scalar field $f_{extr,3D}$ weighted by the extrema values is computed as:

$$f_{extr,3D}(\mathbf{x}) = \sum_{\mathbf{x}_s \in D^3} S\left(\frac{\mathbf{x}_s - \mathbf{x}}{r_s}\right) \times s_{extr,3D}(\mathbf{x}_s) \tag{4.4}$$

where the parameter r_s adjusts the radius of the spherical smoothing. This parameter, which depends on the numerical set-up and the particular configuration, is determined by testing its influence on the detection of the turbulent regions and spots. Once fixed, r_s is taken equal across the cases. This parameter is determined by trial & error and is taken equal to $0.8\Delta x_{interp}$, Δx_{interp} being the streamwise spacing in the interpolated grid. The weighting has been shown to improve the distinction between the TBL and the FST, at least for the considered turbulence intensities. The density scalar field $f_{extr,3D}$ is then interpolated back on the computational grid

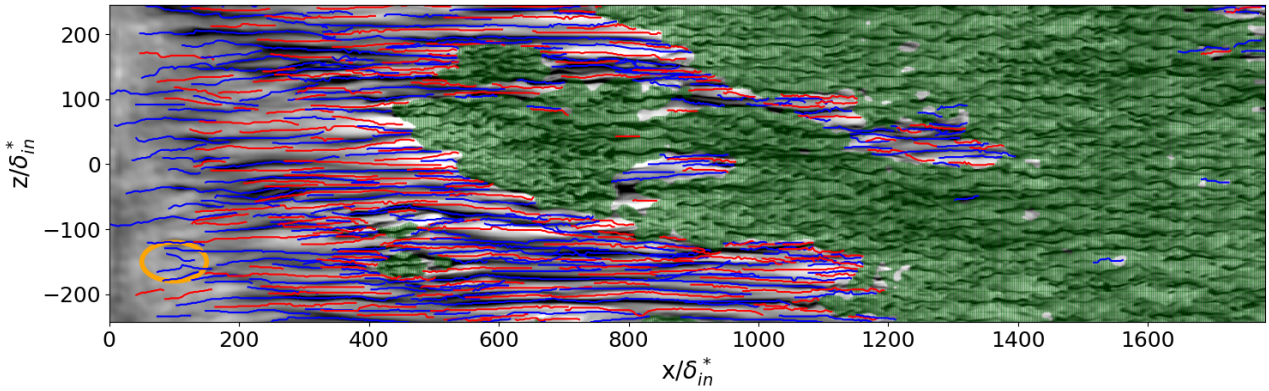

Figure 4.17: Wall-normal snapshot of the streamwise fluctuations at $y/\delta_{99,in}$=1.11 in the high L_f-high T_u Novec case. The turbulent region is displayed in semi-transparent green. The low-speed (high-speed) streaks detected (see section 4.3.4) are also represented in blue (red).

and a binary segmentation is realized using the method of Otsu [264]. A threshold is obtained at each wall-normal location independently and levels are smoothed in the wall-normal direction to ensure continuity in the discrimination. The discrimination is applied for each case using 4220 subvolumes saved during $\sim$68000 time iterations.

The output of the laminar-turbulent discrimination algorithm inside the BL for one snapshot is shown in semi-transparent green in figure 4.17 for the high L_f-high T_u Novec case. We observe that the discrimination can identify the turbulent state, populated with turbulent streaks, and several turbulent spots are captured (around $x/\delta^*_{in} \sim 450$ or 600). Discriminated statistics can be defined: the laminar-conditioned (resp. turbulent-conditioned) statistics correspond to the statistics obtained while averaging in time and in the spanwise direction the laminar (resp. turbulent) regions detected by the algorithm. In particular, the peak of the intermittency distribution inside the BL at each streamwise location can be retrieved, as plotted in figure 4.18 (left). The intermittency function corresponds to the probability of the flow to be turbulent at a given location. A dimensionless streamwise coordinate $\xi = (x - x_{tr})/\Delta x_{tr}$, x_{tr} being the position where $\gamma_{peak} = 0.5$ and Δx_{tr} the distance between $x_{\gamma_{peak}=0.1}$ and $x_{\gamma_{peak}=0.9}$, is used as in Fransson & Shahinfar [47]. The intermittency curves are in a relatively good agreement with the correlation of Fransson & Shahinfar [47], despite the presence of the two competing mechanisms in the high L_f-high T_u case (see section 4.4). The conditioned friction coefficients are plotted in figure 4.18 (middle and right). As in Nolan & Zaki [74], the laminar contribution increases in the transitional region due to the laminar streaks, with a relatively steeper slope due the shorter transitional region. Due to the earlier transition in the high L_f-high T_u case, the laminar-conditioned data deviates rapidly from

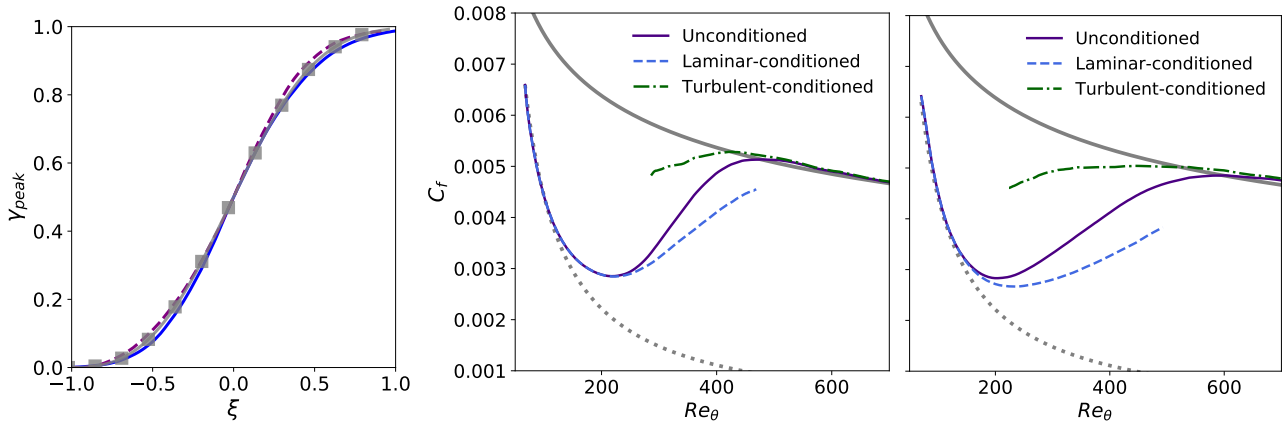

Figure 4.18: Peak intermittency evolutions (left panel) for the low L_f-high T_u (——) and high L_f-high T_u (– – –) cases and correlation of Fransson & Shahinfar [47] (——). Skin friction C_f distribution of the low L_f (middle) and high L_f (right) for unconditioned and conditioned statistics in $T_u = 4\%$ Novec cases, with laminar (·····) and turbulent (——) correlations.

the unconditionned C_f. The turbulent contribution initially exhibits lower friction levels than a fully turbulent correlation due to the effect of the turbulent spot periphery. This calming effect is due to the recovery trail downstream of a turbulent spot, which contains fewer high-frequency fluctuations compared to the turbulent flow in the same region (Schubauer & Klebanoff [265]).

The mean velocity profiles of the unconditioned and conditioned data are shown figure 4.19 for the low L_f-high T_u Novec simulation for various streamwise stations. The time-averaged profiles gradually evolve from a laminar state toward a fully turbulent profile. The laminar-conditioned profiles (middle panel) exhibit the shape characteristic of laminar state, but the profiles are distorted by the presence of laminar streaks. On the contrary, the turbulent profiles reach rapidly a self-similar behavior corresponding to the fully turbulent state, represented here by the time-averaged solution at the last station. The discriminated Reynolds shear stresses shown in figure 4.20 highlight the rapid amplification during transition. The laminar- and turbulent-conditioned data for the two cases show that the laminar part has limited growth with maximal levels below the unconditioned data at γ=0.1. The turbulent-conditioned profiles exhibit large amplitudes with respect to the time-averaged data and gradually decrease along the transitional zone, while remaining above the unconditioned profile γ=0.9.

4.3.4 Streak statistics

To provide a statistical view of laminar streaks, a detection algorithm (Nolan & Zaki [74]) is used. The streaks are identified in the laminar region by the local extrema of the streamwise velocity u in each yz-plane.

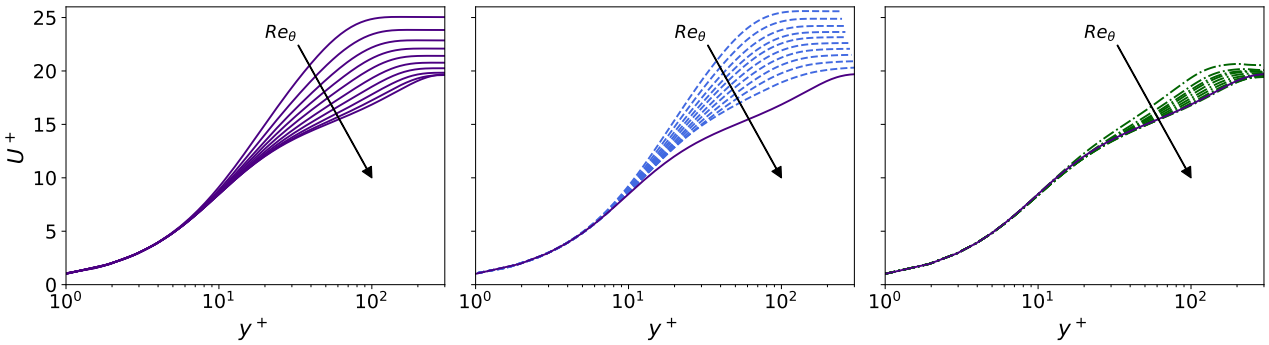

Figure 4.19: Time-averaged (left), laminar-conditioned (middle) and turbulent-conditioned (right) mean streamwise velocity profiles between γ=0.1 and 0.9 every 0.1 for the low L_f-high T_u Novec case. The time-averaged profile at $\gamma = 0.9$ is kept in middle and right panels.

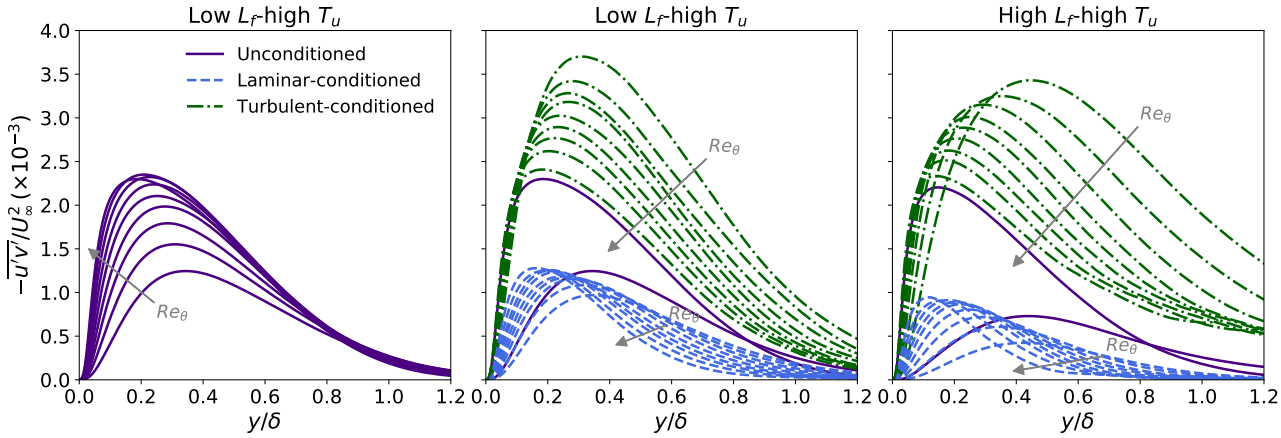

Figure 4.20: Time-averaged Reynolds shear stresses for low L_f-high T_u Novec case (left) and conditioned Reynolds shear stresses for increasing Re_θ values (middle and right), where the unconditioned time-averaged profiles at γ=0.1 and 0.9 are displayed for comparison.

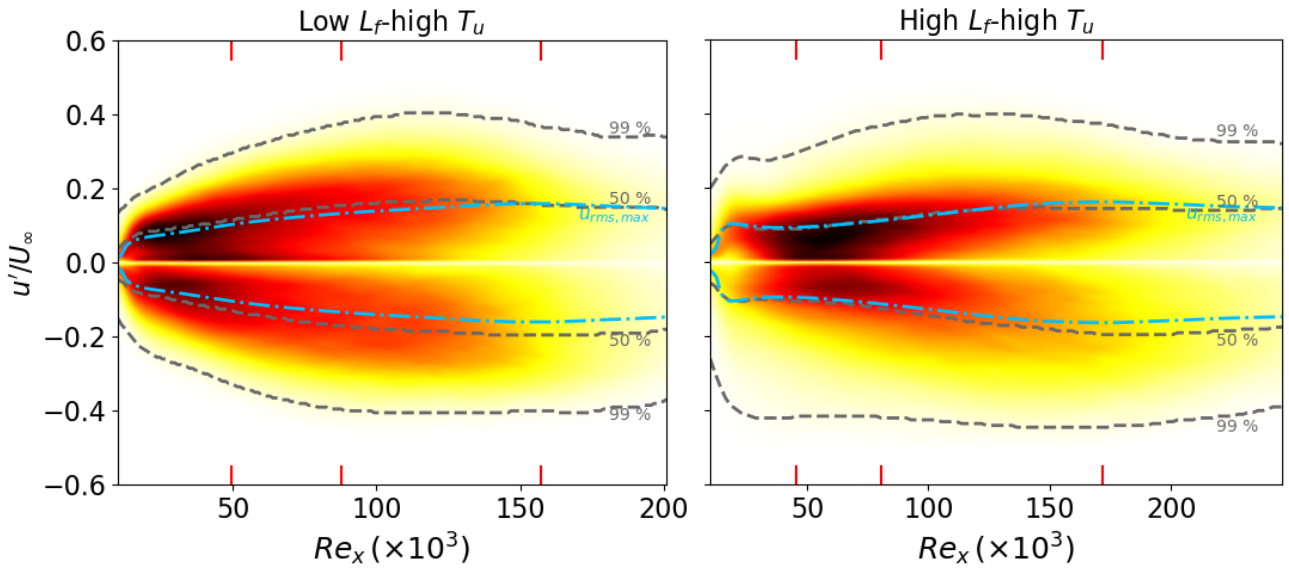

Figure 4.21: 2D density function of the streak amplitude, plotted between the inlet and the station where γ_{peak}=90%. Darker colors denote higher density, color levels between 0 and 3×10^{-7} (low L_f-high T_u) and 2.6×10^{-7} (high L_f-high T_u).

First, the detection is limited to the BL by rejecting extrema found above δ such that u_δ=0.95U_∞. When two extrema in a yz-plane are separated by a distance smaller than a threshold value Δx, only the more intense one is kept. Then, extrema are connected to form streaks by scanning the streamwise direction with the following criteria: extrema separated by a distance lower than $2\Delta x$ belong to the same streak and streaks shorter than $8\Delta x$ are rejected. A population of streaks is then obtained for each of the volumes, each streak being a collection of points characterized by a position and a streamwise fluctuation velocity. An example of the streak detection output is given in figure 4.17. It is worth noting that the streak identification does not distinguish between streamwise streaks and Λ-shaped vortices. An example of a Λ structure detected by the algorithm is circled in orange in the figure.

In figure 4.21, the repartitions of the streak amplitude u' along the streamwise direction, smoothed by a 2D kernel density estimator (KDE) and normalized by the integral, are shown for the T_u=4% Novec cases. A similar distribution as in Nolan & Zaki [74] is obtained for the low L_f-high T_u case, whereas the distribution in the high L_f case differs. In the low L_f case, the distribution of streak amplitudes spreads out quickly in the pretransitional region to reach high intensities, which then remain relatively constant. For the large-scale FST simulation, the median distribution of the low-speed streaks (denoted 50%) rapidly attains a first level and then continues to increase to a second one along the transitional region. In the two cases, very intense

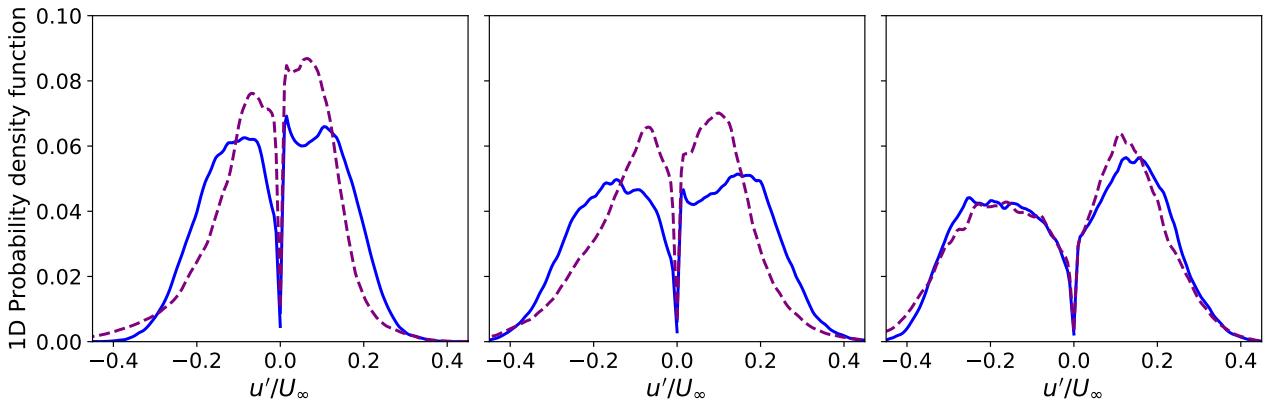

Figure 4.22: Comparison of the streak amplitude distributions at the stations corresponding to $C_{f,min}/2$ (left), $C_{f,min}$ (middle) and γ=0.5 (right). The distributions are normalized by the area under the curve. Line legend as in table 4.2.

low-speed and high-speed streaks are present, with the 1% most intense streaks (marked by the 99% line) reaching amplitudes as high as 40% of U_∞. Even if the values of $u_{rms,max}$ (represented by the cyan dashed line) generally underestimate the low-speed streak amplitudes [74], the median distribution and the $u_{rms,max}$ evolution are in fairly good agreement.

A comparison of the two cases is provided in figure 4.22, which reports the streak amplitude distributions (at stations marked by red ticks in figure 4.21). At the two first stations, the probability density function for the low-L_f case appears more spread toward high amplitudes than for the high-L_f case. Furthermore, for the latter case, an asymmetry between the low-speed and high-speed streaks is noticeable. Since the peaks correspond to the same amplitudes for low- and high-speed streaks, the asymmetry essentially comes from the lower occurrence of high-amplitude high-speed streaks. As the middle of the transitional region is reached (at γ=0.5), all the low-speed streak distributions collapse at $\gamma = 0.5$, even if some discrepancies remain for the high-speed streaks.

In figure 4.23, the 2D probability densities of the high-speed and low-speed streak heights with respect to the wall are given. Similar distribution are found between the two cases. Slightly more differences are observed between low-speed and high-speed streaks distributions, specially in the low L_f-high T_u case, but they remain in a good agreement. Initially, the streak altitude rises according to BL thickening, but at a lower rate, so that the streak population is located closer and closer to the wall relative to the local BL thickness. Then the height remains almost constant.

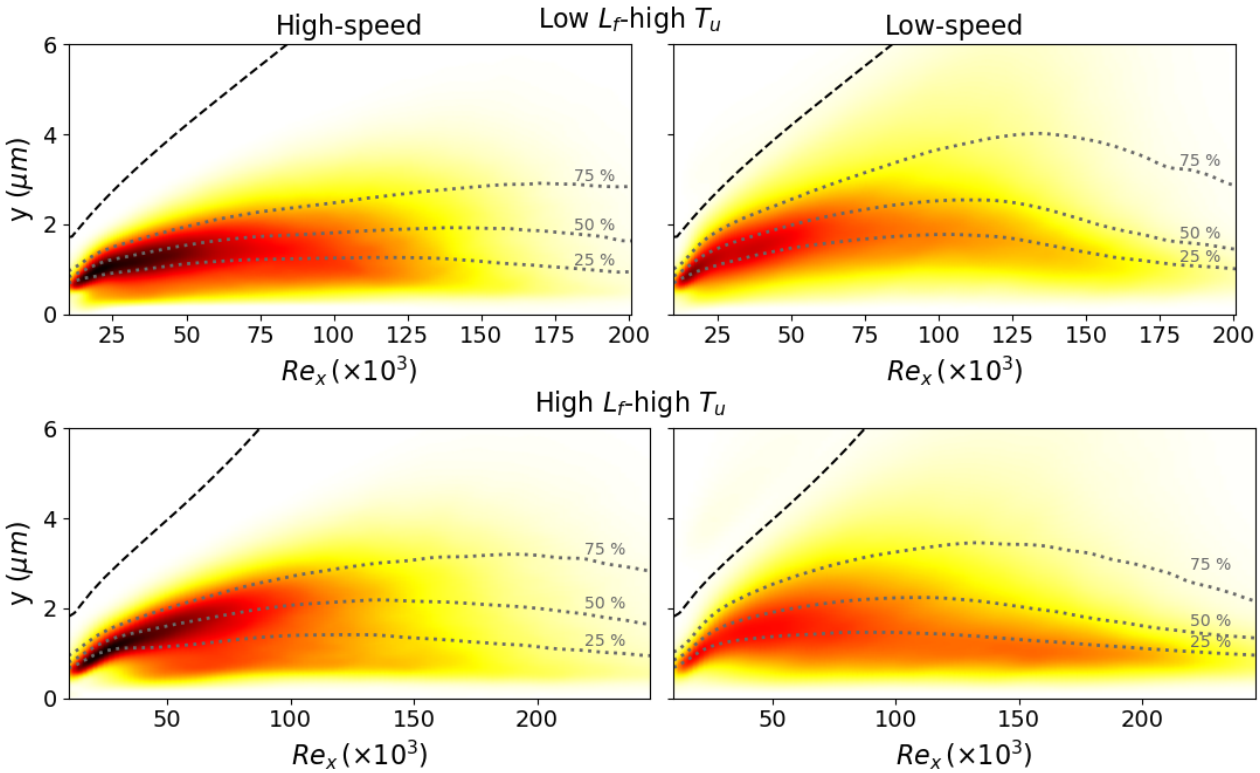

Figure 4.23: 2D density function of the high-speed (left panel) and low-speed (right panel) streak heights, plotted between the inlet and the station where γ=90%. Darker colors denote higher population density (color levels between 0 and 3.4). The boundary layer edge (– – –) corresponds to δ_{99}.

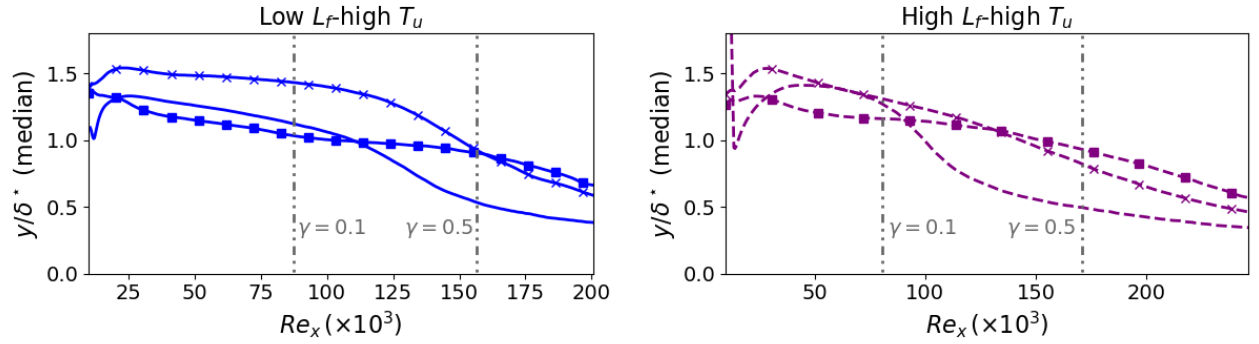

Figure 4.24: Evolution of the median altitude of streaks in the T_u=4% Novec cases. The lines with crosses denote low-speed streaks, the lines with squares the high-speed streaks, and the lines without symbol the wall-normal location of $y(u_{rms,max})$.

The evolutions of the median height for low-speed and high-speed streaks are reported in figure 4.24. For the two cases, the median height normalized by δ^* deviates from the initial value and slowly decreases. As observed by Andersson *et al.* [66], the median height of high-speed streaks is closer to the wall than the one of low-speed streaks. In a linear theory of optimal disturbances, the altitude of low and high-speed streaks would be the same [256] ($\sim$ 1.2-1.4δ^*), but, when solving the full Navier–Stokes equations, low-speed streaks are displaced away from the wall by non-linear interactions [66]. This difference is reduced before the end of the transitional region, and a reverse arrangement is observed in the high L_f simulation. The evolution of $y(u_{rms,max})$ has been added for comparison. The decreasing trend is similar to the one of low-speed streaks, but the location of the maximum of streamwise velocity perturbations generally underestimates the median altitude of streaks. More discrepancies are observed for the high L_f-high T_u simulation, which presents an initial bump in $y(u_{rms,max})$.

4.4 Paths to transition

In all the simulations, laminar low-speed streaks, which are a key element in the formation of turbulent spots in FST-induced transitions and have been investigated in section 4.3, are generated inside the boundary layer. In the high L_f cases, low-speed Λ-shaped structures are also observed. As reported by several authors [57, 76], these Λ-shaped structures can play an important role in the generation of turbulent spots. Therefore, their participation in the transition process is investigated in this section and the competition between these two transition paths is analyzed.

4.4.1 Streak instabilities

Turbulent breakdowns due to low-speed streak instabilities are observed in all the simulations. As the FST levels are relatively high, the streaks rapidly become distorted, making it difficult to clearly distinguish between the sinuous and varicose modes. Also, knowing that the symmetric and anti-symmetric modes have been shown to combine in the case of streak transient growth (Hoepffner *et al.* [70]) or unsteady base streaks (Vaughan & Zaki [72]), no attempt has been made to classify the streak instabilities. An example of each mode is given below for the high L_f-low T_u Novec case to show that, despite the competition with another breakdown mechanism and relatively wider streaks, both modes are active with the larger FST length scale. An example of a sinuous breakdown is illustrated in figure 4.25 using three successive 3D views of the low-speed streak before the breakdown. In the first view, two quasi-streamwise vortices are observed on each side of the

Figure 4.25: Observation of a sinuous-like breakdown in the high L_f-low T_u case at three successive times. Isosurfaces of the streamwise velocity fluctuations: $u' = 0.16U_\infty$ (white), $-0.16U_\infty$ (black). Isosurfaces of the Q-criterion are also depicted in light brown.

low-speed streak. In particular, the streak is flanked by a high-speed streak only on one side. This is similar to the one-sided sinuous mode described in Brandt *et al.* [45], where a high-speed streak approaches a low-speed region on one side. In the last picture, the low-speed streak begins to be fully disrupted, prior to the emergence of a turbulent spot. A varicose-like breakdown is shown in figure 4.26. In the upper right panel, the wall-normal velocity fluctuations exhibit an alternation of positive and negative values over the low-speed streak. Vortices, identified by the red isolines, begin to emerge over this pattern, leading to the formation of alternating V and Λ-vortices (Brandt *et al.* [45]). The low-speed streak (left pictures) is highly perturbed by these horse-shoe structures and disrupted symmetrically relative to the center of the streak.

4.4.2 Λ-shaped structures

An important difference between the low-L_f and high-L_f cases is the presence of low-speed Λ-shaped structures in the latter. The formation of these Λ-shaped structures is illustrated in figure 4.27 through 3D views in the high L_f-low T_u Novec case. First, several quasi-spanwise vortices appear close to the wall due to the interaction of the BL with large FST structure above, as highlighted by $w' = -0.04$ isosurfaces. Similarly to

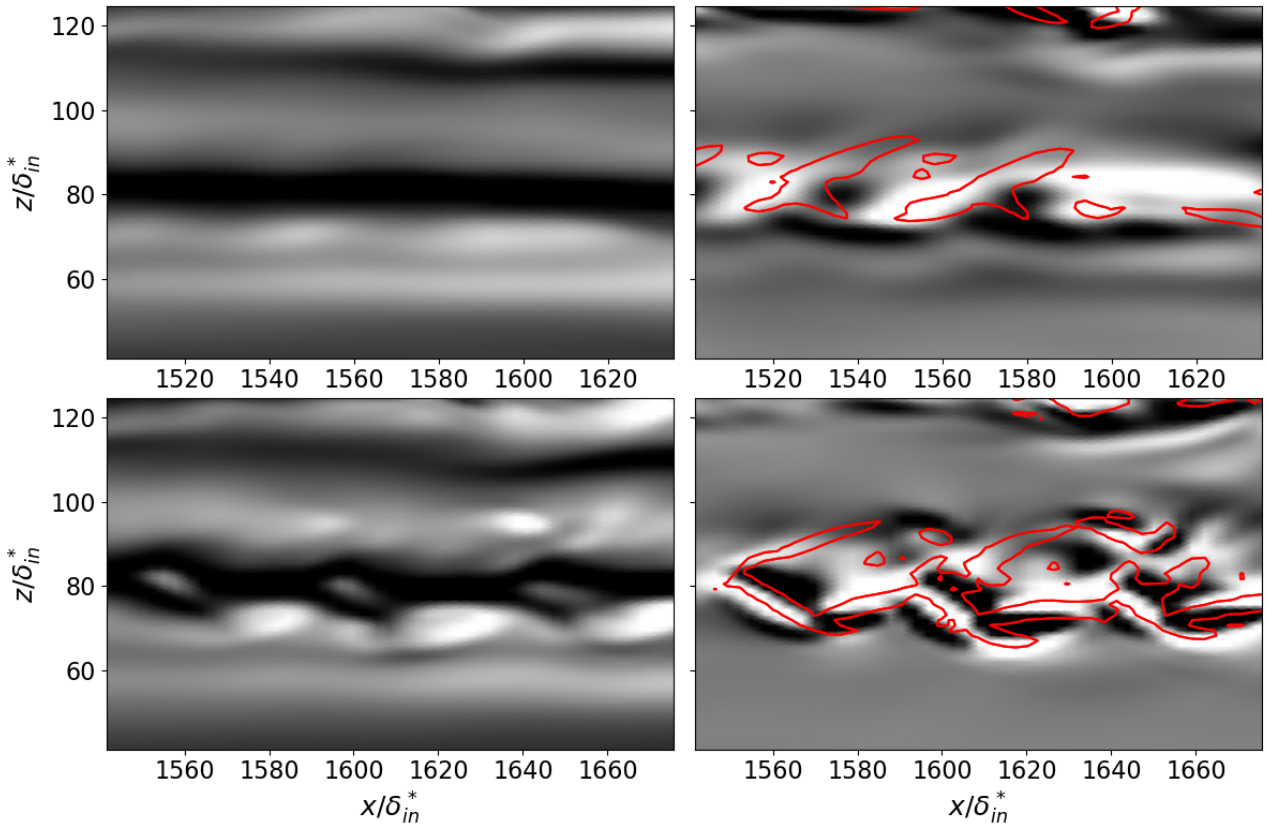

Figure 4.26: Observation of a varicose-like breakdown in the high L_f-low T_u case over two successive times (top and bottom). Streamwise fluctuations (left, $u' = \pm 0.25 U_\infty$ from black to white) and wall-normal velocity fluctuations (right, $v' = \pm 0.01 U_\infty$ (top) and $\pm 0.03 U_\infty$ (bottom) from black to white). Isolines of the Q-criterion projected around the wall-normal position of the plane are plotted in red.

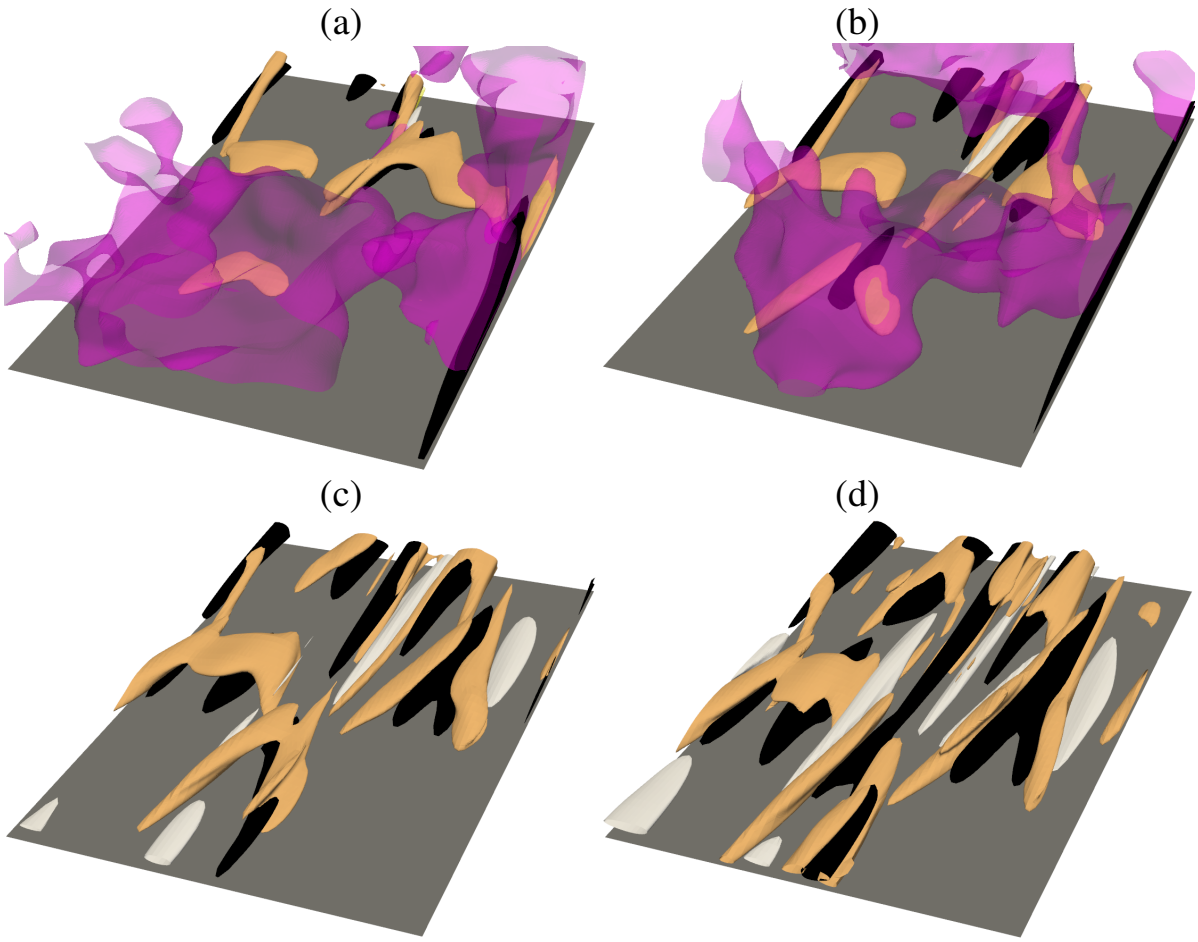

Figure 4.27: Λ-structure formation in the high L_f Novec case with T_u=2.5% at four successive times. Isosurfaces of the streamwise velocity fluctuations ($u' = 0.12U_\infty$ in white, $-0.12U_\infty$ in black), and isosurface of the Q-criterion in light brown. Isosurfaces of the spanwise velocity fluctuations $-0.04U_\infty$ (transparent purple) in top pictures.

Ovchinnikov *et al.* [57], these structures are stretched in the streamwise direction, leading to the formation of Λ-vortices. The strong Λ-vortex in the upper-right corner generates a low-speed patch of velocity which evolves further downstream in the Λ-structure. The Λ-vortex in the bottom of the pictures give rise to a one-leg Λ, whose head then connects to a downstream low-speed streak.

The breakdown of a low-speed Λ-structure is illustrated in figure 4.28 (left). The Λ vortex, flanking the low-speed structures, intensifies and stretches into a hairpin vortex, the tips of which turn into the characteristic Ω shape. As observed in figure 4.28 (right) in a xy-plane located in the middle of the low-speed structure, the breakdown imprints both the spanwise and wall-normal velocity components in the upper half region of the

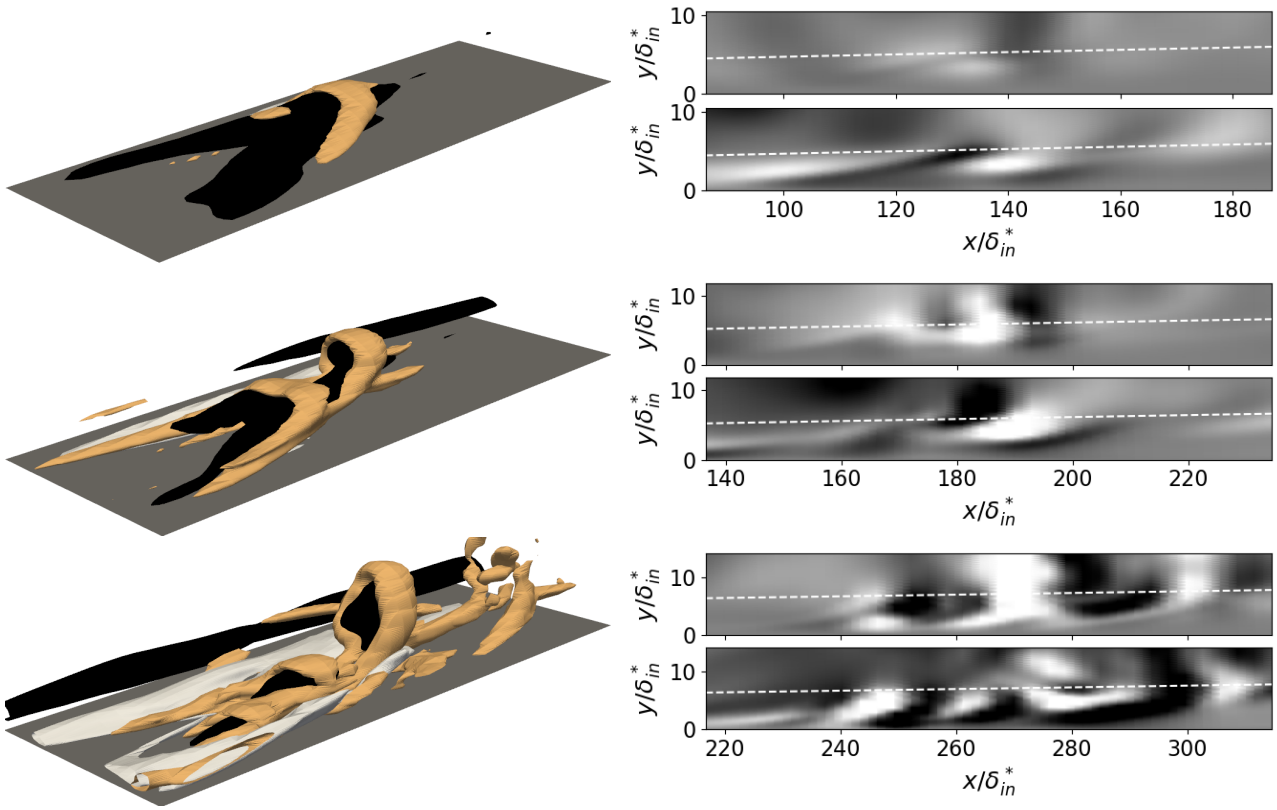

Figure 4.28: Left: Observation of a Λ-structure undergoing turbulent breakdown in the high L_f-high T_u case at three successive times for $z/\delta^*_{in} \in [-11, 1]$. Isosurfaces of the streamwise velocity fluctuations ($u' = 0.2U_\infty$ in white, $-0.2U_\infty$ in black), and isosurface of the Q-criterion in light brown. Right: wall-normal (top) and spanwise (bottom) components of velocity fluctuations at the position z/δ^*_{in}=-6, with levels $\pm 0.07U_\infty$ from black to white and x and y-axis aspect ratio of 1.4, 1.2 and 1.0 for the first, second and third snapshots, respectively.

boundary layer, coherent with the observations in Ovchinnikov *et al.* [57].

Interestingly, these structures are often organized obliquely in an xz-plane, as shown in figure 4.29 (left). A similar organization can be observed in the figure 16 of Ovchinnikov *et al.* [57] (not commented by the authors). As the Λ structures break down into turbulence, an oblique turbulent band may eventually form. In the high L_f-high T_u case, on a total of nine relatively well-defined oblique bands, the angle is estimated between 25° and 40°, with an average value around 30°. This point is further discussed in section 4.4.4.

As reported in section 4.2, a first peak marks the evolution of $u_{rms,max}$ (see figure 4.5) in the large-scale FST simulations around the position where Λ-structures emerge and which is related to their growth. Similarly, the inflection points, observed on $u_{rms,max}$ evolution for the low L_f cases at T_u=2.5% and 4%, are an indication that similar structures may also be present in these simulations. However, no low-speed Λ-shaped structures are

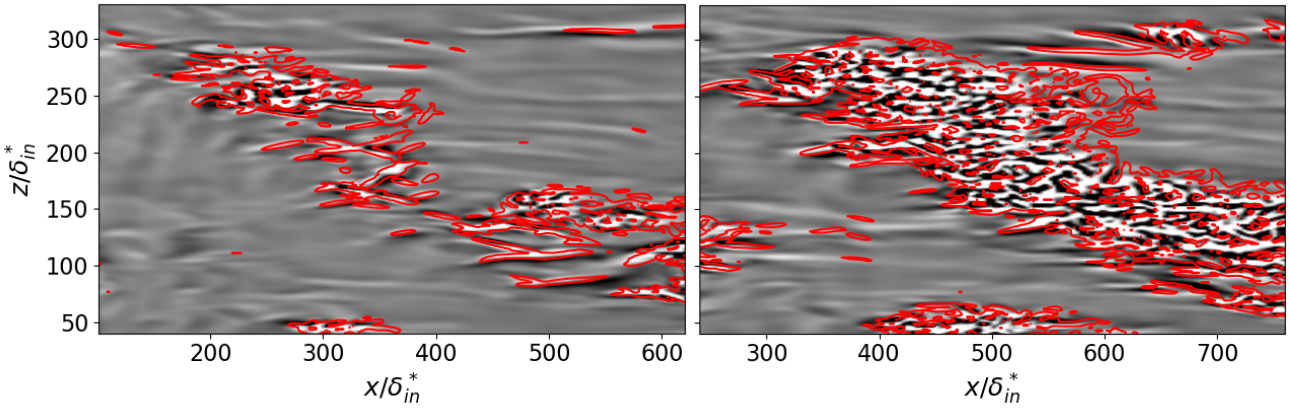

Figure 4.29: Observation of Λ structures in the high L_f-high T_u Novec case organized in a oblique manner (left) and leading to a turbulence band (right). Wall-normal velocity fluctuations ($v' = \pm 0.01 U_\infty$, from black to white). Isolines of the Q-criterion projection around the wall-normal position of the plane plotted in red.

observed by inspection of snapshots of the streamwise fluctuations (*e.g.* figure 4.6). A more careful examination of 2D and 3D visualizations of the low L_f-high T_u case also failed to reveal the presence of low-speed Λ-shaped structures but did reveal the presence of spanwise and Λ-vortices close to the inlet, such as in figure 4.30. With respect to the high-L_f simulations, the vortices are smaller and may not be strong enough to produce the low-speed Λ-structures.

4.4.3 Competition between the two breakdown mechanisms

The competition between these two breakdown scenarios is analyzed via the laminar-turbulent discrimination performed in section 4.3.3. The conditioned $u_{rms,max}$ evolutions are plotted in figure 4.31 for the low L_f-high T_u (left) and high L_f-high T_u (right) cases. The laminar-conditioned curve in the low L_f-high T_u case is initially superimposed on the unconditioned statistics before deviating around $Re_\theta \sim 250$. It does not exhibit the secondary growth observed in the unconditioned curve, related to the eruption of turbulent spots [74]. By contrast, in the high L_f-high T_u case, the laminar-conditioned u_{rms} quickly deviates from the unconditioned data. This early deviation can be attributed to the turbulent breakdown of low-speed Λ-shaped structures near the inlet, which is coherent with the earlier transition onset reported on the C_f evolution in figure 4.4 and the extension of the transitional region.

Based on the laminar-turbulent discrimination (see section 4.3.3), the turbulent spots are tracked in the T_u=4% Novec cases. First, using snapshots of the xz-plane from the binary segmentation, an estimation of the x-z location is obtained for each spot. Then, the evolution of the spot footprint in the different directions

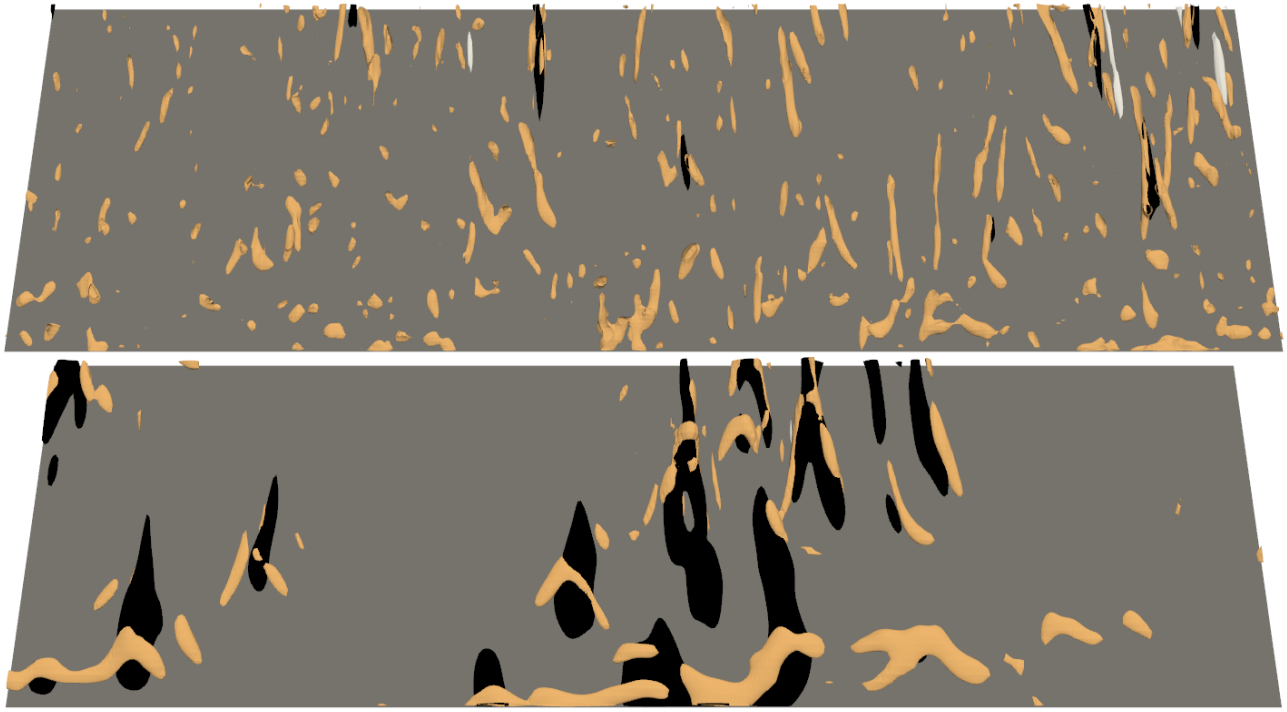

Figure 4.30: Comparison of Λ-structure between low-L_f (top) and high-L_f (bottom) cases at T_u=4% for $x/\delta^*_{in} \in [33, 181]$ and $z/\delta^*_{in} \in [-230, 230]$. Isosurfaces of the streamwise velocity fluctuations ($u' = 0.22U_\infty$ in white, $-0.22U_\infty$ in black), and isosurface of the Q-criterion in light brown.

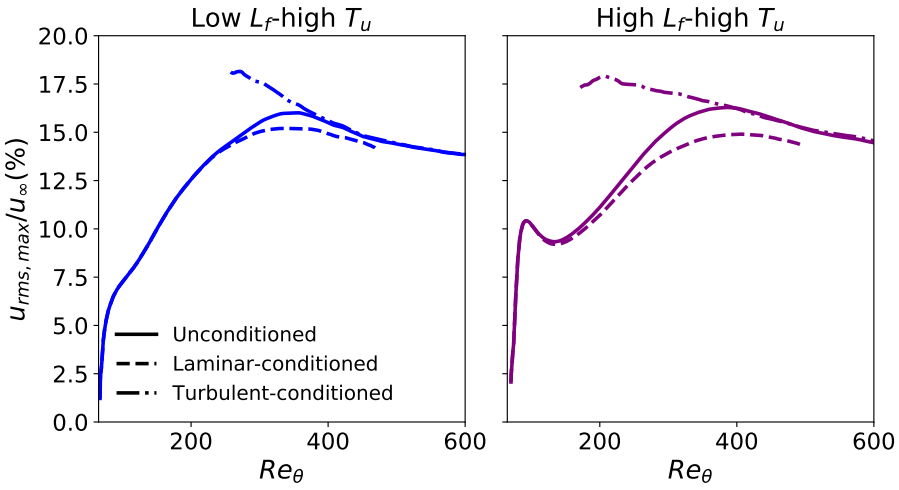

Figure 4.31: Evolution of $u_{rms,max}/U_\infty$ for unconditioned and conditioned statistics for low L_f-high T_u (left panel) and high L_f-high T_u (right panel) cases in Novec.

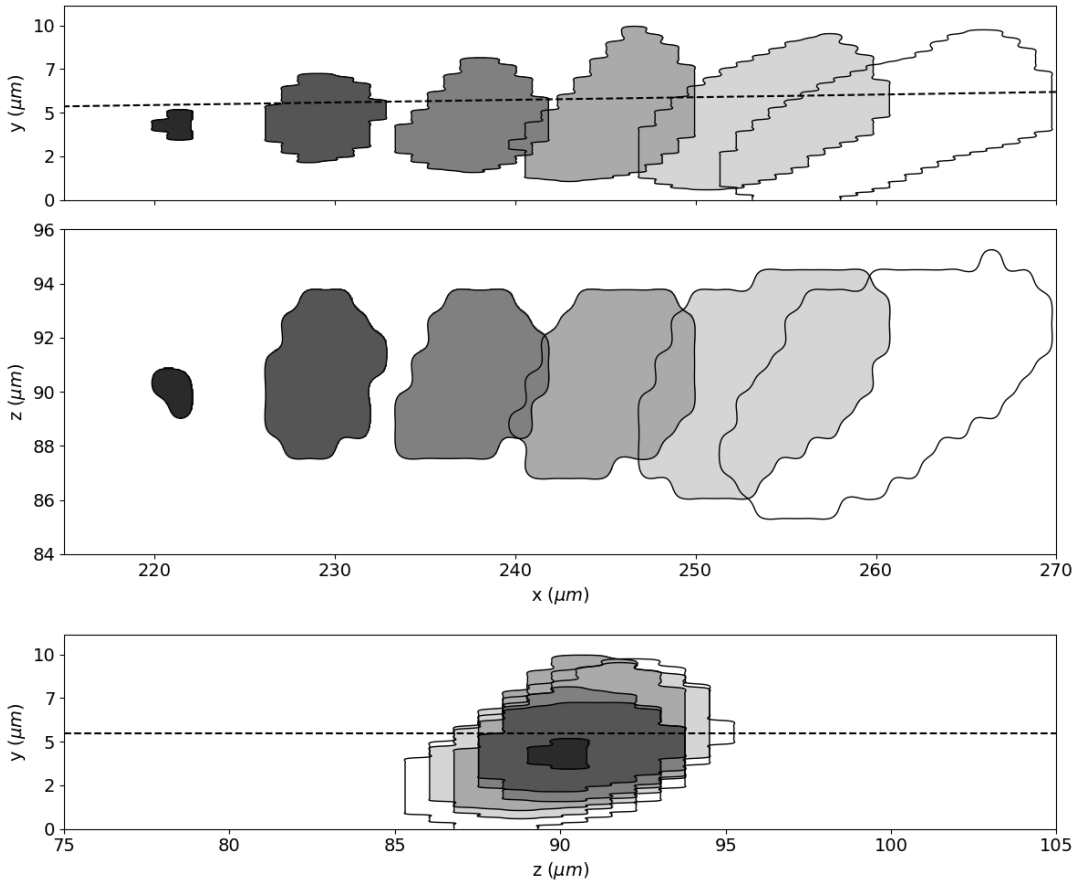

Figure 4.32: Growth of a turbulent spot in the low L_f-high T_u case shown every 80$^{\text{th}}$ time unit. From top to bottom: side, top and front views of the spot footprint. BL thickness δ_{99} (– – –).

is reconstructed and the 3D locations of the spots are determined. An example of an isolated spot in the low L_f-high T_u case is shown figure 4.32. The spot appears relatively high inside the BL at $y \sim 4\,\mu$m and then expands in the three directions. Multiple spots can also appear in the same area, for instance when a low-speed streak is destabilized at several locations. An example is given in figure 4.33, where two spots appear relatively close at $x \sim 395$ and $425\,\mu$m and merge as they spread. A third turbulent patch can be observed near $x \sim 385\,\mu$m, which rapidly melts with the other spots. In the following, spots are only reported if they are sufficiently distant from each other and if they persist for a sufficient time.

A total of N_s=327 and 381 spots are counted for the low L_f-high T_u and high L_f-high T_u cases, respectively. When divided by the spanwise extent of the computational domain, the comparison of N_s/L_z clearly shows a more intense turbulent spot production in the low L_f-high T_u case, consistent with its shorter transition length. The streamwise and wall-normal histograms of spot inception locations are reported in figure 4.34. The

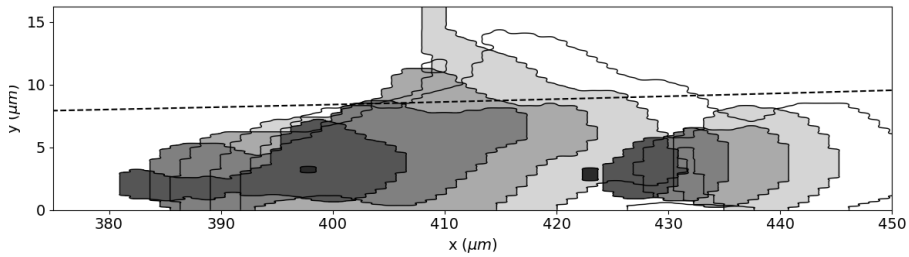

Figure 4.33: Side view of the growth of multiple turbulent spots in the case low L_f-high T_u (shown every 48$^{\text{th}}$ time unit). BL thickness δ_{99} (– – –).

histograms are normalized so that the sum of the bins is equal to 1. The standard shape for spot nucleation rate is recovered for the streamwise distributions of the low-L_f simulation [266, 267]. Increasing L_f gives a more spread distribution, in line with the smoother and wider transition length in the high L_f case. Interestingly, the streamwise distribution in the high L_f case has two maxima, one of which is very close to the inlet and contributes to the spreading of the transition region. The second one (in green) can be related to the turbulent breakdown of laminar streaks, while the first one (in orange) is due to the presence of Λ-shaped turbulent spot precursors, which account for about a third of the total number of spots. No significant differences are observed between the simulations for their wall-normal distribution (figure 4.34, bottom). The maxima of the distributions, associated to streaks instabilities, are located around $y/\delta_{99} \sim 0.4$-0.5, slightly lower than the value (~ 0.55) in the ZPG case of Nolan & Zaki [74]. This reveals that the outer instability is dominant in the simulations and that increasing L_f does not tend to promote inner instabilities (Vaughan & Zaki [72]). Similarly, the first peak associated with Λ structures in the high L_f-high T_u case (in orange in figure 4.34) is located in the outer region (around ~ 0.6), which is coherent with the observations of Ovchinnikov *et al.* [57] and the turbulent breakdown mechanism described in figure 4.28.

The competition between these two mechanisms is further analyzed by looking at the distribution of the laminar streaks amplitude. As in figure 4.21, the repartitions of the streak amplitude u' is plotted again in figure 4.35, this time with the amplitude of the low-speed and high-speed streaks in closest proximity of the turbulent spot locations reported in black circles. In the low-L_f case, the turbulent spots are associated with streak amplitudes u'/U_∞ ~0.2-0.4, coherent with the values found in Nolan & Zaki [74]. The vast majority of the associated streaks lie within the median and the 99$^{\text{th}}$ percentile of the streak population, well above the laminar-conditioned $u_{rms,max}$ evolution which peaks around 0.15 (see figure 4.31). The same observations can be made in the high-L_f simulation for the turbulent spots located beyond $Re_x = 80 \times 10^3$ and which are mainly associated to streaks instabilities. Closer to the inlet, however, the amplitude distribution shows a different shape

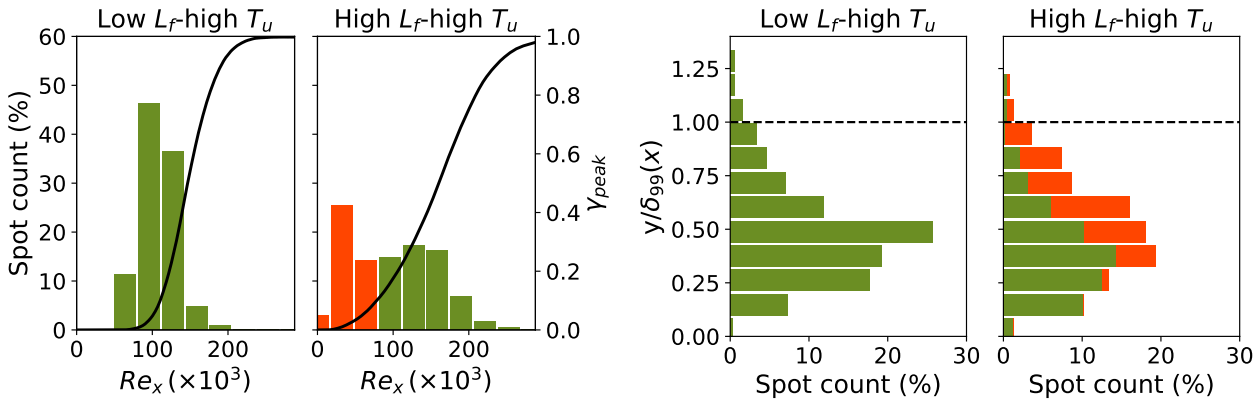

Figure 4.34: Normalized distributions of streamwise (left) and wall-normal (right) positions of the spot inceptions. The solid lines in left panels represent thei intermittency function, and the horizontal dashed lines in right panels denote the BL thickness δ_{99}.

in the high-L_f case. The median distribution of the low-speed streaks (denoted by 50%) quickly reaches a first level and then rises to a second level along the transition region. As the low-speed Λ-shaped are captured by the detection algorithm, the initial small peak in the pre-transitional region is reflected in the median amplitude distribution. This gives an indication of how intense the low-speed Λ structures leading to turbulent breakdowns can be, as the turbulent spots located below $Re_x = 80 \times 10^3$ are associated with amplitudes greater than $0.4U_\infty$ for a non-negligible fraction.

4.4.4 Discussion about linear and nonlinear growth mechanisms

Two competing scenarios emerge from the previous analysis. The classical one, sometimes referred to as *bypass transition in the narrow sense* [77], occurs preferentially when the incoming turbulence intensity is moderate (typically T_u < 2-4%), and has been described in a lot of studies ([55, 40, 45, 268, 43] to cite a few). The classical scenario can be summarized as the linear non-modal growth of streaks, which then experience secondary instabilities (sinuous or varicose) and lead to the generation of turbulent spots. The second scenario is characterized by the appearance of Λ-shaped structures, which are further stretched to hairpin vortices before breaking down to turbulence. This alternative route was first described by [57], who simulated large-scale incoming turbulence impinging on a flat plate with an elliptic leading edge to reproduce T3B experiments. The same phenomenology, called Δ-shaped structure, was obtained in the DNS of Wu *et al.* [76], who excited a flat plate by the periodic passage of a cube of HIT at high intensity. In his recent review, Wu [77] reports that the classical scenario is found with the same setup by reducing the intensity of the incoming turbulence

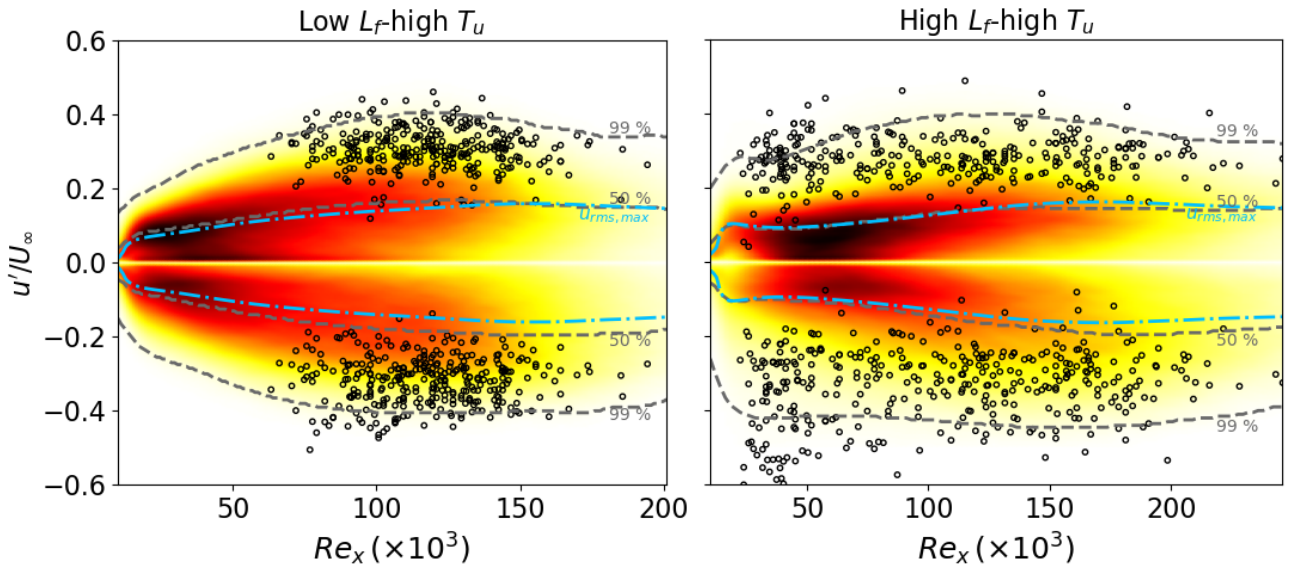

Figure 4.35: 2D density function of the streak amplitude in the $T_u = 4\%$ Novec cases (see figure 4.21) reported with the positive and negative streak amplitudes in closest vicinity to the turbulent spot inception locations in black circles.

($T_u \sim 1.5\%$), which is supported by the present observations. He thus proposed a sub-categorization of bypass transition as a function of the incoming turbulence intensity. In the present study, we also demonstrate that the integral length scale plays a role in the definition of an upper bound for the classical scenario (or, at least, in the definition of what we call a high turbulence intensity). In this section, we discuss the alternative routes of bypass transition in view of earlier works. Even if the conditions of the previous experimental, numerical or theoretical studies are different, a number of common features can be identified through a qualitative comparison.

Spot inceptions due to Λ-shaped/Δ-shaped/hairpin vortices can occur at earlier locations than the streak growth of the classical scenario. We are then confronted with a competition between bypass transition in the narrow sense and nonlinear receptivity mechanisms that "bypass" this route. Depending on the FST parameters (T_u, L_f) and the setup (shape of the leading edge, presence of pressure gradients), either the transition is already achieved due to the nonlinear receptivity or it is partially realized, and the streak growth and breakdown then take over. Similar competition has been described at the lower bound of the classical scenario, in the overlapping range $0.5 < T_u < 1.5\%$. A competition between natural (orderly transition due to TS waves) and bypass transition in the narrow sense can yield complex interactions [43, 269], which has been called *mixed mode transition*. The present case high L_f-low T_u is an example of a competing scenario for the upper bound of the classical scenario. Even for the higher T_u and L_f conditions, only approximately one third of transitional

spots are due to the Λ-shaped events, the rest being due to streaks.

As discussed in section 4.4.2, a striking feature observed when Λ-structures are generated close to the inlet is their oblique arrangement, which is reminiscent of the laminar-turbulent bands described in the context of subcritical turbulence. This intriguing patterning has excited the curiosity of numerous researchers (see the reviews of Manneville [270] and Tuckerman *et al.* [271]). It appears clearly in flows that are linearly stable, meaning that another mechanism, namely a nonlinear response due to the intrinsic nonlinearity of the Navier-Stokes operator, is responsible for the onset of turbulence. The first configuration where band turbulence has been observed is the annular Couette flow. Such banded patterns have also been obtained in wall-bounded turbulence on plane surfaces, namely plane Couette and Poiseuille flows (see [270, 271, 77]). In linearly stable flows, the main analysis approach consists in decreasing the Reynolds number from a fully turbulent state. For instance, in channel flow, the fully turbulent flow gives rise to a patterning regime with turbulent bands exhibiting an almost constant angle of 25° with respect to the mean flow direction [272]. In the present nonlinear transition an angle around 30° has been obtained, even if the bands are less marked since the flow is inhomogenous in the streamwise direction. In order to shed light on the reasons for such a pattern, Xiao & Song [273, 274] have studied the dynamics of the turbulent bands in large channel domains. They found that the downstream end of the band displays fast streak growth, whereas streaks at the upstream end tend to decay. This asymmetry is responsible for the transverse growth of the band [275]. The task is more complex for boundary layers, which can develop unstable TS waves above a low supercritical Re and thus present a less marked subcritical character. Many routes, corresponding to the multiplicity of solutions in phase state, are then possible depending on the characteristics of the inflow. The main way of studying subcritical response of boundary layers consists in finding the disturbances that experiences the largest energy growth at a certain time level, called nonlinear optimal disturbance because a nonlinear optimization problem is solved. For instance, Cherubini *et al.* [276] studied the boundary-layer transition induced by such nonlinear optimal perturbations, which consists in vortices inclined in the streamwise direction surrounding a region of intense streamwise disturbance velocity. This *minimal seed* triggers nonlinear effects that lead to the formation of Λ-vortices rapidly breaking down into turbulent spots. The methodology has been applied to the FST-induced transition in Cherubini *et al.* [277], yielding the same subcategorization as found in the present simulations. For weak inlet perturbations (low T_u and low L_f), the optimal disturbances are laminar streaks corresponding to linear transient growth (the classical scenario). For high T_u and high L_f, the response is dominated by nonlinear structures, that are Λ-vortices turning to hairpin vortices in their more mature phase. The search for *edge*

states, which are sitting on the laminar-turbulent boundary in a phase-space perspective, is another step to find the most probable germs able to drive the transition [278, 279, 280]. Duguet *et al.*[279] obtained the edge state structure as combination of localized streaks and hairpin-like structures that can be self-sustained by a Waleffe-type mechanism [281]. Kerswell [282] summarizes theses approaches as *nonlinear nonmodal stability*, as a counterpoint to the linear nonmodal theory of transient growth [283]. In all scenarios in which nonlinearity plays the essential role, Λ- or harpin-like vortices are present in the boundary layer. More generally, the response of a laminar shear layer to large-amplitude localized disturbances is through the formation of hairpin vortices (see Suponitsky *et al.* [284] and references therein). The latter show that the ubiquitous character of streaks and hairpin vortices in boundary layers is due to the wall shear. Using various shapes of initial disturbances, their results demonstrate that "a small-amplitude initial disturbance (linear case) eventually evolves into a streaky structure independent of its initial geometry and orientation, whereas, a large-amplitude disturbance (strongly nonlinear case) evolves into a hairpin vortex (or a packet of hairpin vortices) independent of its geometry over a wide range of the initial disturbance orientations".

Other alternative bypass scenarios also fall in the category of nonlinear receptivity to intense localized disturbances. For instance, depending on the leading edge bluntness of a flat plate, Nagarajan *et al.* [19] described wavepackets events, that break down into turbulent spots before the development of streak instabilities. In their case, the initial seed is a streamwise vortex due to the stretching/tilting effect at the leading edge [285]. Ovchinnikov *et al.* [57] considered that this route is different from the one with Λ-shaped structure (as found in the present study) for several reasons: (i) the seed for Λ-vortices is a spanwise vorticity perturbation rather than a streamwise one, (ii) the wavepackets are characterized by wall-normal rather than spanwise velocity fluctuations in Nagarajan *et al.* [19], (iii) the wavepacket growth is not confined to the inner part of the boundary layer. In fact, the different nonlinear evolutions are due to different germs: a spanwise vorticity, $\omega_z = \partial v/\partial x - \partial u/\partial y$, amplifies wall-normal disturbances, significant away from the wall, whereas a streamwise vorticity, $\omega_x \sim \partial w/\partial y$, highlights spanwise fluctuations at the wall vicinity. The nonlinear receptivity in Nagarajan *et al.* [19] is not due to intense large-scale events in the FST but to the intensification of freestream turbulence in the leading-edge region, amplifying spanwise fluctuations. A motive for the present research being the transition in turbomachinery, and in particular ORC turbines, it is interesting to mention some earlier studies in that context. Zhao & Sandberg [59] also reported various routes of bypass transition for a high-pressure turbine blade. For low T_u and low L_f, the streak instability mechanism prevails, whereas for high T_u and high L_f, the spot inceptions occur upstream due to intense streamwise vortices generated at

the thick rounded leading edge. A wavepacket scenario is found, close to the observations of Nagarajan *et al.* [19], where near-wall spanwise disturbances precede the breakdown. As in Nagarajan *et al.* [19], the distortion at the leading edge is essential in creating the transition germ. The wavepacket then evolves in a reverse Λ-shaped structure. In the context of transition on compressor blades, Mao *et al.* [286] found that the nonlinear development of high-amplitude disturbances on the pressure side generates Λ-structures, which are further stretched to hairpin vortices before breaking down to turbulence. A link may also be drawn with the presence of Λ-shaped structures in wake-induced transition. For instance, Kyriakides *et al.* [20] provided experiments of the interaction between a cylinder wake and a flat-plate BL, and they observed the formation of secondary vortical structures in the near-wall region. The authors reported that these structures took a characteristic Λ-shape. Pan *et al.* [287], in a similar configuration, reported similar structures, which were due to the deformation of initially 2D spanwise vortices generated inside the BL in response to the von Kármán vortex street and which lead to the formation of a turbulent spot. The same conclusions were drawn in the experimental study of Mandal & Dey [21] (see their figure 4). The low-speed Λ-shaped structures observed in the present study also originate from the interaction with large scales present in the freestream, as in the case of cylinder wakes. This further stresses the importance of FST scales in the generation of such structures. In the case of high-pressure turbine stage, due to the interaction of incoming periodic wakes with the suction side, this breakdown mechanism already competes with streak breakdown for the generation of turbulent spots [22].

4.5 Influence of freestream turbulence on fully turbulent boundary layers

Downstream of the transition region, freestream turbulence (FST) is expected to interact with the turbulent boundary layer (TBL). Early experimental investigations into FST's influence on TBLs reported enhanced heat transfer in the presence of elevated turbulence levels ($T_u \sim 7-10\%$) [288, 289], while no measurable effects were observed for lower intensities ($T_u \leq 3.8\%$) [290, 291]. In addition to increased heat transfer, FST was found to enhance the skin friction coefficient and reduce the wake region of the mean velocity profile [292, 293, 294, 295, 296, 297]. Simonich & Bradshaw [292] initially observed that the integral length scale L_f impacted the Stanton number. Subsequently, Hancock & Bradshaw [293] and Blair [294] reinforced the importance of L_f on FST's influence over TBL. For $T_u \sim 2.5-5.8\%$, Hancock & Bradshaw [295] found that FST mostly affected the outer layer, with larger freestream length scales penetrating further into the BL, while the logarithmic law was little affected. Thole & Bogard [298] further assessed this effect for FST intensities up to 20%. Examining the effects of large-scale FST with intensities up to 10%, Sharp *et al.* [296] observed

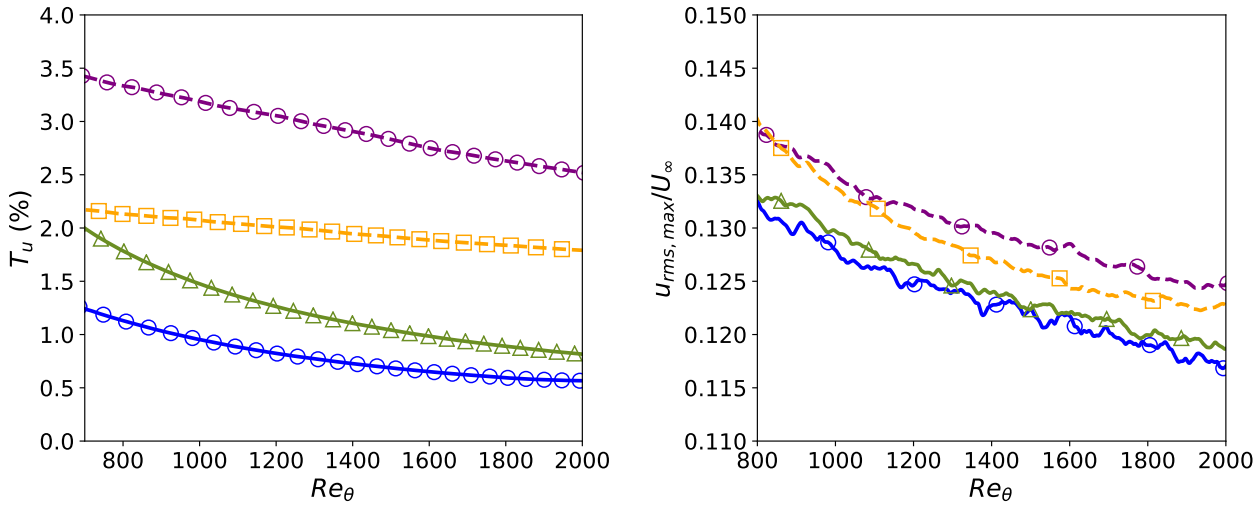

Figure 4.36: Evolution of the FST intensity (left) and $u_{rms,max}/U_\infty$ in the BL (right) for the different Novec cases in the TBL region: low L_f (——), high L_f (- - -) and $T_u = 2.5\%$ (□), 4% (○) and 6.6% (△).

the appearance of an outer peak in the pre-multiplied energy spectra at a much lower Reynolds number than without FST [235]. Nagata *et al.* [297] did not report a similar outer peak for small-scale FST, even if lower FST intensities were investigated ($T_u = 1.3 - 2.4\%$) compared to Sharp *et al.* [296]. This specificity of large-scale FST on TBL was leveraged by Dogan *et al.* [299] to emulate experimental high-Reynolds number TBL. They reported an increase in near-wall streamwise velocity fluctuations with FST intensity. In their DNS, You & Zaki [300] also reported the presence of outer large-scale motions with larger spanwise and streamwise extent than in TBL without FST, anticipating that these structures will long outlive the FST decay. However, Jooss *et al.* [301] demonstrated in their experiment that the outer peak imprinted by the high FST intensity becomes weaker as the FST decays downstream and the wake region is recovered.

To analyze the FST influence on TBL, the fully turbulent region of the present Novec simulations is scrutinized, except for the low L_f-low T_u Novec case, which does not attains a fully turbulent state in the domain. Also, the simulations in air do not extend far enough downstream for the TBL to be analyzed. As the low L_f-high T_u Novec case attains only $Re_\theta \sim 780$, a simulation with the same grid resolution but performed on a narrower domain, the low L_f-high T_u narrow Novec case, ($N_z = 80$ instead of 400) is used to analyze the TBL. In Appendix C.3, the two simulations are compared and shown to be in a perfect agreement in the domain. As reported in figure 4.36 (left) with T_u evolution for the different simulations, the FST intensities in the low L_f are already relatively low at the beginning of the TBL ($\leq 2.0\%$) and further decrease downstream. The high L_f

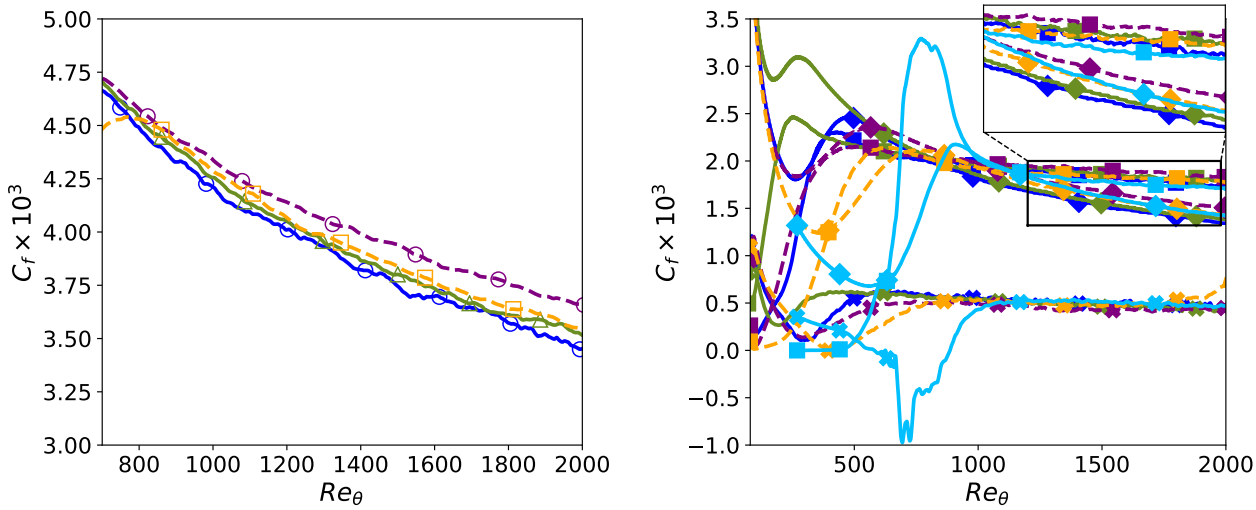

Figure 4.37: Friction coefficient distribution (left) and RD decomposition (right) for the different Novec FST cases: low L_f-high T_u narrow (——), low L_f-very high T_u (——), high L_f-low T_u (- - -) and high L_f-high T_u (- - -) cases. RD decomposition (Eq. 3.5): $C_{f,v}$ (lines with diamond symbols); $C_{f,t}$ (lines with square symbols); $C_{f,x}$ (lines with crosses). The LES-MF case (——) is also reported for the RD decomposition (cf section 3.4.3).

cases maintain more elevated levels of FST, specially the high L_f-high T_u Novec case where T_u decreases from 3.5% to 2.6% along the TBL. This results in larger near-wall streamwise velocity fluctuations, increasing by up to 6% in the high L_f cases compared to the low L_f simulations (see Fig. 4.36 right). The friction coefficient distribution is also affected, as depicted in Fig. 4.37, with differences of almost 5 % between the low l_f-high T_u and high L_f-high T_u cases. The increase of C_f and $u_{rms,max}$ stays coherent with the hierarchy among the simulations in terms of FST intensity above the TBL.

As in section 3.4.3, in order to get more insights on the origins of the differences on the skin friction distribution, a Renard-Deck (RD) decomposition (see Eq. 3.5) is performed and depicted in Fig. 4.37 (right). In accordance with section 4.2.1, the dominant contributions are the turbulent term $C_{f,t}$, and then the viscous one $C_{f,v}$. The term $C_{f,x}$, associated with the boundary layer spatial growth, slowly increases in the transitional region before reaching a similar constant value between the different cases. More differences are observed in the TBL between the cases for the two other contributions. The differences are specially important for the viscous term, where the hierarchy between the cases reported on $u_{rms,max}$ and C_f is recovered. The turbulent contributions exhibit smaller differences but still consequent between the high L_f-high T_u and low L_f-low T_u cases. As a comparison, the LES-MF case of Chapter 3 (see section 3.4.4) is also reported, even if the overlap in terms of Re_θ with the FST cases is limited. Contrary to the LES-MF case, the viscous contributions of the

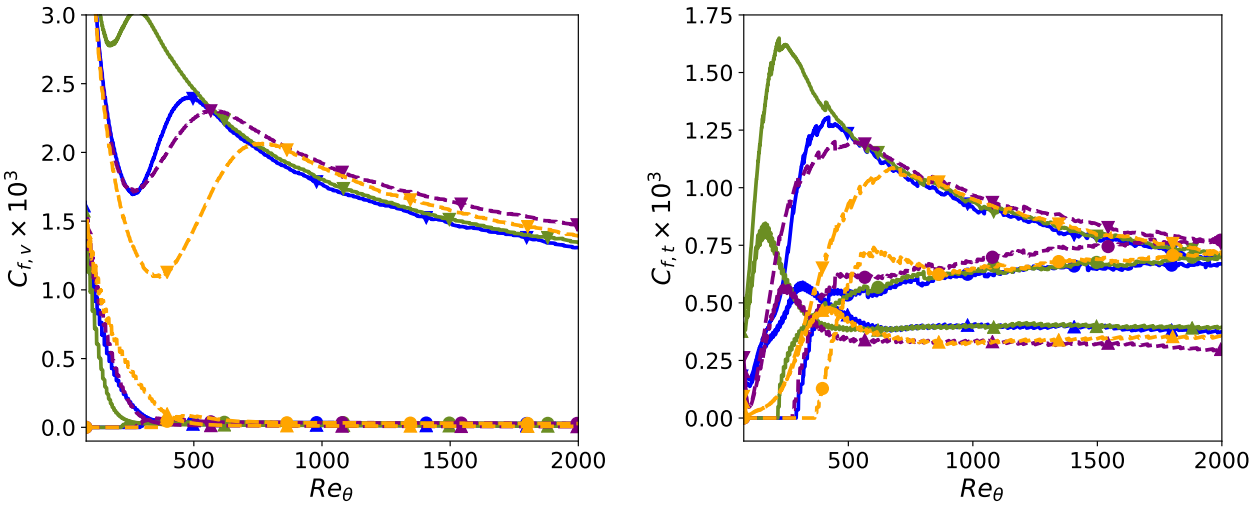

Figure 4.38: Decomposition of $C_{f,v}$ (left) and $C_{f,t}$ (right) in three layers: inner layer (lines with downward triangles); log layer (lines with bullets); outer layer (lines with upward triangles).

FST cases do not exhibit an overshoot on $C_{f,t}$, in line with the absence of overshoot on C_f during the transition (see Fig. 4.4). Unfortunately, the LES-MF case does not really achieve an equilibrium state before the end of the overlap, i.e. $Re_\theta = 2000$, but we observe that $C_{f,t}$ remains lower than in the FST cases, likely due to the absence of FST.

The two main contributions, respectively $C_{f,t}$ and $C_{f,v}$, are decomposed into three subregions which are the inner layer ($0 < y^+ < 30$), the log layer (between $y^+ = 30$ and $y = 0.3\delta$) and the outer layer ($0.3\delta < y < \delta$) as in section 4.2.1. The $C_{f,v}$ term, depicted in Fig. 4.38 (left), is entirely contained in the viscous sublayer, meaning that the FST particularly affects the inner scales, as observed on $u_{rms,max}$ in the TBL (see Fig. 4.36). The turbulent contribution is more distributed in the TBL in Fig. 4.38 (right). The inner-layer and mainly the log-layer exhibit an increase of the turbulent term with the FST intensity above the TBL. Interestingly, the inverse behavior is observed in the last region, possibly due to a reduction in the wake region as the FST increases.

Indeed, as reported in several studies (see for instance [293, 294]), the boundary layer (BL) thickness is affected by the FST. Due to increased FST penetration and consequent mixing in the BL, larger T_u promotes higher momentum flux in the TBL, thus resulting in a lower shape factor H as observed in Fig. 4.39 (left). The ratios of BL thicknesses δ_{99}/δ^* and δ_{99}/θ were used in section 4.2.1 to get some insights about memory loss of inlet conditions and the achievement of an asymptotic state. Compared to the differences reported in Fig.

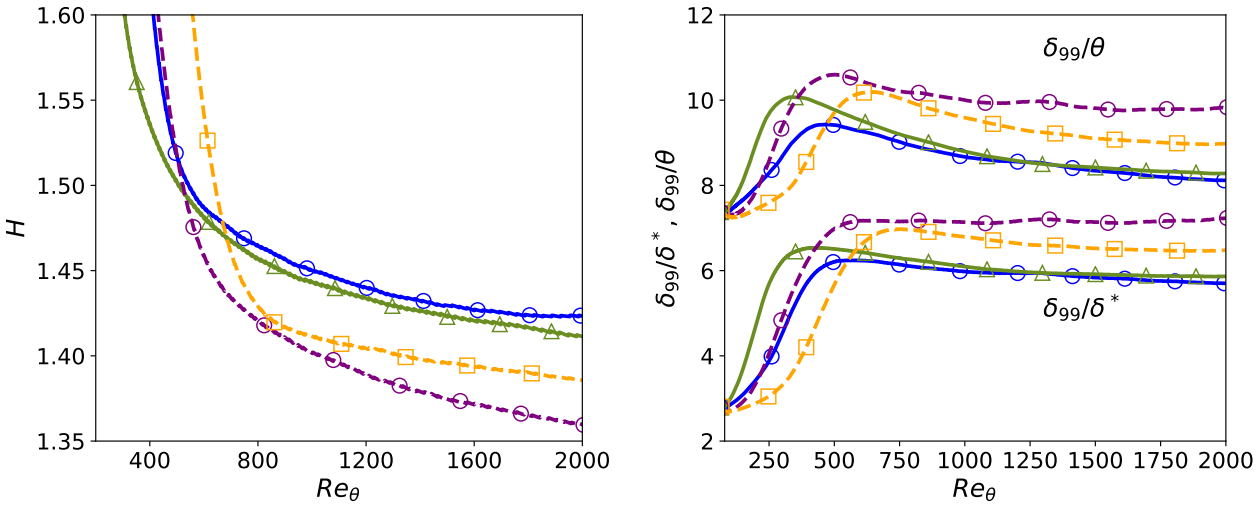

Figure 4.39: Shape factor (left) and ratios of boundary layer thicknesses (right) for the different Novec cases in the TBL region: low L_f (——), high L_f (- - -) and $T_u = 2.5\%$ (□), 4% (○) and 6.6% (△).

3.21, the ratios are also found to be profoundly affected by the FST (Fig. 4.39 right). Due to the influence of the FST which evolves in the streamwise direction, the achievement of an asymptotic state for the TBL is not necessarily expected. Despite this, the mean streamwise velocity profiles at the last station $Re_\theta = 2000$ are compared in Fig. 4.40 (left). As reported in [295, 298, 300], the log-layer is unaffected by the FST. The wake region, however, is reduced by the presence of FST, mainly for the high L_f-high T_u case, but this effect remains relatively limited. The premultiplied spectra at Re_θ=2000 in the high L_f-high T_u case does not exhibit an outer peak, probably due to the relatively low turbulence intensities ($T_u \sim 3\%$) compared for instance to Sharp *et al.* [296] ($T_u \sim 8 - 10\%$).

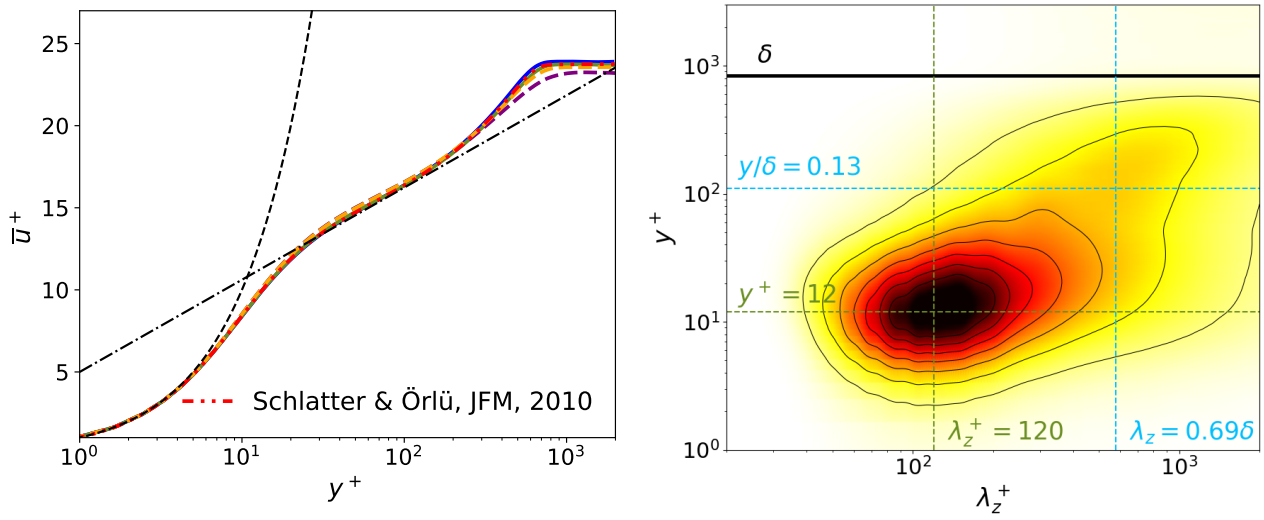

Figure 4.40: Right: Mean streamwise velocity profiles at Re_θ=2000 for low L_f-high T_u narrow (——), low L_f-very high T_u (——), high L_f-low T_u (- - -) and high L_f-high T_u (- - -) cases. Left: Premultiplied spanwise spectra $k_z E_{uu}(k_z)/u_\tau^2$ of streamwise velocity u at Re_θ=2000 in the high L_f-high T_u case.

Chapter Summary

The influence of large-scale disturbances on FST-induced transitions is investigated by means of LES, for perfect and real-gas boundary layers on a zero-pressure gradient flat plate. The integral length scale L_f is increased by a factor of seven between the low- and high-L_f cases. Dense-gas simulations are carried out using the organic vapor Novec in conditions representative of ORC (T_∞=100°C, p_∞=4 bar), at M=0.9 and for various FST intensities. A direct comparison with air flows in low and high-subsonic conditions (M=0.1 and 0.9) is performed.

Influence of the integral length scale on transition:

- Larger FST intensities always promotes transition, whereas L_f conducts to a twofold effect. For T_u=2.5%, a larger L_f accelerates the transition and the opposite is observed at 4%.
- T_u, L_f also influence the transition region length and the laminar streaks sizes.
- L_f influences laminar streaks amplitude distribution, as shown with a detection algorithm.

Dense-gas and compressibility effects on transition:

- Compressibility slightly delays the transition onset due to the generation of thermal streaks.
- Even without thermal streaks, absent in Novec due to its high heat capacity, the transition in the dense-gas BLs is further delayed with respect to air BLs.
- The streak growth is little affected by the compressibility or dense-gas effects.
- Overall, compared to FST parameters, the real-gas and compressibility effects are minor.

Turbulent spot precursors:

- In high L_f cases, presence of low-speed Λ-shaped structures in the BL prior to laminar streaks, in both air and Novec flows. Both larger L_f and T_u promote these structures.
- The early turbulent breakdowns of these Λ compete with streak instability mechanism.
- In the T_u=4% cases, the larger L_f leads to a two-peak distribution of the spots inception.
- Even in this case, the majority of turbulent breakdowns still occurs via streak instabilities.

Influence of FST on turbulent boundary layer (TBL):

- For the moderate FST intensities investigated (T_u<3.5%), no strong effects are observed.
- In the high L_f-high T_u case, the FST slightly increases the skin friction C_f and near-wall streamwise velocity fluctuations in the TBL. The wake region is also affected.
- Renard-Deck C_f decomposition shows that the increase is mostly due to the contribution of the inner viscous layer.

Chapter 5

Leading-edge effects on freestream turbulence induced transition of an organic vapor

In this chapter, a numerical experiment is conducted by means of LES to investigate the FST-induced transition on an idealized blade representative of ORC turbines to shed light into leading-edge receptivity effects. The questions we want to answer concern the influence of large-scale high-intensity incoming turbulence on receptivity and transition, the effect of the high Reynolds number based on blade half-thickness, and the dense-gas peculiarities in this complex process, in particular on turbulent spot characteristics. In the present case, using the semi-minor axes of the ellipse on the suction side and the inlet velocity, we obtain a half-thickness Reynolds number of $478\,000$, one order of magnitude greater than what is currently reported in the litterature (see section 1.3.2). The organization of this chapter is as follows. A presentation of the flow configuration along with the numerical methodology and set-up is provided in section 5.1. In section 5.2, an overview of the flow field is given, with the evolution of the FST at the LE, the characterization of the BL and a more detailed analysis of the transitional region. Then, the turbulent spot precursors and characteristics are discussed in section 5.3.

5.1 Numerical methods and set-up

5.1.1 Idealized blade vane configuration

The idealized vane geometry is adapted from Passmann [114], who conducted experiments to study tip leakage flows, with air as the working fluid. The blade profile is designed as a combination of circular arcs and straight lines. The suction side is inclined at an angle of 4.5° with respect to the pressure side. The chord length

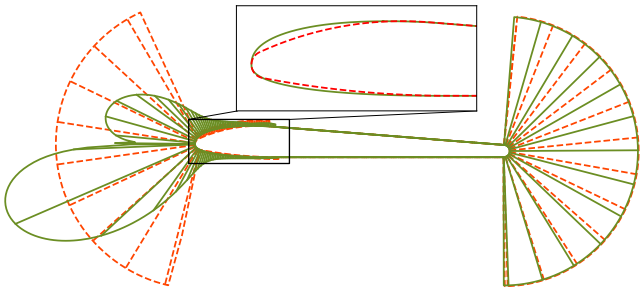

Figure 5.1: Comparison of the original (- - -) and smoothed (——) geometries, along with the profile curvature.

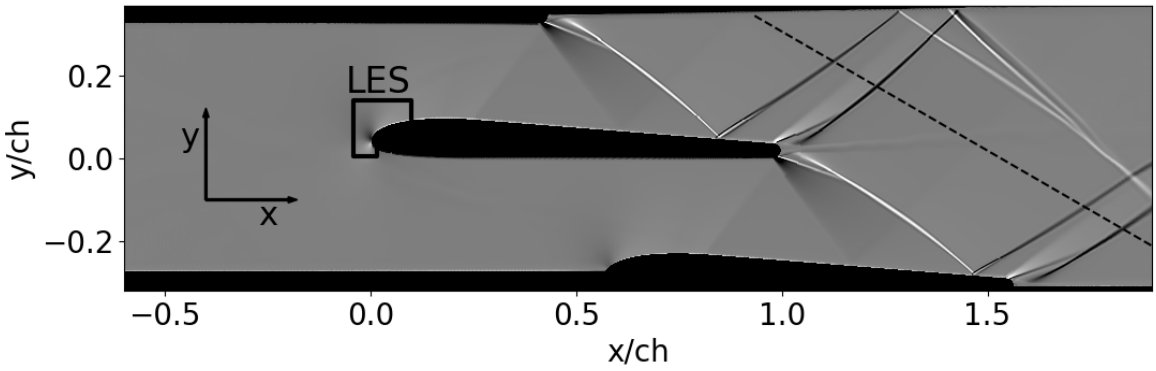

Figure 5.2: Schlieren-like visualization of the idealized blade vane configuration in the RANS simulation: density gradient in y-direction (levels $\pm 10^4$). - - -: line of measure for exit values. The boundaries of the LES domain around the LE are also depicted.

Table 5.1: Thermodynamic and aerodynamic conditions of the RANS simulation.

ch [mm]	M_1	c_1 [m/s]	$p_{0,1}$ [bars]	$T_{0,1}$ [K]	$\rho_{0,1}$ [kg/m^3]	M_2	c_2 [m/s]	Re_{M_2}	π $p_{0,1}/p_2$
61.2	0.55	76	3.8	335	55.0	1.59	87	8.4×10^6	3.6

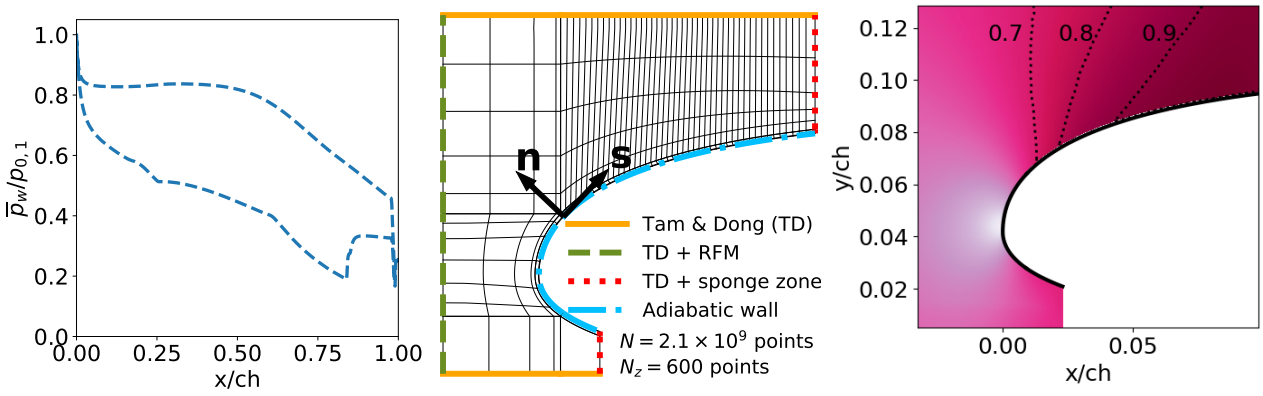

Figure 5.3: Left: pressure distribution $p_w/p_{0,1}$ around the blade in the RANS simulation with p_w the wall pressure and $p_{0,1}$ the inlet total pressure. Middle: computational mesh (1 line out of 100) of the LES along with boundary conditions. Right: LES Mach field (levels between 0.0 and 1.0).

of the profile is ch=62 mm and the thick TE shape is circular, with a diameter of $d_{TE} = 2.4$ mm. A preliminary LES study, detailed in Appendix E, of the laminar-turbulent transition occurring in the blade leading edge (LE) region showed that the original blade geometry of [114] caused incipient flow separation due to the non-smooth curvature distribution. The LE shape was then smoothed to ensure that the laminar-turbulent transition was induced by free-stream turbulence (FST), the most likely mechanism in turbine cascades [42]. The modified LE geometry consists of two super-ellipses defined by $(\frac{a-x}{a})^n + (y/b)^n = 1$ [302], where $n = 2.3$, $a/ch = 18.47\%$, $b/ch = 5.81\%$ for the suction side super-ellipse and $n = 2.4$, $a/ch = 26.70\%$, $b/ch = 4.18\%$ for the pressure side. The upper super-ellipse is connected to the rear part of the suction side by fitting a Bézier curve. The rest of the blade, and especially the TE of the modified geometry, is kept equal to the original one. In figure 5.1, the original and smoothed nose geometries are compared, the smoothed one being closer to the typical shape of turbine stator noses. Note that the pressure distribution on the blade is little affected by the LE modification. Half vanes are used at the top and bottom surfaces of the test section to create quasi-periodic flow conditions. A view of the setup and the flow field is provided in figure 5.2 by a preliminary RANS simulation using the Spalart-Allmaras model, with a similar set-up as the RANS simulations described in chapter 6.

The thermodynamic and aerodynamic conditions of the RANS simulation are given in table 5.1. The inlet

values are calculated one chord upstream of the LE and the exit values are evaluated along the dashed line displayed in figure 5.2, which corresponds to a distance of $0.25ch/\cos\gamma_s$ where $\gamma_s = 60°$ denotes the stagger angle. Stagnation pressure ($p_{0,1} = 3.8$ bars) and temperature ($T_{0,1} = 335$ K) are imposed at the inlet, based on Riemann invariants, whereas a back-pressure condition is used at the outlet. The flow accelerates from $M_1 = 0.55$ to supersonic conditions at the outlet with $M_2 = 1.59$. The fundamental derivative of gas dynamics Γ increases from 0.8 upstream to 0.95 downstream but stays below 1, meaning that the flow occurs inside the dense-gas thermodynamic region. As expected for an isentropic expansion of a dense gas, the sound speed grows (from 76 at the inlet to 87 m.s^{-1} at the outlet), which limits the increase of the Mach number with respect to air flow. A fishtail shock system is generated after the trailing since the flow reaches supersonic speeds. The outlet Reynolds number Re_{M_2}, based on the chord and the outlet velocity $M_2 \times c_2$, is equal to 8.4×10^6, which corresponds to a high Reynolds number compared to previous high-fidelity numerical studies on high-pressure turbines (for instance 0.6×10^6 in [59], 1.1×10^6 in [303] or 1.2×10^6 in [304]). The pressure distribution around the blade, depicted in figure 5.3 (left), is typical of turbines. The pressure coefficient on the suction side drops rapidly in the LE region and then decreases more slowly, before a sharp jump corresponding to the impingement of the shock coming from the blade above on the BL. In the following, we focus on the leading edge region and we investigate the effects of LE on the FST-induced transition, using wall-resolved LES.

5.1.2 LES set-up

Table 5.2: Thermodynamic and aerodynamic conditions at the inlet of LES domain.

M_{in}	c_{in} [m/s]	p_{in} [$bars$]	p_{in}/p_c	T_{in} [°C]	T_{in}/T_c	ρ_{in} [kg/m^3]	ρ_{in}/ρ_c	μ_{in} [Pa.s]	Γ_{in}
0.52	74	3.3	0.17	60	0.75	44.1	0.07	1.26×10^{-5}	0.8

The three-dimensional compressible Navier-Stokes equations are solved using MUSICAA, as described in section 2. The simulation is carried out over a 2D curvilinear multiblock domain. The fluid Novec649 is modeled with the Peng-Robinson-Stryjek-Vera equation of state [13] and the Chung-Lee-Starling model [123] for transport properties (see section 2.2). Spatial discretization uses 10th-order centered finite differences for inviscid fluxes and a 4th-order central scheme for viscous fluxes. A 10th-order selective filtering is applied and a four-stage Runge-Kutta (RK4) algorithm is used for time integration in combination with IRS4 (section 2.4), allowing $CFL \sim 5$ to be achieved close to the walls at an overcost of $\sim 40\%$.

The boundaries of the LES computational domain are sketched in figure 5.2. Due to the high Reynolds

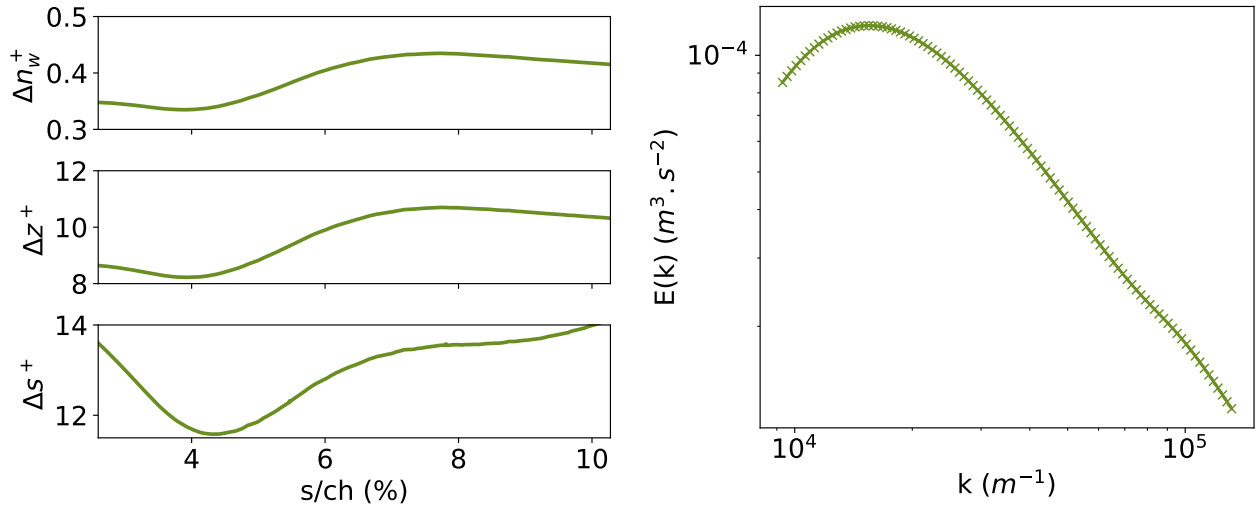

Figure 5.4: (Left) Near-wall resolution of the LES along the suction side in wall units. (Right) Initial kinetic energy spectra for the inlet synthetic turbulence, where the cross denotes the amplitude of the modes.

number, transition is estimated to occur early on the blade, so a reduced computational domain encompassing only the blade nose region is selected. Moreover, to limit computational cost, only the suction side is considered in this study. The simulation is initialized by means of a companion RANS simulation, realized in similar conditions as the ones described in section 5.1.1 with lower order schemes and on a coarser mesh. Boundary conditions are indicated in figure 5.3 (middle). Periodicity is enforced in the spanwise direction and adiabatic no-slip conditions are applied at the wall. Non-reflecting Tam & Dong's conditions [128] are applied at the inlet, top and outflow boundaries. Furthermore, at inlet and top boundaries, we impose mean flow values extracted from the companion RANS simulation. The stochastic velocity field $\mathbf{u}'_{in}$, constructed with RFM as explained in section 2.3.4.3, is entered using the Tam & Dong's inlet boundary condition. The synthetic turbulence is windowed at the inlet corners to avoid injecting it too close from the bottom and top boundary conditions. Finally, a sponge zone combining grid stretching and a Laplacian filter is added at the outlet.

Table 5.3: Inlet FST characteristics for current LES configuration (LE) and for LESs realized over a FP (Chapter 4), along with computational grid properties.

Case	$L_{f,in}$ [μm]	$Re_{L_{f,in}}$	$T_{u,in}$ (%)	Re_{FST}	$\Delta x^+ \times \Delta y_w^+ \times \Delta z^+$
LE - Inlet	79	10450	4.3	430	13×0.4×10
FP-low L_f -high T_u	6.8	1950	4.0	76	13×1.0×11
FP-high L_f -low T_u	47	13600	2.5	340	27×0.9×11
FP-high L_f -high T_u	46	13250	4.0	530	28×0.9×11

The thermodynamic conditions at the inlet of the LES domain, given in table 5.2, correspond to relatively dilute conditions for Novec649 compared to critical values, with $p_{in}/p_c = 0.17$ and $T_{in}/T_c = 0.75$. However, due to the high density of Novec649, the flow Reynolds number is high, so that the LES grid already contains more than 2 billion points for the small region considered (figure 5.3 (middle)), with 600 points in the spanwise direction corresponding to $L_z \sim 1\%ch$. The BL along the suction side, which experiences a flow accelerating from $M = 0.5$ at the inlet to almost 1.0 at the outlet of the LES domain (figure 5.3 (right)), attains a momentum thickness θ_{end} such that $Re_{\theta_{end}} = 1600$ at the end of the domain. With $L_z/\theta_{end} = 90$ and $L_y/\theta_{end} > 655$ above the BL, the size of the domain is very large compared to the BL to avoid confinement effects. A near-wall resolution typical of wall-resolved LES is achieved, with a normal resolution $\Delta n^+ \sim 0.3 - 0.5$, a spanwise resolution $\Delta z^+ \sim 8 - 11$ and a tangential resolution $\Delta s^+ \sim 12 - 14$ (see figure 5.4 left). The constraint is relaxed in the freestream but the resolution is fine enough to fully resolve the injected synthetic turbulence. The timestep is fixed to $\Delta t = 2.36 \times 10^{-9}$ s, which corresponds to a maximum CFL of approximately 5. The application of IRS4 in the ξ and η-directions represents an overcost of 50% and therefore a saving factor of 3.5 in terms of calculation time is obtained compared to the use of an explicit time scheme with CFL=1. The simulation is run for 250 000 iterations, and the spanwise and temporal averaged statistics are collected for the last 120 000 iterations until temporal convergence of the statistics is achieved. This corresponds to approximately three flow-through times. The overall cost is approximately 1.7 millions CPU hours on 11 000 AMD Rome cores. In addition, a database of 4096 planes and 2048 subvolume snapshots of the velocity field is stored during 45 000 iterations for more detailed analysis.

The FST characteristics of the LES at the inlet are given in table 5.3. The turbulence intensity, chosen to be representative of turbines, corresponds to $T_{u,in} = 4.3\%$. At the beginning of the BL transition region (Re_θ ~250), T_u is reduced to approximately 3.5%. The longitudinal integral length scale L_f is determined close to the inlet (at $(x - x_{LE})/ch = -3.2\%$) by integration of the temporal autocorrelation function f of the velocity signal:

$$L_f = U_{in} \int_0^{t_s} f(\tau) d\tau \tag{5.1}$$

where t_s corresponds to the recording time and $U_{in} = M_{in} \times c_{in}$. Using the first zero crossing of f as the truncation value, as in Kurian & Fransson [254], the longitudinal integral length scale is $L_f \approx 79\,\mu$m. This estimated L_f and the corresponding Reynolds number Re_{L_f}=10 450 are representative of large-scale incoming disturbances compared to the BL thickness ($L_f/\theta_{end} \approx 11$). In the following, LES results for the blade LE are compared with flat-plate (FP) simulations of Chapter 4, as they were conducted under similar incoming flow

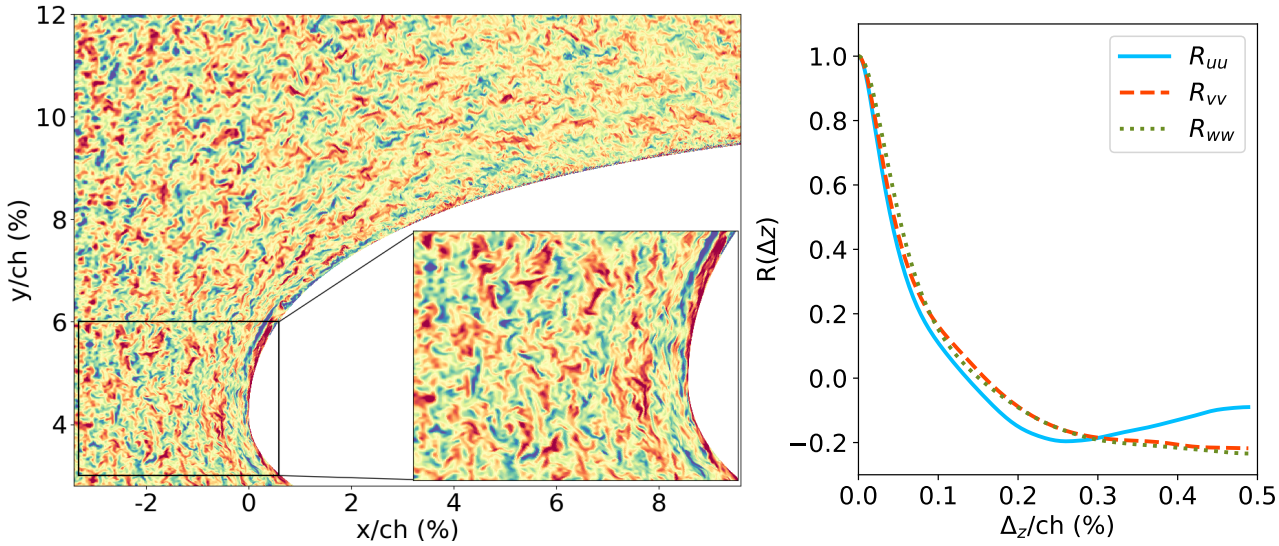

Figure 5.5: Left: mid-span plane of the spanwise fluctuations w' with a focus on the LE (levels $\pm 0.05 \times c_{in}$). Right: spanwise correlations of the velocity components 2.5% ahead of the LE.

conditions ($p_\infty = 4$ bars, $T_\infty = 100°$C, $M_\infty = 0.9$). The inlet FST characteristics of the FP cases are summarized in table 5.3. In particular, the integral length scales and corresponding Reynolds numbers, $Re_{L_{f,in}}$, have similar order of magnitudes between the FP-high L_f cases and the LE simulation.

5.2 Characterization of the flow field

5.2.1 Evolution of the FST around the LE

A view of the incoming inlet turbulence is shown in figure 5.5 (left), where the FST is injected sufficiently far away from the LE to have some time to adapt ($L_f/(x_{LE} - x_{in}) = 3.3\%$). Flow acceleration by the external pressure gradient results in the elongation of the incoming structures in the streamwise direction, causing anisotropy downstream. The FST structures, although relatively large compared to the BL, are small compared to the LE. Compared to the half-thickness of the suction side $b/ch = 5.81\%$, L_f/b is equal to 2.2%. The spanwise extent of the domain is taken sufficiently large with respect to the FST, with $L_f/L_z = 13.1\%$. This is further assessed in figure 5.5 (right), where the first zero-crossing of the velocity spanwise correlations is attains for $\Delta z/ch \sim 0.15\%$.

In order to characterize the injected FST, one-dimensional energy spectra of the three fluctuating velocity components are plotted in figure 5.6 (left). The energy spectra exhibit an inertial range with a $-5/3$ law over

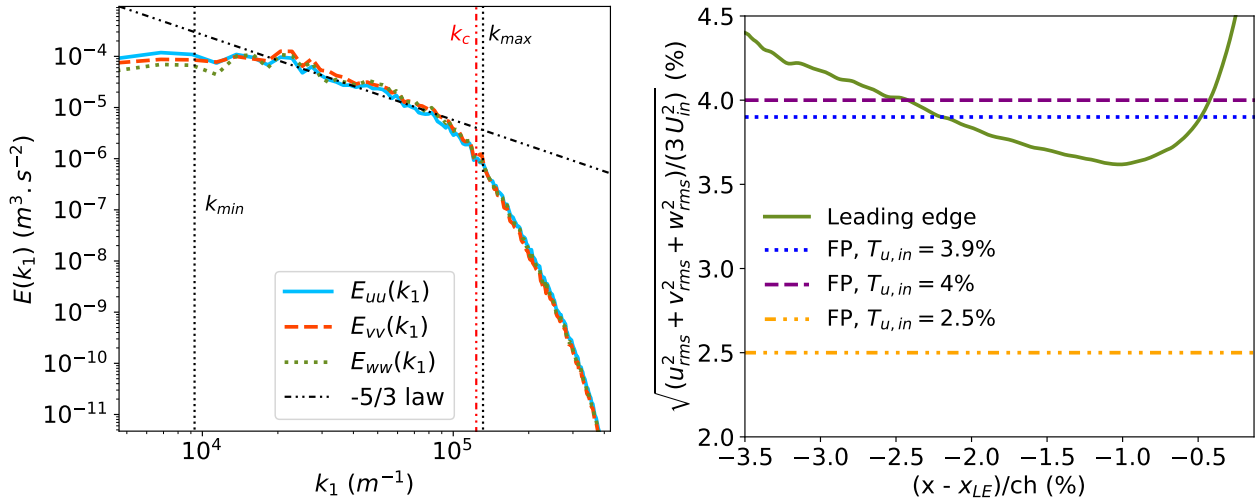

Figure 5.6: Left: Energy spectra of the velocity components 2.5% chord ahead of the LE, along with the minimal k_{min} and maximal k_{max} wavenumbers of injected modes and the cutoff wavenumber k_c of the numerical scheme. Right: FST intensity evolution in the region ahead of the LE.

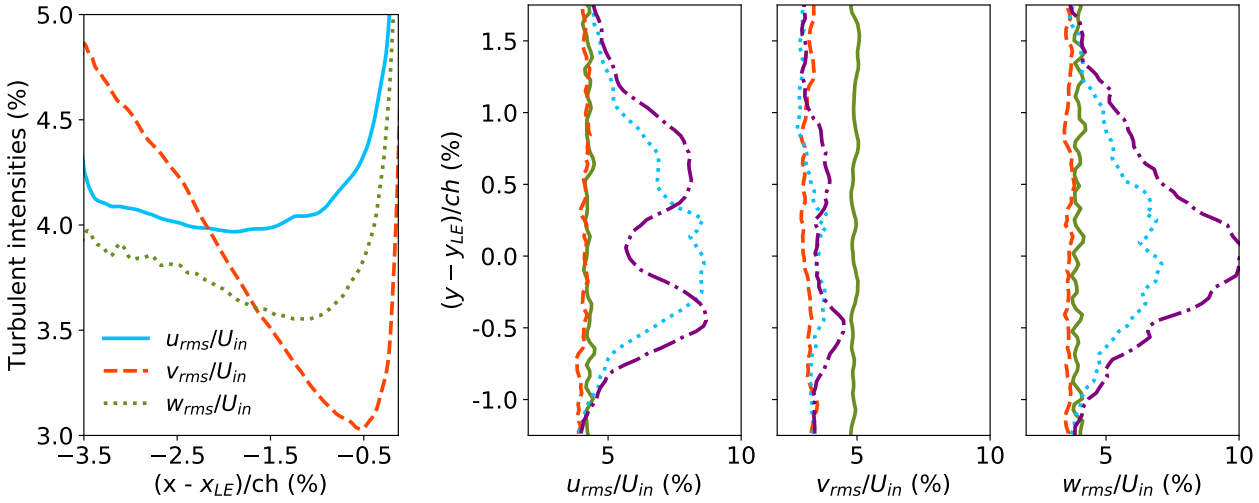

Figure 5.7: Left: evolution of the rms of the 3 velocity components in the region ahead of the LE. Right: Vertical profiles of the 3 velocity components rms at $(x - x_{LE})/ch = -3.5$ % (——), -1 % (– – –), -0.1 % (·····) and -0.02 % (– · – · –)

approximately one decade. The maximal wavenumber k_{max} of RFM modes is close to the finite-difference scheme resolvability, $k_c = 2\pi/5\Delta x$, meaning that the computational grid captures all the injected turbulence. The FST intensity evolution, defined here as $\sqrt{(u_{rms}^2 + v_{rms}^2 + w_{rms}^2)/3}$, is depicted in figure 5.6 (right). It is normalized by U_{in} rather than the local velocity magnitude in order to observe the velocity fluctuation intensities evolution without the influence of the mean velocity variations. The levels between 4.3% and 3.6% are comparable to FP simulations in Chapter 4 with high T_u. Just ahead of the LE, the FST intensity increases sharply due to the presence of the stagnation point, as reported by Xiong & Lele [64]. Indeed, the close-up view of the spanwise velocity fluctuations w' in figure 5.5 (left), shows that the turbulent structures wrap around the LE, which enhances the velocity fluctuations. The evolution of the root mean square (rms) amplitude for each velocity components are plotted in figure 5.7 (left). At the inlet, the FST is characterized by a small anisotropy, with $v_{rms,in}/u_{rms,in} = 1.14$ and $w_{rms,in}/u_{rms,in} = 0.95$. The horizontal u' and spanwise w' fluctuations slowly decay due to the dissipation while the decrease of v'_{rms} is more pronounced, due to the distortion of the turbulence by the LE. Approaching the LE, the intensification of turbulence is visible for the three velocity components. Vertical profiles of u_{rms}, v_{rms} and w_{rms} at different positions before the LE are reported in figure 5.7 (right). The FST decay between the 2 first stations (more intense for v') is followed by an important rise of the fluctuations around the position of the LE (smaller for v'). Very close to the LE (between $(x - x_{LE})/ch = -0.1$ % and -0.02 %), the horizontal component is lowered while the spanwise velocity fluctuations are further increased.

The distortion and intensification of turbulence near the LE are in agreement with the theoretical study by Goldstein & Wundrow [62] and promote the formation and amplification of streamwise vorticity in this region, as illustrated in figure 5.8. The selection of spanwise fluctuations by the stretching process results in large-scale elongated structures, identified by the black and white isosurfaces of the spanwise velocity in the left of the figure. Smaller-scale streamwise vortices are located in shear zones, corresponding to the spanwise gradient of the spanwise velocity. The mean position δ_{99} is added in transparent blue in figure 5.8 (middle), showing that the vortical activity is above the BL. The streamwise vorticity filaments are clustered at the interface of the large-scale structures, as highlighted in the right picture. These streamwise vortices play a key role in the FST-induced transition as they can lead to the formation of streamwise streaks inside the transitional BL through the lift-up effect [63]. The fact that they appear as large-scale clusters rather than single vortices is related to the high half-thickness Reynolds number in the present configuration and will affect the subsequent formation of streamwise streaks, as discussed in the next section.

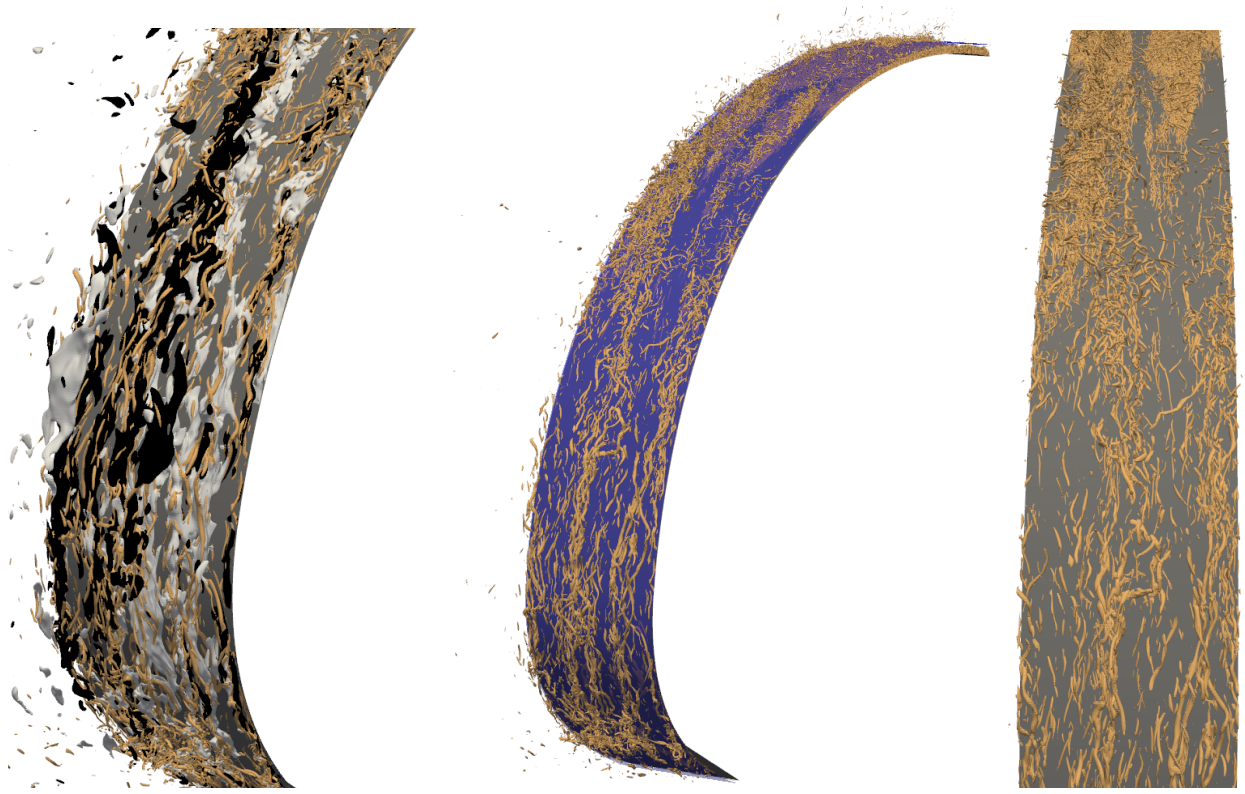

Figure 5.8: Isosurfaces of the Q-criterion (light brown) in the LE region. Isosurfaces of spanwise fluctuations are also plotted in the left picture for levels $-0.075 \times c_{in}$ (black) and $0.075 \times c_{in}$ (white). δ_{99} mean position along the wall is added in transparent blue in the middle picture.

5.2.2 Characterization of the BL

To characterize the BL evolution along the suction side, various flow quantities are analyzed. First, the distribution of wall pressure, normalized by the total pressure $p_{0,1}$, is reported in figure 5.9(a) for the LES and the RANS simulations, where a fair agreement is obtained. The curve exhibits an important pressure decay close to the LE, which results in an initially very high acceleration. The evolution of the acceleration parameter K, defined as $K = \frac{\nu}{U_e^2}\frac{dU_e}{ds}$ (ν being the kinematic viscosity and U_e the mean velocity at the BL edge) is plotted in figure 5.9(b) as a function of the curvilinear abscissa s. The edge velocity is determined thanks to the condition of vanishing mean velocity gradient, which has been shown to work relatively well along blades except near the trailing edge [305]. The positions of minimal and maximal C_f are also reported to figure out the transition region. The flow exhibits a highly favorable pressure gradient (FPG) close to the LE, which decreases further downstream, tending toward a nearly constant value of about 1.5×10^{-7} (slightly favorable PG) in the fully turbulent region, where the TBL reaches equilibrium. This is also confirmed by the nearly linear growth of the boundary layer thickness δ_{99} in figure 5.9(c). The shape factor $H = \delta^*/\theta$ (with δ^* the displacement thickness and θ the momentum thickness), a good indicator of the boundary layer state, is also depicted in figure 5.9(c). As the FPG weakens in the laminar region, H increases until the onset of transition, where it drops before reaching a plateau in the fully turbulent BL. The distribution of C_f in figure 5.9(d) is compared with the ZPG-FP results (Chapter 4) and with the FST-induced transition in air flow of Wu & Moin [228]. Compared to FP cases with similar L_f, the strong FPG in the laminar region delays the onset of transition and may affect the length of the transitional region.

The turbulence above the transitional and turbulent BL is characterized by plotting in figure 5.10 (left) the FST intensity, defined here as $T_u = \sqrt{{u_{rms}}^2 + {v_{rms}}^2 + {w_{rms}}^2}/\sqrt{\overline{u}^2 + \overline{v}^2 + \overline{w}^2}$. Along the transitional region, the FST intensity is decreasing from 3.5 to 2.5%, which corresponds to relatively high levels but lower than the FP case with an equivalent T_u at inlet. This may partly explain the lengthening of the transitional region noted in figure 5.9(d). The evolution of rms values for tangential u_s, wall-normal u_n and spanwise w velocities above the BL are reported in figure 5.10 (right) to characterize the turbulence anisotropy. As already mentioned in section 5.2.1, the tangential component initially exhibits a much lower level compared to the two others. In contrast, the initial level of w_{rms} is particularly high with $w_{rms} \sim 8\%$. As the flow acceleration slows down, the difference between the three components decreases but the FST remains anisotropic, with $w_{rms}/u_{s,rms} \sim 1.2 - 1.4$ and $u_{n,rms}/u_{s,rms} \sim 1.45 - 1.6$.

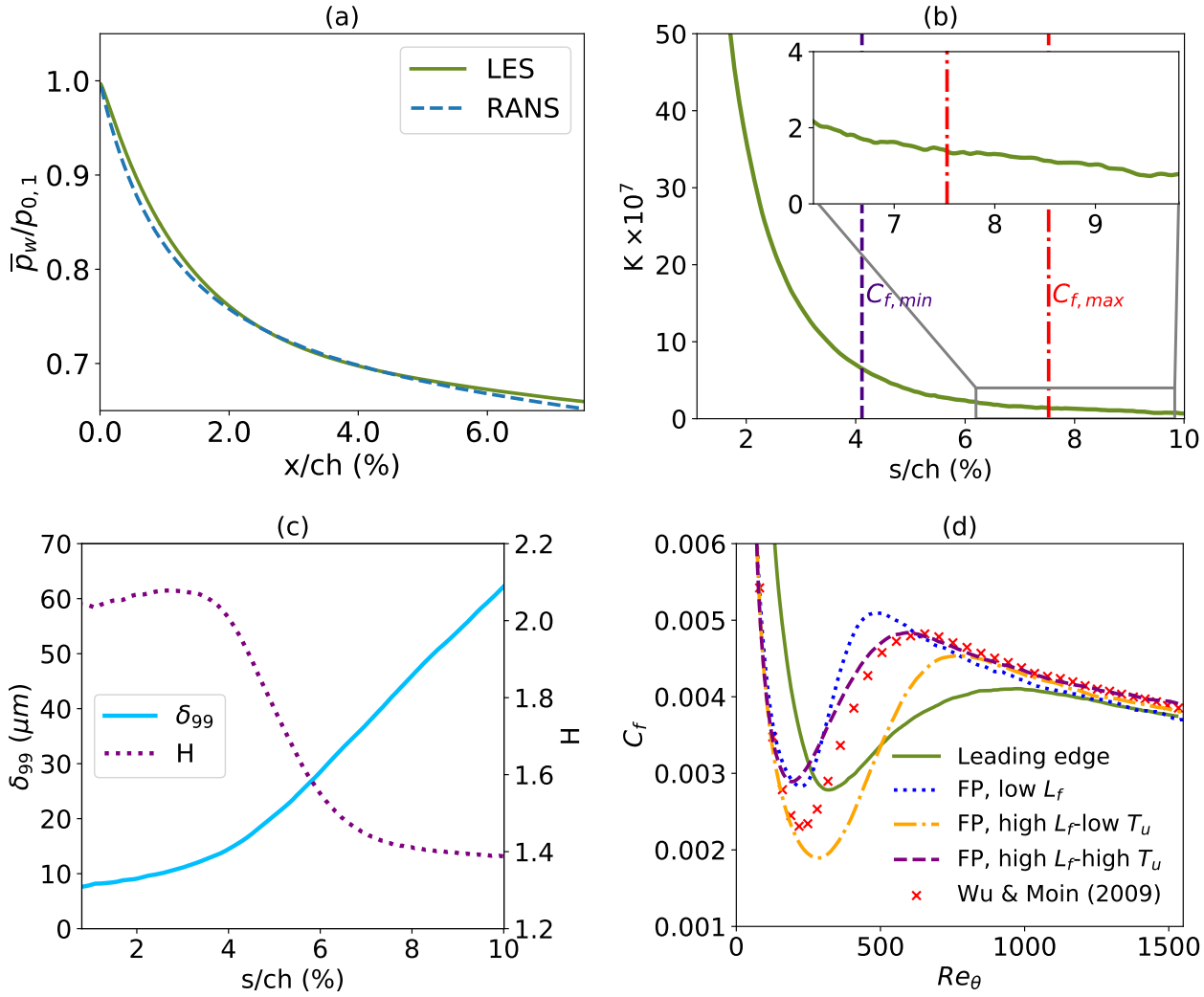

Figure 5.9: (a) Mean pressure distribution, (b) acceleration parameter K, (c) BL thickness δ_{99} and shape factor H and (d) friction coefficient C_f evolution. The C_f evolution of the FP LES (Chapter 4) are also depicted in figure (d).

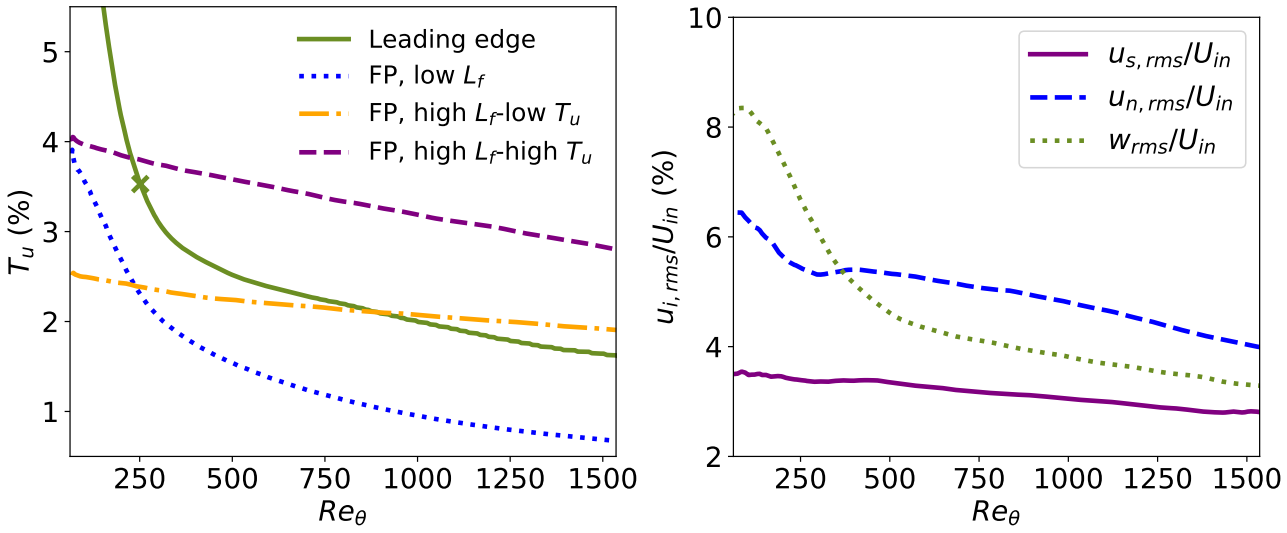

Figure 5.10: Left: T_u evolution above the BL versus Re_θ for the LE simulation, along with FP LES results (Chapter 4). The cross denotes the value at $Re_\theta = 250$ which corresponds to the beginning of the transitional region. Right: evolution of the rms of the tangential, normal and spanwise velocity components above the BL.

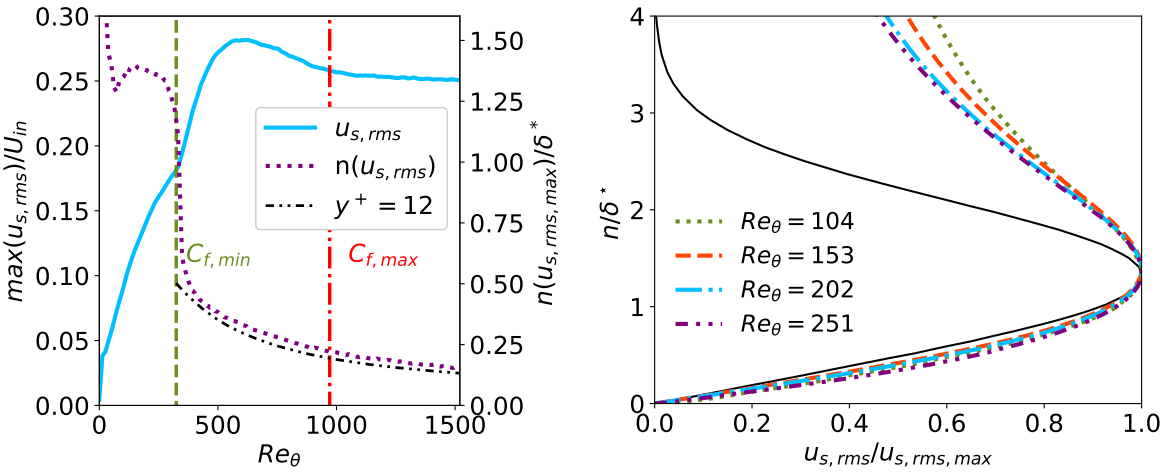

Figure 5.11: Left: evolution of $u_{s,rms,max}/U_{in}$ and its distance from the wall $n(u_{rms,max})/\delta^*$. The position of minimal and maximal C_f are also depicted, along with the height corresponding to $y^+ = 12$. Right: comparison of $u_{s,rms}$ profiles with optimal response [256, 257].

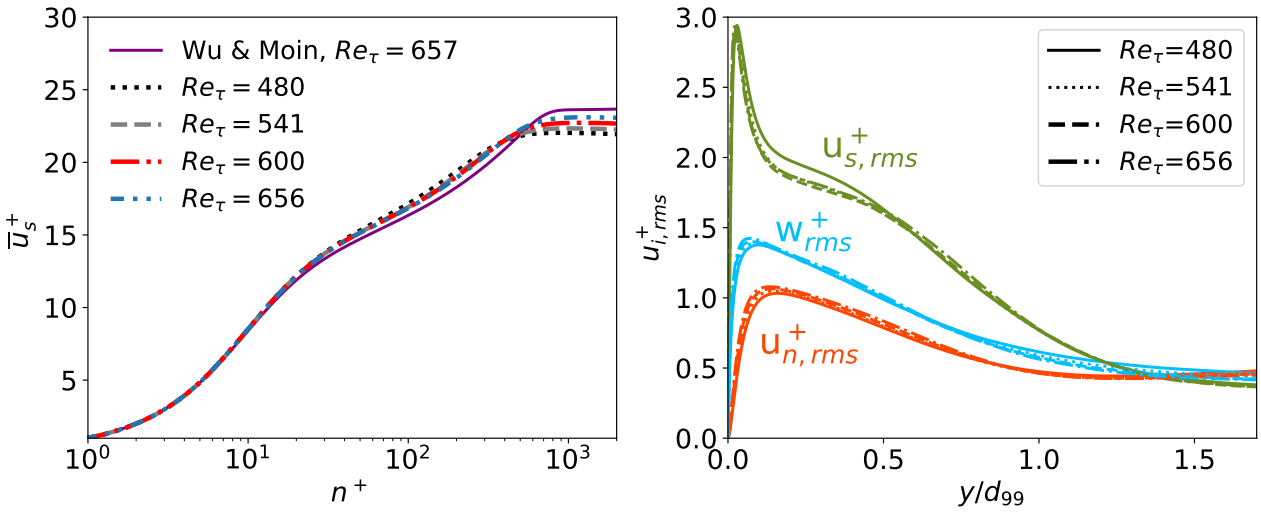

Figure 5.12: Mean velocity u_s (left) and turbulent intensities (right) profiles in the TBL.

The evolution of the maximum of $u_{s,rms}$ inside the BL is plotted in figure 5.11 (left), along with its wall-normal location. A first rapid increase of $u_{s,rms,max}$ is observed, followed by a second one starting at $C_{f,min}$ before reaching a peak. The second growth is related to the appearance and spreading of turbulent spots, which is consistent with the location $n(u_{s,rms,max})/\delta^*$ moving from values at $1.2-1.4$ towards a lower level in the TBL around $y^+ \sim 12$ (which corresponds to near-wall turbulent streaks [232]). The initial increase can be associated to the energy growth in the early development of the streaks, as the associated location around 1.4 is coherent with the optimal perturbation theory [256, 257]. Moreover, the $u_{s,rms}$ profiles in the pre-transitional BL, depicted in figure 5.11 (right), show good agreement with the optimal disturbances, which consist of streamwise vortices developing into streamwise streaks [256].

The velocity mean and fluctuating profiles, reported in 5.12, present a self-similar behavior suggesting that an equilibrium TBL is obtained. The effect of a favorable pressure gradient is expected to reduce the wake [306], but, compared to the ZPG profile of Wu & Moin [228], only a slight alteration of the wake law is observed. This is due to the small pressure gradient (K=1.5×10^{-7}). This could also be an influence of the FST intensity above the TBL. In their experimental investigation of a TBL subjected to FST, Joos et al. [301] reported an influence on the TBL mean profiles for $T_u \sim 2.5$-3%. Since $T_u \leq 2\%$, a weak influence is expected. Concerning the small deviation of the log law from a canonical ZPG TBL, it is mainly related to the FPG, since log-law region is persistent for external turbulence levels up to 20% [298].

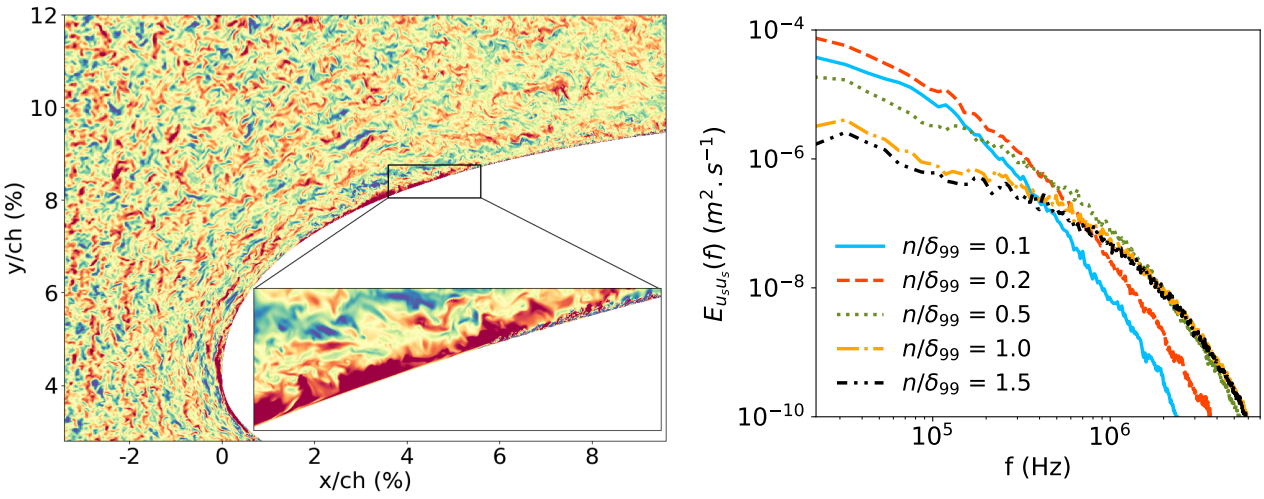

Figure 5.13: Left: mid-span plane of the spanwise fluctuations w' with a focus on the BL (levels $\pm 0.05 \times c_{in}$). Right: temporal 1D energy spectra of $\overline{u}_s$ at $Re_\theta = 195$ at different height in and outside the BL.

5.2.3 Analysis of the transitional region

We now analyze the transitional region in more detail. A close-up view of the freestream spanwise fluctuations interacting with the BL in a mid-span plane is depicted in figure 5.13 (left). The turbulent structure between $2 < x/ch < 4$ is spread along the wall and relatively large compared to the BL thickness, and strongly disrupts the BL. Besides, the BL shear acts as a low-pass filter, admitting low-frequency content in the FST to penetrate the inner region while short-wavelength components do not. This phenomenon, know as the shear sheltering effect [307, 308], is indeed observed here, for instance on the temporal energy spectra of the tangential velocity component plotted in figure 5.13 (right): the lower the position of the spectra in the BL, the more the high frequency content is filtered out. The BL remains however strongly marked by the low frequency content in the FST which, given the large size of incoming structures compared to the BL, carries most of the FST intensity.

Snapshots of u'_s, u'_n and w' in a wall-normal plane starting at the LE stagnation point are reported in figure 5.14. For comparison, the streamwise velocity fluctuations at the same normalized wall-distance are shown for the FP high L_f-low T_u case, using the same physical length. Since inlet FST conditions are similar, a first striking point is the transition delay. Furthermore, pre-transitional Klebanoff modes, clearly visible on the FP case, are difficult to observe in the tangential fluctuations on the blade. The laminar streaks are not present everywhere and rather appear in a localized manner. Their distribution is connected with the formation of streamwise vortices at the LE at the interfaces of FST structures. In the 3D view of figure 5.15, taken at the

same instant, the occurence of low-speed laminar streaks (in black) is more clearly educed and their connection with the incoming streamwise vortices outside the BL is clear. No streaks are detected in the spaces between the large-scale clusters of streamwise vortices. Intense streamwise patches (in red on the tangential component of figure 5.14) correspond to the impact of large-scale events from the external turbulence, and can be correlated with coherent spanwise movements for the spanwise fluctuations (bottom plot). The streamwise streaks forming in the BL are relatively short and already disturbed by the large-scale spanwise fluctuations. It is worth noting that the wall-normal fluctuations, shown in figure 5.14 (center), have levels ten times lower than u'_s and w' and are only significant in turbulent regions (such as in the turbulent spots observed at $s/ch \sim 4.5 - 5\%$).

In the BL populated with streaks, the spanwise distance where a negative minimum in R_{uu} appears is used to determine the mean half spanwise wavelength of the streaks [47]. However, in our case, the transitional region is populated with other structures than streaks and the correlation will rather give information on the average spacing between the structures present. The spanwise correlation functions of the tangential velocity, $R_{u_s u_s}$, are evaluated at the wall-normal position of maximal $u_{s,rms}$ for $75 < Re_\theta < 1370$, averaged in time, and reported in figure 5.16. For $Re_\theta < 140$, the first negative minimum is hardly constant and is located around $\Delta z/ch \approx$ 0.1-0.2 %, which would correspond to structures separated by a distance of 0.2-0.4% of chord. This size is that of large-scale structures wrapped on the LE. For locations greater than $Re_\theta = 590$, the first distinct local minimum (marked by an arrow) corresponds to the spacing of near-wall turbulent streaks. Laminar streaks would be associated to a local minimum in between. Its absence indicates that the Klebanoff streaks hardly mark the flow and their population within the BL is rather low.

To get more information concerning the size of the structures populating the BL, premultiplied spanwise spectra of the three velocity components between Re_θ=75 and 1370 are reported in figure 5.17. Scrutinizing first the normal velocity fluctuations, as inferred from figure 5.14, the spectra amplitudes are very low and increase only from Re_θ=285 with the appearance of turbulent spots. The large structures arising from the wrapping of FST around the LE mark the $k_z E_{u_s u_s}(k_z)$ and $k_z E_{ww}(k_z)$ spectra. The characteristic size of these structures are between 9 and $23\theta_{end}$ (delimited in figure 5.17 by vertical lines with squares), of same order of magnitude as the inlet integral length scale $L_f \approx 11\theta end$. Similarly to u_n, the premultiplied spectra for the two other components are marked by the near-wall turbulent streaks for $470 < Re_\theta < 1370$ (delimited by lines with crosses). The laminar streaks would correspond to peaks in between ($2.5 \leq \lambda_z/\theta_{end} \leq 9.0$). In fact, no clear dominant peak appears in this range. At station Re_θ=75, a small peak can be identified on the $k_z E_{ww}(k_z)$ spectrum around λ_z/θ_{end}=4.5, which is taken as an estimation of the mean spanwise distance between laminar

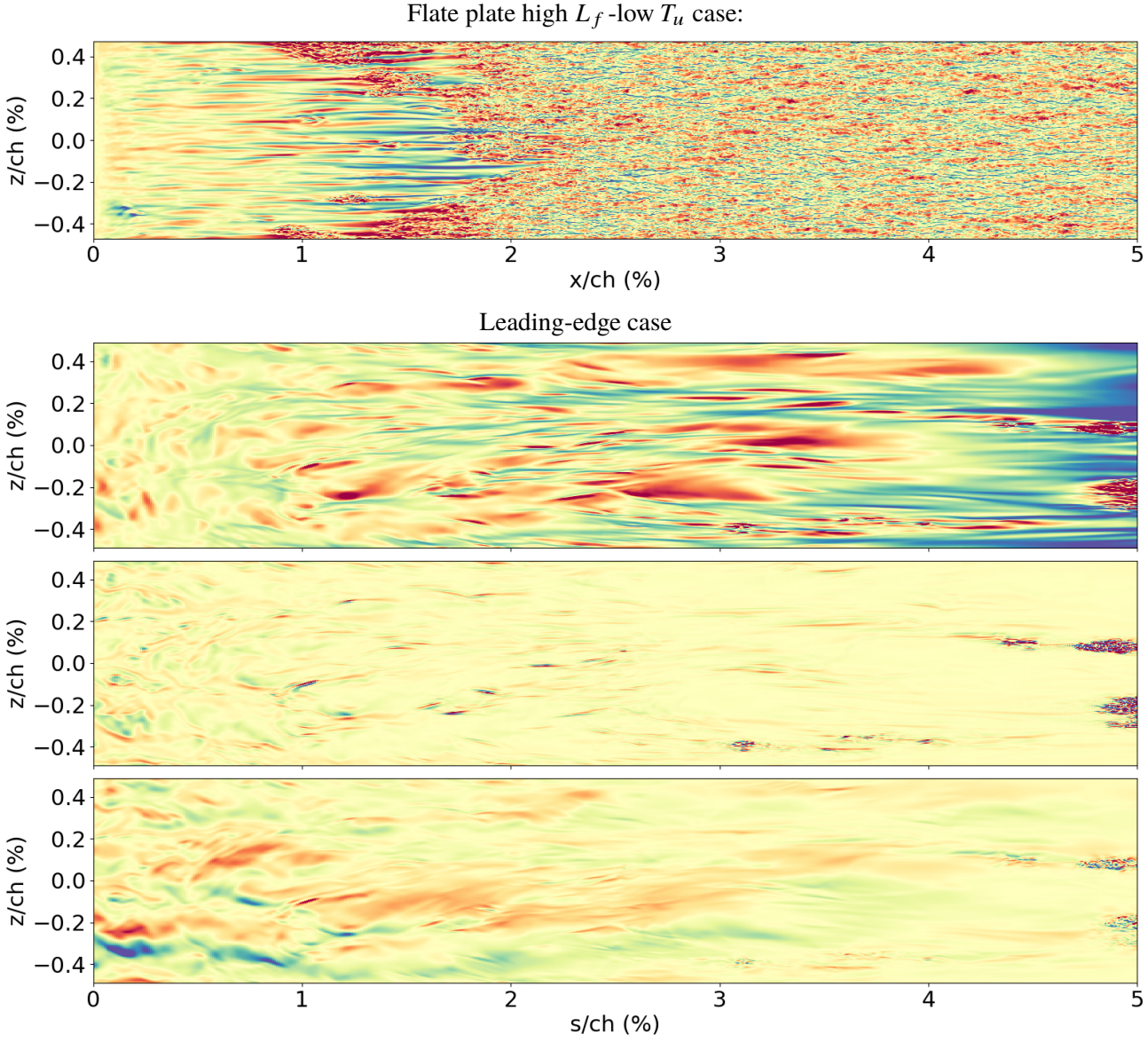

Figure 5.14: FP high L_f -low T_u case: snapshot of tangential velocity fluctuations (levels $\pm 0.24 \times c_{in}$) at $n^+ \sim 20$. LE case: Snapshot of tangential (top, levels $\pm 0.1 \times c_{in}$), normal (middle, levels $\pm 0.01 \times c_{in}$) and spanwise (bottom, levels $\pm 0.1 \times c_{in}$) velocity fluctuations at $n^+ \sim 15$. Negative and positive values are respectively in blue and red.

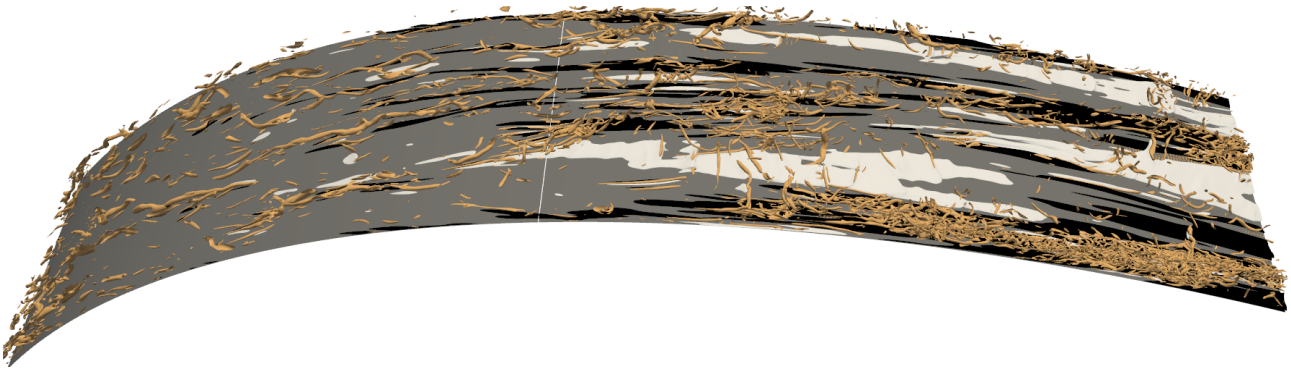

Figure 5.15: Isosurfaces of the tangential velocity fluctuation u'_s for $-0.09c_{in}$ (black) and $0.09c_{in}$ (white), along with the Q-criterion (light brown), at the same instant as figure 5.14 from the LE to $s/ch \approx 3.5\%$.

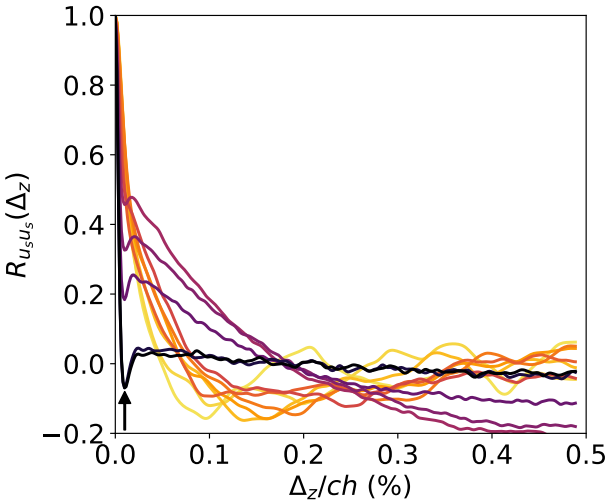

Figure 5.16: Spanwise correlation function of the tangential velocity fluctuations. From light yellow to dark purple: Re_θ = 75, 130, 185, 235, 285, 335, 410, 590, 705, 820, 1160 and 1370. The arrow denotes the local minimum corresponding to near-wall turbulent streaks.

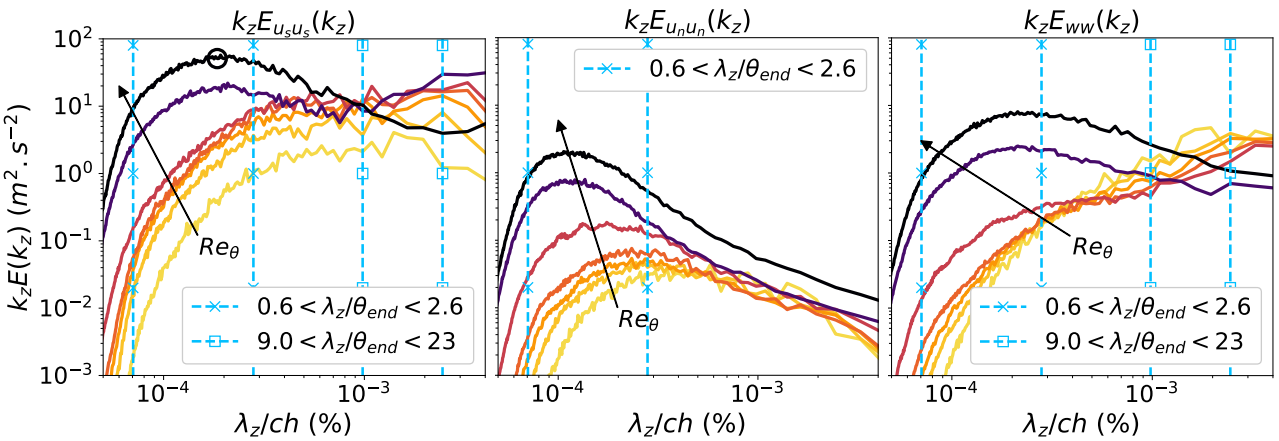

Figure 5.17: Premultiplied spanwise spectra of tangential (left), normal (middle) and spanwise (right) velocities. From light yellow to dark purple: Re_θ = 75, 130, 185, 235, 285, 470 and 1370. The range between the lines marked with crosses corresponds to the turbulent streaks, while the lines with squares delimit the range corresponding to the large structures forming at the LE. The circle on the spectra $k_z E_{u_s u_s}(k_z)$ at Re_θ = 1370 denotes the position of the near-wall turbulent streaks at λ_z^+ = 120 [232].

streaks. When non-dimensionalized by $T_{u,in}L_{f,in}$, this corresponds to $\lambda_{z,streaks}/(T_{u,in}L_{f,in})$= 9.1. Franson & Shahinfar (2020) [47] proposed an estimator of the spanwise distance between streaks based on their intensive experimental databases of FST-induced transition over FP. It is defined as $\lambda_{z,FS} = L_f\, T_u(\mathscr{D}_1\, Re_{FST}^{-1/\sqrt{2}} + \mathscr{D}_2)^2$, with$(\mathscr{D}_1, \mathscr{D}_2) = (186, 0.8)$. For $T_{u,in}$=4.3% and $L_{f,in}$= 79 μm, we obtain $\lambda_{z,FS}/(T_{u,in}L_{f,in})$=11, in reasonable agreement with the previously estimated value.

In summary, contrary to the FP cases (Chapter 4) and even if the $u_{s,rms}$ transitional profiles are compatible with the optimal perturbation theory, the laminar streaks are not the dominant structures in the transitional boundary layer. An approximate estimation of their spanwise spacing is in agreement with experiments for ZPG BL [47]. As in the FP cases, the spanwise distance between streamwise streaks is mostly dependent on the FST parameters, and the order of magnitude is not changed by the mild FPG. The laminar streaks are relatively short and strongly perturbed. They arise as small clusters, due to the presence of intense structures at the LE that promote the formation of streamwise vortices at their interfaces. This scenario contrasts with the observations made by Faúndez Alarcón et al. [60] on a thin profile or by Zhao & Sandberg [59] on a stator blade. The use of an organic vapor has minimal impact on stability thresholds, but the implied elevated Reynolds number in proportion to the developing boundary layer mostly accounts for this situation. Large-scale clusters disrupt the formation of streaks, which remain limited to furrows and experience difficulty developing in the high-acceleration region.

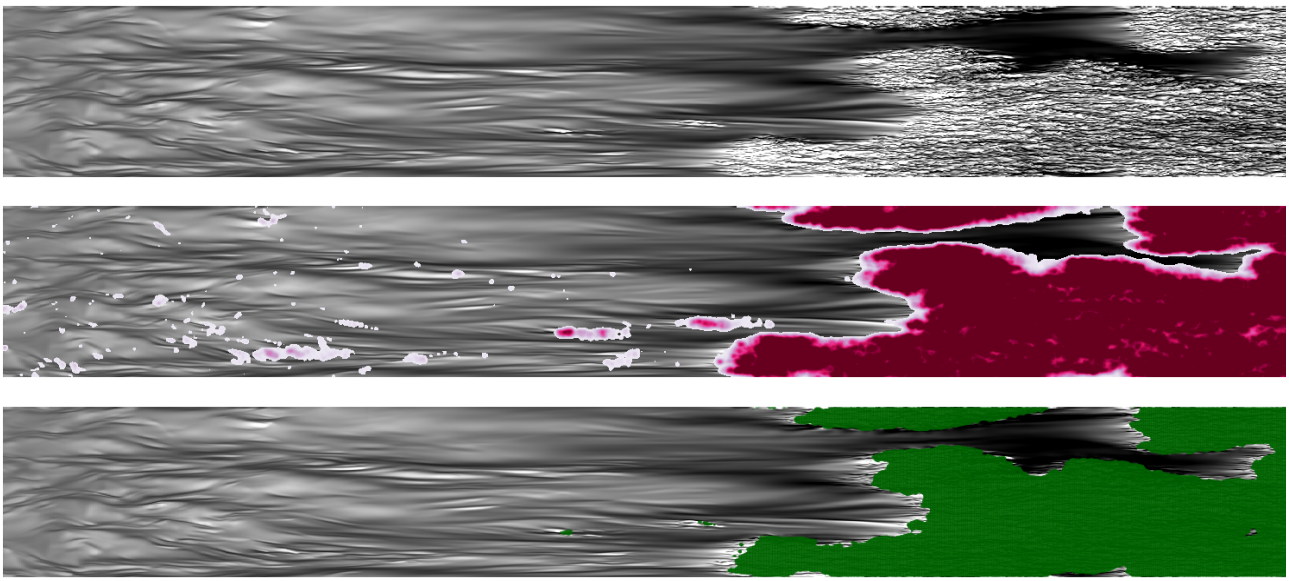

Figure 5.18: Different steps of the laminar-turbulent discrimination exemplified in a wall-normal plane at $n^+ \sim 15$. Top: tangential velocity field of the snapshot considered here (levels $\pm 0.2 c_{in}$, from black to white). Middle: Density of the extrema of u'_n and w' from low values in white to high values in red (values close to 0 has been removed). Bottom: Binary segmentation based on threshold [264] (green).

5.3 Turbulent spots generation and growth

Since the laminar streaks are not the main structures populating the transitional boundary layer as might have been expected, it is interesting to further investigate the role of the low-speed streak instabilities in the formation of turbulent spots. Two possibilities are considered here: either the low-speed streaks are directly destabilized due to their highly perturbated environment or the mechanism behind the inception of turbulent spots is different.

To gain understanding about this, a laminar-turbulent discrimination is applied over the transitional region, allowing the identification of turbulent spot precursors. The method, adapted from Durovic [263], is presented in section 4.3.3. The discrimination is applied to 2048 instantaneous sub-volumes, extending from the stagnation point at LE to Re_θ=1210. An example of the output of the discrimination algorithm is given in figure 5.18. The extrema density of u'_n and w' is relatively high in the TBL. Two hot spots are present in the transitional BL and corresponds to the birth of two turbulent spots. The thresholding of the density field finalizes the laminar-turbulent discrimination, which correctly captures the TBL and the turbulent spots, as observed in figure 5.18 (bottom).

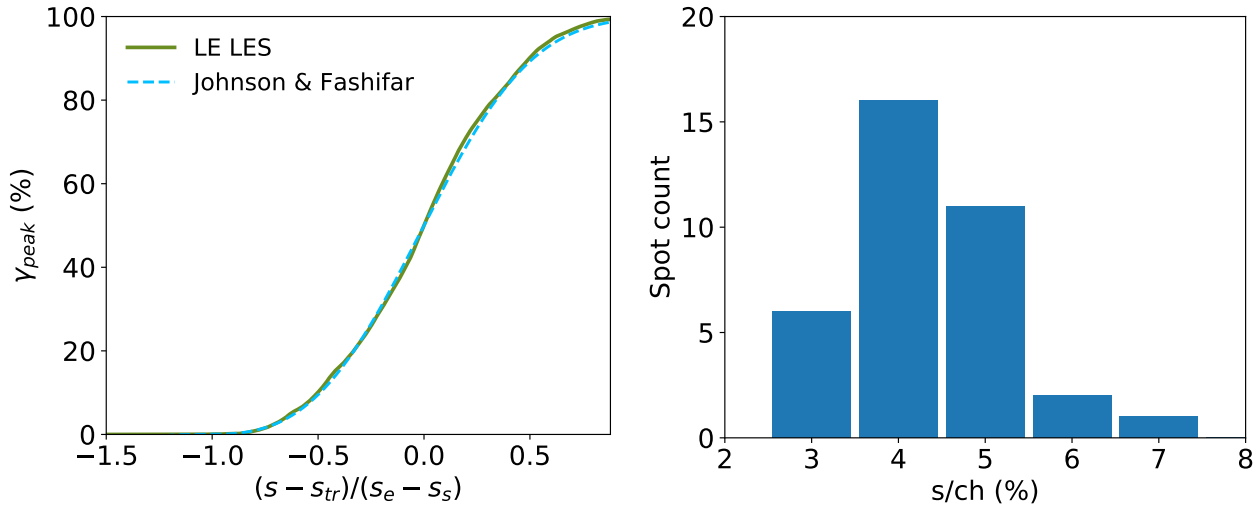

Figure 5.19: Left: peak intermittency evolution, along with the correlation of [309]. Right: distribution along the tangential direction of the spot inceptions.

Using the discrimination algorithm, the distribution of the intermittency factor γ_{peak}, which is the probability that the flow at a point is turbulent, is calculated from the time and span-averaged segmented binary field. Here, $\gamma_{peak}(s)$ is defined as the peak of the intermittency distribution inside the BL at each streamwise location s. The evolution is plotted in figure 5.19 (left) as a function of the dimensionless streamwise coordinate $\xi = \frac{s-s_{tr}}{\Delta s_{tr}}$, with s_{tr} defined as the position where $\gamma_{peak} = 0.5$ and Δs_{tr} the distance between $s_{\gamma_{peak}=0.1}$ and $s_{\gamma_{peak}=0.9}$. The evolution is in very good agreement with the experimental correlation of Johnson & Fashifar [309], which gives good confidence in the discrimination procedure. The inception locations of the turbulent spots, highlighted by the laminar-turbulent discrimination, are tracked using snapshots of sz-planes. In total, 36 spots are detected and their location along the tangential direction is reported in figure 5.19 (right). The distribution shape is in good agreement with the results in the literature [74, 266, 267].

These inception locations are used to track the origin of the spots. Interestingly, despite the scarcity of laminar streaks within the transitional BL, all the breakdown events are linked to low-speed streaks. Two breakdown mechanisms are identified, namely streak instabilities and streak interactions. An example of the first scenario is given in figure 5.20. The streak seems already disturbed during its growth and is rapidly disrupted downstream by the high levels of perturbation around it, leading to the formation of a turbulent spot. Due to the perturbed environment, it is not possible to distinguish between sinuous and varicose-type breakdowns.

In fact, a large part of the turbulent breakdowns originates from interactions between neighboring laminar

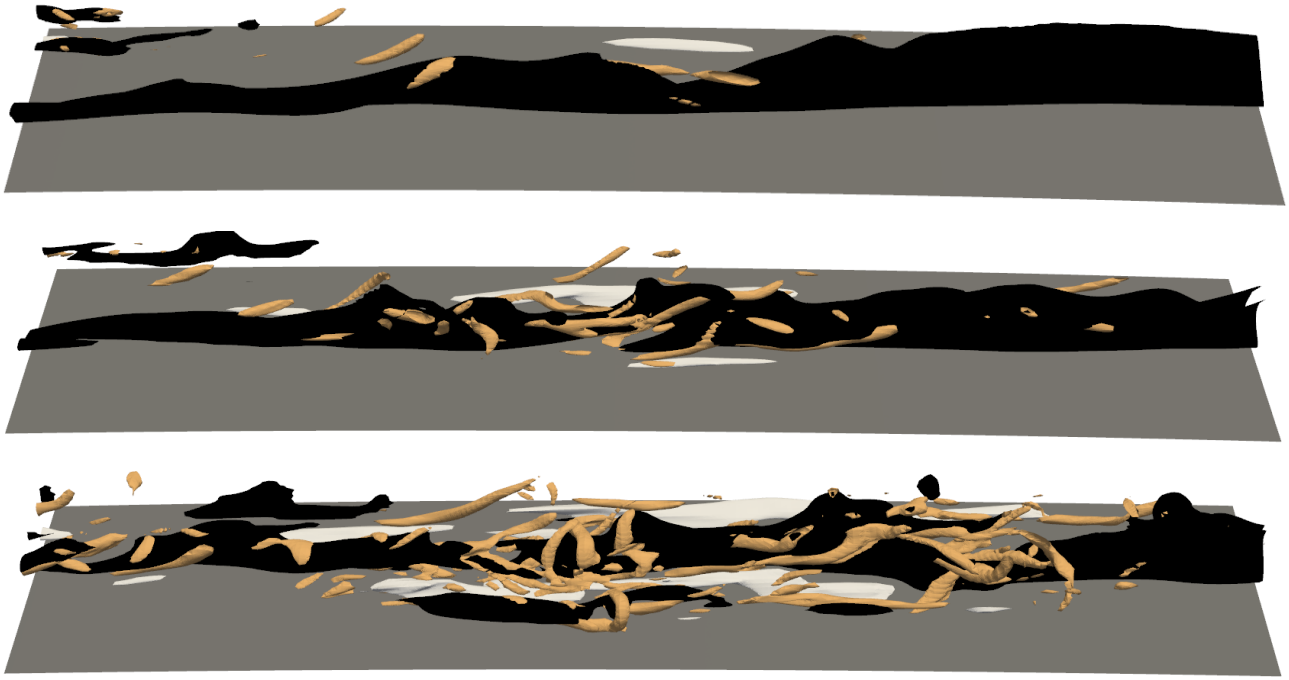

Figure 5.20: 3D observation of a streak instability at three different times between $0.32\% < z/ch < 0.4\%$ and $3.10\% < s/ch < 3.59\%$ (top), $3.43\% < s/ch < 3.92\%$ (middle) and $3.76\% < s/ch < 4.25\%$ (bottom). Isosurfaces of u'_s for $-0.17c_{in}$ (black) and $0.17c_{in}$ (white), along with Q-criterion in light brown.

streaks, which can collide due to the highly disturbed environment. As emphasized by Brandt & Lange [68], the collision between the tail of a low-speed streak and the head of a high-speed streak may cause the turbulent breakdown. In figure 5.21, an example of interaction is illustrated. Two low-speed streaks, flanked by a high-speed one, get closer before finally merging, leading to the collision of the high-speed streak with the newly merged streak. In figure 5.21 (middle), the strong vortices associated with the low-speed streaks are seen to interact, causing the downstream melting. This breakdown scenario bears similarity with the vortex interaction described by Zhao & Sandberg [59], because the intense vortices observed can be traced back to the LE and because a low and high-speed streak are involved. Moreover, as reported in [59], the turbulent spot that emerges from this interaction takes a relatively different shape from traditional turbulent spots (see figure 5.22). However, a little further downstream, this transient effect fades away and the spot recovers a relatively classical shape, with a relatively well defined V-shaped nose.

For large-scale intense FST, previous FP results (Chapter 4) showed that Λ-vortices, as described in the review of Wu [77], can bypass the role of streaks in spot formation. In the present simulation, low-speed Λ-shaped structures, similar to those observed by Ovchinnikov et al. [57], are also observed but they do not lead to turbulent spots. An example is shown in figure 5.23 (left), where this Λ-shaped structure is flanked on each side by the vortices that generated it and is connected downstream to a low-speed streak. Λ-vortices usually emerges close to the LE, where the strong pressure gradient prevents them from transitioning and tends to realign them in the streamwise direction. The modulation by large-scale structures, whose presence can be guessed from the absence of low-speed structures in figure 5.23 (right), may disturb their evolution.

We are now interested in characterizing the turbulent spots, such as the one depicted in figure 5.24. It exhibits the classical features, with a well-defined arrow-shaped head, the lateral wings and the calmed region behind. Surprisingly, we also observe the formation of spanwise oriented vortices under the spot and in its trail in figure 5.24 (top), similar to those reported in [86, 78] for turbulent spots in supersonic flows. This phenomenon has been shown to be enhanced by isothermal wall conditions, which reduces the temperature variations inside the BL. In our case, the high specific heat of Novec649 plays a similar role and significantly reduces friction heating, explaining the observation of these spanwise oriented vortices that also imprint the normal velocity fluctuations (see figure 5.24 (bottom)). However, contrary to air flows where these structures are generally reported at $M \geq 3$, the organic vapor BL exhibits these wall vortices at Mach numbers between 0.75 and 1.0.

As emphasized by Unnikrishnan & Gaitonde [310], the spanwise wall structures may persist downstream in

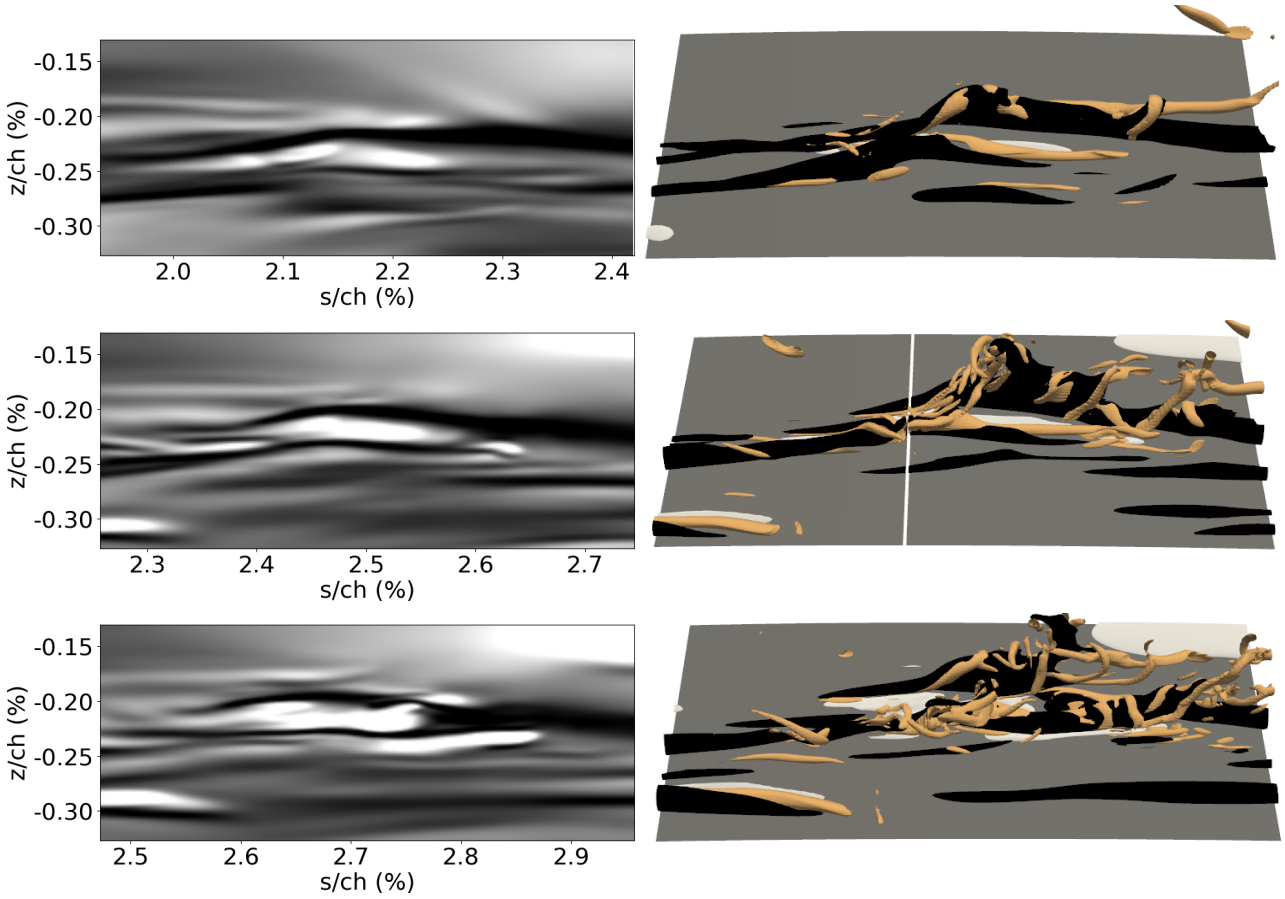

Figure 5.21: Observation of streak interaction leading to the formation of a turbulent spot at three successive times. Left: tangential velocity fluctuations u'_s at $n^+ \sim 11$ (levels $\pm 0.1 c_{in}$, from black to white). Rigth: isosurfaces of u'_s for $-0.1 c_{in}$ (black) and $0.1 c_{in}$ (white), along with Q-criterion in light brown.

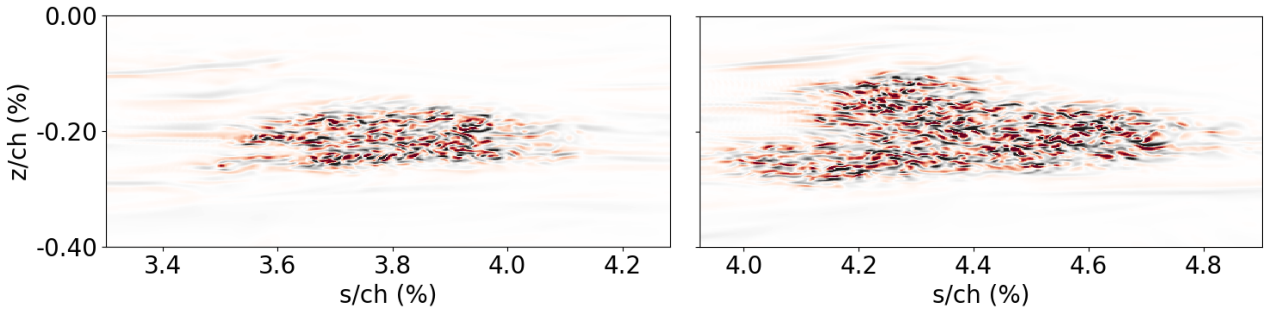

Figure 5.22: Evolution of the turbulent spot shape originating from the streak interaction in figure 5.21. Tangential velocity fluctuations u'_n at $n^+ \sim 11$ (levels $\pm 0.05 c_{in}$).

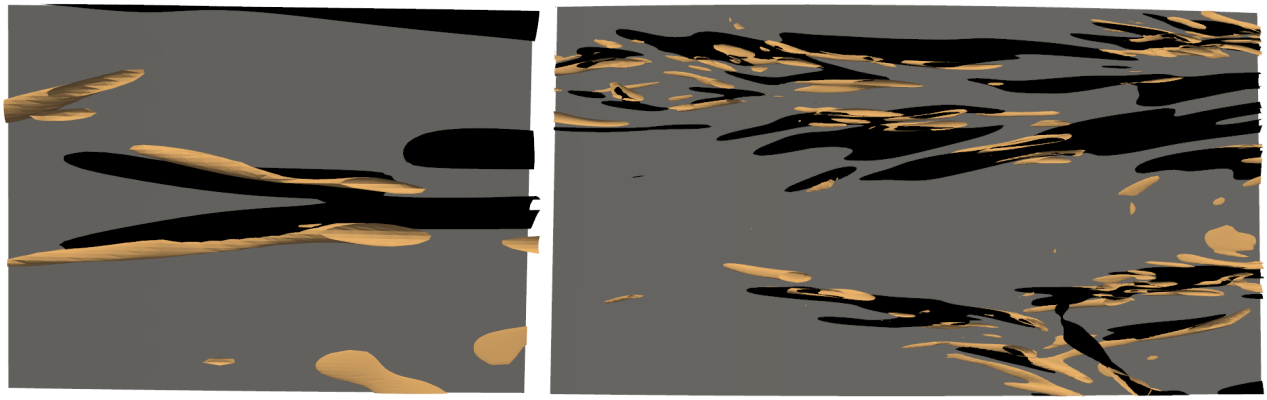

Figure 5.23: Observation of low-speed Λ-shaped structures inside the BL at $1.35\% \leq s/ch \leq 1.57\%$ (left) and at $0.89\% \leq s/ch \leq 1.73\%$ (right). Isosurfaces of u'_s for $-0.05c_{in}$ (black), along with Q-criterion in light brown.

the fully turbulent region. Inspecting a 3D snaspshot in the TBL region in figure 5.25, these spanwise vortices are difficult to observe from above (right panel) but, looking from below (left panel), they are clearly identified. One reason which could explain their presence in the fully turbulent region is the existence of turbulent spots inside the TBL, as demonstrated by Wu et al. [76] who termed them turbulent–turbulent spots. Similarly to cold wall [78], the dramatic reduction of friction heating by the Novec649 high specific heat might also influence the spreading rate of the turbulent spots. To confirm this, the spreading half-angle of the turbulent spots is estimated as far as possible. Indeed, spots appearing too close to each other rapidly merge, which does not allow to follow their evolution over a sufficient time. In other instances, the spreading of the spot can be significantly disturbed on one side by the large-scale structures in the BL. This is highlighted in figure 5.26 where the spreading of the two spots appearing at s/ch=3.5% and 3.8% is inhibited by the presence of the large-scale structure. At the same time, the two turbulent spots appearing around s/ch ~4.8% and 5.3% have increased significantly in proportion between the three consecutive figures. The combined effect of the FPG and the modulation of turbulent spots by the large structures is also an explanation for the larger extent of the transitional region length reported in figure 5.9(d).

In total, the spreading angle is evaluated for 10 relatively undisturbed spots. The position of lateral wing tips is collected every 1100 temporal iterations for as long as possible, then fitted by a least square regression line, depicted in figure 5.27 (left). Then, using the intersection coordinates s_i and z_i of the lines, the spreading half-angle α is estimated. A mean angle $\overline{\alpha} = 4.2°$ is obtained, with a minimal and maximal value of 3.2° and 5.4°, respectively. In figure 5.27, the range evolution of the spreading half-angle α obtained experimentally

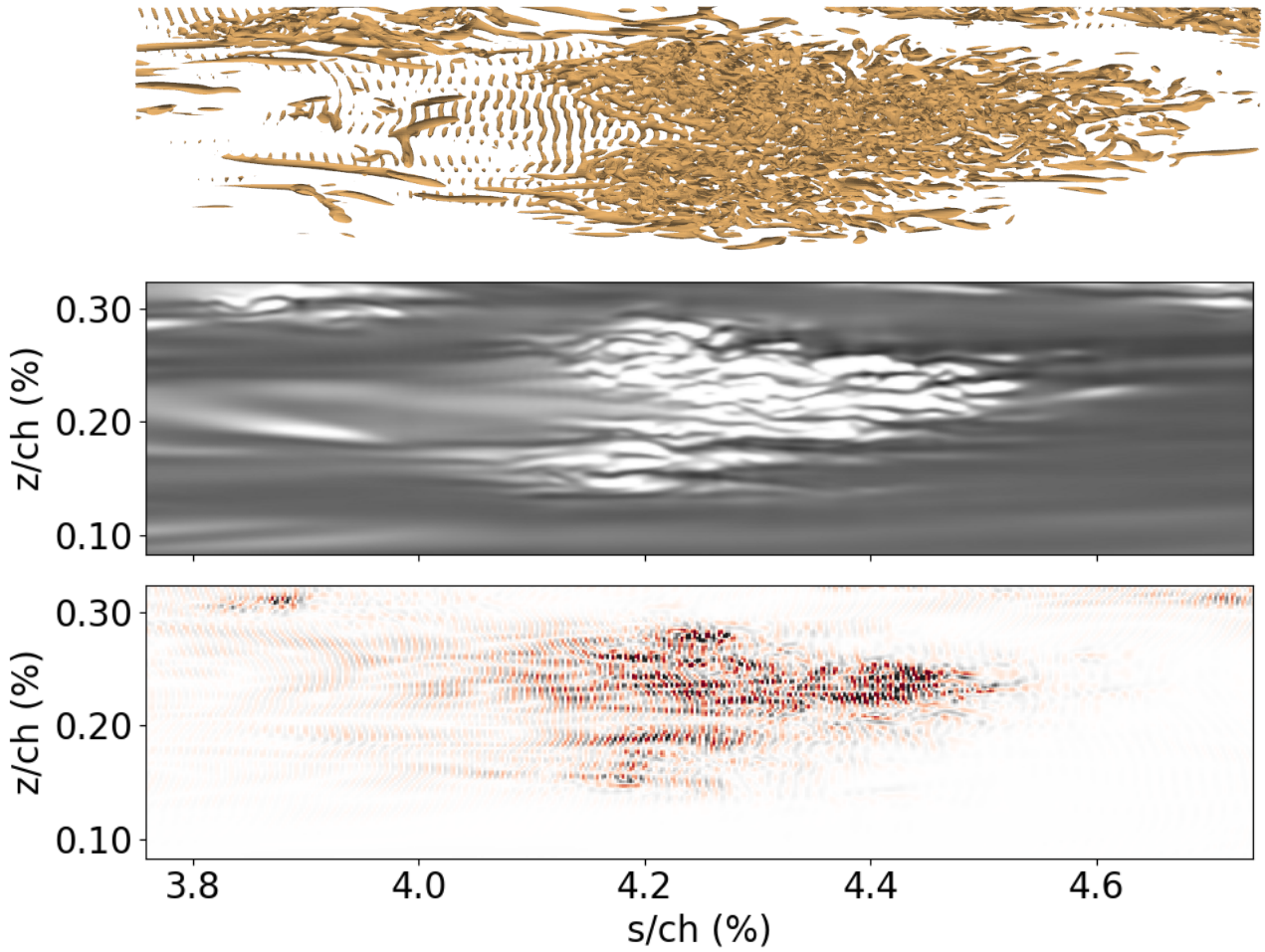

Figure 5.24: Turbulent spots characteristics and observation of near-wall spanwise vortices. Top: Q-criterion in light brown. Middle: tangential velocity fluctuations u'_s at $n^+ \sim 5.9$ (levels $\pm 0.2 c_{in}$, from black to white). Bottom: wall-normal velocity fluctuations u'_n at $n^+ \sim 0.7$ (levels $\pm 0.0025 c_{in}$).

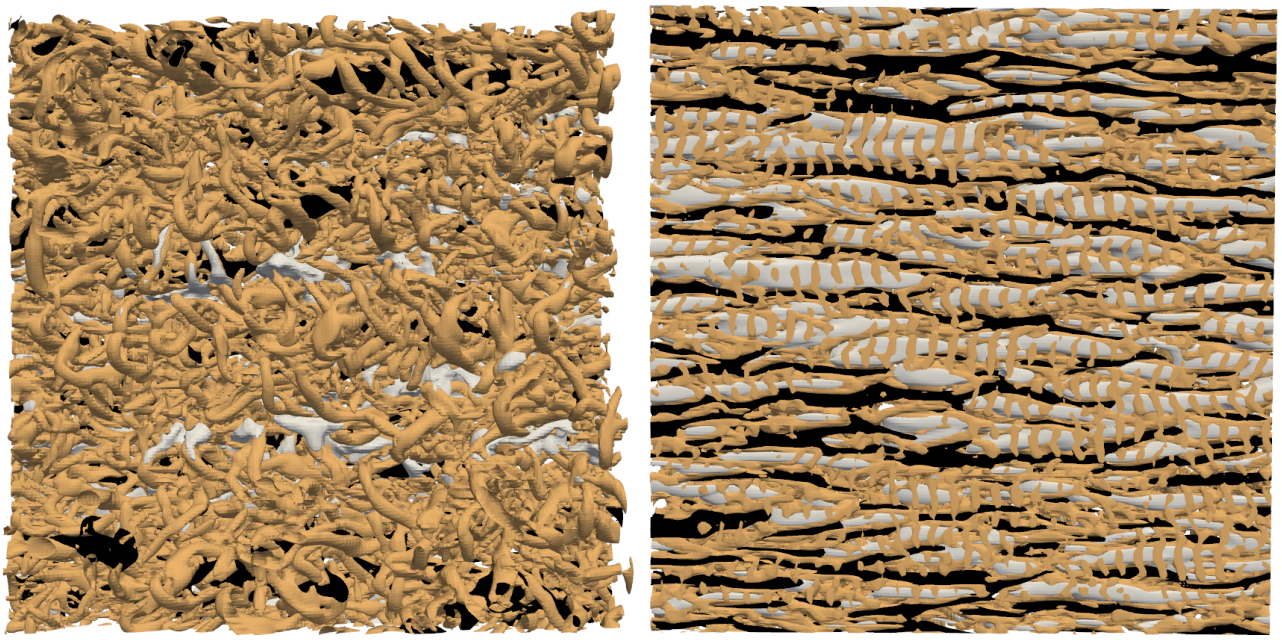

Figure 5.25: 3D visualization from above (left) and below (right) of isosurfaces of tangential velocity fluctuations u'_s (levels $\pm 0.01 \times c_{in}$)) and Q-criterion in the TBL at $7.35\% \leq s/ch \leq 7.68\%$ and $0.0\% \leq z/ch \leq 0.33\%$.

by Fischer [84] is plotted, along with numerical results of turbulent spots in supersonic flows [85, 78], which take values in agreement with the experimental ones. In the figure, the effects of a cold wall (denoted isoth.) in reducing α is noticeable. The incompressible results of Nolan & Zaki [74] are also plotted, where we can observe the small effect of a FPG on α, which reduces from $12°$ to $10°$ compared to ZPG. The angle $\overline{\alpha}$ estimated in the current LES is significantly below the observed trend with a difference with the experimental curve of Fischer [84] similar to the one obtain by Redford et al. [78] between adiabatic (adiab.) and isothermal (isoth.) walls. Based on the small influence of FPG on α in Nolan & Zaki [74], the mild FPG is not expected here to play a significant role in the lateral spreading growth reduction observed. Thus, the lower observed value must be a consequence of the Novec649 properties, in particular its high specific heat which acts similarly to a cold wall.

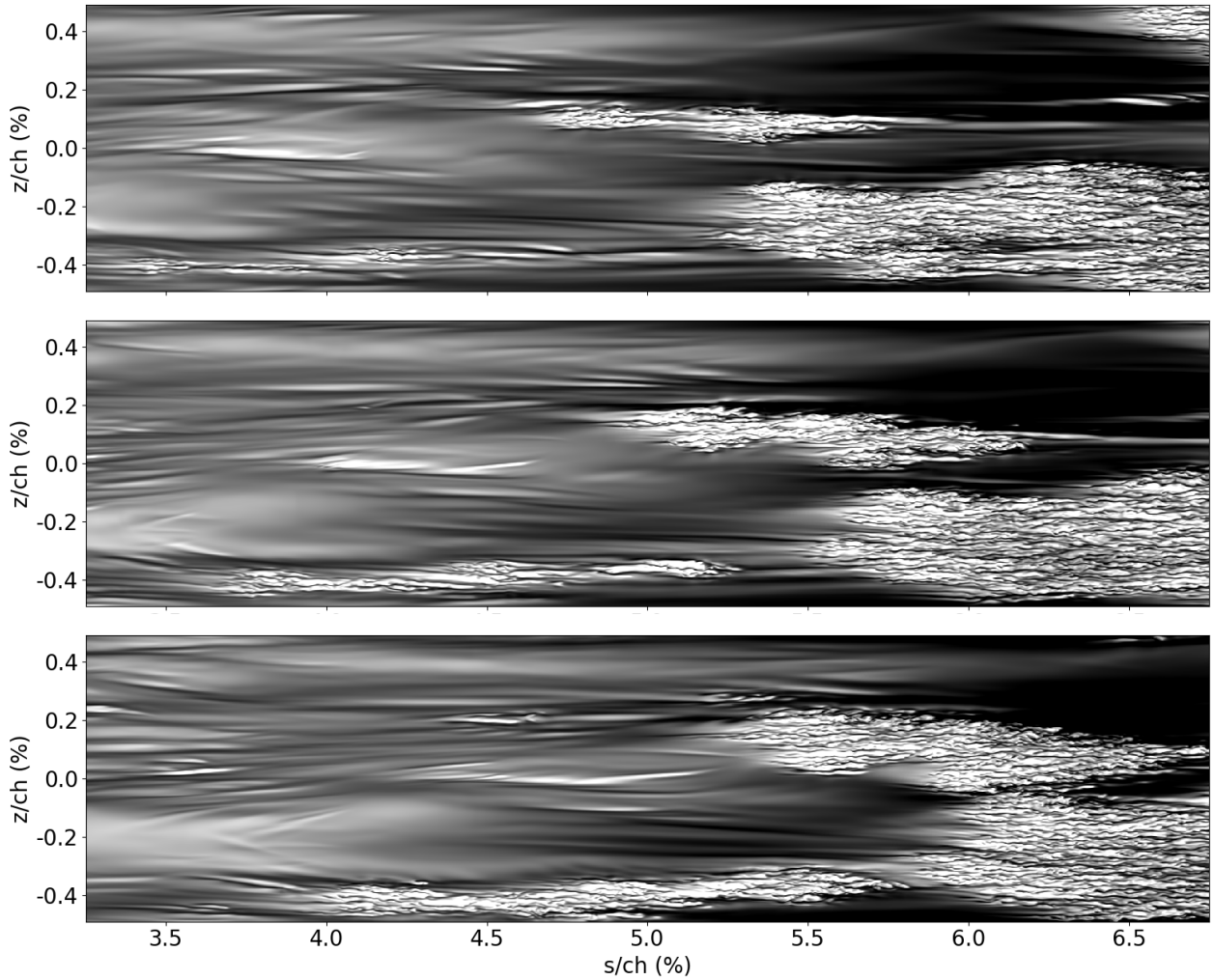

Figure 5.26: Observation of a large structure modulating the lateral spreading of turbulent spots. Tangential velocity fluctuations u'_s at $n^+ \sim 15$ (levels $\pm 0.2 c_{in}$, from black to white).

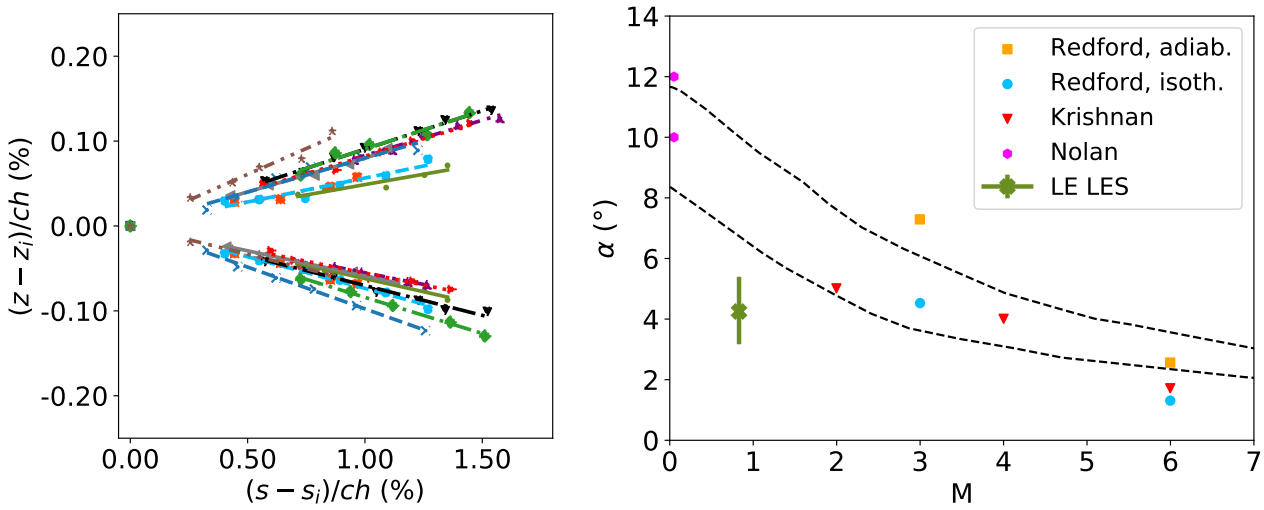

Figure 5.27: Left: evolution of the lateral wing tip for the evaluated spots centered along the intersection point of the least square regression lines. Right: evolution of the spreading half-angle α with the Mach in supersonic flows obtained experimentally [84] (- - -) and numerically [85, 78], along with estimated $\overline{\alpha}$ for the current LE LES. The incompressible results of [74] are also reported for ZPG ($\alpha = 12°$) and FPG ($\alpha = 10°$).

Chapter Summary

The FST transition of the organic vapor Novec649 past the leading-edge (LE) region of a blade vane representative of ORC turbines is studied with wall-resolved LES. The dense gas flow accelerates from M=0.5 up to 1. Compared to previous studies, the Reynolds number based on the blade half-thickness is one order of magnitude greater ($\approx 478\,000$) due to the high density of Novec649. The transition, which occurs early ($x/ch \sim 5\%$), is thoroughly analyzed.

Interaction of the FST with the LE and the boundary layer (BL):

- Due to the high-Reynolds-number conditions, FST structures are small compared to the LE characteristic size but large compared to the BL thickness.
- The inlet FST wraps around the LE by stretching and tilting, which amplifies fluctuations acting on the developing BL.
- These wrapped structures appear as clusters of small-scale streamwise vortices, which lead downstream to the formation of laminar streaks. This large-scale spanwise arrangement, as clusters, modulates the laminar streaks and the spanwise spreading of turbulent spots.
- The combined effect of FPG and modulation lengthens the transition compared to ZPGFP.

Turbulent breakdowns origins:

- Origins of turbulent spot are tracked through laminar-turbulent discrimination.
- Precursors: low-speed laminar streaks through streak instabilities and streak interactions.
- No obvious canonical streak instabilities (sinuous or varicose) are observed.
- Second mechanism: interaction and collision between neighboring streaks.
- High FPG prevents Λ-shaped structures near the stagnation point to participate to transition.

Influence of Novec on turbulent spot characteristics:

- Turbulent spots bear strong similarities with those in supersonic flows on cold walls.
- Due Novec's high thermal capacity, presence of spanwise-oriented vortices close to the wall in turbulent spots and TBL, as reported for isothermal walls in air.
- Paradoxical enhancement of compressibility effect: reduction of spots lateral spreading angle α compared to air at $M = 0.9$ and comparable to cold-wall supersonic air flows.

Chapter 6

Investigation of a transonic dense gas flow over an idealized blade vane configuration

In this chapter, the flow around the full idealized blade vane configuration is now investigated. Results obtained for Novec649 are contrasted with those calculated for air, to highlight the role of the organic fluid complexity. To mitigate the computational burden of LES at the very high Reynolds number at stake, hybrid RANS/LES simulations are considered, in particular Delayed Detached Eddy Simulation (DDES). The latter uses RANS to model attached boundary layers and automatically switches to LES in regions with sufficient grid resolution. Although the RANS region prevents an accurate resolution of boundary layer transition, this is not expected to be critical for the considered configuration, as most of the boundary layer is expected to be mostly turbulent due to early transition after the LE (as discussed in Chapter 5). However, the LES mode of DDES is activated in the shear layers and wake region downstream of the trailing edge, which dramatically improves the description of the wake dynamics and its effect on vane losses. The simulations are compared with steady and unsteady RANS computations, showing significant differences in the computed loss coefficients. The chapter is organized as follows. Numerical methods and simulation set-up are presented in section 6.1. Numerical results for various flow conditions are discussed in section 6.2. Finally, a detailed analysis of the blade losses and their decomposition into different contributions is performed in section 6.3.

6.1 Numerical methods and set-up

6.1.1 Numerical methods

The compressible Navier-Stokes equations are solved by the in-house finite-difference flow solver MUSICAA, as described in section 2. Simulations are performed on multi-block curvilinear structured domains using generalized coordinate transformations. The governing equations are complemented by equations of state and transport equation laws suitable for complex organic fluids. In particular, the thermodynamic behavior of Novec649 is modeled using the Peng-Robinson-Stryjek-Vera equation of state [13], and the Chung-Lee-Starling models [123] are used to describe the variations of the transport properties with temperature and density (see section 2.2). For air flows, we simply use the usual perfect gas equation of state and the Sutherland law for viscosity. As detailed in section 2.3.5, turbulence effects are modeled by using either a RANS formulation together with the Spalart-Allmaras turbulence model, or a DDES hybrid RANS/LES formulation, namely the Delayed DES-Shear Layer Adapted (DDES-SLA) approach of [183]. The latter is based on a modified formulation of the Spalart-Allmaras model specifically designed to accelerate the transition to resolved turbulence in separated shear layers (see section 2.3.5.3). The DDES-SLA strategy has been shown to improve wake predictions compared to URANS and DDES (see Appendix D).

In the following RANS and DDES-SLA simulations, the inviscid fluxes of the mean flow equations are discretized using 4th-order or 10th-order central finite differences, respectively, while viscous fluxes are discretized using a 4th-order finite differences in all cases. Fourth- or tenth-order selective filtering is applied to eliminate spurious grid-to-grid oscillations, respectively for RANS and DDES-SLA. The filter is equipped with a low-order shock capturing term activated locally by a combination of Jameson's shock sensor and Ducros' dilatation/vorticity sensor. As the repeated application of the filter at each time step can lead to an overdissipation when using small time steps (or CFL numbers), the filtering coefficient χ_f is replaced by $\min(\chi_f, \text{CFL})$ as recommended in [153], so that the shocks are sharply captured in steady computations. The RANS transport equations are discretized using a 5-point third-order scheme in all cases. For unsteady RANS and DDES, the time integration is performed with a low-storage RK4 scheme supplemented with the IRS4 operator (see section 2.4), allowing an increase of the maximum allowable CFL by a factor of 5 compared to the explicit time integration for an overcost of $\sim 40\%$ per iteration. A less expensive second-order IRS operator is used for steady-state RANS simulations.

Boundary conditions based on the Riemann invariants are prescribed at the inlet/outlet boundaries of the

Case	ch [mm]	M_1	c_1 [m/s]	$p_{0,1}$ [bars]	$T_{0,1}$ [K]	M_2	c_2 [m/s]	Re_{M_2} ($\times 10^6$)	π $\frac{p_{0,1}}{p_2}$	$\gamma_{pv,1}$	$\gamma_{pv,2}$	Γ_1	Γ_2
Novec-1	61.2	0.55	76	3.76	335	1.52	87.5	8.4	3.6	0.82	0.97	0.78	0.96
Novec-2	61.2	0.58	60	15.5	433	1.43	90.5	12.5	3.2	0.55	0.89	0.47	0.87
Air	246	0.51	343	4.0	308	1.61	285	8.4	4.9	1.40	1.40	1.20	1.20

Table 6.1: Thermodynamic and aerodynamic conditions of simulations. Mixed-out values are taken from DES cases, along the line of measure plotted in figure 6.2.

computational domain. Specifically, the stagnation pressure and temperature are imposed at the inlet, along with the flow angle and an eddy viscosity value equal to 10 times the physical viscosity, while a back-pressure condition is used at the outlet. A sponge zone combining controlled grid stretching and a Laplacian filter is added at the outlet to avoid spurious reflections. Adiabatic no-slip wall conditions are imposed at all solid walls.

6.1.2 Operating conditions

The idealized blade vane configuration, presented in details in section 5.1.1, is investigated in different flow conditions. First, numerical simulations are performed with Novec649 for two sets of inlet thermodynamic conditions: Case Novec-1 corresponds to relatively dilute conditions representative of the CLOWT facility, with a total pressure of $p_{0,1} = 3.8$ bar and a total temperature of $T_{0,1} = 335$ K (see table 6.1). For the Novec-2 case, which corresponds to Point C in section 2.2, the inlet stagnation conditions are chosen such that the fundamental derivative of gas dynamics Γ is equal to 0.41, close to the minimum value achievable for Novec649 in the dry vapor region ($\Gamma_{min} = 0.35$).

The inlet values are calculated one chord upstream of the LE and the exit values are evaluated along the line of measure (plotted in figure 6.2), which corresponds to a distance of $0.25 \times ch/\cos(\chi)$, where $\chi = 60°$ denotes the stagger angle and t corresponds to the inter-blade distance. A uniform mixed-out final state was assumed and a constant area mixing calculation was performed to determine the exit values. Based on the conservation of mass, momentum, and energy, and using the non-uniform flow field along the line of measure as the initial state, the method matches this input state to a mixed-out state where the flow properties are uniform [311]. The exit Reynolds number Re_{M_2}, based on the chord and the exit Mach number M_2, is equal to 8.5×10^6. For comparison, a simulation with air is also performed, where the chord is rescaled to 246 mm in order to match the outlet Reynolds number of the Novec-1 simulation (see table 6.1).

6.1.3 Numerical set-up

The simulations are performed on structured grids with multi-block topology. A grid convergence study is performed on the Novec-1 case for 2D RANS simulations in Appendix F.1. Overall, the results between the three different grids collapse perfectly and the medium grid, composed of 306k points with 1020 points along the blade, is retained to perform all the RANS simulations in the different cases. The RANS methodology has been validated for the air case using the experimental data of [114] (see Appendix F.2). The present DDES-SLA approach has also been previously validated for the well-known VKI LS59 turbine cascade using the experimental data of [312] and LES, as detailed in Appendix D. The results showed that DDES-SLA yields good agreement with LES and experimental results, and captures the correct vortex shedding regime in the unsteady turbulent wake behind the blades.

The present DDES-SLA simulations are performed with a 3D mesh of 102 million points. First, the 2D vane is discretized with a mesh of 850k points, which is finer than that used for RANS simulations. The mesh is particularly refined in the wake region to ensure that DDES-SLA switches to LES mode. The 2D mesh is then uniformly extruded in the spanwise direction. The spanwise length of the domain is $\Delta_z/ch = 0.14\%$, which is large enough to avoid truncation of the largest turbulent spanwise structures. The total number of grid points in the spanwise direction is $N_z = 120$. Due to the high cost of the simulations, a mesh convergence study was not performed. Instead, the resolution in the wake region was evaluated using the velocity spectra. A typical velocity spectrum E_{vv} (for the vertical velocity component) extracted in the wake at the measurement line is shown in figure 6.1 for the Novec-1 case. The time signal was recorded during 300 000 iterations, which corresponds to about twenty vortex shedding cycles. The spectrum exhibits an inertial range with a -5/3 law over almost one decade and the wake frequency of the wake (i.e. the Strouhal number St) is well below the cutoff wavenumber of the numerical scheme.

6.2 Flow field characterization

A schlieren-like visualization of the transonic configuration is given in figure 6.2, where several regions of interest in the flow are identified. Region 1 around the blade LE corresponds to the laminar-turbulent transition region, which has been extensively studied in chapter 5 and will not be considered further here. The second region of interest (region 2) corresponds to the interaction of a shock generated by the upper wall (emulating the TE of the neighboring blade) with the boundary layer at the suction side. A fine-detail analysis of the flow

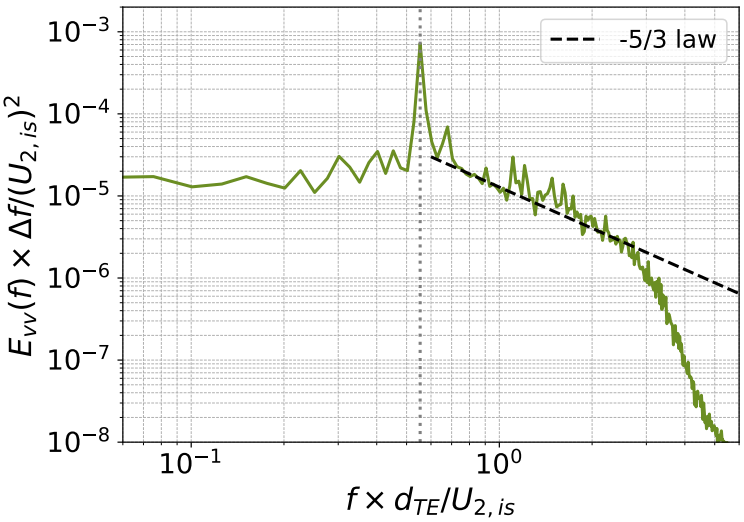

Figure 6.1: Energy spectra of the velocity component v in the wake at the measure line location in the Novec-1 DDES. ··· ·····: Strouhal number.

dynamics in the interaction region is not possible with the present flow model because DDES-SLA operates in RANS mode in the attached boundary layer. The last region corresponds to the wake, which plays a crucial role in the generation of turbine losses [11]. Since RANS simulations fail to predict the base region and the near-wake profile [97], and unsteady RANS simulations are not expected to accurately predict the vortex shedding frequency and the wake mixing process [11, 42], the latter region is solved in LES mode thanks to the DDES-SLA approach.

In the following, the role of the thermodynamic behavior of the fluid, in particular the fundamental derivative of the gas dynamics and the isentropic exponent, is first examined (section 6.2.1). The unsteady wake dynamics is then analyzed in section 6.2.2.

6.2.1 Non-ideal effects on the gas dynamics

As shown in table 6.1 both Novec-1 and Novec-2 cases are characterized by inlet and outlet values of the fundamental derivative of gas dynamics (respectively, Γ_1 and Γ_2) smaller than one, i.e. the flow occurs in the dense gas region. In the Novec-1 case, the gas behavior is only weakly non-ideal throughout the vane. In the Novec-2 case, the flow enters the vane under relatively non-ideal conditions, but as the organic vapor expands, its thermodynamic state moves toward more dilute, weakly non-ideal conditions. The dense gas flows lead to a reverse behavior of the speed of sound compared to perfect gases, namely, $\left(\frac{\partial c}{\partial \rho}\right)_s < 0$ so that the speed of sound

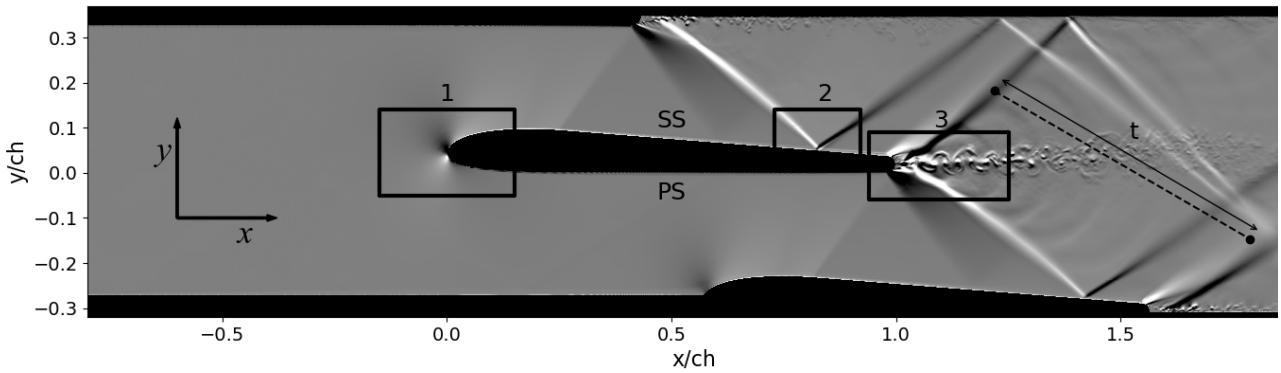

Figure 6.2: Schlieren-like visualization of the idealized blade vane configuration in the Novec-1 DDES case: density gradient in y-direction (levels $\pm 0.5 \times 10^4$); - - -: line of measure; identification of regions of interest in the flow (1 to 3) and of pressure (PS) and suction side (SS).

increases while the flow expands, limiting the increase of the Mach number with respect to air flow. As the non-ideality of the flows increases, shock waves become weaker and the expansion ratio π achievable with the present geometry also decreases. Specifically, π is significantly lower in the Novec-2 flow ($\pi_{Novec-2} = 3.17$) than in air ($\pi_{air} = 4.95$). To get more insights, the isentropic Mach number M_{is} distributions of the air and Novec simulations are compared in figure 6.3. In line with the differences observed in pressure ratio, the isentropic Mach number distribution levels around the blade decreases with the isentropic exponent. Moreover, a difference in the position of the reflected shock at the suction side is noticed.

As in the DDES the attached BLs are modeled by the RANS equations, no differences between the DDES and RANS simulations are observed in this region of the flow, as shown in figure 6.3. In table 6.2, some relevant exit quantities are reported for both RANS and DDES simulations, showing an overall good agreement between the two approaches. This is the case for the pressure ratio and $M_{2,is}$. The exit angle β_2 is also well captured by the RANS methodology, along with the opening angle of the fishtail shocks α_o in the different cases. The opening angle is directly related to the exit Mach number and, as the expansion ratio π decreases, α_o increases, being larger in more non-ideal Novec649 cases.

The wake region is displayed for the RANS and DDES Novec-1 case in figure 6.4 (a). The supersonic flow around the TE generates an expansion fan when the flow turns around the TE, followed by a shock at the separation location (line 1) and the formation of free shear layers (line 3), leading to a confluence region where the fish-tail shock waves are produced as the flows from either side of the blade meet and turn in a shared direction [313]. The turning angle of the flow at the suction (resp., pressure) side, which corresponds to the angle between the suction (resp., pressure) side and the shear layer, depends strongly on the thermodynamic state

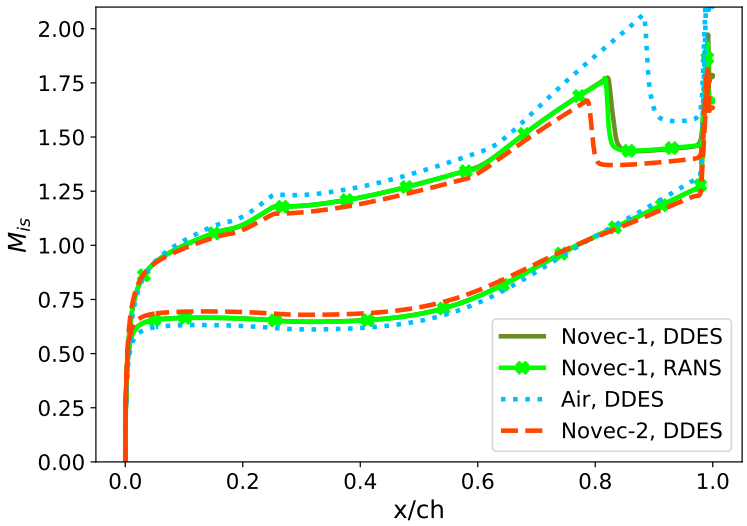

Figure 6.3: Isentropic Mach number distribution around the blade in the different cases.

Flow	Simu.	$M_{2,is}$	π $p_{0,1}/p_2$	β_2 [°]	α_o [°]	α_{tf} [°]
Air	DDES	1.701	4.94	2.2	66.0	19.0
	RANS	1.702	4.95	1.8	65.0	13.5
Novec-1	DDES	1.586	3.60	3.5	71.0	19.5
	RANS	1.586	3.60	3.5	70.0	12.5
Novec-2	DDES	1.502	3.17	5.0	77.5	18.0
	RANS	1.501	3.17	5.0	76.0	13.5

Table 6.2: Comparison of global outlet quantities between DDES and RANS simulations, where β_2, α_o and α_{tf} denotes the outflow angle, the fish-tail opening angle and the mean turning flow angle (averaged between the suction and pressure side) at the TE, respectively.

of the fluid [314, 90]. Compared to DDES, RANS simulation overestimate the length of the circulation bubble due to a lower turning angle. The mean turning flow angle α_{tf}, defined as the average between the suction and pressure side, for the different simulations is reported in table 6.2. According to the present DDES results, the three flows exhibit similar mean turning flow angle. However, the expansion does not start at the same Mach number for the three cases, and the two flows cannot be directly compared. To get some insights of how the non-ideal flow behavior affects the turning flow angle, the variation of the Prandtl-Meyer function $\Delta\nu$ associated with the expansion at the suction side is evaluated. For Novec649, we use the expression of the Prandl-Meyer function for non-ideal gases as given in [314]. The latter relies on the assumption that the working fluid behaves as a polytropic perfect gas with an equivalent isentropic exponent γ_{pv} and that the fluid remains outside the

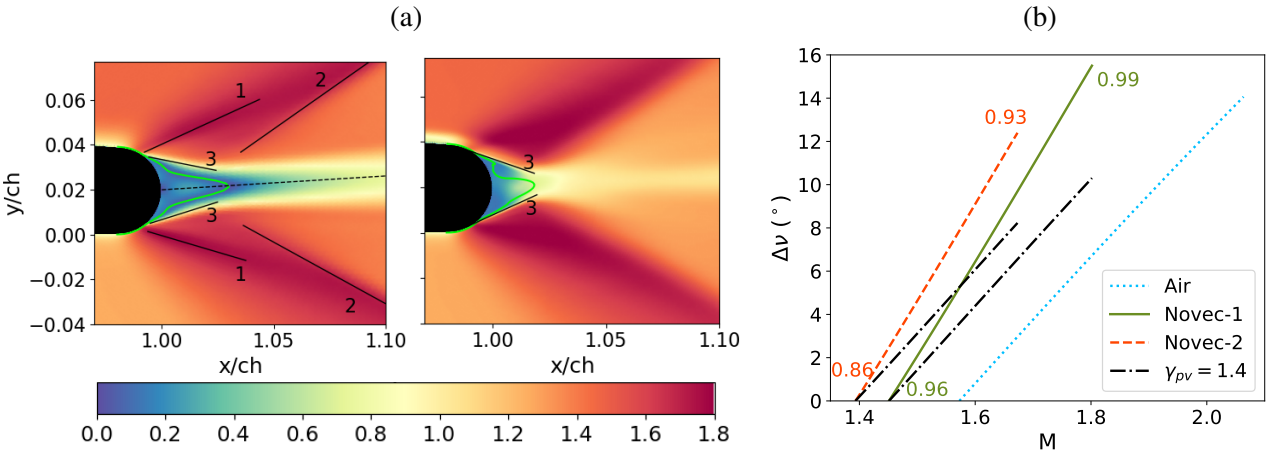

Figure 6.4: (a) Averaged Mach number field in the trailing edge region in the RANS (left) and DDES (right) case. 1: separation shock; 2: trailing edge shocks; 3: free shear layers. —— denotes the contour of the recirculation bubble with the criteria $u = 0$. (b) Variation of Prandtl-Meyer function with Mach number for the TE expansion prior to separation at the suction side in the DDES.

thermodynamic region where nonclassical effects are present, which is the case in the present configuration. In figure 6.4 (b) we plot the variation of the Prandtl-Meyer function $\Delta\nu$ as a function of the Mach number at the beginning of the supersonic expansion M for perfect gases with isentropic exponents corresponding to cases Novec-1 and Novec-2, as well as for a perfect diatomic gas ($\gamma = 1.4$). Starting with the same initial Mach number, more non-ideal gases lead to significantly greater values of $\Delta\nu$ for a given turning angle, hence to higher Mach numbers at the end of the expansion. In practice however, the upstream Mach number decreases when moving to Novec-1 and then to Novec-2. As a consequence the effective overall variation of $\Delta\nu$ is approximately the same for all cases.

6.2.2 Unsteady wake dynamics

Boundary layer separation occurring at the TE leads to the formation of large coherent structures, due to the roll-up of the shear layers. For supersonic flow conditions, vortex shedding is enhanced downstream of the oblique shocks generated at the reattachment point downstream of the TE, and its frequency is mainly determined by the distance between the feet of the shocks. In DDES-SLA simulations, the RANS mode is disabled downstream of the TE, the turbulent viscosity μ_t is greatly reduced, and the flow rapidly transitions to resolved turbulence, as shown in the bottom panel of figure 6.5 (a). This is in sharp contrast to the unsteady RANS solution shown in the top part of the figure, which is characterized by large, coherent 2D vortex shedding. In addition, the increased momentum mixing in the DDES simulations leads to a much shorter recirculation

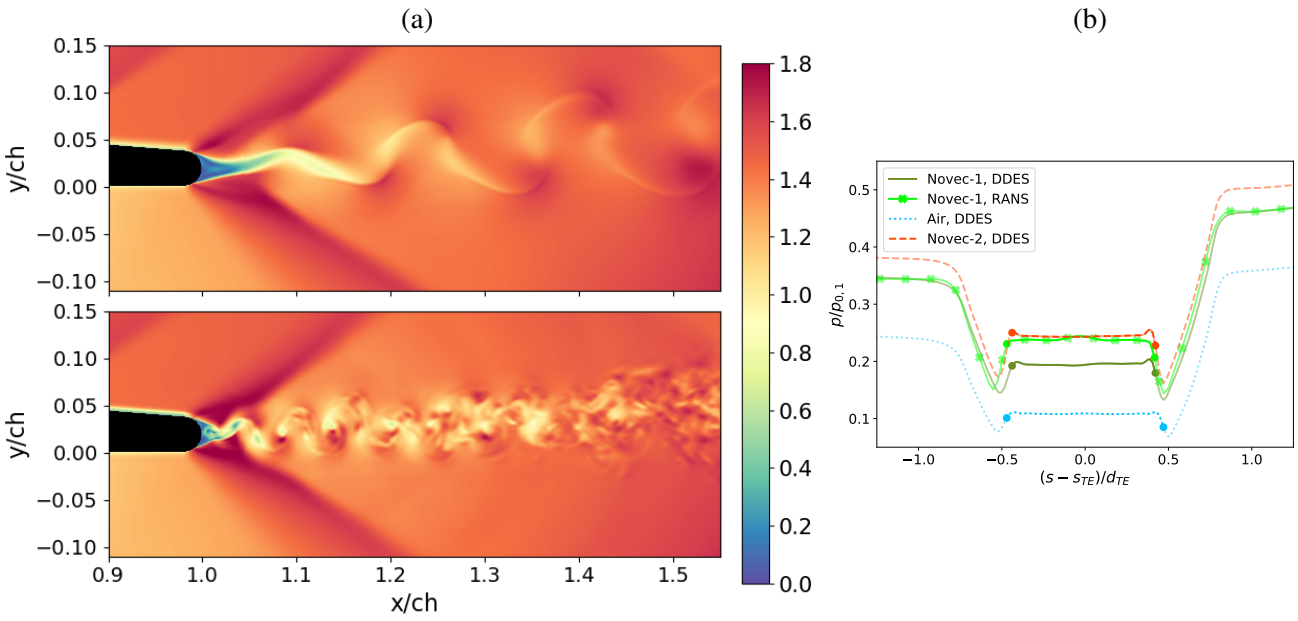

Figure 6.5: (a) Instantaneous Mach number field in the trailing edge region in the 2D URANS (top) and DDES (bottom) Novec-1 case. (b) Pressure distribution around the trailing edge for the different DDES, along with RANS simulation in the Novec-1 case. ● denotes the separation locations, used as limits to calculate the average back pressure p_b, and $s - s_{TE}$ is the curvilinear abscissa relative to the trailing edge position.

bubble behind the blade TE compared to RANS. This results in larger values of the turning angle α_{tf} in DDES than in RANS. The correct capture of the wake flow and the base region is crucial as it has a major impact on the base pressure and therefore on the estimation of the wake-related losses, which can represent a significant percentage of total losses [11] (see section 6.3).

The pressure distribution around the TE is plotted in figure 6.5 (b) for the three DDES simulations. In all cases, the TE base flow is characterized by a constant-pressure region comprised between the separation locations on both sides of the blade (the separation points are highlighted by the bullets). The back pressure increases with increasing outlet Mach number [313]. RANS results for the Novec-1 configuration are also reported in the figure. While the pre-separation expansion is similar for RANS and DDES, the RANS simulation exhibits a stronger separation shock, leading to a significantly higher back pressure. This results in an inaccurate evaluation of the blade losses, as discussed in the next section.

The profiles of selected fluctuating quantities across the wake are reported in figure 6.6. Due to the high specific heat of Novec649, temperature fluctuations are greatly reduced compared to air, as depicted in the bottom left panel of this figure. As shown in the right panel of figure 6.6 (right), representing the profile of the total temperature T_0 across the wake, the high heat capacity of Novec649 also prevents the phenomenon of

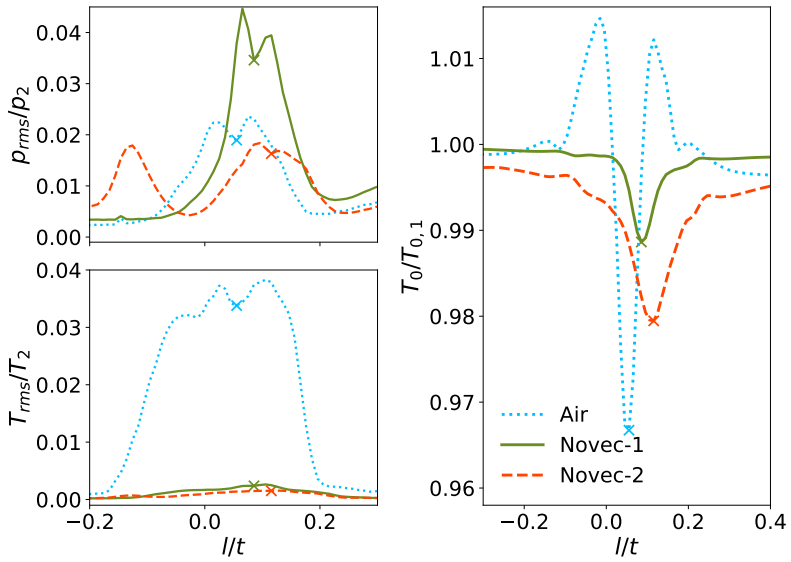

Figure 6.6: Root-mean square pressure (top left), root-mean square temperature (bottom left) and total temperature (right) profiles along the line of measure. The cross denotes the center of the wake.

so-called "energy separation" [11], corresponding to an increase of the total temperature at the borders of the wake due to the intermittent shedding of vortices. In turn, the pressure fluctuations are reinforced in the dense gas, as illustrated by the profiles of fluctuating pressure p_{rms} reported in the top left panel. This results in the appearence of intense acoustic waves generated by the vortex shedding, visualized in figure 6.7 (a) by means of contour plots of the fluctuating pressure. The acoustic waves strength, evaluated as $p_{rms}/\overline{p}$ at a location outside the wake highlighted by a symbol in figure 6.7 (a), is increased by $\sim 50\%$ in Novec-1 case compared to air.

We complete the study with an analysis of the unsteady content in the wake. Unlike vortex shedding under subsonic conditions, which has been studied for example in [11], the literature on supersonic trailing edge wakes is relatively scarce and leads to contradictory conclusions. On the one hand, studies [315, 316, 317] show that the characteristic frequency in the wake of a flat plate is independent of Mach and Reynolds numbers and is equal to 0.3. On the other hand, studies of transonic turbine wakes [318, 319] show an increase of the Strouhal number with Mach number, mainly due to the strong modification of the trailing edge shock system. Using the velocity power density spectra extracted at the measurement line in the wake (such as the one in figure 6.1), the Strouhal number $St = f \times d_{TE}/U_{2,is}$, based on the trailing edge thickness and exit velocity and corresponding to the vortex shedding frequency, is evaluated for the DDES simulations, and the results are shown in figure 6.7 (b) along with experimental results for the Strouhal number in supersonic turbine TE wakes available in the literature. Despite the scatter in the results, we observe a clear trend for St to increase with Mach number.

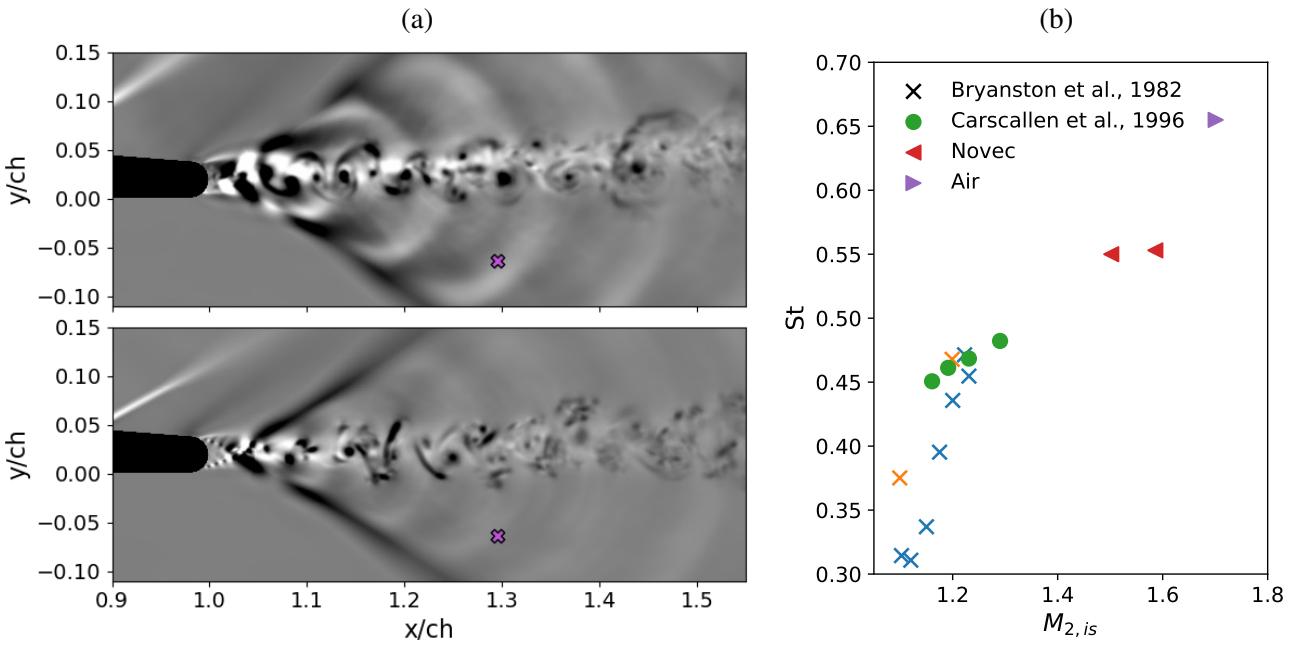

Figure 6.7:

Interestingly, despite a lower Mach number, the Novec-2 flow has a similar Strouhal number very close to that of the Novec-1 case, probably due to the higher Reynolds number of this flow. Note that, according to the unsteady RANS simulations performed for the Novec-1 case, the Strouhal number is estimated to be $St = 0.18$, which is well below the values predicted by DDES or found in the literature. In addition, we observed that the unsteadiness of the wake in URANS is very sensitive to the approximation scheme and computational mesh (not shown for brevity), which gives little confidence in the robustness of the method and further invalidates the ability of URANS to correctly capture the unsteady wake.

6.3 Analysis of blade losses

In this Section we examine the loss mechanisms in detail. First, we consider the enthalpy loss coefficient, defined as:

$$\zeta_{out} = 1 - \frac{h_{0,1} - h_2}{h_{0,1} - h_{2,is}} \tag{6.1}$$

To remove the influence of the upper and lower walls and to extract the contribution of a single blade to the losses, the evaluation of ζ_{out} is based on the mixed-out state along the measurement line comprised between the inter-blade meridional lines, as shown in figure 6.8. The figure also reports typical iso-contours of the

Flow	Simu.	ζ_{out} (%)	ζ_{pass} (%)	ζ_{TE} (%)	ζ_{Den} (%)	$C_{p,b}$
Air	DDES	6.1	1.7	4.4	8.0	-0.23
	RANS	5.1	1.9	3.2	6.7	-0.16
Novec-1	DDES	7.5	2.1	5.4	8.1	-0.24
	RANS	6.2	2.4	3.8	6.1	-0.12
Novec-2	DDES	8.1	2.1	6.0	7.5	-0.21
	RANS	6.6	2.2	4.4	5.5	-0.09

Table 6.3: Losses estimations for the different flows and simulations.

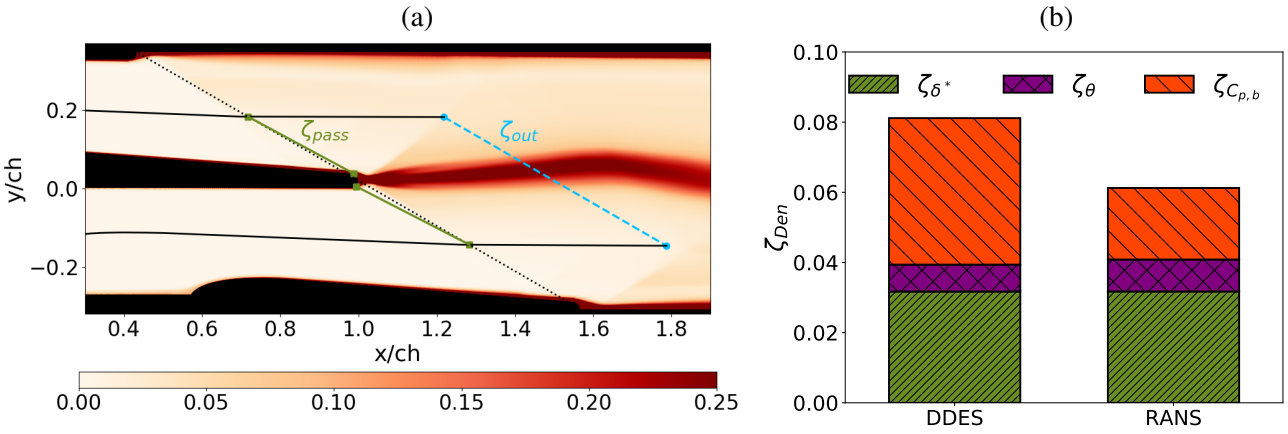

Figure 6.8: (a) Entropy deviation $(\overline{s} - s_1)/s_1$ in the Novec-1 case, along with the control lines used for the estimation of the losses. (b) Denton's loss decomposition in the Novec-1 case for the DDES and RANS simulations.

entropy deviation with respect to the inlet value, showing that most of the entropy generation is associated with the turbulent wake. The study of Ref. [88] showed that, for a fixed pressure ratio π, the losses increase as the isentropic exponent γ_{pv} decreases and that, for a fixed γ_{pv}, losses increase when π is decreased. The present results for ζ_{out}, reported in Table 6.3, exhibit a similar trend, with both RANS and DDES predicting an increase of the loss coefficient as γ_{pv} and π decrease. However, RANS simulations systematically underestimate the loss coefficient by $\sim 20\%$ compared to DDES, mainly due to the overestimated back pressure in RANS.

The reasons for the observed discrepancies between DDES and RANS are further investigated by performing a loss breakdown analysis. The losses are decomposed into two contributions: a contribution corresponding to the losses in the passage vane, ζ_{pass}, and a contribution from the flow downstream of the the TE, ζ_{TE}. A control line L_{pass} aligned with the blades TEs is defined by connecting the separation points to the meridional lines (see figure 6.8). The global passage losses are then evaluated by introducing the loss coefficient:

$$\zeta_{pass} = \frac{h_{pass} - h_{pass,is}}{h_{0,1} - h_{pass,is}} \tag{6.2}$$

where h_{pass} and $h_{pass,is}$ are the mass-averaged enthalpy and isentropic enthalpy along the control line L_{pass}, respectively. Then the trailing edge losses are evaluated as the difference between ζ_{out} and ζ_{pass}. The values calculated for various cases are reported in table 6.3. Based on the previous breakdown, passage losses account for only $\sim 25-30\%$ of the total losses in the various DDES simulations, and most of the losses are generated downstream of the TE. The percentage contributions of ζ_{pass} and ζ_{TE} to the total losses are about the same for the three flows and are little affected by the non-ideal conditions. As expected, the differences between DDES and RANS simulations are mainly due to the miscalculation of the TE losses in RANS, with an error of $\sim 30\%$.

To further study how the base pressure affects the losses, the decomposition of the loss coefficient proposed by Denton [10] is considered. This coefficient is decomposed into several terms corresponding to the main physical mechanisms responsible for the losses:

$$\zeta_{Den} = \underbrace{-\frac{C_{pb} d_{TE}}{l_{th}}}_{\zeta_{C_{p,b}}} + \underbrace{\frac{2\theta}{l_{th}}}_{\zeta_{\theta}} + \underbrace{\left(\frac{\delta^* + d_{TE}}{l_{th}}\right)^2}_{\zeta_{\delta^*}} \tag{6.3}$$

where θ and δ^* are the momentum and displacement thicknesses at TE upstream of the separation points, respectively, $C_{pb} = (p_b - p_2)/(\frac{1}{2}\rho_{2,is}U_{2,is})$ is the base pressure coefficient, d_{TE} is the TE thickness and l_{th} is the throat width. The terms $\zeta_{C_{p,b}}$, ζ_{θ} and ζ_{δ^*} correspond to the profile loss, the momentum loss and the blockage losses, respectively. Values of the total loss ζ_{Den}, reported in table 6.3, do not differ much from ζ_{out}. However, different trends of the loss coefficients are predicted by the DDES and the RANS simulations. The contributions of the different terms in eq. (6.3) are reported in figure 6.8 for the case Novec-1. DDES and RANS show similar momentum and blockage losses, but the losses associated with base pressure differ between the two simulations. As a result, the blockage losses, which were the main source of losses in RANS, become the second source of losses after the base pressure losses in DDES. This decomposition also highlights that the trailing edge losses ζ_{TE} are mostly related to the base pressure. Similar considerations apply to the other cases.

Chapter Summary

The transonic flow of the organic vapor Novec649 through an idealized turbine vane configuration is studied using the DDES-SLA methodology [183], designed to accelerate the transition to resolved turbulence in separated shear layers while applying RANS modeling in turbulent attached boundary layers. This simulation strategy allows to accurately resolve the most relevant turbulent wake dynamics. DDES-SLA simulations are performed in Novec and air, to see the influence of the non-ideality on the expansion, and compared to RANS simulations.

Influence of the non-ideality of the flow:

- Novec flows display a lower isentropic exponent γ_{pv} than air and expand in the dense-gas region, leading to an opposite behavior of the speed of sound compared to perfect gas.
- With these relative dilute conditions, no significant non-ideal phenomena are observed, and the overall flow topology is similar to that obtained in air.
- These conditions essentially impact the maximal achievable pressure ratio.

Unsteady wake dynamics:

- The Strouhal number is mainly dependent on M, but also on Reynolds number.
- Due to the large heat capacity of Novec, the phenomenon of energy separation is suppressed.
- On the other hand, pressure fluctuations and in particular acoustic waves are enhanced.

Analysis of blade losses:

- The losses increase as γ_{pv} and the pressure ration is reduced.
- Majority of losses occur in the wake region, mainly driven by the base pressure as highlighted by Denton's loss decomposition.
- RANS simulations significantly underestimate the base pressure, leading to an error of 30% in TE loss estimation.
- Unsteady RANS simulations provide limited improvement due to an inability to capture correct wake unsteadiness.

Chapter 7

Conclusion and perspectives

General conclusion

This thesis aims to provide more insights on the physical mechanisms involved in loss process in dense gas flows under conditions representative of ORC turbines, with a particular focus on transition and wake losses. This is essential in order to improve the performance of ORC systems, which will play an increasingly important role in energy generation in the future. This goal is pursued through high-fidelity simulations, which are a key tool in refining our understanding of the physical phenomena involved in ORC turbines, ultimately aiming for higher efficiency. As it is an important source of losses, a large part of the present work is focused on dense-gas boundary layers and on freestream turbulence (FST) induced transition, which represent the dominant transition mechanism in turbines and has not been yet studied in a dense gas. The thesis then takes a more general look at profile losses, which are not linked solely to boundary layers but also to wake development at the trailing edge and eventually shocks in transonic expansions. In particular, the fluid considered is the Novec649, identified as a good candidate working fluid in ORC systems. In the relatively dilute conditions considered, representative of CLOWT facility used by the German partner in the research project, the Peng-Robinson-Stryjek-Vera cubic equation of state and the Chung-Lee-Starling model selected provides thermodynamic quantities in good agreement with reference laws. The numerical strategy to solve the compressible Navier-Stokes equations relies on high-order finite differences algorithms minimizing dissipation and dispersion errors. The Runge-Kutta algorithm selected for temporal integration is combined with a fourth-order implicit residual smoothing (IRS4) strategy to reduce the CFL constraint in wall-bounded flows. The IRS4, which permits a reduction of the computational cost by a factor 4, is implemented in a curvilinear multi-block and parallel paradigm and is improved to enhance its robustness. This numerical strategy is assessed against several canonical cases and

against our reference DNS of a Novec turbulent boundary layer. Due to less frequent filtering, the LES strategy with implicit time integration even outperforms the LES with explicit time integration.

Under the mild operating conditions considered in this thesis, Novec flows are characterized by values of the fundamental derivative of fluid dynamics lower than one and occur in the dense gas region. Dense gas boundary layers are found to be only slightly more stable than air, both in natural and bypass transitions, and transition mechanisms remain unaffected. More significant dense gas effects are observed on the idealized blade vane configuration, with the diminution of the speed of sound during Novec's expansion, which leads to a lower pressure ratio achieved compared to air. As the expansions move towards more non-ideal conditions, the losses of the turbine increase. The specific heat, which are in general high in complex organic vapor, has greater effects on the flows. The high thermal capacity of Novec leads to the suppression of several compressible effects observed on light perfect gas flows at the high-subsonic and transonic speeds considered. In fully turbulent boundary layers, due to the significant reduction of the overheating at the wall, the skin friction distribution is found to collapse on incompressible references and, even if genuine compressibility effects are nevertheless observed on thermo-physical quantities, dynamical properties are similar to low-speed air flows. The high specific heat of Novec also suppresses thermal streaks in Novec's boundary layers and in particular, the energy separation phenomena is absent in the wake of an idealized blade using Novec vapor. In addition, in the investigation of FST-induced transition around the leading edge, spanwise-oriented vortices are observed near the wall in turbulent spots and in the turbulent boundary layer, mirroring the observations made for supersonic airflows over cold wall. Another interesting feature of Novec flows is that, while the thermal mode is suppressed, the acoustic mode is reinforced compared to air. This is for instance observed above turbulent boundary layers, but also downstream of the trailing edge in the wake region where pressure fluctuations are strengthened.

Another important characteristic of flows in ORC is that they generally occur at very high Reynolds numbers, due to the high density of organic vapors. In bypass transitions typical of ORC turbines, large-scale disturbances therefore interact with very thin boundary layer. The FST-induced transition study performed in the present thesis reveals that, in such conditions, the classical scenario (linear non-modal growth of streaks undergoing secondary instabilities) can be "bypassed" by a nonlinear receptivity mechanism (non-linear non-modal growth of Λ-shaped structures, further stretched to hairpin vortices before breaking down to turbulence). The present study highlights the influence of the integral length scale of the FST in the competition between the two different transition mechanisms. The alternative scenario falls in the category of nonlinear receptivity to intense localized disturbances which can be relevant for other alternative bypass scenarios encountered in

turbomachinery, for instance when involving receptivity process around thick leading-edge [19] or in wake-induced transition [20, 21, 22]. In addition to leading-edge and freestream disturbances characteristics, the stabilizing pressure gradients encountered in turbines can also influence the path to transition. The FST-induced transition investigation around the leading-edge of the idealized blade unveils that, in this case, the high favorable pressure gradient prevents Λ-shaped structures to participate in the transition and that the transition occurs via streak instabilities and streak interactions. The scale separation induced by the high Reynolds number conditions leads to FST structures wrapping around the large leading-edge and organized in a large-scale spanwise arrangement of clusters of small-scale streamwise vortices. This spanwise arrangement deeply modulates the laminar streaks formation and the spanwise spreading of turbulent spots downstream.

These high Reynolds number conditions have long been an obstacle to the application of high-fidelity methods in ORC design and tools commonly used are mostly based on steady Reynolds-averaged Navier-Stokes (RANS) models. The investigation of the idealized blade vane reveals that the losses prediction can be greatly underestimated in RANS simulations compared to a higher fidelity method such as the DDES-SLA approach retained for this configuration. Even if the global features of the flow (shock topology, thermodynamic outflow quantities, ...) are well captured in RANS simulations, the base pressure coefficient is however severely underestimated compared to DDES. As the wake losses are found to be dominant in this transonic configuration, this leads to an error of 20% in the estimation of the enthalpy loss coefficient. To continue with the study, it is planned to carry out additional simulations under the conditions of the on-going experimental investigation [115], which should provide insightful comparisons.

Perspectives

The results obtained in the present thesis reinforce the importance of scale resolving simulations to improve loss prediction in ORC turbines, particularly in the context of shape optimization [320] which mainly relies on RANS simulations for the moment. For such optimizations procedure, an attractive approach to limit the number of high-fidelity simulations may be to perform a multi-fidelity optimization [321], for instance between RANS and LES as in Zhang *et al.* [322]. Even with such multi-fidelity approach, performing high-fidelity simulations will remain necessary and, as already outlined, generalizing high-fidelity simulations for ORC flows represent a significant challenge due to the high Reynolds number conditions. In the context of this work, the use of the IRS4 in the simulations has considerably reduced the computational cost. It would be interesting to continue improving the implicit residual smoothing strategy, for instance by looking at its combination with other

Runge-Kutta schemes. Furthermore, as the IRS operator can be interpreted as an implicit sine filter, it could be beneficial to test other implicit filter formulations, for instance implicit tangent filters (Raymond & Garder [323]). A key avenue for improvements is also the development of a GPU solver, which has recently expanded the scope of numerical simulation capabilities and enabled to perform simulations previously very challenging to attain (see for instance Nardini *et al.* [324]). Despite the improvements outlined above, the realization of LES at very high Reynolds numbers will remain very costly from a computational point of view, mainly due to the presence of boundary layers that need to be modeled to limit the computational burden. The choice was made here in the idealized blade vane configuration to model the boundary layers with RANS equations, justified by the early transition, but, in a more complex configurations, the transition could be significantly delayed by a favorable pressure gradient so it would be interesting to integrate a transition model into the RANS-LES approaches available in the solver. Moreover, a sensitivity remains in DDES-type methods about the gray area between the RANS and LES modes. To analyze the gray area influence in the present case and following the example of the leading edge FST-induced transition study conducted, an LES study specifically on the trailing edge region of the idealized blade vane configuration could be of interest. A parametric numerical study (DNS/LES) of unsteady wake formation in a more canonical configuration such as a flat plate, much studied in subsonic conditions (see for instance [325, 326, 327, 328, 11, 329]) but relatively less so in supersonic conditions [330, 313], is also an interesting line of research, specially if extended to higher Reynolds number and organic vapors. Besides, the DDES-SLA approach selected could also have an influence on the flow upstream of the trailing edge. In particular, the shock-boundary layer interaction (SBLI) occurring at the suction side, which is an intensive field of research (see for instance the review of Gaitonde [331]), is only captured through RANS modeling. The study of SBLI in dense-gas flows in more canonical configurations would represent itself a very interesting area of research. Furthermore, other wall-model LES approaches could also be considered, such as wall-stress modeling, already applied successfully on complex flows (Larsson *et al.* [332], Bose & Park [333]), for instance on the SBLI phenomenon (De Vanna *et al.* [334]). With such approaches, the prediction of boundary layers development would be improved and would also integrate a part of the velocity fluctuations in the turbulent boundary layer, which could enhance the wake development prediction. Taking into account the transition in this type of model is also a major challenge, while the phenomenon of bypass transition is itself still being actively studied.

Even in the simplified leading-edge configuration considered in this thesis, the mechanisms involved in the FST-induced transition are significantly complicated compared to zero-pressure-gradient flat plates. The

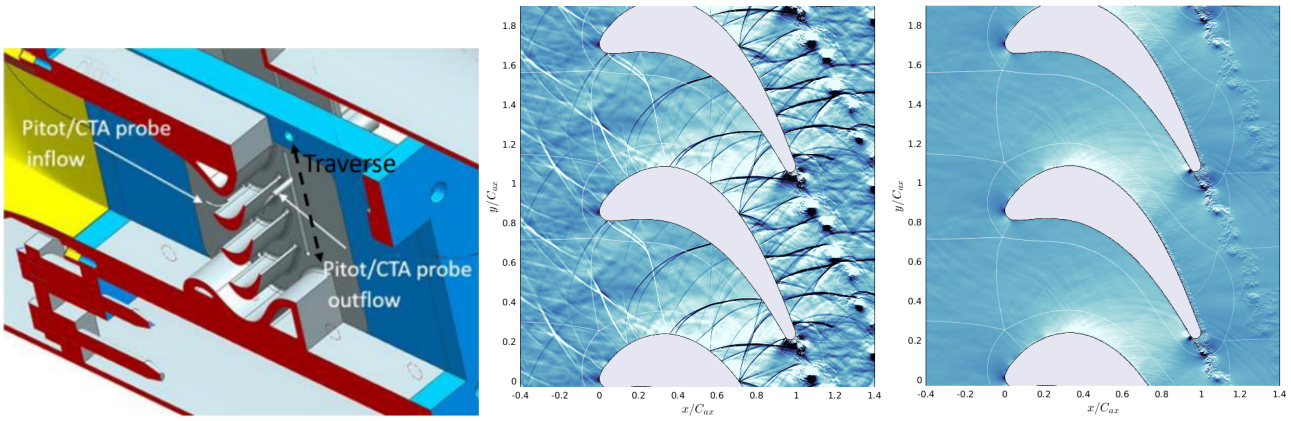

Figure 7.1: Left: Experimental set-up [338] and Schlieren-like vizualisation of the Novec649 flow on the smooth (middle) and rough (right) blades [337].

sensitivity of transition on leading-edge characteristics can be quite high [19, 335] and should be further investigated in conditions representative of ORC turbomachinery applications. Another interesting possibility would be to consider other types of freestream disturbances, such as wakes which have already been shown to influence the transition path [22]. Finally, an additional degree of complexity can be introduced when roughness effects are taken into account (see the review of Bons [336]). As the admissible sand grain roughness is function of the Reynolds number [336], the influence of roughness on flow is reinforced in ORC turbines. Roughness not only cause earlier boundary layer transition but also impact the blade losses, generally by decreasing the turbine performance. Interestingly, an ongoing numerical investigation performed by Gloerfelt *et al.* [337], aiming to reproduce experiments performed in CLOWT facility on LS59 blade with Novec649 (Hake *et al.* [338]), unveils that roughness can affect the vortex shedding regime, switching from a transonic regime for the smooth surface to a detached regime for the rough surface (see Fig. 7.1), and thus lead to an unexpected diminution of the profile losses. In this thesis, the choice was made to study an isolated blade with periodic boundary conditions, so as to concentrate on the profile losses. Besides, in more realistic configurations, the losses also originate from secondary flows, i.e. end-walls or tip leakage [**?**], and further investigations of ORC turbines encompassing all these source of losses, such as in Giauque *et al.* [107], are needed. Future studies should also concentrate on the interaction between blades of adjacent rows. Introducing passing wakes at the inlet to the domain is a first way of taking this interaction into account [339, 340, 22]. The investigation can be further complicate by simulating a single rotor-stator stage [341], the complete multistage [342] or even integrating additional upstream elements [343].

It is worth noting that an important proportion of the numerical challenges encountered in ORC turbine are

not specific to ORCs, but are also encountered in other systems using non-ideal compressible fluids, such as supercritical CO2 applications also seen as one of the promising avenues for power generation. In the future, axial compressors operating with organic vapors will become more common, for example in large-scale heat pump applications which are a close-cousin of ORC systems, and would also benefit from more investigations. Finally, the high Reynolds number conditions encountered and studied in ORC turbines can be of direct interest to airflow applications such as wind turbines. Advances made in one field of application will therefore benefit the others.

Acknowledgements This research has been funded by the Agence Nationale de la Recherche through the ANR-20-CE92-0019 project Regal-ORC. This work was granted access to the HPC resources of IDRIS, TGCC and CINES under the project 1736 made by GENCI (Grand Equipement National de Calcul Intensif).

List of publications

Journal papers

- A. Bienner, X. Gloerfelt, Ö. Yalçın and P. Cinnella, "Multiblock parallel high-order implicit residual smoothing time scheme for compressible Navier-Stokes equations", *Computer and Fluids*, vol. 269, p. 106138, 2023 - **Published**
- X. Gloerfelt, A. Bienner, and P. Cinnella, "High-subsonic boundary-layer flows of an organic vapour", *Journal of Fluid Mechanics*, vol. 971, p. A8, 2023 - **Published**
- A. Bienner, X. Gloerfelt, and P. Cinnella, "Influence of large-scale freestream turbulence on bypass transition in air and organic vapor flows", *Journal of Fluid Mechanics* - **Submitted**
- A. Bienner, X. Gloerfelt, and P. Cinnella, "Leading-edge effects on freestream turbulence induced transition of an organic vapor", *Flow, Turbulence and Combustion*, 2023 - **Published**
- A. Bienner, X. Gloerfelt, and P. Cinnella, "Investigation of transonic flows through an idealized ORC turbine vane using Delayed Detached Eddy simulations", *Applied Thermal Engineering* - **Submitted**

Conferences

- **AERO2022**: A. Bienner, X. Gloerfelt and P. Cinnella, "Numerical study of boundary-layer transition in a high-subsonic organic vapor flow", *56th 3AF Conference*, March 28-30, 2022, Toulouse, France
- **ICCFD11**: A. Bienner, X. Gloerfelt and P. Cinnella, "Assessment of a high-order implicit residual smoothing time scheme for multiblock curvilinear meshes", *Eleventh International Conference on Computational Fluid Dynamics*, July 11-15, 2022, Maui, HI, USA
- **TSFP12**: A. Bienner, X. Gloerfelt, P. Cinnella, L. Hake, S. aus der Wiesche and S. Strehle, "Study of bypass transition in dense-gas boundary layers", *12th International Symposium on Turbulence and Shear Flow Phenomena*, July 19-22, 2022, Osaka, Japan (Online)
- **DLES13**: A. Bienner, X. Gloerfelt and P. Cinnella, "Leading-edge effects in freestream turbulence induced transition in a dense gas flow", *Direct and Large-Eddy Simulation 13*, October 26-29, 2022, Udine, Italy

- **NICFD 2022**: L. Hake, S. aus der Wiesche, S. Sundermeier, A. Bienner, X. Gloerfelt and P. Cinnella, "Grid-generated decaying turbulence in an organic vapour flow", *4th International Seminar on Non-Ideal Compressible-Fluid Dynamics for Propulsion and Power*, November 3-4, 2022, London, United Kingdom

- **ORC2023**: A. Bienner, X. Gloerfelt, P. Cinnella, L. Hake and S. aus der Wiesche, "High-fidelity simulation of a transonic dense gas flow over an idealized blade vane configuration", *7th International Seminar on Organic Rankine Cycle Power Systems*, September 4-6 2023, Seville, Spain

- **ETMM14**: A. Bienner, C. Matar, Ö. Yalçın, X. Gloerfelt and P. Cinnella, "Advances in scale-resolving simulations of complex flows using high-order finite differences and implicit time stepping", *14th International ERCOFTAC Symposium on Engineering Turbulence Modelling and Measurements*, September 6-8 2023, Barcelona, Spain

- **GT2024**: X. Gloerfelt, L. Hake, A. Bienner, C. Matar, P. Cinnella and S. aus der Wiesche, "Roughness effects on dense-gas turbine flow: comparison of experiments and simulations", *ASME Turbo Expo 2024 Turbomachinery Technical Conference and Exposition*, June 24-28 2024, London, United-Kingdom

- **GT2024**: L. Hake,, S. aus der Wiesche, S. Sundermeier, M. Passmann, A. Bienner, X. Gloerfelt and P. Cinnella, "Investigation of a transonic dense gas flow over an idealized blade vane configuration", *ASME Turbo Expo 2024 Turbomachinery Technical Conference and Exposition*, June 24-28 2024, London, United-Kingdom

Appendix A

Decaying turbulence

A study of the decay of grid-generated homogeneous isotropic turbulence (HIT) for Novec649 has been conducted as a preliminary step to the investigation of FST induced transition. In the following, we first present a validation of our numerical results against the reference experiments of Comte-Bellot & Corrsin [344]. Then, we present the experimental campaign conducted in CLOWT and comparisons with our simulations. This work was presented at the 4th NICFD Conference [345].

A.1 Validation of temporally decaying HIT

The simulations are carried out in a cubic computational domain of dimensions $[0;2\pi L_{ref}]^3$, with air modeled as a perfect gas. To validate our numerical strategy, the experiment of Comte-Bellot & Corrsin [344] is selected. In such experiment, isotropic turbulence is generated using different grids. We consider the configuration with a square-rod grid of mesh $M = 5.08\,\text{cm}$ ($Re_M = 34000$). The mean flow is convected at $U_0 = 10\,\text{m.s}^{-1}$ before a contraction yielding $U = 12.7\,\text{m.s}^{-1}$ in the test section. For $U_0 t/M > 40$, homogeneous turbulence was obtained. At station $U_0 t/M = 42$, the measured integral viscous length scale, Kolmogorov scale and turbulent intensity are $L_f = 2.4$ cm, $\eta = 0.029$ cm and $u'/\sqrt{3} = 22.2\,\text{cm.s}^{-1}$, respectively. In the present simulations, the domain length $2\pi L_{ref}$ is taken equal to $10.8M$ as in [346]. The simulation is initialized at $U_0 t/M = 42$ using a von Kármán-Saffman turbulence spectrum based on the measured values of L_f and η. To improve the fitting of the initial spectrum, a bottleneck correction is applied [163]:

$$E(k) = 1.453\frac{(u'^2 k^4/k_e^5}{\exp(17/6\log(1+(k/k_e)^2)} \times \exp\left(-1.5c_K(k\eta)^2\right) \times \left[(1+0.522\left(\frac{1}{\pi}\arctan(10\log_{10}(k\eta)+12.58)+\frac{1}{2}\right)\right] \quad \text{(A.1)}$$

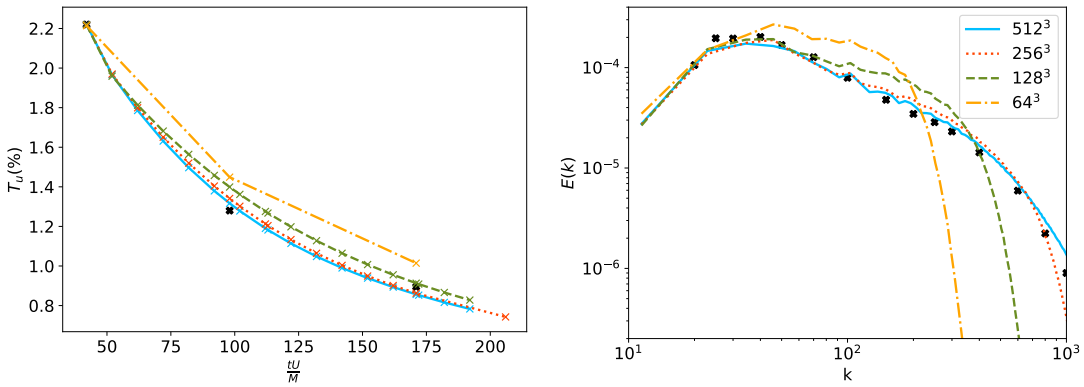

Figure A.1: Comparison of the numerical results using various grids (filtering amplitude $\chi = 0.01$) with Comte-Bellot & Corrsin measurements [344] (**x**). (Left) Evolution of the turbulence intensity T_u. (Right) Turbulent kinetic energy spectra at $x/M = 98$.

with $k_e = 0.747/L_f$ and $c_K = 1.613$. The initial turbulent field is synthesized using the following procedure. First, a stochastic field $\mathbf{u}_{ini} = (u_{ini}\ v_{ini}\ w_{ini})^T$ with Gaussian probability density function is generated in the physical space and transformed into Fourier space to impose the incompressibility condition $\hat{\mathbf{u}}.\mathbf{k} = 0$. The velocity components are given by $\hat{u} = i(k_y w_{ini} - k_z v_{ini})$, $\hat{v} = i(k_z u_{ini} - k_x w_{ini})$ and $\hat{w} = i(k_x v_{ini} - k_y u_{ini})$, normalized and modified to match the von Kármán-Saffman spectrum (A.1). An inverse Fourier transform gives the velocity field in the physical space, which is scaled with the target turbulent intensity u', corresponding to a turbulent Mach number $M_t = 1.12 \times 10^{-3}$. Finally, the pressure field is initialized with the hydrodynamic pressure by solving the Poisson problem.

First, we compare the results obtained for different grid resolutions: 64^3, 128^3, 256^3 and 512^3. The filter amplitude χ is set equal to 0.01. The evolution of the turbulent intensity T_u and the turbulent kinetic energy spectra at $x/M = 98$ are plotted in Fig. A.1. We observe that the 512^3 grid fairly reproduces the experimental T_u evolution and the spectra. The reduction of the number of points moves the cut-off to lower wavenumbers and an accumulation of energy begins to appear. A similar numerical *pile-up* has been observed in [347] and seems to be due to the explicit filtering. The consequences of this pile-up are also visible on the T_u evolution.

To quantify the effect of filtering, another simulation with a filter amplitude $\chi = 0.1$ is carried out. Additionally, two simulations are conducted using an explicit sub-grid-scale (SGS) model and $\chi = 0.01$ and 0.001. For simplicity, we use the Smagorinsky SGS model, with constants $C_s = 0.18$ and $C_i = 0.11$. The spectra are plotted in Fig. A.2 (right). By decreasing the filter coefficient from $\chi = 0.1$ to $\chi = 0.01$ in the implicit LES, we observe that the pile-up is flattened. However, in Fig. A.2 (left), we see that $1/T_u^2$ is lower, i.e. the turbulent

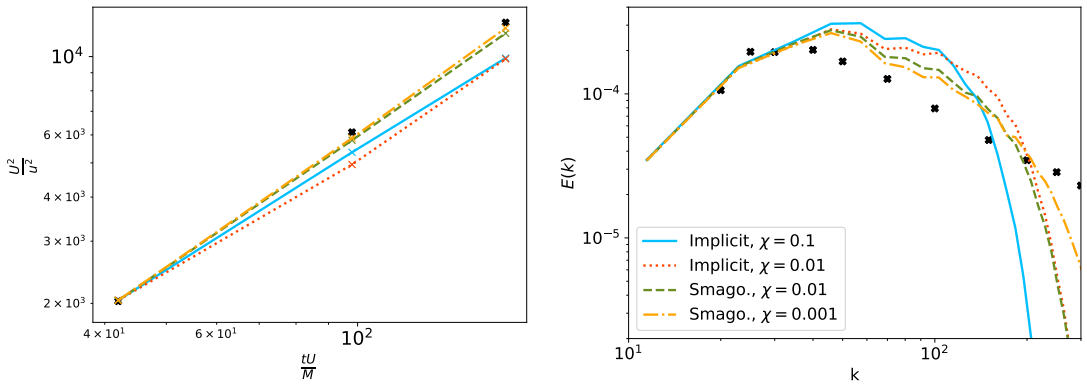

Figure A.2: Comparison of numerical results with and without explicit SGS model on a grid of 64^3 points and two values of the filtering amplitude (**x**: Comte-Bellot & Corrsin experiment). (Left) Evolution of $1/T_u^2$. (Right) Spectra at $x/M = 98$

intensity is increased when reducing the filtering. The pile-up is reduced when using the Smagorinsky model but it is still present. It has been shown experimentally that the turbulence intensity undergoes a power-law decay [348]:

$$\frac{U^2}{u'^2} = A_1 \left(\frac{x - x_0}{M} \right)^{-n} \tag{A.2}$$

We observe a similar decay exponent n between in Smagorinsky model results and measurements. Based on the preceding observations, the 512^3 resolution with Smagorinsky model is retained to simulate the decaying grid turbulence in Novec649.

A.2 Grid turbulence in organic vapor

The measurements of grid-generated turbulence in the small-dimension, high-Reynolds-number CLOWT facility are rather challenging for various reasons. Due to the high density of Novec649, a first constraint is given by the mechanical resistance of the grid. For rod diameters below 1 mm, the grid was structurally unstable or could even be seriously damaged. A second constraint in compressible flow experiments is the choking Mach number of the grid, which decreases for smaller grid sizes. Note that, due to the test section dimensions, mesh sizes greater than 4 mm could not be used without affecting the homogeneity of the flow. Finally, at the high Reynolds numbers encountered in Novec649, hot-wire sensors resolve only a small part of the turbulent scales. The mesh Reynolds number, $Re_M = U_0 M/\nu$, could be lowered by reducing M. However, this also decreases the choking Mach number. Given the above mentioned constraints, a compromise solution has been selected, corresponding to a rod diameter $d = 1$ mm, a mesh size M=4 mm, leading to a theoretical choking

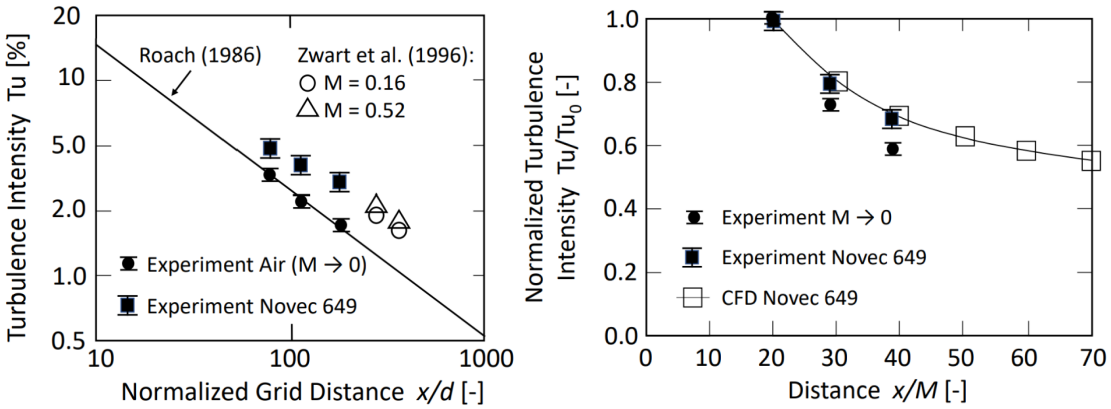

Figure A.3: Decay of the turbulent intensity T_u against grid distance compared with other experiments (left) and decay of the turbulent intensity compared with the numerical simulation (right).

Mach number of approximately 0.25. However running the experiments close to chocking conditions affected turbulence homogeneity. In the end, the experiment was conducted at 100°C and 2 bars with a freestream Mach number of 0.1, which corresponds to $Re_M \approx 72000$. Hot-wire measurements were performed at three stations, namely $x/d = 80$, 109 and 157.

The companion numerical simulations were initialized to achieve the integral length scale $L_f = 2.8$ mm and the turbulent Mach number $M_t = 0.003$ ($T_u = 3$ %) measured at the station $x/d = 80$. At such conditions, a DNS simulation would require approximately 1500^3 points, which is too expensive. Instead, a grid of 500^3 points is used, along with the numerical strategy presented in the preceding section. The decay of the turbulent intensity T_u is plotted in Fig. A.3 (left), along with the correlation $T_u = 0.8(x/d)^{-5/7}$ of Roach [349] and the experimental values from Zwart et al. [350], who conducted a turbulence grid experiment with a compressible flow of an ideal gas. The decay of Tu for CLOWT experiments with air are in excellent agreement with Roach's correlation. A weaker decay is observed for the organic vapor Novec649. Interestingly, the observed decay trend agrees reasonably well with compressible flow measurements of Zwart et al. [350]. The comparison with the simulation is shown in Fig. A.3 (right). The value at a distance $x/d = 80$ was selected as reference for the turbulence intensity to compare results for air and Novec649 in the same diagram. The numerical prediction for Novec649 is in good agreement with experimental data. The predicted decay exponent, $n = 1$, is in fair agreement with the data of Fig. A.3 (left).

Appendix B

Assessment of the synthetic turbulence strategy on spatially decaying HIT

As described in section 2.3.4.3, synthetic turbulence is introduced at the inlet in the present thesis using Random Fourier Modes (RFM). To assess this strategy, several spatial HIT have been performed on uniform grids, using resolution close to the ones of the low L_f simulations in section 4. The spatial HIT are performed to reproduce the freestream turbulence (FST) evolution of the incompressible T3A experiment [58], and are realised with Novec and a freestream Mach number of 0.9. The FST characteristics $Re_{L_f} = 1728$ and $T_{u,in} = 4.0$ %, which give a fair comparison with the experiment, are selected. First, to investigate the influence of the resolution, 3 different grids are tested: $N_x \times N_y \times N_z$=$960 \times 40 \times 40$, $1760 \times 80 \times 80$ and $3200 \times 160 \times 160$ for the coarse, medium and fine grid, respectively. The domain lengths are the same with $L_y = L_z$. In the y-direction, the inlet turbulence is windowed by a van Driest-type damping function (as for flat-plate calculations in section 4), which results in an effective injection zone $N_y \times N_z = 30 \times 40$, 70×80 and 150×160, corresponding to $\sim 9L_f$. The coarse grid is equivalent to a resolution of 32^3 in temporal decay simulations, the medium grid to 64^3 and the fine to approximately 128^3 (see Appendix A). Each simulation is realised with $N = 100$, which is shown hereafter to be a good compromise in terms of the overcost implied by RFM calculations. The initial target spectra and the turbulence intensity evolution are plotted in Fig. B.1. The coarse grid underestimates the T_u evolution due to the too low wavenumber cut-off. The results for the medium and fine grids are similar, which is coherent with the grid requirements established for temporal decay, in particular to avoid a significant pile-up in the spectra. Note that the advection distance in FST-induced transition simulations will be shorter, reducing further the pile-up effect. The medium grid is shown to capture the most energetic scales in fair agreement with T3A measurements and is selected as the FST resolution target for the FST-induced transition studies in

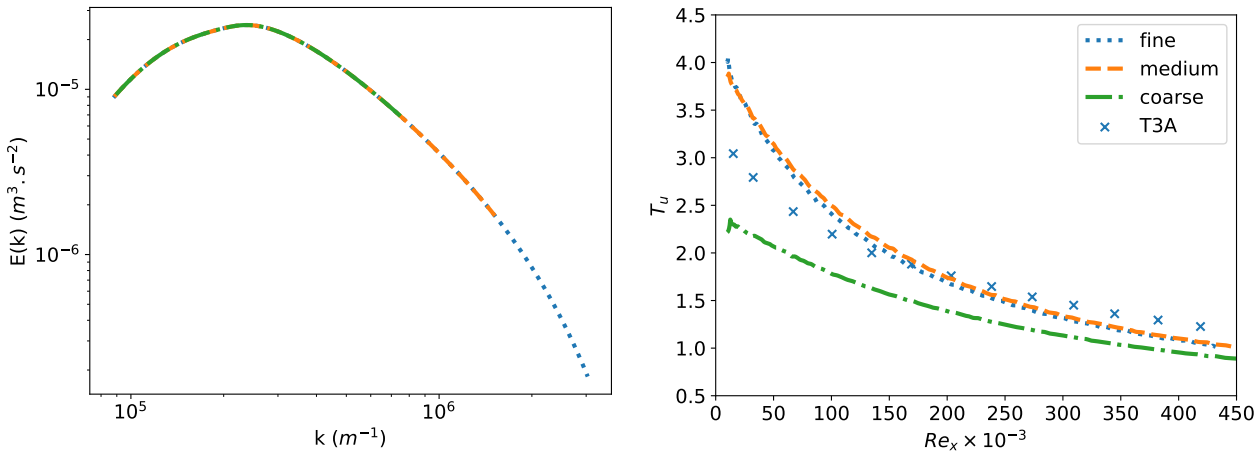

Figure B.1: Comparison of the coarse, medium and fine grids. (Left) Initial von Kármán-Saffman spectra. (Right) Evolution of the turbulence intensity in the streamwise direction, along with T3A experiments [58].

Chapters 4 and 5.

Keeping the medium grid, the influence of the number of injected modes is now tested with $N = 50$, $N = 100$ and $N = 150$. For the T_u evolution, not shown here, all the cases are superposed, therefore meaning that even 50 injected modes are sufficient in this configuration to get the correct T_u evolution. To discriminate the cases, the isotropy for the different simulations is plotted Fig. B.2. For all the cases, an inhomogeneity is observed, specially at the inlet and along the whole streamwise between $T_{u,y}$ and the 2 other components of T_u. However, for $N = 100$ and 150, it is limited to 20 % at the inlet and reduced to 9 % at $Re_x = 50 \times 10^3$ whereas for $N = 50$, it varies from 40 % to 20 %. Moreover, the $T_{u,x}$ and $T_{u,z}$ curves rapidly collapses with $N = 100$ and 150 where it takes a little longer with $N = 50$. As no improvements is observed with $N = 150$ and to limit the overcost due to the calculation of RFM, $N = 100$ is retained in the present work.

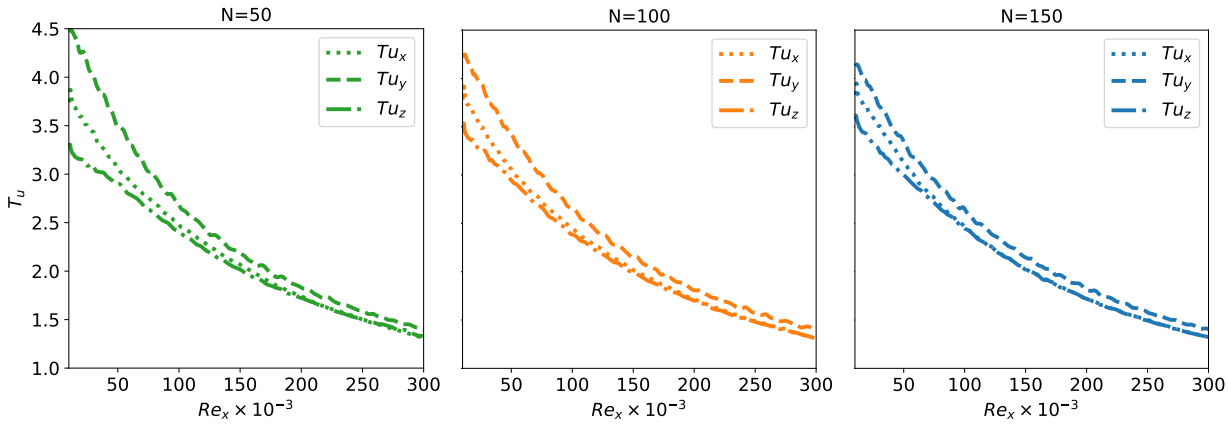

Figure B.2: Comparison of the isotropy of T_u for different number of modes N injected.

Appendix C

Assessment of the synthetic turbulence strategy on FST-induced transitions

C.1 Validation of the synthetic turbulence for the T3A benchmark case

The inlet synthetic turbulence strategy is validated against the T3A benchmark experiment [58]. The flow is simulated in air at M=0.5 and the freestream thermodynamic quantities are p_∞=101 300 Pa and T_∞=298.15 K. As the integral length scale L_f is not characterized in the experiment, the FST characteristics are determined thanks to preliminary simulations of spatially decaying HIT (see Appendix B), in order to match the evolution of the FST intensity in the T3A experiment, as recommended by Pinto & Lodato [46], who also used synthetic turbulence for this benchmark case. The selected values are $Re_{L_{f,in}}$=1728, and $T_{u,in}$=3.9%, coherent with the ones found by Pinto & Lodato [46] (Re_{L_f}=1950, T_u=3.5%). The turbulence intensity evolution, plotted in figure C.1 (left), is in fair agreement with the experimental T_u decay. The Reynolds number at the inlet is $Re_{x,in}$=10^4 and the simulation is initialized with the similarity solution of a laminar boundary layer. The computational domain used is $N_x \times N_y \times N_z = 1920 \times 204 \times 62$ and has a resolution $\Delta x^+ \times \Delta y^+_w \times \Delta z^+ = 13 \times 1.1 \times 13$, which is equivalent to the ones of the low-L_f cases considered in this paper. One major flaw of the method, as discussed in [46], is the value of the injection height h in Eq.(4.1), which is a tunable parameter that may influence the onset of transition. Three different injection heights, corresponding to $h/\delta_{99,in}$ = 1.35, 1.69 and 2.22, have been tested, all chosen to inject synthetic turbulence above $\delta_{99,in}$ (see figure C.1 middle). The C_f distributions, in figure C.1 (right), show that when the injection height is increased, the onset of transition is delayed. However, the slope of the C_f rise and the transition region length are very close. The injection height h=1.69$\delta_{99,in}$ is the one that better reproduces the transition location of the T3A experiment. The streamwise fluctuating velocity profiles along the transition region are reported in figure C.2. They are in good agreement with the experimental ones

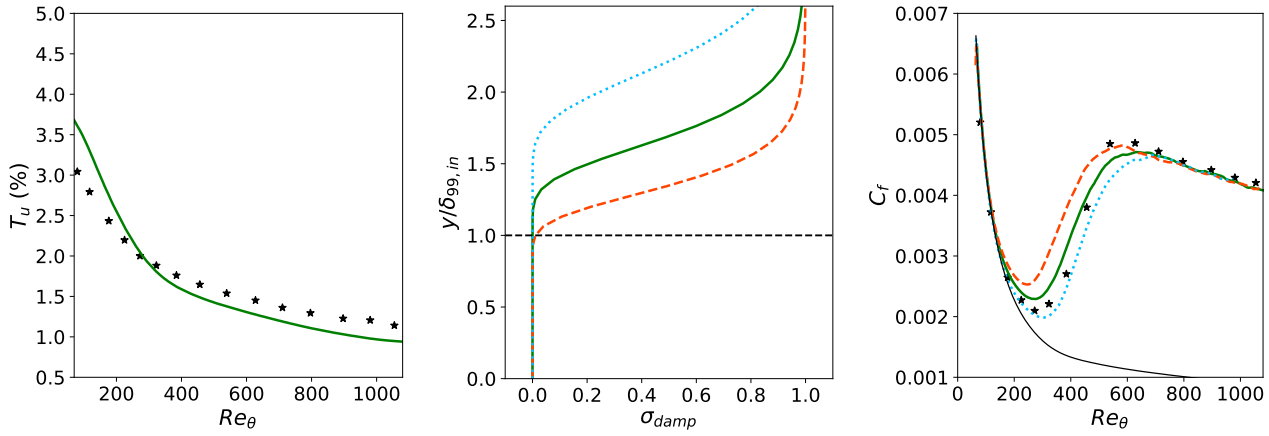

Figure C.1: Turbulence intensity T_u evolution (left), damping function σ_{damp} (middle) and friction coefficient C_f evolution (right) for the three cases: $h/\delta_{99,in} = 1.35$ (– – –), 1.69 (——) and 2.22 (·····). Comparison with T3A experiment (⋆).

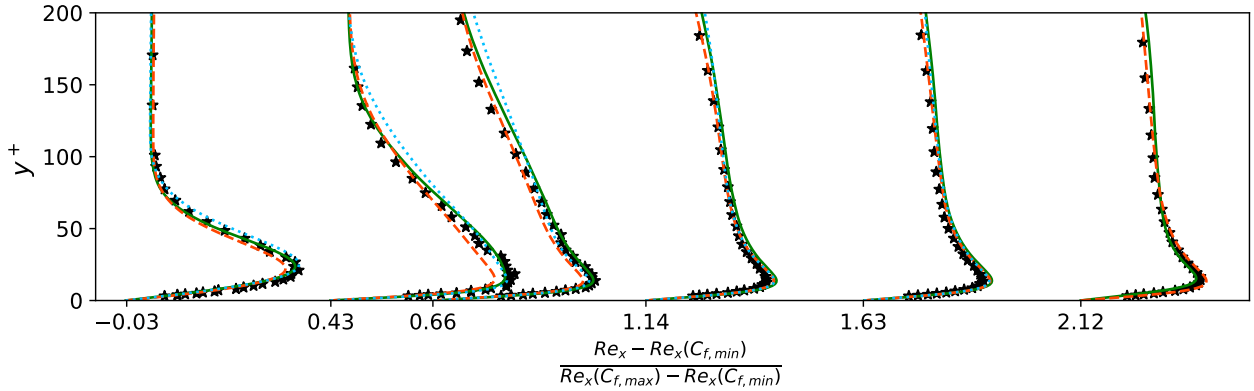

Figure C.2: Streamwise fluctuating velocity: $0.1 \times \frac{u_{rms}}{u_\tau} + \frac{Re_x - Re_x(C_{f,min})}{Re_x(C_{f,max}) - Re_x(C_{f,min})}$. Legend as in figure C.1.

for the intermediate height. When the streamwise coordinate Re_x is scaled by the beginning ($Re_x(C_{f,min})$) and the end ($Re_x(C_{f,max})$) of the transitional region, the streamwise fluctuating velocity profiles for the two other cases are also in good agreement. Therefore, the parameter h can influence the precise location of the transition, but the present strategy can be used to study the transitional region and in particular the effects of the FST characteristics over it (as long as the injection height is kept constant between cases and the synthetic turbulence is injected above the BL).

Case	Flow	N_{modes}	$T_{u,in}$ (%)	$Re_{L_f,t}$ Theo.	Points $N_x \times N_y \times N_z$	Resolution $\Delta x^+ \times \Delta y_w^+ \times \Delta z^+$
LES	Air0.9	100	4.0	17280	704×480×800	21×0.8×9
DNS1	Air0.9	100	4.0	17280	1120×840×1600	10.5×0.8×4.4
DNS2	Air0.9	116	4.0	17280	1120×840×1600	10.5×0.8×4.4

Table C.1: Computational grid and FST properties of the high L_f-high T_u Air M=0.9 case with LES and DNS resolutions.

C.2 Influence of the grid resolution

To assess the LES resolution and its influence on the FST-induced transition, the high L_f-high T_u Air M=0.9 configuration is simulated on a finer computational mesh, obtained by taking the LES domain with the same L_y and L_z dimensions and reducing by two Δx and Δz. The grid step at the wall Δy_w is kept equal but the streching in the y-direction is reduced to keep $\Delta y \leq \Delta x$, resulting in a total of 840 points (see table C.2) and a DNS-like resolution, with $\Delta x^+ \times \Delta y_w^+ \times \Delta z^+ = 10.5 \times 0.8 \times 4.4$ in the TBL. The RFM discretization and number of modes are kept the same as in LES . Looking at the friction coefficient C_f evolution (figure C.3 left), the transition is slightly shifted upstream in the DNS compared to the LES but remains overall very close to the LES. The u_{rms} profiles in the transitional region (figure C.3 right) are almost superimposed, with only slight deviations observed at the last two stations.

Using the same grid, another DNS is run with k_{max} increased to match the DNS resolution limit in the freestream region, resulting in $N = 116$ RFM modes, in order to investigate the influence of the selected upper bound for RFM. Whether for C_f evolution or u_{rms} profiles, the two DNS collapse perfectly, providing a first validation of the choice of the RFM wavenumber bounds. This is also an indication that the excitation at high frequencies does not influence the transition. The RFM discretization strategy is further assessed in appendix C.3.

C.3 Influence of the discretization of RFM wavenumbers

To further assess the influence of the RFM discretization, the low L_f-high T_u Novec case is performed on a computational domain with a spanwise extent reduced by a factor 5, with N_z=80 rather than 400, which corresponds to $L_z \sim 10 L_f$ (see table C.2). The grid resolution is kept identical. Using the same number of RFM modes (N=100), k_{min}, and therefore the discretization of RFM wavenumbers, are modified to match the

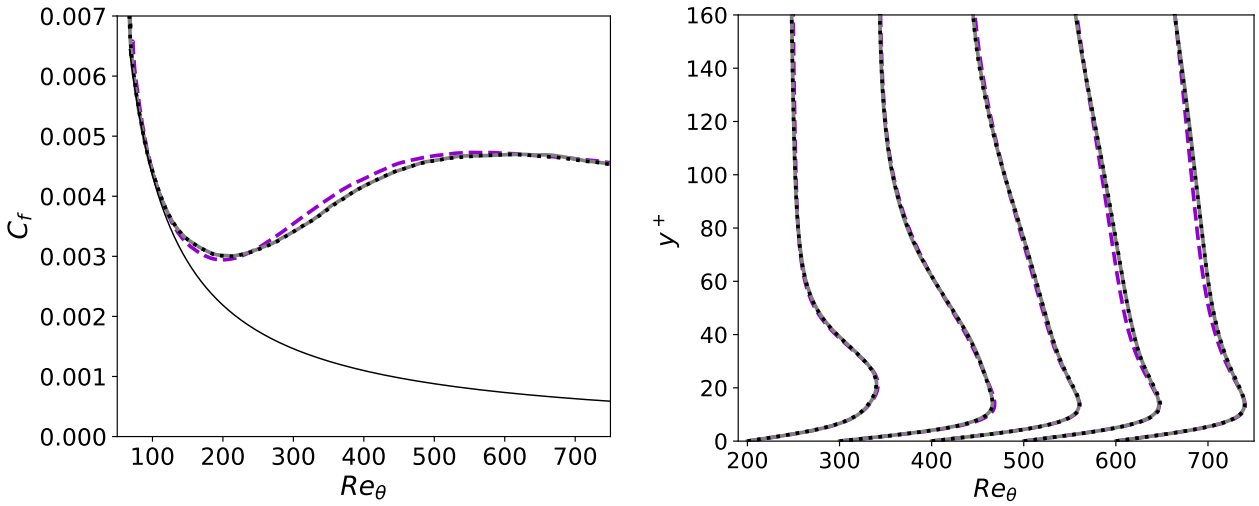

Figure C.3: Friction coefficient evolution (left) and streamwise fluctuating velocity $50 \times \frac{u_{rms}}{u_\tau} + Re_\theta$ (right) for the high L_f-high T_u Air M=0.9 configuration with LES resolution with N=100 modes (- - -) and DNS resolution with N=100 (·····) and N=116 (——) RFM modes.

Case	Flow	N_z	$T_{u,in}$ (%)	$Re_{L_f,t}$ Theo.	$Re_{L_f,c}$ Calc.	Re_{FST} Calc.	Resolution $\Delta x^+ \times \Delta y^+_w \times \Delta z^+$
Large	Novec	400	4.0	1728	1950	78	13×1.0×11
Narrow	Novec	80	4.0	1728	1900	76	13×1.0×11

Table C.2: Computational grid and FST properties of the low L_f-high T_u Novec case with the large and narrow computational domain.

spanwise extent of the narrow domain, leading to the inlet energy spectrum target in figure C.4. The increase of k_{min} between the large and narrow domain results in a better discretization of the spectra in the narrow case. This leads to an estimated $Re_{L_f,c}$ slightly different and closer to the target, with 1900 instead of 1950.

The C_f distributions shown in figure C.4 (right) are in almost perfect agreement, with slight differences at the end of the transition. Streamwise fluctuating velocity profiles in the transition region and in the TBL shortly after the end of transition are shown in figure C.5. The profiles perfectly match, except for a slight discrepancy at Re_θ=300. This comparison demonstrates that, as long as the RFM modes are relatively well discretized around the maximum peak of the spectrum, the discretization of the RFM has negligible effect on the transition.

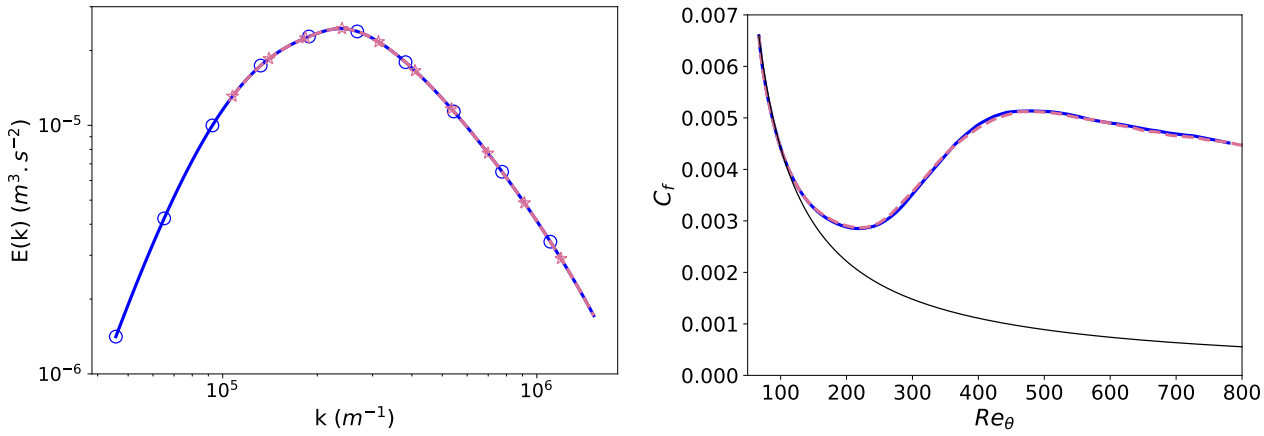

Figure C.4: Inlet energy spectra target (left), with marker every 1 discrete mode out of 10, and friction coefficient evolution (right) for the low L_f-high T_u Novec configuration with large (——) and narrow (- - -) spanwise extent.

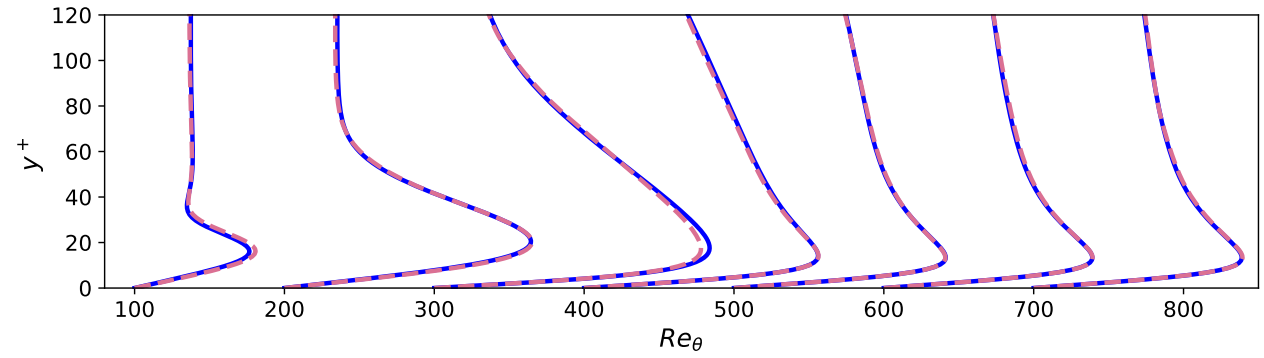

Figure C.5: Streamwise fluctuating velocity: $50 \times \frac{u_{rms}}{u_\tau} + Re_\theta$. Legend as in figure C.4.

Appendix D

Validation of the RANS-LES strategy

To validate our RANS-LES strategy, based on the DDES-SLA approach [183], we investigate the transonic flow through the VKI LS59 turbine cascade [312]. As part of a European project, this rotor blade was tested inside 4 different wind tunnels to determine how the environment influences the experimental results. Here, only the Goettingen (GO) and Braunschweig (BS) experiments are considered, with a chord $C = 60$ mm and 100 mm respectively. To enforce the boundary layer (BL) transition, the GO blades were equipped with a trip wire on the suction side at $X/C = 0.60$. Here, the GO blade without trip wire is simulated using RANS, DDES, DDES-SLA and LES approaches. In particular, we select the conditions corresponding to an inlet flow angle $\beta_1 = 30°$, an outlet isentropic Mach $M_{2,is} = 0.99$, an exit Reynolds number based on the chord $Re_{M_2} \approx 8e5$ and a total temperature $T_0 = 290$ K. The simulations are run without FST. To observe its influence on the LES, where the BL is effectively resolved and not assumed to be turbulent as in RANS simulations, a trip wire is added in the LES+trip case. Stagnation pressure and temperature are imposed at the inlet, based on Riemann invariants, whereas a back-pressure condition is used at the outlet. The LES are realized on a structured curvilinear grid of $\sim$ 150 millions points and a resolution at the wall $\Delta n_w^+ \sim 1$ and $\Delta s_w^+ \sim 50$ in the normal and tangential direction respectively. The spanwise direction is meshed using 240 points, giving $\Delta z^+ \sim 15$ and $L_z/C = 9.8\%$. In the wake, the cell are relatively uniform and roughly 0.2% of C. Concerning RANS and hybrid RANS-LES simulations, a mesh with 2 millions points and $n_z = 50$ is used, leading to $L_z/c_{ax} \approx 25\%$, $\Delta n_w^+ \sim 1.0 - 1.5$ and cell sizes around 0.6% of C in the wake region.

As observed on the isentropic Mach number M_{is} evolution displayed in Fig.D.1, the flow accelerates along the suction side up to $X/C \approx 0.6$ before slowing down (X denotes the rotated coordinate

$$x\cos(\chi) - y\sin(\chi)$$

with $\chi = 33°$ the stagger angle). The flow is also characterized by a rapid acceleration on the rear half of the pressure side. The different cases perfectly matches along the pressure side whereas some differences are observed on the suction side after the sonic condition. The LES+trip case is in very good accordance with GO exp., with a second local peak caused by the trip wire at $X/C = 0.6$ absent from the other cases. Interestingly, the LES without trip wire, whose BL remains laminar along the suction side, bears similitude with the BS exp. and notably at the end of the suction side. The RANS and DDES simulations are relatively close, meaning that the DDES strategy does not significantly affect the BL, and exhibit a local peak lower than in experiments at $X/C \approx 0.55$ and similar to the LES one. On the contrary, the DDES-SLA simulation displays a strong shock at this position.

Schlieren-like visualizations of the simulations, based on the density gradient in the y direction, are compared against the GO exp. in Fig.D.2. As in the GO exp., the LES+trip simulation exhibits on the suction side a first steady normal shock wave before the trip wire. The BL separation and reattachment, caused by the trip wire, generates a second steady oblique shock, hardly noticeable on the experimental Schlieren in Fig.D.2 f). At the end of the suction side, a normal shock wave similar to GO is also obtained. On the contrary, the shock topology of the LES simulation without trip wire is different, with unsteady shock waves generated around $X/C \approx 0.6$ and ≈ 0.99 less intense. As for the M_{is} evolution, the shock distribution in the RANS and DDES simulations is

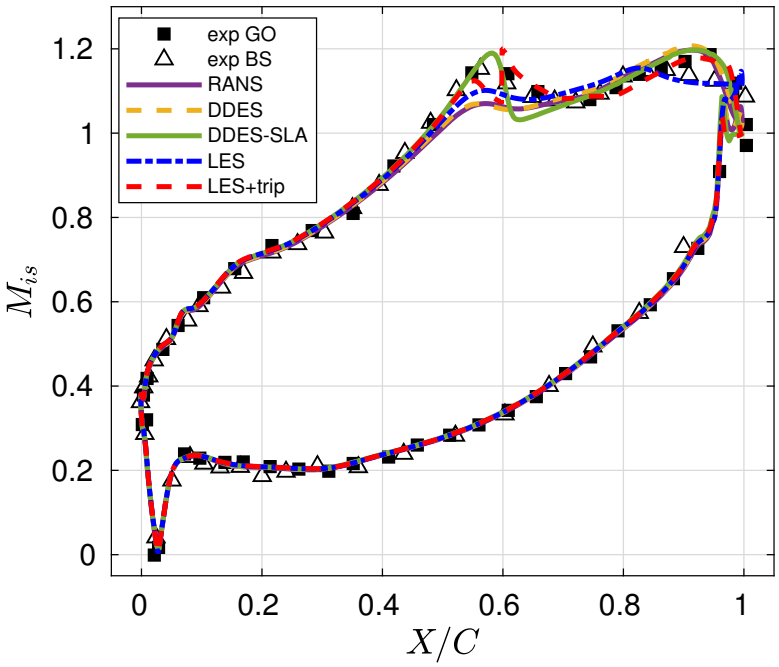

Figure D.1: Surface isentropic Mach number.

Case	M_2	β_2	ζ	St
LES+trip	0.960	66.91°	0.048	0.27
LES	0.942	66.42°	0.074	0.18
URANS	0.947	66.55°	0.061	0.17
DDES	0.946	66.55°	0.066	0.18
DDES-SLA	0.956	66.75°	0.053	0.24
expe GO	0.957	67.02°	0.049	-

Table D.1: Flow quantities at exit: Mach number M_2, angle β_2, loss coefficient ζ and Strouhal number St.

similar and is relatively close to the LES without trip wire. Interestingly, except for the oblique shocks coming from the trip wire, the same shock topology as in GO is recovered for the DDES-SLA. As expected, passing from URANS to DDES and to DDES-SLA, the wake become more and more turbulent and ceases to be 2D.

As reported in Tab.D.1, exit flow quantities similar to the GO exp are recovered for the LES+trip case. The BL state at the TE, laminar in the LES case and turbulent in the LES+trip case, significantly affects the characteristics of the wake, with a Strouhal number of $St = 0.27$ for the LES+trip case and $St = 0.18$ for the LES case. Compared to GO and LES-trip, the URANS and DDES simulations fails to predict a correct wake development and similar wake characteristics to the LES case are obtained. Even if differences remains, the wake state prediction capabilities are improved with the DDES-SLA approach and yields satisfactory results.

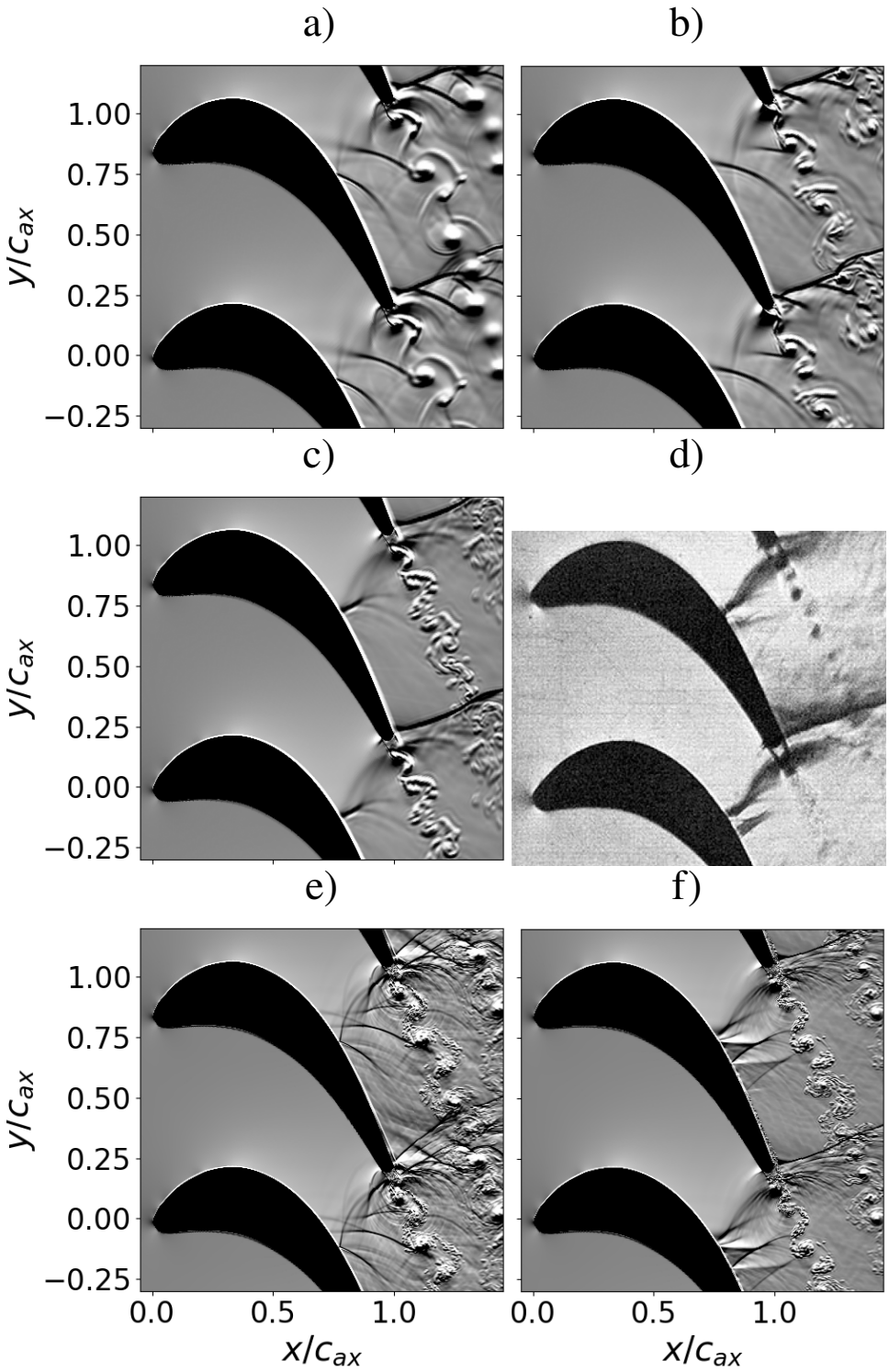

Figure D.2: Schlieren-like visualization of the flow around the VKI-LS59 blade. a) URANS, b) DDES, c) DDES-SLA, d) GO exp. [312], e) LES, f) LES+trip.

Appendix E

Investigation of the laminar-turbulent transition on the original blade geometry

While studying the laminar-turbulent transition for the idealized vane configuration, we first performed in a preliminary study a LES on a subregion of the idealized blade geometry of [114] centered around the LE. This geometry was designed to investigate tip gap effects on losses in the CLOWT facility (using air as the working fluid). The profile consists of simple circular arcs and straight lines. The rear parts of pressure and suction side are composed of straight lines. The suction side is inclined at an angle of 4.5° with respect to the pressure side. The chord length of the profile is set at ch=62 mm and a thick rounded TE shape was chosen (diameter of 2.4 mm). This preliminary investigation was conducted in a Novec649, using the same thermodynamic conditions and numerical set-up than in Chapter 5 (see section 5.1). A computational domain of 350 millions points was used, with a resolution $\Delta n_w^+ \times \Delta s^+ \times \Delta z^+ \sim 0.3 \times 25 \times 10$, where s and n denote the curvilinear abscissa along the blade and the wall-normal distance, respectively (Δn_w^+ being the resolution at the wall). The incoming FST has an intensity $T_u = \sqrt{(u'^2 + v'^2 + w'^2)/3}/U_{in} = 5\%$ and a Reynolds number $Re_{L_f} = 18 \times 10^3$, based on the turbulence integral length-scale L_f. Snapshots in mid-span and wall-normal planes are displayed in Fig. E.1 and E.2. The flow accelerates from $M = 0.5$ up to $M = 1.1$ at the outlet. FST has not yet impacted the leading-edge that the transition has already occurred on the pressure and suction side, meaning that the transition is not induced by the FST. The early turbulent front at $s = 1.5$ mm, which is clearly identified on the wall-normal slice, results from an incipient flow separation occuring at a curvature discontinuity resulting from the connection of two circles forming the idealized blade geometry (see Fig. 5.1). The sensitivity of the flow to geometric curvature irregularities is accentuated by the high Reynolds conditions of the flow. As detailed in section 5.1.1, to avoid incipient flow separation, the idealized blade profile investigated in Chapters 5 and 6 is a

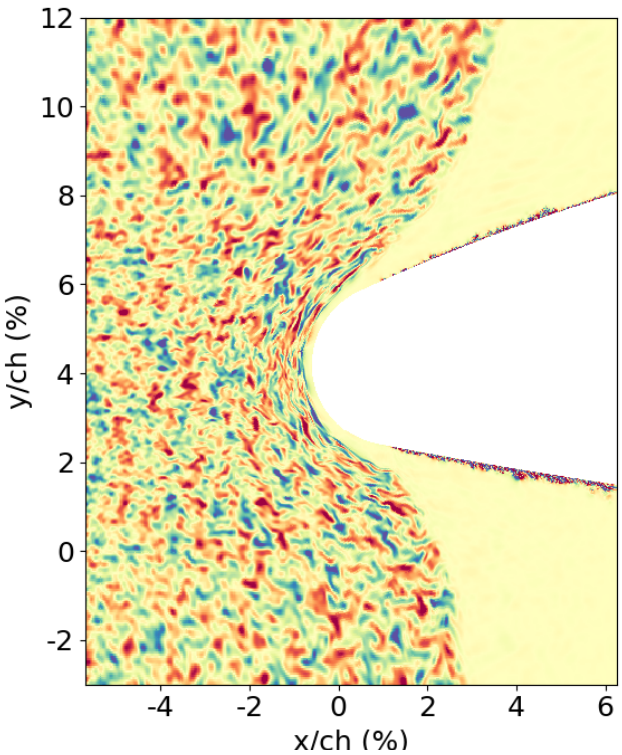

Figure E.1: Snapshot of the spanwise fluctuations w' in a mid-span plane at $n^+ \sim 10$ for the original geometry. Levels: $\pm 0.05 \times c_{in}$

smoothed version of this one.

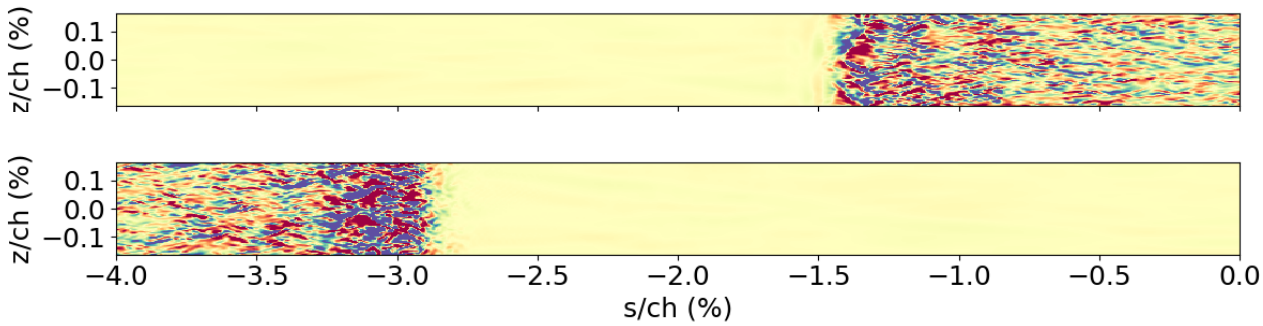

Figure E.2: Snapshot of the spanwise fluctuations w' in a wall-normal plane at $n^+ \sim 10$ for the original geometry.
Levels: $\pm 0.05 \times c_{in}$

Appendix F

RANS validations in the idealized blade vane configuration

F.1 Grid quality

A mesh sensitivity analysis is performed for the Novec-1 case (described in Chapter 6) to asses the quality of the computational grid in RANS simulations. The study uses three different grids composed of 212 k, 306 k and 416 k points, respectively. The grid with 306 k points, called hereafter medium grid, corresponds to the one used in the RANS simulation in this study. Between two successive grids, the mesh is refined in both the boundary layer region and in the wake region. A wall-normal resolution $\Delta n_w^+ \sim 1.0$ at the wall is used in all the grids, and the stretching increases as the grid is coarsened. The isentropic Mach distribution around the blade and pressure along the line of measure are shown in figure F.1. Results for the three grids are nearly superposed, giving good confidence in the quality of the grid. The near-wall grid resolution is also assessed in figure F.2 by inspecting the mean velocity profiles in the boundary layer, at a station $x/ch = 0.5$ on the suction side. Velocity profiles computed in the different grids are superposed, further confirming grid independency of the present RANS simulations. Due to the large heat capacity of Novec649, the velocity profile follows very well the incompressible law of the wall for zero-pressure-gradient, despite the supersonic conditions in the vane.

F.2 Validation of the RANS for air configuration

Finally, the present RANS methodology is assessed against the experimental results of Passman [114] with air (using the original leading-edge geometry). The 2D computational grid of 234 000 points has a resolution $\Delta n_w^+ \sim 1.0-1.2$ and $\Delta s/ch \sim 0.30\%$, with 720 points along the blade. The computational domain extends from

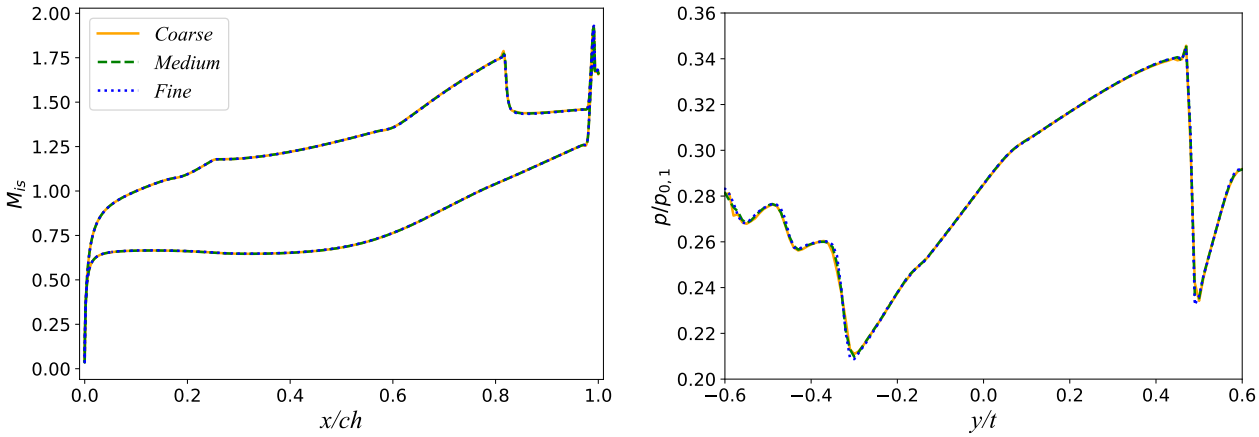

Figure F.1: Isentropic Mach distribution around the blade (top) and pressure along the line of measure (bottom) in the RANS Novec-1 case for the coarse (N_{pts} = 212 k), the medium (306 k) and the fine (416 k) grids.

1.5 chords upstream of the leading edge to 2 chords downstream of the trailing edge. At the inlet, a total pressure of $p_{0,1} = 4$ bars and a total temperature of $T_{0,1} = 308$ K are imposed. A comparison of the shock system in the TE region with an experimental Schlieren picture is proposed in figure F.3. The numerical simulation correctly reproduces the fishtail shock system and the position of the oblique shock waves. Moreover, the pressure distribution along the blade in figure F.3 (right) is also in good agreement with the experimental one. To check the grid convergence, RANS is also run on a finer mesh, with $\Delta s/ch \sim 0.22\%$ and 900 points along the blade. The pressure distribution perfectly matches the medium grid one, showing that mesh independency is achieved on the medium grid.

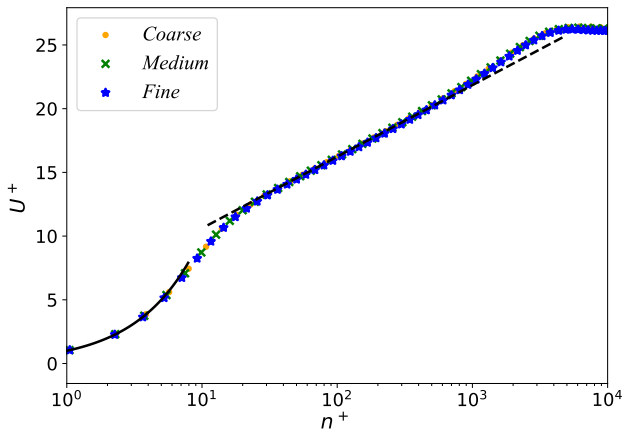

Figure F.2: Mean velocity profile in the RANS Novec-1 case at $x/ch = 0.5$ at the suction side for the coarse (N_{pts} = 212k), the medium (306 k) and the fine (416 k) grids.

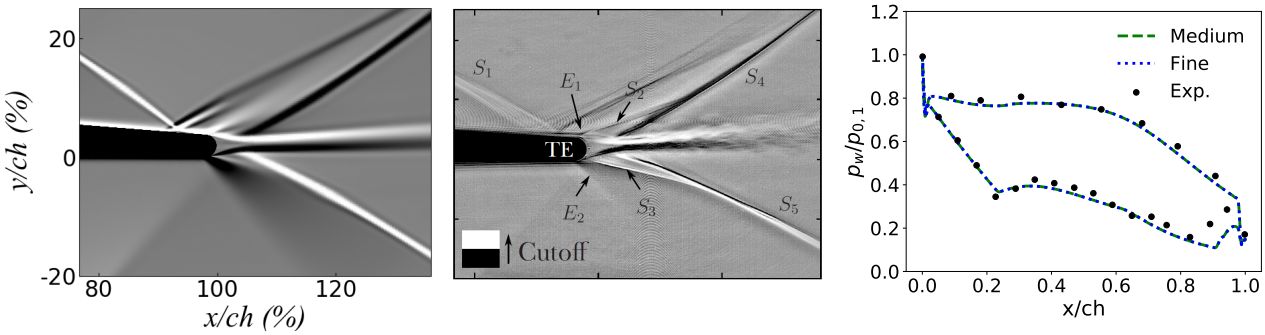

Figure F.3: Schlieren visualizations of the shock system in RANS (left) and Passmann's experiment (middle). Right: pressure distribution around the blade from experiments and RANS simulations.

Bibliography

[1] P. Colonna, E. Casati, C. Trapp, T. Mathijssen, J. Larjola, T. Turunen-Saaresti, and A. Uusitalo, "Organic Rankine cycle power systems: from the concept to current technology, applications, and an outlook to the future," *Trans. ASME J. Eng. Gas Turbines Power*, vol. 137, no. 10, p. 100801, 2015.

[2] H. Chen, D. Y. Goswami, and E. K. Stefanakos, "A review of thermodynamic cycles and working fluids for the conversion of low-grade heat," *Renew. Sustain. Energy Rev.*, vol. 14, no. 9, pp. 3059–3067, 2010.

[3] "Enertime website," https://www.enertime.com/en, accessed: January 22, 2024.

[4] A. Guardone, P. Colonna, M. Pini, and A. Spinelli, "Nonideal compressible fluid dynamics of dense vapors and supercritical fluids," *Ann. Rev. Fluid Mech.*, vol. 56, pp. 241–269, 2024.

[5] J. Harinck, A. Guardone, and P. Colonna, "The influence of molecular complexity on expanding flows of ideal and dense gases," *Phys. Fluids*, vol. 21, p. 086101, 2009.

[6] P. Thompson, "A fundamental derivative in gas dynamics," *Phys. Fluids*, vol. 14, no. 9, pp. 1843–1849, 1971.

[7] H. A. Bethe, "The theory of shock waves for an arbitrary equation of state," Office of Scientific Research and Development, Tech. Rep. 545, 1942.

[8] Y. B. Zel'Dovich and Y. P. Raizer, *Physics of Shock Waves and High-Temperature Hydrodynamic Phenomena*. Academic, New York, 1966.

[9] F. Alshammari, M. Usman, and A. Pesyridis, "Expanders for organic Rankine cycle technology," in *Organic Rankine Cycle Technology for Heat Recovery*. IntechOpen, 2018, ch. 3.

[10] J. Denton, "Loss mechanisms in turbomachines," *Trans. ASME J. Turbomach.*, vol. 115, pp. 621–656, 1993.

[11] C. Sieverding and M. Manna, "A review on turbine trailing edge flow," *MDPI Int. J. Turbomach. Propuls. Power*, vol. 5, no. 2, pp. 1–60, 2020.

[12] D.-Y. Peng and D. Robinson, "A new two-constant equation of state," *Ind. Eng. Chem. Fund.*, vol. 15, no. 1, pp. 59–64, 1976.

[13] R. Stryjek and J. Vera, "PRSV: An improved Peng-Robinson equation of state for pure compounds and mixtures," *Can. J. Chem. Eng.*, vol. 64, no. 2, pp. 323–333, 1986.

[14] G. Aubard, P. Stefanin Volpiani, X. Gloerfelt, and J.-C. Robinet, "Comparison of subgrid-scale viscosity models and selective filtering strategy for large-eddy simulations," *Flow Turbul. Combust.*, vol. 91, no. 3, pp. 497–518, 2013.

[15] X. Gloerfelt and P. Cinnella, "Large eddy simulation requirements for the flow over periodic hills," *Flow Turbul. Combust.*, vol. 103, no. 1, pp. 55–91, 2019.

[16] A. Jameson, W. Schmidt, and E. Turkel, "Numerical solutions of the Euler equations by finite volume methods using Runge-Kutta time-stepping schemes," *AIAA P. 81-1259*, 1981.

[17] P. Cinnella and C. Content, "High-order implicit residual smoothing time scheme for direct and large eddy simulations of compressible flows," *J. Comput. Phys.*, vol. 277, pp. 72–100, 2016.

[18] X. Gloerfelt, A. Bienner, and P. Cinnella, "High-subsonic boundary-layer flows of an organic vapour," *J. Fluid Mech.*, vol. 971, p. A8, 2023.

[19] S. Nagarajan, S. Lele, and J. Ferziger, "Leading-edge effects in bypass transition," *J. Fluid Mech.*, vol. 572, pp. 471–504, 2007.

[20] N. K. Kyriakides, E. G. Kastrinakis, S. G. Nychas, and A. Goulas, "Aspects of flow structure during a cylinder wake-induced laminar/turbulent transition," *AIAA J.*, vol. 37, no. 10, pp. 1197–1205, 1999.

[21] A. C. Mandal and J. Dey, "An experimental study of boundary layer transition induced by a cylinder wake," *J. Fluid Mech.*, vol. 684, pp. 60–84, 2011.

[22] T. Wang, Y. Zhao, J. Leggett, and R. Sandberg, "Direct numerical simulation of a high-pressure turbine stage: Unsteady boundary layer transition and the resulting flow structures," *Trans. ASME J. Turbomach.*, vol. 145, no. 12, p. 121009, 2023.

[23] M. Cramer, S. Whitlock, and G. Tarkenton, "Transonic and boundary layer similarity laws in dense gases," *Trans. ASME J. Fluids Eng.*, vol. 118, no. 3, pp. 481–485, 1996.

[24] A. Kluwick, "Interacting laminar boundary layers of dense gases," *Acta Mech.* [Suppl], vol. 4, pp. 335–349, 1994.

[25] ——, "Internal flows of dense gases," *Acta Mech.*, vol. 169, pp. 123–143, 2004.

[26] ——, "Non-ideal compressible fluid dynamics: a challenge for theory," *J. Phys. Conf. Ser.*, vol. 821, no. 1, p. 012001, 2017.

[27] P. Cinnella and P. Congedo, "Inviscid and viscous aerodynamics of dense gases," *J. Fluid Mech.*, vol. 580, pp. 179–217, 2007.

[28] A. Chakravarthy, "Investigation of dense gas effects on transition to turbulence over a flat plate boundary layer," Master's thesis, Delft University of Technology (supervised by R. Pecnik, J. Ren & O. Marxen), 2018.

[29] X. Gloerfelt, J.-C. Robinet, L. Sciacovelli, P. Cinnella, and F. Grasso, "Dense gas effects on compressible boundary layer stability," *J. Fluid Mech.*, vol. 893, pp. A–19–1–41, 2020.

[30] L. Sciacovelli, P. Cinnella, and X. Gloerfelt, "Direct numerical simulations of supersonic turbulent channel flows of dense gases," *J. Fluid Mech.*, vol. 821, pp. 153–199, 2017.

[31] ——, "A priori tests of RANS models for turbulent channel flows of a dense gas," *Flow Turbul. Combust.*, vol. 101, no. 2, pp. 295–315, 2018.

[32] T. Chen, B. Yang, M. Robertson, and R. Martinez-Botas, "Direct numerical simulation of real-gas effects within turbulent boundary layers for fully-developed channel flows," *J. Glob. Power Propuls. Soc.*, vol. 5, pp. 216–232, 2021.

[33] A. Giauque, A. Vadrot, P. Errante, and C. Corre, "A priori analysis of subgrid-scale terms incompressible transcritical real gas flows," *Phys. Fluids*, vol. 23, p. 085126, 2021.

[34] L. Sciacovelli, X. Gloerfelt, D. Passiatore, P. Cinnella, and F. Grasso, "Numerical investigation of high-speed turbulent boundary layers of dense gases," *Flow Turbul. Combust.*, vol. 105, pp. 555–579, 2020.

[35] B. Yang, T. Chen, and R. Martinez-Botas, "Bypass laminar-turbulent transition on a flat plate of organic fluids using DNS method," in *Proceedings of the 4th International Seminar on Non-Ideal Compressible Fluid Dynamics for Propulsion and Power (NICFD 2022)*. Springer, 2023, vol. 29, pp. 53–61.

[36] F. Pizzi, "Development and assesment of physical based profile loss model for ORC turbine based on boundary layer analysis," Master's thesis, Politecnico di Milano (supervised by P. Gaetani & M. Pini), 2017.

[37] D. Dijkshoorn, "Simulation of two-dimensional steady state boundary layers applied to nonideal gas flows," Master's thesis, Delft University of Technology (supervised by C. De Servi, A. Head & R. Pecnik), 2020.

[38] M. Pini and C. De Servi, "Entropy generation in laminar boundary layers of non-ideal fluid flows," in *Selected Contributions from the 2nd International Seminar on Non-Ideal Compressible Fluid Dynamics for Propulsion and Power, NICFD 2018*, F. di Mare, A. Spinelli, and M. Pini, Eds. Springer, 2020, pp. 104–117.

[39] T. Sayadi and P. Moin, "Investigation of non-ideal effects in compressible boundary layers of dense vapors through direct numerical simulations," *Phys. Fluids*, vol. 36, p. 016145, 2024.

[40] M. Matsubara and P. H. Alfredsson, "Disturbance growth in boundary layers subjected to free-stream turbulence," *J. Fluid Mech.*, vol. 430, pp. 149–168, 2001.

[41] R. Mayle, "The role of laminar-turbulent transition in gas turbine engines," *Trans. ASME J. Turbomach.*, vol. 113, pp. 509–537, 1991.

[42] R. Sandberg and V. Michelassi, "Fluid dynamics of axial turbomachinery: blade and stage-level simulations and models," *Ann. Rev. Fluid Mech.*, vol. 54, pp. 255–285, 2022.

[43] P. Durbin and X. Wu, "Transition beneath vortical disturbances," *Ann. Rev. Fluid Mech.*, vol. 39, pp. 107–128, 2007.

[44] T. A. Zaki, "From streaks to spots and on to turbulence: exploring the dynamics of boundary layer transition," *Flow Turbul. Combust.*, 2013.

[45] L. Brandt, P. Schlatter, and D. Henningson, "Transition in boundary layers subject to free-stream turbulence," *J. Fluid Mech.*, vol. 517, pp. 167–198, 2004.

[46] B. Pinto and G. Lodato, "Synthetic freestream disturbance for the numerical reproduction of experimental zero-pressure-gradient bypass transition test cases," *Flow Turbul. Combust.*, vol. 103, pp. 25–54, 2019.

[47] J. Fransson and S. Shahinfar, "On the effect of free-stream turbulence on boundary-layer transition," *J. Fluid Mech.*, no. 899, p. A23, 2020.

[48] S. Muthu, S. Bhushan, and D. K. Walters, "Identification of a pressure–strain correlation-based bypass transition onset marker," *Trans. ASME J. Fluids Eng.*, vol. 143, 2021.

[49] P. Jonas, O. Mazur, and V. Uruba, "On the receptivity of the by-pass transition to the length scale of the outer stream turbulence," *Eur. J. Mech. B/Fluids*, vol. 19, pp. 707–722, 2000.

[50] V. Ovchinnikov, U. Piomelli, and M. M. Choudhari, "Inflow conditions for numerical simulations of bypass transition," *42nd AIAA Aerospace Sciences Meeting and Exhibit 5 - 8 January, Reno, Nevada, AIAA P., 2004-0591*, pp. 1–14, 2004.

[51] P. S. Klebanoff, "Effect of freestream turbulence on the laminar boundary layer," *Bull. Amer. Phys. Soc.*, vol. 10, no. 11, p. 1323, 1971.

[52] J. M. Kendall, "Experiments on boundary-layer receptivity to freestream turbulence," *AIAA P. 98-0530, American Institute of Aeronautics and Astronautic*, pp. 1–14, 1998.

[53] ——, "Experimental study of disturbances produced in a pre-transitional laminar boundary layer by weak freestream turbulence," *AIAA P. 85-1695, American Institute of Aeronautics and Astronautic*, pp. 1–11, 1985.

[54] K. J. A. Westin, A. Boiko, B. G. B. Klingmann, V. V. Kozlov, and P. H. Alfredsson, "Experiments in a boundary layer subjected to free stream turbulence. part 1. boundary layer structure and receptivity," *J. Fluid Mech.*, pp. 193–218, 1994.

[55] R. Jacobs and P. Durbin, "Simulations of bypass transition," *J. Fluid Mech.*, vol. 428, pp. 185–212, 2001.

[56] J. Fransson and P. H. Alfredsson, "On the disturbance growth in an asymptotic suction boundary layer," *J. Fluid Mech.*, vol. 482, pp. 51–90, 2003.

[57] V. Ovchinnikov, M. Choudhari, and U. Piomelli, "Numerical simulations of boundary-layer bypass transition due to high-amplitude free-stream turbulence," *J. Fluid Mech.*, vol. 613, pp. 135–169, 2008.

[58] P. E. Roach and D. H. Brierley, "The influence of a turbulent free stream on zero pressure gradient transitional boundary layer development. Part 1: testcases T3A and T3B." *Numerical Simulation of Unsteady Flows and Transition to Turbulence*, pp. 319–347, 1992.

[59] Y. Zhao and R. Sandberg, "Bypass transition in boundary layers subject to strong pressure gradient and curvature effects," *J. Fluid Mech.*, vol. 888, pp. 1–33, 2020.

[60] J. M. Faúndez Alarcón, P. Morra, A. Hanifi, and D. S. Henningson, "Disturbance growth on a NACA0008 wing subjected to free stream turbulence," *J. Fluid Mech.*, vol. 944, p. A44, 2022.

[61] J. H. Watmuff, "Detrimental effects of almost immeasurably small freestream nonuniformities generated by wind-tunnel screens," *AIAA J.*, vol. 36, no. 3, pp. 379–386, 1998.

[62] M. E. Goldstein and D. W. Wundrow, "On the environmental realizability of algebraically growing disturbances and their relation to Klebanoff modes," *Theor. Comput. Fluid Dyn.*, vol. 10, pp. 171–186, 1998.

[63] L. Brandt, "The lift-up effect: the linear mechanism behind transition and turbulence in shear flows," *Eur. J. Mech.*, vol. 47, pp. 80–96, 2014.

[64] Z. Xiong and K. S. Lele, "Stagnation-point flow under free-stream turbulence," *J. Fluid Mech.*, vol. 590, pp. 1–33, 2007.

[65] J. Mans, "Streak development and breakdown during bypass transition," Ph.D. dissertation, Eindhoven Univ. Tech., 2007.

[66] P. Andersson, L. Brandt, A. Bottaro, and D. Henningson, "On the breakdown of boundary layer streaks," *J. Fluid Mech.*, vol. 428, pp. 29–60, 2001.

[67] L. Brandt and D. Henningson, "Transition of streamwise streaks in zero-pressure-gradient boundary layers," *J. Fluid Mech.*, vol. 472, pp. 229–261, 2002.

[68] L. Brandt and H. C. Lange, "Streak interactions and breakdown in boundary layer flows," *Phys. Fluids*, vol. 20, pp. 024 107,1–16, 2008.

[69] P. Schlatter, L. Brandt, H. C. de Lange, and D. S. Henningson, "On streak breakdown in bypass transition," *Phys. Fluids*, vol. 20, pp. 101 505,1–15, 2008.

[70] J. Hoepffner, L. Brandt, and D. Henningson, "Transient growth on boundary layer streaks," *J. Fluid Mech.*, vol. 537, pp. 91–100, 2005.

[71] P. A. Durbin, "Perspectives on the phenomenology and modeling of boundary layer transition," *Flow Turbul. Combust.*, vol. 99, pp. 1–23, 2017.

[72] N. J. Vaughan and T. A. Zaki, "Stability of zero-pressure-gradient boundary layer distorted by unsteady klebanoff streaks," *J. Fluid Mech.*, 2011.

[73] M. J. P. Hack and T. A. Zaki, "Streak instabilities in boundary layers beneath free-stream turbulence," *J. Fluid Mech.*, vol. 741, pp. 280–315, 2014.

[74] K. P. Nolan and T. A. Zaki, "Conditional sampling of transitional boundary layers in pressure gradients," *J. Fluid Mech.*, vol. 728, pp. 306–339, 2013.

[75] R. Bose and P. Durbin, "Helical modes in boundary layer transition," *Phys. Rev. Fluids*, vol. 1, p. 073602, 2016.

[76] X. Wu, P. Moin, J. M. Wallace, J. Skarda, L.-D. Adrián, and J.-P. Hickey, "Transitional–turbulent spots and turbulent–turbulent spots in boundary layers," *Proc. Natl. Acad. Sci. U. S. A.*, vol. 114, p. E5292–E5299, 2017.

[77] X. Wu, "New insights into turbulent spots," *Ann. Rev. Fluid Mech.*, vol. 55, no. 1, pp. 45–75, 2023.

[78] J. A. Redford, N. D. Sandham, and G. T. Roberts, "Numerical simulations of turbulent spots in supersonic boundary layers: effects of Mach number and wall temperature," *Progr Aerosp Sci*, vol. 52, p. 67–79, 2012.

[79] B. Cantwell, D. Coles, and P. Dimotakis, "Structure and entrainment in the plane of symmetry of a turbulent spot," *J. Fluid Mech.*, vol. 87, p. 641–672, 1978.

[80] H. W. Emmons, "The laminar–turbulent transition in a boundary layer. Part I." *J. Aero. Sci*, vol. 18, pp. 490–498, 1951.

[81] M. Gad-El-Hak, R. F. Blackwelderf, and J. J. Riley, "On the growth of turbulent regions in laminar boundary layers," *J. Fluid Mech.*, vol. 110, pp. 73–95, 1981.

[82] I. Wygnanski, M. Solokov, and D. Friedman, "On a turbulent 'spot' in a laminar boundary layer," *J. Fluid Mech.*, vol. 78, p. 785–819, 1976.

[83] I. Wygnanski, M. Zilberman, and J. Haritonidis, "On the spreading of a turbulent spot in the absence of a pressure gradient," *J. Fluid Mech.*, vol. 123, pp. 69–90, 1982.

[84] M. C. Fischer, "Spreading of a turbulent disturbance," *AIAA J.*, vol. 10, no. 7, pp. 957–959, 1972.

[85] L. Krishnan and N. D. Sandham, "Effect of Mach number on the structure of turbulent spots," *Intl J. Heat Fluid Flow*, vol. 27, pp. 542–550, 2006.

[86] A. Jocksch and L. Kleiser, "Growth of turbulent spots in high-speed boundary layers on a flat plate," *Intl J. Heat Fluid Flow*, vol. 6, p. 1543–57, 2008.

[87] F. Tosto, A. Giuffré, P. Colonna, and M. Pini, "Flow deviation and critical choking in transonic turbine cascades operating with non-ideal compressible flows," *J. Global Power Propul. Soc.*, vol. 6, pp. 181–199, 2022.

[88] D. Baumgärtner, J. Otter, and A. Wheeler, "The effect of isentropic exponent on transonic turbine performance," *Trans. ASME J. Turbomach.*, vol. 142, no. 8, p. 081007, 2020.

[89] M. Cramer and L. Best, "Steady, isentropic flows of dense gases," *Phys. Fluids A*, vol. 3, no. 4, pp. 219–226, 1991.

[90] A. Romei, D. Vimercati, G. Persico, and A. Guardone, "Non-ideal compressible flows in supersonic turbine cascades," *J. Fluid Mech.*, vol. 882, pp. A12–1–A12–26, 2020.

[91] A. Romei, D. Vimercati, A. Guardone, and G. Persico, "Amplification of operational uncertainty induced by nonideal flows in supersonic turbine cascades," *Trans. ASME J. Eng. Gas Turbines Power*, vol. 142, no. 8, p. 081006, 2020.

[92] J.-C. Hoarau, P. Cinnella, and X. Gloerfelt, "Large eddy simulations of strongly non ideal compressible flows through a transonic cascade," *Energies*, vol. 14, no. 3, pp. 772–1–772–20, 2021, open Access.

[93] D. Vimercati, G. Gori, A. Spinelli, and A. Guardone, "Non-ideal effects on the typical trailing edge shock pattern of ORC turbine blades," *Energy Procedia*, vol. 129, pp. 1109–116, 2017.

[94] C. C. Conti, A. Fusetti, A. Spinelli, and A. Guardone, "Shock loss measurements in non-ideal supersonic flows of organic vapors," *Exp. Fluids*, vol. 63, 2022.

[95] F. Alshammari, A. Pesyridis, A. Karvountzis-Kontakiotis, B. Franchetti, and Y. Pesmazoglou, "Experimental study of a small scale organic Rankine cycle waste heat recovery system for a heavy duty diesel engine with focus on the radial inflow turbine expander performance," *Appl. Energy*, vol. 215, pp. 543–555, 2018.

[96] S. aus der Wiesche, "Experimental investigation techniques for non-ideal compressible fluid dynamic," *Int. J. Turbomach. Propuls. Power.*, vol. 8, no. 2, p. 11, 2023.

[97] F. Durá Galiana, A. Wheeler, and J. Ong, "A study of trailing-edge losses in organic Rankine cycle turbines," *Trans. ASME J. Turbomach.*, vol. 138, p. 121003, 2016.

[98] A. Spinelli, G. Cammi, S. Gallarini, M. Zocca, F. Cozzi, P. Gaetani, V. Dossena, and A. Guardone, "Experimental evidence of non-ideal compressible effects in expanding flow of a high molecular complexity vapor," *Exp. Fluids*, vol. 59, p. 126, 2018.

[99] M. C. Robertson, P. J. Newton, T. Chen, and R. F. Martinez-Botas, "Development and Commissioning of a Blowdown Facility for Dense Gas Vapours," ser. Turbo Expo: Power for Land, Sea, and Air, vol. Volume 3: Coal, Biomass, Hydrogen, and Alternative Fuels; Cycle Innovations; Electric Power; Industrial and Cogeneration; Organic Rankine Cycle Power Systems, 2019, p. V003T28A002.

[100] M. Zocca, A. Guardone, G. Cammi, F. Cozzi, and A. Spinelli, "Experimental observation of oblique shock waves in steady non-ideal flows," *Exp. Fluids*, vol. 60, p. 101, 2019.

[101] G. Gori, M. Zocca, G. Cammi, A. Spinelli, P. M. Congedo, and A. Guardone, "Accuracy assessment of the non-ideal computational fluid dynamics model for siloxane MDM from the open-source SU2 suite," *Eur. J. Mech. B/Fluids*, vol. 79, pp. 109–120, 2020.

[102] F. Reinker, E. Kenig, M. Passmann, and S. aus der Wiesche, "Closed loop organic wind tunnel (CLOWT): Design, components and control system," *Energy Procedia*, vol. 129, pp. 200–207, 2017, 4 International Seminar on ORC Power Systems, ORC2017, 13-15 September 2017, Milano, Italy.

[103] A. Head, "Novel experiments for the investigation of non-ideal compressible fluid dynamics: the ORCHID and first results of optical measurements," Ph.D. dissertation, TU Delft Flight Performance and Propulsion, 2021.

[104] L. Hake, S. Sundermeier, S. aus der Wiesche, C. Matar, P. Cinnella, and X. Gloerfelt, "Investigation of the turbulence level and the vortex shedding in a turbine cascade working with an organic vapor at subsonic Mach numbers," in *7^{th} International Seminar on ORC Power Systems (ORC2023)*, no. 26, Seville, Spain, 4-6 September 2023.

[105] C. Matar, P. Cinnella, and X. Gloerfelt, "Large eddy simulation of a dense organic vapor flow through a supersonic turbine vane," in *ETMM14 - 14th International ERCOFTAC Symposium on Engineering Turbulence Modelling and Measurements*, Barcelona, Spain, September 6-8 2023, pp. 1–6.

[106] P. Cinnella and X. Gloerfelt, "Insights into the turbulent flow of dense gases through high-fidelity simulations," *Comput. Fluids*, vol. 267, p. 106067, 2023.

[107] A. Giauque, D. Schuster, and C. Corre, "High-fidelity numerical investigation of a real gas annular cascade with experimental validation," *Phys. Fluids*, vol. 35, no. 12, p. 126119, 2023.

[108] A. Meroni, M. Geiselhart, W. Ba, and F. Haglind, "Preliminary design of radial-inflow turbines for organic Rankine cycle power systems considering performance and manufacturability aspects," in *5th International Seminar on ORC Power Systems*, vol. 57, Athens, Greece, September 9-11 2019.

[109] M. White and A. Sayma, "Fluid selection for small-scale Rankine cycle plants: Can you draw some lines in the sand?" in *IIR International Rankine 2020 Conference - Heating, Cooling and Power Generation*, vol. 1161, Glasgow, UK, July 26-29 2020.

[110] F. Reinker, K. Hasselmann, S. aus der Wiesche, and E. Kenig, "Thermodynamics and fluid mechanics of a closed blade cascade wind tunnel for organic vapors," *Trans. ASME J. Eng. Gas Turbines Power*, vol. 138, pp. 052 601–1–052 601–8, 2016.

[111] C. Matar, P. Cinnella, X. Gloerfelt, F. Reinker, and S. aus der Wiesche, "Investigation of non-ideal gas flows around a circular cylinder," *Energy*, vol. 268, p. 126563, 2023.

[112] C. Matar, X. Gloerfelt, and P. Cinnella, "Numerical investigation of transonic non-ideal gas flows around a circular cylinder at high Reynolds number," *Flow Turbul. Combust.*, vol. 112, p. 375–395, 2024.

[113] L. Hake, S. Sundermeier, S. aus der Wiesche, A. Bienner, X. Gloerfelt, C. Matar, and P. Cinnella, "CFD-supported data reduction of hot-wire anamometry signals for compressible organic vapor flows," *J. Phys. Conf. Ser.*, vol. 2511, p. 012011, 2023.

[114] M. Passman, "Experimentelle untersuchungen zu transsonischen schaufel-spaltströmungen in axialturbinen," Ph.D. dissertation, Universität der Bundeswehr Hamburg, 2021.

[115] L. Hake, S. aus der Wiesche, S. Sundermeier, M. Passmann, A. Bienner, X. Gloerfelt, and P. Cinnella, "Investigation of a transonic dense gas flow over an idealized blade vane configuration," in *Proc. ASME Turbo Expo.*, vol. GT2024-127215, London, United Kingdom, June 24-28 2024.

[116] A. Bienner, X. Gloerfelt, O. Yalçın, and P. Cinnella, "Multiblock parallel high-order implicit residual smoothing time scheme for compressible Navier-Stokes equations," *Comput. Fluids*, vol. 269, p. 106138, 2023.

[117] P. Thomas and C. Lombard, "Geometric conservation law and its application to flow computations on moving grids," *AIAA J.*, vol. 17, no. 10, pp. 1030–1037, 1979.

[118] X. Deng, M. Mao, G. Tu, H. Liu, and H. Zhang, "Geometric conservation law and applications to high-order finite difference schemes with stationary grids," *J. Comput. Phys.*, vol. 230, no. 4, pp. 1100–1115, 2011.

[119] J. Martin and Y. Hou, "Development of an equation of state for gases," *AIChE Journal*, vol. 1, no. 2, pp. 142–151, 1955.

[120] R. Span and W. Wagner, "Equations of state for technical applications. I. Simultaneously optimized functional forms for nonpolar and polar fluids," *Intl J. Thermophys.*, vol. 24, no. 1, pp. 1–39, 2003.

[121] E. Lemmon, M. Huber, and M. McLinden, *NIST standard reference database 23: Reference fluid thermodynamic and transport properties – REFPROP, Version 9.1.*, National Institute of Standards and Technology, 2013, available at: http://www.nist.gov/srd/nist23.cfm.

[122] T. Chung, L. Lee, and K. Starling, "Applications of kinetic gas theories and multiparameter correlation for prediction of dilute gas viscosity and thermal conductivity," *Ind. Eng. Chem. Fundam.*, vol. 23, no. 4, pp. 8–13, 1984.

[123] T. Chung, M. Ajlan, L. Lee, and K. Starling, "Generalized multiparameter correlation for nonpolar and polar fluid transport properties," *Ind. Eng. Chem. Res.*, vol. 27, no. 4, pp. 671–679, 1988.

[124] C. Wen, X. Meng, M. Huber, and J. Wu, "Measurement and correlation of the viscosity of 1,1,1,2,2,4,5,5,5-nonafluoro-4-(trifluoromethyl)-3-pentanone," *J. Chem. Eng. Data*, vol. 62, pp. 3603–3609, 2017.

[125] C. Tam and J. Webb, "Dispersion-relation-preserving finite difference schemes for computational acoustics," *J. Comput. Phys.*, vol. 107, pp. 262–281, 1993.

[126] C. Bogey and C. Bailly, "A family of low dispersive and low dissipative explicit schemes for noise computation," *J. Comput. Phys.*, vol. 194, pp. 194–214, 2004.

[127] F. Hu, M. Hussaini, and J. L. Manthey, "Low-dissipation and low-dispersion runge–kutta schemes for computational acoustics," *J. Comput. Phys.*, vol. 124, no. 1, pp. 177–191, 1996.

[128] C. Tam and Z. Dong, "Radiation and outflow boundary conditions for direct computation of acoustic and flow disturbances in a nonuniform mean flow," *J. Comput. Acous.*, vol. 4, no. 2, pp. 175–201, 1996.

[129] C. Tam, "Advances in numerical boundary conditions for computational aeroacoustics," *J. Comput. Acous.*, vol. 6, no. 4, pp. 377–402, 1998.

[130] K. Thompson, "Time dependent boundary conditions for hyperbolic systems," *J. Comput. Phys.*, vol. 68, pp. 1–24, 1987.

[131] T. Poinsot and S. Lele, "Boundary conditions for direct simulations of compressible viscous flows," *J. Comput. Phys.*, vol. 101, pp. 104–129, 1992.

[132] N. Okong'o and J. Bellan, "Consistent boundary conditions for multicomponent real gas mixtures based on characteristic waves," *J. Comput. Phys.*, vol. 176, no. 2, pp. 330–344, 2002.

[133] J. R. Carlson, "Inflow/outflow boundary conditions with application to fun3d," NASA, *Tech. Memorandum* 217181, 2011.

[134] P. Congedo, C. Corre, and P. Cinnella, "Numerical investigation of dense-gas effects in turbomachinery," *Comput. Fluids*, vol. 49, pp. 290–301, 2011.

[135] X. Gloerfelt and J.-C. Robinet, "Silent inflow condition for turbulent boundary layers," *Phys. Rev. Fluids*, vol. 2, p. 124603, 2017.

[136] M. McLinden, R. Perkins, E. Lemmon, and T. Fortin, "Thermodynamic properties of 1,1,1,2,2,4,5,5,5-nonafluoro-4-(trifluoromethyl)-3-pentanone: vapor pressure, (p, ρ, t) behavior, and speed of sound measurements, and an equation of state," *J. Chem. Eng. Data*, vol. 60, pp. 3646–3659, 2015.

[137] K. Tanaka, "Measurement of $p\rho t$ properties of 1,1,1,2,2,4,5,5,5-nonafluoro-4-(trifluoromethyl)-3-pentanone in the near-critical and supercritical regions," *J. Chem. Eng. Data*, vol. 61, pp. 3958–3961, 2016.

[138] R. Perkins, M. Huber, and M. Assael, "Measurement and correlation of the thermal conductivity of 1,1,1,2,2,4,5,5,5-nonafluoro-4-(trifluoromethyl)-3-pentanone," *J. Chem. Eng. Data*, vol. 63, no. 8, pp. 2783–2789, 2018.

[139] 3M manufacturer, "Novec 649 Engineered fluid," 2009.

[140] E. Lemmon, M. Huber, and M. McLinden, *NIST standard reference database 23: Reference fluid thermodynamic and transport properties – REFPROP, Version 9.1.*, National Institute of Standards and Technology, 2013.

[141] E. Vogel, C. Küchenmeister, E. Bich, and A. Laesecke, "Reference correlation of the viscosity of propane," *J. Phys. Chem. Ref. Data.*, vol. 27, pp. 947–970, 1998.

[142] P. Neufeld, A. Janzen, and R. Aziz, "Empirical equations to calculate 16 of the transport collision integrals $\omega(l,s)^*$ for the Lennard-Jones (12-6) potential," *J. Chem. Phys.*, vol. 57, pp. 1100–1102, 1972.

[143] G. Olchowy and J. Sengers, "Crossover from singular to regular behavior of the transport properties of fluids in the critical region," *Phys. Rev. Lett.*, vol. 61, no. 1, pp. 15–18, 1988.

[144] C. Kennedy and A. Gruber, "Reduced aliasing formulations of the convective terms within the Navier-Stokes equations," *J. Comput. Phys.*, vol. 227, pp. 1676–1700, 2008.

[145] G. Coppola, F. Capuanoa, S. Pirozzoli, and L. de Luca, "Numerically stable formulations of convective terms for turbulent compressible flows," *J. Comput. Phys.*, vol. 382, pp. 86–104, 2019.

[146] A. Edoh, N. Mundis, A. Karagozian, and V. Sankaran, "Balancing aspects of numerical dissipation, dispersion, and aliasing in time-accurate simulations," *Int. J. Numer. Meth. Fluids*, vol. 92, pp. 1506–1527, 2020.

[147] Y. Kuya and S. Kawai, "Modified wavenumber and aliasing errors of split convective forms for compressible flows," *J. Comput. Phys.*, vol. 464, p. 111336, 2022.

[148] S. Nagarajan, S. Lele, and J. Ferziger, "A robust high-order compact method for large eddy simulation," *J. Comput. Phys.*, vol. 191, pp. 392–419, 2003.

[149] X. Gloerfelt and P. Lafon, "Direct computation of the noise induced by a turbulent flow through a diaphragm in a duct at low Mach number," *Comput. Fluids*, vol. 37, pp. 388–401, 2008.

[150] H. Song, A. Ghate, K. Matsuno, J. West, A. Subramaniam, L. Brown, and S. Lele, "Robust high-resolution simulations of compressible turbulent flows without filtering," *AIAA Aviation Forum,* 27 June-1 July, Chicago, Illinois, AIAA Paper 2022-4122, 2022.

[151] S. Lele, "Compact finite difference schemes with spectral-like resolution," *J. Comput. Phys.*, vol. 103, pp. 16–42, 1992.

[152] D. Gaitonde and M. Visbal, "Padé-type higher-order boundary filters for the Navier-Stokes equations," *AIAA J.*, vol. 38, no. 11, pp. 2103–2112, 2000.

[153] A. Edoh, N. Mundis, C. Merkle, A. Karagozian, and V. Sankaran, "Comparison of artificial-dissipation and solution-filtering stabilization schemes for time-accurate simulations," *J. Comput. Phys.*, vol. 375, pp. 1424–1450, 2018.

[154] J. Kim and D. Lee, "Adaptive nonlinear artifical dissipation model for computational aeroacoustics," *AIAA J.*, vol. 39, no. 5, pp. 810–818, 2001.

[155] H. Yee, N. Sandham, and M. Djomehri, "Low-dissipative high-order schock-capturing methods using characteristic-based filters," *J. Comput. Phys.*, vol. 150, pp. 199–238, 1999.

[156] E. Lamballais, R. Vicente Cruz, and R. Perrin, "Viscous and hyperviscous filtering for direct and large-eddy simulation," *J. Comput. Phys.*, vol. 431, p. 110115, 2021.

[157] F. Ducros, V. Ferrand, F. Nicoud, C. Weber, D. Darracq, C. Gacherieu, and T. Poinsot, "Large-eddy simulation of the shock/turbulence interaction," *J. Comput. Phys.*, vol. 152, pp. 517–549, 1999.

[158] R. C. Swanson and E. Turkel, "On central-difference and upwind schemes," *J. Comput. Phys.*, vol. 101, pp. 292–306, 1992.

[159] W. Béchara, C. Bailly, P. Lafon, and S. Candel, "Stochastic approach to noise modeling for free turbulent flows," *AIAA J.*, vol. 32, no. 3, pp. 455–463, 1994.

[160] C. Bailly, P. Lafon, and S. Candel, "A stochastic approach to compute noise generation and radiation of free turbulent flows," *AIAA P. 95-092*, 1995.

[161] A. Smirnov, S. Shi, and I. Celik, "Random flow generation technique for large eddy simulation and particle-dynamics modeling," *Trans. ASME J. Fluids Eng.*, vol. 123, pp. 359–371, 2001.

[162] P. Batten, U. Goldberg, and S. Chakravarthy, "Reconstructed sub-grid methods for acoustics prediction at all Reynolds numbers," *AIAA P. 2002-2511*, 2002.

[163] H. Kang, S. Chester, and C. Meneveau, "Decaying turbulence in an active-grid-generated flow and comparisons with large-eddy simulation," *J. Fluid Mech.*, vol. 480, pp. 129–160, 2003.

[164] A. Yoshizawa, "Statistical theory for compressible turbulent shear flows, with the application to subgrid modeling," *Phys. Fluids*, vol. 29, pp. 2152–2164, 1986.

[165] G. Erlebacher, M. Hussaini, C. Speziale, and T. Zang, "Toward the large-eddy simulation of compressible turbulent flows," *J. Fluid Mech.*, vol. 238, pp. 155–185, 1992.

[166] P. Moin and J. Kim, "Numerical investigation of turbulent channel flow," *J. Fluid Mech.*, vol. 118, pp. 341–377, 1982.

[167] U. Piomelli, P. Moin, and J. Ferziger, "Model consistency in large eddy simulation of turbulent channel flows," *Phys. Fluids*, vol. 31, no. 7, pp. 1884–1891, 1988.

[168] V. Borue and S. Orszag, "Self-similar decay of three-dimensional homogeneous turbulence with hyper-viscosity," *Phys. Rev. E*, vol. 51, no. 2, pp. R856–R859, 1995.

[169] A. Cook and W. Cabot, "A high-wavenumber viscosity for high-resolution numerical methods," *J. Comput. Phys.*, vol. 195, no. 2, pp. 594–601, 2004.

[170] G.-S. Karamanos and G. Karniadakis, "A spectral-vanishing viscosity method for large-eddy simulations," *J. Comput. Phys.*, vol. 163, pp. 22–50, 2000.

[171] J. Boris, F. Grinstein, E. Oran, and R. Kolbe, "New insights into large eddy simulation," *Fluid Dyn. Res.*, vol. 10, pp. 199–228, 1992.

[172] C. Fureby and F. Grinstein, "Large eddy simulation of high-Reynolds number free and wall-bounded flows," *J. Comput. Phys.*, vol. 181, pp. 68–97, 2002.

[173] S. Stolz and N. Adams, "Large-eddy simulation of high-Reynolds-number supersonic boundary layers using the approximate deconvolution model and rescaling and recycling technique," *Phys. Fluids*, vol. 15, no. 8, pp. 2398–2412, 2003.

[174] D. Rizzetta, M. Visbal, and G. Blaisdell, "A time-implicit high-order compact differencing and filtering scheme for large-eddy simulation," *Int. J. Numer. Meth. Fluids*, vol. 42, pp. 665–693, 2003.

[175] C. Bogey and C. Bailly, "Large eddy simulations of round jets using explicit filtering with/without dynamic Smagorinsky model," *Intl J. Heat Fluid Flow*, vol. 27, pp. 603–610, 2006.

[176] J. Mathew, R. Lechner, H. Foysi, J. Sesterhenn, and R. Friedrich, "An explicit filtering method for large eddy simulation of compressible flows," *Phys. Fluids*, vol. 15, no. 8, pp. 2279–2289, 2003.

[177] P. R. Spalart and S. R. Allmaras, "A One-Equation Turbulence Model for Aerodynamic Flows," *30th AIAA Aerospace Sciences Meeting and Exhibit 6 - 9 January, Reno, Nevada, AIAA P., 92-0439*, pp. 1–22, 1992.

[178] A. Crivellini, V. D'Alessandro, and F. Bassi, "A Spalart–Allmaras turbulence model implementation in a discontinuous galerkin solver for incompressible flows," *J. Comput. Phys.*, vol. 241, pp. 388–415, 2013.

[179] P. Spalart, W. Jou, W. Strelets, and S. Allmaras, "Comments on the feasability of LES for wings and on a hybrid RANS/LES approach," 1st AFSOR Int. Conf. on DNS/LES, Ruston, LA, 1998.

[180] P. R. Spalart, "Detached-eddy simulation," *Ann. Rev. Fluid Mech.*, vol. 41, no. 1, pp. 181–202, 2009.

[181] P. R. Spalart and M. Strelets, "Detached-eddy simulation: steps towards maturity and industrial value," *Ercoftac Bulletin*, p. 120, 2019.

[182] P. R. Spalart, S. Deck, M. L. Shur, K. D. Squires, M. K. Strelets, and A. Travin, "A new version of detached-eddy simulation, resistant to ambiguous grid densities," *Theoret. Comput. Fluid Dynamics*, vol. 20, pp. 181–195, 2006.

[183] M. L. Shur, P. R. Spalart, M. K. Strelets, and A. K. Travin, "An enhanced version of DES with rapid transition from RANS to LES in separated flows," *Flow Turbul. Combust.*, vol. 95, pp. 709–737, 2015.

[184] O. Yalçın, "Delayed Detached-Eddy Simulation based predictions of boundary layer transition and cavity flow noise," Ph.D. dissertation, Middle East Technical University, 2021.

[185] H. Choi and P. Moin, "On the space-time characteristics of wall-pressure fluctuations," *Phys. Fluids A*, vol. 2, no. 8, pp. 1450–1460, 1990.

[186] A. Jameson and T. Baker, "Solution of the Euler equations for complex configurations," *AIAA P. 83-1929*, 1983.

[187] R. Haelterman, J. Vierendeels, and D. Van Heule, "Optimization of the Runge-Kutta iteration with residual smoothing," *J. Comput. Appl. Math.*, vol. 234, pp. 253–271, 2010.

[188] J.-C. Hoarau, P. Cinnella, and X. Gloerfelt, "Large eddy simulation of turbomachinery flows using a high-order implicit residual smoothing scheme," *Comput. Fluids*, vol. 198, pp. 104 395–1–104 395–13, 2020.

[189] A. Lerat, "Une classe de schémas aux différences implicites pour les systèmes hyperboliques de lois de conservation," *C. R. Acad. Sci.*, vol. 288A, p. 1033, 1979.

[190] A. Lerat, J. Sidès, and V. Daru, "An implicit finite-volume method for solving the Euler equations," in *Lecture Notes in Physics*, vol. 170, 1982, pp. 343–349.

[191] A. Lerat, "Implicit methods of second order accuracy for the Euler equations," *AIAA J.*, vol. 23, no. 1, pp. 33–40, 1985.

[192] K. Khalfallah, G. Lacombe, and A. Lerat, "Analysis of implicit treatments for centred Euler solver," *Comput. Fluids*, vol. 22, no. 2/3, pp. 381–406, 1993.

[193] L. Martinelli and A. Jameson, "Validation of a multigrid method for the Reynolds averaged equations," *AIAA P. 88-0414*, 1988.

[194] R. Swanson, E. Turkel, and C.-C. Rossow, "Convergence acceleration of Runge-Kutta schemes for solving the Navier-Stokes equations," *J. Comput. Phys.*, vol. 224, pp. 365–388, 2007.

[195] B. van Leer, C.-H. Tai, and K. Powell, "Design of optimally smoothing multi-stage schemes for the Euler equations," *AIAA P. 89-1933*, 1989.

[196] P. Jorgenson and R. Chima, "An unconditionally stable Runge-Kutta method for unsteady flows," *AIAA P. 89-0205*, 1989, also NASA Technical Memorandum 101347.

[197] E. Turkel, R. Swanson, V. Vatsa, and J. White, "Multigrid for hypersonic viscous two- and three-dimensional flows," *AIAA P. 91-1572*, 1991, also NASA Contractor Report 187603, ICASE Report No.91-57.

[198] J. Blazek, N. Kroll, R. Radespiel, and C.-C. Rossow, "Upwind implicit residual smoothing method for multi-stage schemes," *AIAA P. 91-1533*, 1991.

[199] J. Blazek, *Computational Fluid Dynamics: Principles and Applications*, third edition ed. Oxford: Butterworth-Heinemann, 2015, ch. Chapter 9 - Acceleration Techniques, pp. 283–335.

[200] L. Wigton and R. Swanson, "Variable coefficient implicit residual smoothing," in *Twelfth International Conference on Numerical Methods in Fluid Dynamics*, ser. Lecture Notes in Physics, K. Morton, Ed., vol. 371. Springer, Berlin, Heidelberg, 1990.

[201] M. Ni, G. Xi, and S. Wang, "Construction of high-order accuracy implicit residual smoothing schemes," *Appl. Math. Mech.*, vol. 21, no. 4, pp. 407–414, 2000.

[202] P. Cinnella and A. Lerat, "A fully implicit third-order scheme in time and space for compressible turbulent unsteady flow simulations," in *European Congress on Computational Methods in Applied Sciences and Engineering (ECCOMAS)*, Barcelona, Spain, 11-14 September 2000.

[203] J. Strikwerda, "Initial boundary value problems for the method of lines," *J. Comput. Phys.*, vol. 34, pp. 94–107, 1980.

[204] V. Couailler and N. Liamis, "Unsteady Euler and Navier-Stokes flows simulations with an implicit Runge-Kutta method," in *Computational Fluid Dynamics'94*. J. Wiley, 1994, pp. 917–924.

[205] B. Gustafsson, "On the implementation of boundary conditions for the method of lines," *BIT Numer. Math.*, vol. 38, p. 293–314, 1998.

[206] M. Gasparo and S. Pieraccini, "Implicit residual smoothing in a parallel 2D Euler solver," *Intl J. Computer Math.*, vol. 72, pp. 313–324, 1999.

[207] A. Povitsky and P. Morris, "A high-order compact method in space and time based on parallel implementation of the Thomas algorithm," *J. Comput. Phys.*, vol. 161, pp. 182–203, 2000.

[208] J. Choi and J. J. Dongarra, "ScaLAPACK: a scalable linear algebra library for distributed memory concurrent computers," *Proceedings of the Fourth Symposiumon the Frontiers of Massively Parallel Computation*, pp. 120–127, 1992.

[209] E. Polizzi and A. Sameh, "SPIKE: A parallel environment for solving banded linear systems," *Comput. Fluids*, vol. 36, pp. 113–120, 2007.

[210] K. Ki-Ha, K. Ji-Hoon, P. Xiaomin, and C. Jung-Il, "PaScaL TDMA: A library of parallel and scalable solvers for massive tridiagonal systems," *Computer Phys. Commun.*, vol. 260, p. 107722, 2021.

[211] C. Borel and F. Roux, "Implicit multi-domain method for unsteady compressible inviscid fluid flows around 3D projectiles," in *Conference on Parallel Computational Fluid Dynamics,* 10-12 June 1991, K. Reinsch, W. Schmidt, A. Ecer, J. Häuser, and J. Periaux, Eds. Stuttgart, Germany: Elsevier Science Publishers B.V., 1992, pp. 47–58.

[212] A. Lerat and Z.-N. Wu, "Stable conservative multidomain treatments for implicit Euler solvers," *J. Comput. Phys.*, vol. 123, pp. 45–64, 1996.

[213] Z.-N. Wu and H. Zou, "Grid overlapping for implicit parallel computation of compressible flows," *J. Comput. Phys.*, vol. 157, pp. 2–43, 2000.

[214] M. Visbal and D. Gaitonde, "High-order-accurate methods for complex unsteady subsonic flows," *AIAA J.*, vol. 37, no. 10, pp. 1231–1239, 1999.

[215] T. Pulliam, "Artificial dissipation models for the Euler equations," *AIAA J.*, vol. 24, no. 12, pp. 1931–1940, 1986.

[216] H. Choi and P. Moin, "Effect of the computational time-step on numerical solutions of turbulent flow," *J. Comput. Phys.*, vol. 113, pp. 1–4, 1994.

[217] A. Vreman and J. Kuerten, "Comparison of direct numerical simulation databases of turbulent channel flow at Re_τ=180," *Phys. Fluids*, vol. 26, p. 015102, 2014.

[218] P. Parnaudeau, J. Carlier, D. Heitz, and E. Lamballais, "Experimental and numerical studies of the flow over a circular cylinder at Reynolds number 3900," *Phys. Fluids*, vol. 20, p. 085101, 2008.

[219] "4th International Workshop on High-Order CFD Methods, sponsored by NASA, AIAA, DLR and Army Research Office (ARO)," In: June 3-4, 2015 at the Eccomas / 6th European Conference on CFD (ECFD VI), Crete, Case AS1, https://how4.cenaero.be/content/as1-dnsles-infinite-cylinder-re3900.

[220] C. Norberg, "Effects of Reynolds number and low-intensity free stream turbulence on the flow around a circular cylinder," Chalmers University of Technology, Department of Applied Thermoscience and Fluid Mechanics, Gothenburg, Sweden, Tech. Rep. 87-2, 1987.

[221] L. M. Lourenco and C. Shih, "Characteristics of the plane turbulent near wake of a circular cylinder, a particle image velocimetry study," 1994, published in Ref.[351].

[222] M. Thompson and K. Hourigan, "The shear-layer instability of a circular cylinder wake," *Phys. Fluids*, vol. 17, p. 021702, 2005.

[223] O. Lehmkuhl, I. Rodríguez, R. Borrell, and A. Oliva, "Low-frequency unsteadiness in the vortex formation region of a circular cylinder," *Phys. Fluids*, vol. 25, p. 085109, 2013.

[224] G. Tian and Z. Xiao, "New insight on large-eddy simulation of flow past a circular cylinder at subcritical Reynolds number 3900," *AIP Advances*, vol. 10, p. 085321, 2020.

[225] P. Elofsson and P. Alfredsson, "An experimental study of oblique transition in plane Poiseuille flow," *J. Fluid Mech.*, vol. 358, pp. 177–202, 1998.

[226] S. Berlin, M. Wiegel, and D. Henningson, "Numerical and experimental investigations of oblique boundary layer transition," *J. Fluid Mech.*, vol. 393, pp. 23–57, 1999.

[227] P. Schlatter and R. Örlü, "Assessment of direct numerical simulation data of turbulent boundary layers," *J. Fluid Mech.*, vol. 659, pp. 116–126, 2010.

[228] X. Wu and P. Moin, "Direct numerical simulation of turbulence in a nominally zero-pressure-gradient flat-plate boundary layer," *J. Fluid Mech.*, vol. 360, p. 5–41, 2009.

[229] C. Wenzel, B. Selent, M. Kloker, and U. Rist, "DNS of compressible turbulent boundary layers and assessment of data/scaling-law quality," *J. Fluid Mech.*, vol. 842, pp. 428–468, 2018.

[230] C. Bogey and C. Bailly, "Turbulence and energy budget in a self-preserving round jet: direct evaluation using large-eddy simulation," *J. Fluid Mech.*, vol. 627, pp. 129–160, 2009.

[231] J. Sillero, J. Jimenez, and R. Moser, "One-point statistics for turbulent wall-bounded flows at Reynolds numbers up to $\delta^+ \approx 2000$," *Phys. Fluids*, vol. 25, p. 105102, 2013.

[232] P. Schlatter, Q. Li, G. Brethouwer, A. Johansson, and D. Hennigson, "Simulations of spatially evolving turbulent boundary layers up to $re_\theta = 4300$," *Intl J. Heat Fluid Flow*, vol. 31, pp. 251–261, 2010.

[233] G. Eitel-Amor, R. Örlü, and P. Schlatter, "Simulation and validation of a spatially evolving turbulent boundary layer up to $Re_\theta = 8300$," *Intl J. Heat Fluid Flow*, vol. 47, pp. 57–69, 2014.

[234] J. Capon, "High-resolution frequency-wavenumber spectrum analysis," *Proc. IEEE*, vol. 57, no. 8, pp. 1408–1418, 1969.

[235] N. Hutchins and I. Marusic, "Evidence of very long meandering features in the logarithmic region of turbulent boundary layers," *J. Fluid Mech.*, vol. 579, pp. 1–28, 2007.

[236] E. R. van Driest, "The turbulent boundary layer with variable Prandtl number," in *50 Jahre Grenzschichtforschung: Eine Festschrift in Originalbeiträgen*, H. Görtler and W. Tollmien, Eds. Wiesbaden: Vieweg+Teubner Verlag, 1955, pp. 257–271.

[237] M. Morkovin, "Effects of compressibility on turbulent flows," in *Mécanique de la Turbulence*. Paris: CNRS, 1962, pp. 367–380.

[238] X. Gloerfelt and F. Margnat, "Effect of Mach number on boundary layer noise," *20th AIAA/CEAS AeroAcoustics Conference,* 16-20 June, Atlanta, Georgia, AIAA Paper 2014-3291, 2014.

[239] L. Erm and P. Joubert, "Low-Reynolds-number turbulent boundary layers," *J. Fluid Mech.*, vol. 230, pp. 1–44, 1991.

[240] L. Castillo and T. Johansson, "The effects of the upstream conditions on a low Reynolds number turbulent boundary layer with zero pressure gradient," *J. Turbulence*, vol. 3, p. 031, 2002.

[241] P. Schlatter and R. Örlü, "Turbulent boundary layers at moderate Reynolds numbers: inflow length and tripping effects," *J. Fluid Mech.*, vol. 710, pp. 5–34, 2012.

[242] I. Marusic, K. Chauhan, V. Kulandaivelu, and N. Hutchins, "Evolution of zero-pressure-gradient boundary layers from different tripping conditions," *J. Fluid Mech.*, vol. 783, pp. 379–411, 2015.

[243] J. Poggie, N. Bisek, and R. Gosse, "Resolution effects in compressible, turbulent boundary layer simulations," *Comput. Fluids*, vol. 120, pp. 57–69, 2015.

[244] J. Kim, P. Moin, and R. Moser, "Turbulence statistics in fully developed channel flow at low Reynolds number," *J. Fluid Mech.*, vol. 177, pp. 133–166, 1987.

[245] K. Fukagata, K. Iwamoto, and N. Kasagi, "Contribution of Reynolds stress distribution to the skin friction in wall-bounded flows," *Phys. Fluids*, vol. 14, p. L73, 2002.

[246] T. Gomez, V. Flutet, and P. Sagaut, "Contribution of Reynolds stress distribution to the skin friction in compressible turbulent channel flows," *Phys. Rev. E*, vol. 79, p. 035301, 2009.

[247] N. Renard and S. Deck, "A theoretical decomposition of mean skin friction generation into physical phenomena across the boundary layer," *J. Fluid Mech.*, vol. 790, pp. 339–367, 2016.

[248] W. Li, Y. Fan, D. Modesti, and C. Cheng, "Decomposition of the mean skin-friction drag in compressible turbulent channel flows," *J. Fluid Mech.*, vol. 875, pp. 101–123, 2019.

[249] Y. Fan, W. Li, and S. Pirozzoli, "Decomposition of the mean friction drag in zero-pressure-gradient turbulent boundary layers," *Phys. Fluids*, vol. 31, p. 086105, 2019.

[250] P. Zhang and Z. Xia, "Contribution of viscous stress work to wall heat flux in compressible turbulent channel flows," *Phys. Rev. E*, vol. 102, p. 043107, 2020.

[251] C. Wenzel, T. Gibis, and M. Kloker, "About the influences of compressibility, heat transfer and pressure gradients in compressible turbulent boundary layers," *J. Fluid Mech.*, vol. 930, p. A1, 2022.

[252] D. Xu, J. Wang, and S. Chen, "Skin-friction and heat-transfer decompositions in hypersonic transitional and turbulent boundary layers," *J. Fluid Mech.*, vol. 941, p. A4, 2022.

[253] A. C. Mandal, L. Venkatakrishnan, and J. Dey, "A study on boundary-layer transition induced by free-stream turbulence," *J. Fluid Mech.*, vol. 660, pp. 114–146, 2010.

[254] T. Kurian and J. Fransson, "Grid-generated turbulence revisited," *Fluid Dyn. Res.*, vol. 41, p. 021403, 2009.

[255] T. Sayadi and P. Moin, "Large eddy simulation of controlled transition to turbulence," *Phys. Fluids*, vol. 24, p. 114103, 2012.

[256] P. Andersson, M. Berggren, and D. Henningson, "Optimal disturbances and bypass transition in boundary layers," *Phys. Fluids*, vol. 11, no. 1, pp. 134–150, 1999.

[257] P. Luchini, "Reynolds-number-independent instability of the boundary layer over a flat surface: optimal perturbations," *J. Fluid Mech.*, vol. 404, pp. 289–309, 2000.

[258] P. Ricco and X. Wu, "Response of a compressible laminar boundary layer to free-stream vortical disturbances," *J. Fluid Mech.*, vol. 587, pp. 97–138, 2007.

[259] E. Marensi, P. Ricco, and X. Wu, "Nonlinear unsteady streaks engendered by the interaction of free-stream vorticity with a compressible boundary layer," *J. Fluid Mech.*, vol. 817, pp. 80–121, 2017.

[260] A. Tumin and E. Reshotko, "Optimal disturbances in compressible boundary layers," *AIAA J.*, vol. 41, no. 12, pp. 2357–2363, 1984.

[261] D. Ohno, B. Selent, M. Kloker, and U. Rist, "Direct numerical simulation of bypass transition under free-stream turbulence for compressible flows," in *International Conference on High Performance Computing in Science and Engineering '21*, W. Nagel, D. Kröner, and M. Resch, Eds. Springer, 2023, pp. 223–238.

[262] S. Mamidala, A. Weingärtner, and J. Fransson, "A comparative study of experiments with numerical simulations of free-stream turbulence transition," *J. Fluid Mech.*, vol. 951, p. A46, 2022.

[263] K. Durovic, "Direct numerical simulation of boundary - layer transition with free-stream turbulence," Ph.D. dissertation, KTH Royal Institute of Technology, 2022.

[264] N. Otsu, "A threshold selection method from grey-level histograms." *IEEE Trans. Syst. Man Cybern.*, vol. 9, pp. 62–66, 1979.

[265] G. B. Schubauer and P. S. Klebanoff, "Contributions on the mechanics of boundary layer transition," Natl. Adv. Commit. Aeronaut.,Washington, DC, Tech. Rep. 1289, 1955.

[266] T. Kreilos, T. Khapko, P. Schlatter, Y. Duguet, D. S. Henningson, and B. Eckhardt, "Bypass transition and spot nucleation in boundary layers," *Phys. Rev. Fluids*, vol. 4, pp. 043 602,1–13, 2016.

[267] M. Dellacasagrande, D. Lengani, D. Simoni, J. Pralits, K. Durovic, A. Hanifi, and D. Henningson, "Statistical characterization of free-stream turbulence induced transition under variable Reynolds number, free-stream turbulence, and pressure gradient," *Phys. Fluids*, vol. 33, pp. 094 115,1–17, 2021.

[268] J. Mans, H. de Lange, and A. van Steenhoven, "Sinuous breakdown in a flat plate boundary layer exposed to free-stream turbulence," *Phys. Fluids*, vol. 19, p. 088101, 2007.

[269] R. Bose and P. A. Durbin, "Transition to turbulence by interaction of free-stream and discrete mode perturbations," *Phys. Fluids*, vol. 28, pp. 114 105,1–19, 2016.

[270] P. Manneville, "Laminar-turbulent patterning in transitional flows," *Entropy*, vol. 19, p. 316, 2017.

[271] L. Tuckerman, M. Chantry, and D. Barkley, "Patterns in wall-bounded shear flows," *Ann. Rev. Fluid Mech.*, vol. 52, pp. 343–367, 2020.

[272] P. Kashyap, Y. Duguet, and O. Dauchot, "Flow statistics in the transitional regime of plane channel flow," *Entropy*, vol. 22, p. 1001, 2020.

[273] X. Xiao and B. Song, "The growth mechanism of turbulent bands in channel flow at low Reynolds numbers," *J. Fluid Mech.*, vol. 883, p. R1, 2020.

[274] ——, "Kinematics and dynamics of turbulent bands at low Reynolds numbers in channel flow," *Entropy*, vol. 22, p. 1167, 2020.

[275] Y. Duguet and P. Schlatter, "Oblique laminar-turbulent interfaces in plane shear flows," *Phys. Rev. Lett.*, vol. 110, p. 034502, 2013.

[276] S. Cherubini, P. De Palma, J.-C. Robinet, and A. Bottaro, "The minimal seed of turbulent transition in a boundary layer," *J. Fluid Mech.*, vol. 689, p. 221–253, 2011.

[277] S. Cherubini, J.-C. Robinet, and P. De Palma, "Numerical study of the effect of freestream turbulence on by-pass transition in a boundary layer," *Energy Procedia*, vol. 45, pp. 578–587, 2014, aTI 2013 - 68th Conference of the Italian Thermal Machines Engineering Association.

[278] S. Cherubini, P. De Palma, J.-C. Robinet, and A. Bottaro, "Edge states in a boundary layer," *Phys. Fluids*, vol. 23, p. 051705, 2011.

[279] Y. Duguet, P. Schlatter, D. Henningson, and B. Eckhardt, "Self-sustained localized structures in a boundary-layer flow," *Phys. Rev. Lett.*, vol. 108, p. 044501, 2012.

[280] D. Biau, "Laminar-turbulent separatrix in a boundary layer flow," *Phys. Fluids*, vol. 24, p. 034107, 2012.

[281] F. Waleffe, "On a self-sustaining process in shear flows," *Phys. Fluids*, vol. 9, pp. 883–900, 1997.

[282] R. Kerswell, "Nonlinear nonmodal stability theory," *Ann. Rev. Fluid Mech.*, vol. 50, pp. 319–345, 2018.

[283] P. Schmid, "Nonmodal stability theory," *Ann. Rev. Fluid Mech.*, vol. 39, pp. 129–162, 2007.

[284] V. Suponitsky, E. Avital, and M. Gaster, "On the three-dimensionality and control of incompressible cavity flow," *Phys. Fluids*, vol. 17, no. 104103, 2005.

[285] M. Goldstein, "Effect of free-stream turbulence on boundary layer transition," *Phil. Trans. R. Soc. A*, vol. 372, p. 20130354, 2014.

[286] X. Mao, T. Zaki, S. Sherwin, and H. Blackburn, "Transition induced by linear and nonlinear perturbation growth in flow past a compressor blade," *J. Fluid Mech.*, vol. 820, pp. 604–632, 2017.

[287] C. Pan, J. J. Wang, P. F. Zhang, and L. H. Feng, "Coherent structures in bypass transition induced by a cylinder wake," *J. Fluid Mech.*, vol. 603, pp. 367–389, 2008.

[288] S. Sugawara, T. Sato, H. Komatsu, and H. Osaka, "Effect of free stream turbulence on flat plate heat transfer," *Trans. Japan Soc. Mech. Engrs*, vol. 19, no. 80, pp. 18–25, 1953.

[289] C. E. Feiler and E. B. Yeager, "Effect of large-amplitude oscillations on heat transfer," NASA Technical Report, Tech. Rep. R-142, 192.

[290] W. C. Reynolds, W. M. Kays, and S. J. Kline, "Heat transfer in the turbulent incompressible boundary layer. I - Constant wall temperature," NASA Technical Memorandum, Tech. Rep. 12-1-58W, 1958.

[291] J. Kestin, "The effect of free-stream turbulence on heat transfer rates," *Adv. Heat Transfer*, vol. 3, 1966.

[292] J. C. Simonich and P. Bradshaw, "Effect of free-stream turbulence on heat transfer through a turbulent boundary layer," *Trans. ASME J. Heat Transfer*, vol. 100, no. 4, pp. 671–677, 1978.

[293] P. E. Hancock and P. Bradshaw, "The effect of free-stream turbulence on turbulent boundary layers," *J. Fluid Mech.*, vol. 105, pp. 284–289, 1983.

[294] M. F. Blair, "Influence of free-stream turbulence on turbulent boundary layer heat transfer and mean profile development, Part I—Experimental data," *Trans. ASME J. Heat Transfer*, vol. 105, no. 1, pp. 33–40, 1983.

[295] P. E. Hancock and P. Bradshaw, "Turbulence structure of a boundary layer beneath a turbulent free stream," *J. Fluid Mech.*, vol. 205, pp. 45–76, 1989.

[296] N. S. Sharp, S. Neuscamman, and Z. Warhaft, "Effects of large-scale free stream turbulence on a turbulent boundary layer," *Phys. Fluids*, vol. 21, no. 9, p. 095105, 2009.

[297] K. Nagata, Y. Sakai, and S. Komori, "Effects of small-scale freestream turbulence on turbulent boundary layers with and without thermal convection," *Phys. Fluids*, vol. 23, no. 6, p. 065111, 2011.

[298] K. A. Thole and D. G. Bogard, "High freestream turbulence effects on turbulent boundary layers," *Trans. ASME J. Fluids Eng.*, vol. 118, pp. 276–284, 1996.

[299] E. Dogan, R. J. Hearst, and B. Ganapathisubramani, "Modelling high Reynolds number wall–turbulence interactions in laboratory experiments using large-scale free-stream turbulence," *Phil. Trans. R. Soc. A*, vol. 375, no. 2089, p. 20160091, 2017.

[300] J. You and T. A. Zaki, "Conditional statistics and flow structures in turbulent boundary layers buffeted by free-stream disturbances," *J. Fluid Mech.*, vol. 866, p. 526–566, 2019.

[301] Y. Jooss, L. Li, T. Bracchi, and R. J. Hearst, "Spatial development of a turbulent boundary layer subjected to freestream turbulence," *J. Fluid Mech.*, vol. 911, pp. A4,1–28, 2021.

[302] R. Narasimha and S. N. Prasad, "Leading edge shape for flat plate boundary layer studies," *Exp. Fluids*, vol. 17, pp. 358–360, 1994.

[303] D. Dupuy, L. Gicquel, N. Odier, N. Duchaine, and T. Arts, "Analysis of the effect of intermittency in a high-pressure turbine blade," *Phys. Fluids*, vol. 32, pp. 095 101.1–19, 2020.

[304] R. Bhaskaran and S. Lele, "Large eddy simulation of free-stream turbulence effects on heat transfer to a high-pressure turbine cascade," *J. Turbulence*, vol. 11 N6, 2010.

[305] R. Vinuesa, A. Bobke, R. Örlü, and P. Schlatter, "On determining characteristic length scales in pressure-gradient turbulent boundary layers," *Phys. Fluids*, vol. 28, no. 5, pp. 1–13, 2016.

[306] S. Kline, W. Reynolds, F. Schraub, and P. Runstadler, "The structure of turbulent boundary layers," *J. Fluid Mech.*, vol. 30, no. 4, pp. 741–773, 1967.

[307] R. G. Jacobs and P. A. Durbin, "Shear sheltering and the continuous spectrum of the Orr-Sommerfeld equation," *Phys. Fluids*, vol. 10, no. 8, 1998.

[308] J. C. R. Hunt and P. A. Durbin, "Perturbed vortical layers and shear sheltering," *Fluid Dyn. Research*, vol. 24, pp. 375–404, 1999.

[309] M. W. Johnson and A. Fashifar, "Statistical properties of turbulent bursts in transitional boundary layers," *Intl J. Heat Fluid Flow*, vol. 15, pp. 283–290, 1994.

[310] S. Unnikrishnan and D. V. Gaitonde, "First-mode-induced nonlinear breakdown in a hypersonic boundary layer," *Comput. Fluids*, vol. 191, pp. 1–14, 2019.

[311] A. Prasad, "Calculation of the mixed-out state in turbomachine flows," in *Proc. ASME Turbo Expo.*, vol. GT2004-54021, Vienna, Austria, June 14-17 2004.

[312] R. Kiock, F. Lehthaus, N. Baines, and C. Sieverding, "The transonic flow through a plane turbine cascade as measured in four European wind tunnels," *Trans. ASME J. Eng. Gas Turbines Power*, vol. 108, pp. 277–284, 1986.

[313] C. Sieverding, M. Stanislas, and J. Snoeck, "The base pressure problem in transonic turbine cascades," *Trans. ASME J. Eng. Power*, vol. 102, pp. 711–718, 1980.

[314] A. Wheeler and J. Ong, "The role of dense gas dynamics on organic rankine cycle turbine performance," *Trans. ASME J. Eng. Gas Turbines Power*, vol. 135, p. 102603, 2013.

[315] W. Behrens and D. R. S. Ko, "Experimental stability studies in wakes of two-dimensional slender bodies at hypersonic speeds," *AIAA J.*, vol. 9, pp. 851–857, 1971.

[316] V. I. Lysenko, "Experimental studies of stability and transition in high-speed wakes," *J. Fluid Mech.*, vol. 392, pp. 1–26, 1999.

[317] S. L. Gai, D. P. Hughes, and M. S. Perry, "Large-scale structures and growth of a flat plate compressible wake," *AIAA J.*, vol. 40, pp. 1164–1169, 2002.

[318] P. J. Bryanston-Cross and J. J. Camus, "Auto and cross correlation measurements in a turbine cascade using a digital correlator," in *Proceedings of the ASME 1982 International Gas Turbine Conference and Exhibit*, vol. ASME paper 82-GT-132, London, UK, April 18-22 1982.

[319] W. E. Carscallen, H. U. Fleige, and J. P. Gostelow, "Transonic turbine vane wake flows," in *Proc. ASME Intl Gas Turbine Aeroengine Congr. Exhib.*, vol. ASME paper 96-GT-419, Birmingham, UK, June 10-13 1996.

[320] G. Persico, P. Rodriguez-Fernandez, and A. Romei, "High-fidelity shape-optimization of non-conventional turbomachinery by surrogate evolutionary strategies," *Trans. ASME J. Turbomach.*, vol. 141, p. 081010, 2019.

[321] A. Serafino, B. Obert, and P. Cinnella, "Multi-fidelity robust design optimization of an ORC turbine for high temperature waste heat recovery," *Energy*, vol. 269, p. 126538, 2023.

[322] Y. Zhang, R. D. Dwight, M. Schmelzer, J. F. Gomez, Z.-H. Han, and S. Hickel, "Customized data-driven RANS closures for bi-fidelity LES–RANS optimization," *J. Comput. Phys.*, vol. 432, p. 110153, 2021.

[323] W. Raymond and A. Garder, "A review of recursive and implicit filters," *Monthly Weather Review*, vol. 119, pp. 477–495, 1991.

[324] M. Nardini, T. O. Jelly, M. Kozul, R. D. Sandberg, P. Vitt, and G. Sluyter, "Direct numerical simulation of transitional and turbulent flows over multi-scale surface roughness—Part II: The effect of roughness on the performance of a high-pressure turbine blade," *Trans. ASME J. Turbomach.*, vol. 146, no. 3, p. 031009, 2023.

[325] D. R. Boldman, P. F. Brinich, and M. E. Goldstein, "Vortex shedding from a blunt trailing edge with equal and unequal external mean velocities," *J. Fluid Mech.*, vol. 75, pp. 721–735, 1976.

[326] C. H. Sieverding and H. Heinemann, "The influence of boundary layer state on vortex shedding from flat plates and turbine cascades," *Trans. ASME J. Turbomach.*, vol. 112, pp. 181–187, 1990.

[327] J.-P. Hickey, F. Hussain, and X. Wu, "Role of coherent structures in multiple self-similar states of turbulent planar wakes," *J. Fluid Mech.*, vol. 731, p. 312–363, 2013.

[328] M. M. Rai, "Shed vortex structure and phase-averaged velocity statistics in symmetric/asymmetric turbulent flat plate wakes," *Phys. Fluids*, vol. 30, no. 5, p. 055104, 2018.

[329] A. Rossiter, G. Pullan, and A. Melzer, "The influence of boundary layer state and trailing edge wedge angle on the aerodynamic performance of transonic turbine blades," *Trans. ASME J. Turbomach.*, vol. 145, p. 041008, 2023.

[330] J. F. Nash, V. G. Quincey, and J. Callinan, "Experiments on two-dimensional base flow at subsonic and transonic speeds," Aero. Res. Coun., Lond., *Tech. Memorandum* No.3427, 1963.

[331] D. V. Gaitonde, "Progress in shock wave/boundary layer interactions," *Prog. Aerosp. Sci.*, vol. 72, pp. 80–99, 2015.

[332] J. Larsson, S. Kawai, J. Bodart, and I. Bermejo-Moreno, "Large eddy simulation with modeled wall-stress: recent progress and future directions," *Bull. JSME*, vol. 3, pp. 15–00 418, 2016.

[333] S. T. Bose and G. I. Park, "Wall-modeled large-eddy simulation for complex turbulent flows," *Ann. Rev. Fluid Mech.*, vol. 50, pp. 535–561, 2018.

[334] F. De Vanna, M. Bernardini, F. Picano, and E. Benini, "Wall-modeled les of shock-wave/boundary layer interaction," *Intl J. Heat Fluid Flow*, vol. 98, p. 109071, 2022.

[335] S. B. Mamidala, A. Weingärtner, and J. H. M. Fransson, "Leading-edge pressure gradient effect on boundary layer receptivity to free-stream turbulence," *J. Fluid Mech.*, vol. 935, p. A30, 2022.

[336] J. P. Bons, "A review of surface roughness effects in gas turbines," *Trans. ASME J. Turbomach.*, vol. 132, pp. 021 004,1–16, 2010.

[337] X. Gloerfelt, L. Hake, A. Bienner, C. Matar, P. Cinnella, and S. aus der Wiesche, "Roughness effects on dense-gas turbine flow: comparison of experiments and simulations," in *Proc. ASME Turbo Expo.*, vol. GT2024-125144, London, United Kingdom, June 24-28 2024.

[338] L. Hake, F. Reinker, R. Wagner, S. aus der Wiesche, and M. Schatz, "The profile loss of additive manufactured blades for organic Rankine cycle turbines," *Int. J. Turbomach. Propuls. Power*, vol. 7, pp. 1–13, 2022.

[339] T. A. Zaki, J. G. Wissink, P. A. Durbin, and W. Rodi, "Direct computations of boundary layers distorted by migrating wakes in a linear compressor cascade," *Flow Turbul. Combust.*, vol. 83, pp. 307–322, 2009.

[340] V. Michelassi, L.-W. Chen, R. Pichler, and R. D. Sandberg, "Compressible direct numerical simulation of low-pressure turbines—Part II: Effect of inflow disturbances," *Trans. ASME J. Turbomach.*, vol. 137, pp. 071 005,1–12, 2015.

[341] D. Papadogiannis, F. Duchaine, F. Sicot, L. Gicquel, G. Wang, and S. Moreau, "Large eddy simulation of a high pressure turbine stage: effects of sub-grid scale modeling and mesh resolution," in *Proc. ASME Turbo Expo.*, vol. GT2014-25876, Düsseldorf, Germany, June 16-20 2014.

[342] V. Brunet, E. Croner, A. Minot, J. de Laborderie, E. Lippinois, S. Richard, J.-F. Boussuge, J. Dombard, F. Duchaine, L. Gicquel, T. Poinsot, G. Puigt, G. Staffelbach, L. Segui, O. Vermorel, N. Villedieu, J.-S. Cagnone, K. Hillewaert, M. Rasquin, G. Lartigue, V. Moureau, V. Couaillier, E. Martin, M. de la Llave Plata, J.-M. Le Gouez, and F. Renac, "Comparison of various CFD codes for LES simulations of turbomachinery: From inviscid vortex convection to multi-stage compressor," in *Turbo Expo: Power for Land, Sea, and Air*, ASME, Ed., no. GT2018-75523, 2018.

[343] F. Duchaine, J. Dombard, and L. Gicquel, "Integrated large eddy simulation of combustor and turbine interactions: effect of turbine stage inlet condition," in *Proc. ASME Turbo Expo.*, vol. GT2017-63473, Charlotte, NC, USA, June 26-30 2017.

[344] G. Comte-Bellot and S. Corrsin, "Simple Eulerian time correlation of full and narrow-band velocity signals in grid-generated, 'isotropic' turbulence," *J. Fluid Mech.*, vol. 48, no. 2, pp. 273–337, 1971.

[345] L. Hake, S. aus der Wiesche, S. Sundermeier, A. Bienner, X. Gloerfelt, and P. Cinnella, "Grid-generated decaying turbulence in an organic vapour flow," in *Proceedings of the 4th International Seminar on Non-Ideal Compressible Fluid Dynamics for Propulsion and Power (NICFD 2022)*, ser. ERCOFTAC series, E. S. T. K. I. S. A. P. M. G. A. White, M., Ed. Springer, 2023, vol. 29, pp. 181–190.

[346] S. Ghosal, "An analysis of numerical errors in Large-Eddy Simulations of turbulence," *J. Comput. Phys.*, vol. 125, pp. 187–206, 1996.

[347] J. Boudet, J. Caro, L. Shao, and E. Lévêque, "Numerical studies towards practical large-eddy simulation," *J. Thermal Science*, vol. 16, pp. 328–336, 2007.

[348] W. K. George, "The decay of homogeneous isotropic turbulence," *Phys. Fluids*, vol. 4, pp. 1492–1509, 1992.

[349] P. E. Roach, "The generation of nearly isotropic turbulence by means of grids," *Int. J. Heat and Fluid Flow*, vol. 8, pp. 82–92, 1987.

[350] P. J. Zwart, R. Budwig, and S. Tavoularis, "Grid turbulence in compressible flow," *Exp. in Fluids*, vol. 23, pp. 520–522, 1997.

[351] P. Beaudan and P. Moin, "Numerical experiments on the flow past a circular cylinder at sub-critical reynolds number," NASA Ames/Stanford University, CTR Annual Research Briefs, 1994.

List of Acronyms

AD	Artificial Dissipation
AMD	Advanced Micro Devices
BL	Boundary Layer
BZT	Bethe–Zel'dovich–Thompson
CFC	ChloroFluoroCarbon
CFD	Computational Fluid Dynamics
CFL	Courant–Friedrichs–Lewy
CLOWT	Closed-Loop Organic-Vapor Wind Tunnel
CPU	Central Processing Unit
DES	Detached Eddy Simulation
DDES	Delayed Detached Eddy Simulation
DDES-SLA	Delayed Detached Eddy Simulation-Shear Layer Adapted
DG	Dense gases
DNS	Direct Numerical Simulation
EoS	Equation of State
FD	Finite Differences
FIK	Fukagata-Iwamoto-Kasagi
FP	Flate Plate
FPG	Favorable Pressure Gradient
FST	FreeStream Turbulence
GCL	Geometric Conservation Law
GENCI	Grand Equipement National de Calcul Intensif
GPU	Graphical Processing Unit
HIT	Homogeneous Isotropic Turbulence
HPC	High Parallel Computing
IDDES	Improved Delayed Detached Eddy Simulation
IRS	Implicit Residual Smoothing
IRS1	One-sided first-order Implicit Residual Smoothing
IRS2	second-order Implicit Residual Smoothing
IRS4	fourth-order Implicit Residual Smoothing
IDRIS	Institut du Développement et des Ressources en Informatique Scientifique
KDE	Kernel Density Estimator

LE	Leading-Edge
LES	Large-Eddy Simulation
LST	Linear Stability Theory
MPI	Message Passing Interface
MUSCL	Monotonic Upstream-centered Scheme for Conservation Laws
MUSICAA	Multiblock Solver In Computational Aerodynamics and Aeroacoustics
NIST	National Institute of Standards and Technology
ORC	Organic Rankine Cycle
PIV	Particle Image Velocimetry
PRSV	Peng-Robinson-Stryjek-Vera
RANS	Reynolds-Averaged Navier Stokes
RD	Renard-Deck
REGAL-ORC	REal-GAs effects on loss mechanisms of ORC turbine flows
RFM	Random Fourier Modes
RK	Runge-Kutta
RK4	four-stage low-storage Runge-Kutta
SF	Selective Filtering
SGS	Sub-Grid Scale
SRS	Scale Resolving Simulations
TBL	Turbulent Boundary Layer
TE	Trailing-Edge
TGCC	Très Grand Centre de Calcul du CEA
TKE	Turbulent Kinetic Energy
TS	Tollmien-Schlichting
ZPG	Zero-Pressure Gradient
ZPGFP	Zero-Pressure Gradient Flat Plate

List of Symbols

Roman Letters

c	Sound speed
ch	Chord of the blade
c_p	Isobaric specific heat
c_v	Isochoric specific heat
$c_{v,\infty}$	Ideal gas isochoric specific heat
C_p	Pressure coefficient
C_f	Skin friction coefficient
d_{TE}	Diameter of the trailing edge
$\mathscr{D}$	Viscous stress tensor
e	Internal energy
E	Total specific energy
E_c	Eckert number
$E_{\bullet\bullet}$	Power spectra of $\bullet$ (u,v,w,u_s,...)
f	Frequency
F	Non-dimensional frequency
$\widehat{g}$	Amplification operator of the left hand side
$\widehat{\mathscr{G}}$	Amplification operator of the right hand side
h	Enthalpy
H	Shape factor
$\mathscr{H}$	Total enthalpy
J	Jacobian of the coordinate transformation
$\mathfrak{J}$	ratio of relative M variations to relative ρ variations at constant s
k	Wavenumber
K	Acceleration parameter
L^*	Blasius length scale
$L_\bullet$	Length of the domain in the $\bullet$-direction (x,y,z)
L_f	Integral length scale of the FST
M	Mach number
M	Turbulent Mach number
$\mathscr{M}$	Molar mass
n	Direction normal to the wall
ngh	Number of ghost points
$N_\bullet$	Number of points in the $\bullet$-direction (x,y,z)
p	Pressure
p_0	Total pressure
p_c	Critical pressure
Pr	Prandtl number
Pr_t	Turbulent Prandtl number

$\mathbf{q}$	Heat flux
R	Gas constant
R_g	Individual gas constant
$R_{\bullet\bullet}$	Correlation function of $\bullet$ (u,v,w,u_s,...)
$Re_\bullet$	Reynolds number based on $\bullet$ (x,L^*,u_τ,θ,...)
s	Entropy, Tangential direction in Chapters 5 & 6
St	Strouhal number
t	Time
T	Temperature
T_0	Total temperature
T_c	Critical temperature
T_u	FST intensity
u	Streamwise velocity
$u_\bullet$	Velocity in the $\bullet - direction$(s,n)
u_τ	Friction velocity
$\mathbf{u}$	Velocity vector
$\mathbf{U}$	Vector of conservative variables
v	Transversal velocity
V_c	Critical molar volume
v	specific volume
w	Spanwise velocity
x	Streamwise direction
y	Tranversal direction
z	Spanwise direction
Z	Compressibility factor
Z_c	Critical compressibility factor

Greek Letters

δ, δ_{99}	Boundary layer thickness at 99% of edge velocity
δ^*	Displacement boundary layer thickness
Δt	Timestep
$\Delta\bullet$	Grid step in the $\bullet$-direction (x, y, z, ξ, η)
ϵ	Dissipation rate
ε_0	Amplitude of inlet oblique modes
γ	Specific heat ratio
γ_{pv}	Isentropic exponent
γ_{peak}	Intermittency distribution function
Γ	Fundamental derivative of fluid dynamics
ω	Angular frequency
$\omega_\bullet$	Vorticity in the $\bullet$-direction (x,y,z)
ϕ	Phase
π	Pressure ratio

ρ	Density
ρ_0	Total density
ρ_c	Critical density
ξ	First direction of the curvilinear domain
η	Second direction of the curvilinear domain
θ	Momentum boundary layer thickness
$\theta_\bullet$	Contravariant velocity in the $\bullet$-direction (ξ, η)
θ_1	Smoothing parameter of IRS1
θ_2	Smoothing parameter of IRS2
θ_4	Smoothing parameter of IRS4
σ	CFL number
$\boldsymbol{\tau}_\bullet$	Viscous stress vector in the $\bullet$-direction
μ	Dynamic viscosity
μ_0	Dilute-gas limit viscosity
μ_p	Dense-gas effects contribution to μ in the Chung-Lee-Starling model
ν	Kinematic viscosity
λ	Thermal conductivity
λ_0	Dilute-gas limit thermal conductivity
λ_p	Dense-gas effects contribution to λ in the Chung-Lee-Starling model
λ_e	Spectral radius of the inviscid flux Jacobians
$\lambda_\bullet^e$	Spectral radius of the inviscid Jacobian matrix in $\bullet$-direction
λ_v	Spectral radius of the viscous flux Jacobians
λ_x	Streamwise wavelength
λ_z	Spanwise wavelength
$\lambda_{z,FS}$	Estimator of spanwise scales of laminar streaks from Fransson & Shahinfar [47]
$\overline{\omega}$	Acentric factor
$\overline{\xi}$	Dipole moment
$\overline{\xi_r}$	Reduced dipole moment
Ω^*	Lennard-Jones collision integral
ψ	Eucken-type correlation extended to polyatomic gases
Ψ	Wave angle
χ	Stagger angle
χ_f	Filtering coefficient
ζ_{out}	Enthalpy loss coefficient
ζ_{pass}	Enthalpy loss coefficient in the passage vane
ζ_{TE}	Enthalpy loss coefficient after the trailing edge
ζ_{Den}	Denton loss coefficient
$\zeta_{C_{p,b}}$	Contribution of the profile loss in Denton loss coefficient
ζ_θ	Contribution of the momentum loss in Denton loss coefficient
ζ_{δ^*}	Contribution of the blockage losses in Denton loss coefficient

Subscripts

$\bullet_\infty$	Freestream thermodynamic value
$\bullet_1$, $\bullet_{in}$	Inlet thermodynamic value
$\bullet_2$, $\bullet_{end}$	Outlet thermodynamic value
$\bullet_w$	Wall thermodynamic value
$\bullet_e$	Thermodynamic value at the edge of the boundary layer
$\bullet_{rms}$	Root-mean square value
$(\bullet)_T$	Isothermal evolution
$(\bullet)_\rho$	Evolution at constant density
$(\bullet)_s$	Isentropic evolution
$(\bullet)_t$, $\frac{\partial \bullet}{\partial t}$	Time derivative

Superscripts

$\overline{\bullet}$	Mean of the quantity
$\bullet'$	Fluctuations
$\bullet^+$	Quantity scaled by inner scales
$\bullet^e$	Inviscid
$\bullet^v$	Visco-thermal

Operators

$\mathscr{D}$	Dissipation term
$\mathscr{F}$	Numerical flux
$\mathscr{J}$	Implicit operator
$\mathscr{R}$	Space approximation operator
$\nabla(\bullet)$	Gradient
$\delta(\bullet)$	Difference operator
$\delta^+(\bullet)$	Upward difference operator
$\delta^-(\bullet)$	Backward difference operator
$\mu(\bullet)$	Average operator
$\widehat{\bullet}$	Fourier space

Arts et Métiers Sciences et Technologies

Aurélien BIENNER

Real gas effects on freestream turbulence induced transition and losses in ORC turbines

HESAM UNIVERSITÉ

RÉSUMÉ: Les cycles de Rankine organique (ORC) apparaissent comme l'une des solutions pour répondre aux défis énergétiques et environnementaux actuels, en raison de leur important potentiel énergétique. L'un des composants clés des ORC est le détendeur, généralement une turbine. Pour les petits systèmes, cette dernière fonctionne dans les régimes transsoniques à supersoniques et peut être influencée par les propriétés de la vapeur organique utilisée, présentant ainsi des effets non idéaux. Dans cette étude, nous examinons les transitions de couche limite (CL) et le mécanisme des pertes au sein des turbines dans des conditions représentatives des ORC pour le fluide Novec649. Nous débutons par la présentation des premières simulations numériques directes (DNS) et des simulations à grandes échelles (LES) de CL transitionnant et turbulentes de Novec dans des conditions subsoniques élevées. Dans l'état turbulent, les profils des propriétés dynamiques de l'écoulement sont peu affectés par les propriétés du gaz et demeurent très proches de la DNS incompressible, malgré la vitesse élevée de l'écoulement subsonique, même si de véritables mais très faibles effets de compressibilité sont présents. Notre stratégie LES est validée par rapport à la DNS et est utilisée pour étudier l'influence de la fréquence et de l'amplitude du forçage sur l'état turbulent établi. Ensuite, pour la première fois, nous étudions, par LES, la transition induite par la turbulence extérieure (FST) de CL de gaz dense sur des plaques planes et autour du bord d'attaque d'une turbine. En raison du nombre de Reynolds élevé, les fines CL interagissent avec de larges structures turbulentes qui peuvent, pour des intensités relativement élevées, favoriser un mécanisme de transition non linéaire au lieu du mécanisme classique de transition par stries laminaires. Comparées au Novec, les CL d'air se révèlent légèrement plus instables mais conservent globalement des caractéristiques similaires, notamment en ce qui concerne les mécanismes de transition observés. Enfin, l'écoulement autour d'une configuration idéalisée d'aube est abordé au moyen de simulations DDES (Delayed Detached-Eddy Simulations), permettant une analyse fine des phénomènes instationnaires. À mesure que la non-idéalité de l'écoulement augmente, le rapport de pression diminue et les pertes augmentent. Comparativement à l'air, la capacité thermique élevée du Novec réduit les fluctuations de température, éliminant ainsi le phénomène dit de séparation d'énergie, tout en accentuant les fluctuations de pression dans le sillage. En comparaison avec les DDES, les simulations RANS conduisent à une sous-estimation des pertes d'environ 20%.

Mots clés: ORC, Turbines, Simulations hautes-fidélités, Transition induite par la FST, Pertes

ABSTRACT: Organic Rankine Cycle (ORC) systems appear as one of the solutions to answer the current energy and environmental challenges, owing to their significant potential for generating power. A key component for ORC is the expander, most often a turbine. For small systems, the latter works in the transonic to supersonic regimes and can be affected by the properties of the organic vapor used and exhibit strong non-ideal effects. In the present study, we investigate boundary layer (BL) transitions and losses mechanism in turbines under conditions representative of ORC for the organic vapor Novec649. We begin by reporting the first direct numerical simulation (DNS) and large-eddy simulations (LES) of transitional and turbulent BL of Novec at high-subsonic conditions. In the turbulent state, the profiles of dynamic flow properties are little affected by the gas properties and remain very close to incompressible DNS, despite the high-subsonic flow speed and even if genuine but very small compressibility effects are present. Our LES strategy is validated against the reference DNS and is used to investigate the influence of forcing frequency and amplitude on the established turbulent state. Then, for the first time, we investigate freestream turbulence (FST)-induced transition of dense-gas BL on flat plates and around the leading-edge of a turbine by means of LES. Due to the high Reynolds number conditions, the thin BL experience large-scale incoming turbulent structures which can, for relatively high intensities, promote a non-linear transition mechanism instead of the classical laminar streak transition mechanism. Compared to Novec flows, air BL are found to be slightly more unstable but retains overall similar characteristics, in particular concerning the transition mechanisms observed. Finally, the flow around an idealized blade vane configuration is tackle by means of Delayed Detached-Eddy Simulations (DDES), allowing fine-detail analysis of unsteady flow phenomena. As the non-ideality of the flow increases, a lower pressure ratio is achieved and the losses increases. With regards to air, Novec's high heat capacity reduces temperature fluctuations, suppressing the so-called energy separation phenomena, while accentuating pressure fluctuations in the wake. Compared to DDES, RANS simulations leads to an underestimation of the losses by about 20%.

Keywords: ORC, Turbines, High-fidelity simulations, FST-induced transition, Losses